ELECTRONIC STRUCTURES OF IRON AND MANGANESE OXIDES

WITH APPLICATIONS TO THEIR MINERALOGY

by

DAVID MICHAEL SHERMAN

B.A. (Chemistry) University of California, Santa Cruz
(1980)

B.S. (Earth Sciences) University of California, Santa Cruz
(1980)

Submitted to the Department of
Earth, Atmospheric, and Planetary Sciences
in Partial Fulfillment of the
Requirements of the Degree of

DOCTOR OF PHILOSOPHY

at the

MASSACHUSETTS INSTITUTE OF TECHNOLOGY

August, 1984

© Massachusetts Institute of Technology 1984

Signature of Author _____
Department of Earth, Atmospheric, and Planetary Sciences
August 10, 1984

Certified by _____
Roger G. Burns, Thesis Supervisor

Accepted by _____
Chairman, Departmental Committee

MASSACHUSETTS INSTITUTE OF TECHNOLOGY
SEP 19 1984
LIBRARIES
WITHDRAWN FROM MIT LIBRARIES

Lindgren

2

ELECTRONIC STRUCTURES OF IRON AND MANGANESE OXIDES WITH APPLICATIONS TO THEIR MINERALOGY

by

DAVID MICHAEL SHERMAN

Submitted to the Department of
Earth, Atmospheric and Planetary Sciences
on August 10, 1984
in partial fulfillment of the requirements for the
Degree of Doctor of Philosophy in Geochemistry

ABSTRACT

The electronic structures of iron and manganese oxide and related minerals are investigated using Self-Consistent Field Xα Scattered Wave molecular orbital calculations on finite atomic clusters. Calculations on FeO_6, FeO_4, MnO_6 and $FeO_4(OH)_2$ coordination polyhedra are used to investigate the nature of chemical bonds, electronic spectra, magnetism, and mechanisms of electron transport in these minerals. Agreement between observed and predicted electronic spectra, geochemical behavior, and physical properties shows that much of the electronic structures of transition metal oxides can be understood in terms of a localized electron description. The highly-delocalized orbitals arising from the Fe or Mn 4s and 4p atomic orbitals, however, are less reliably described by clusters of this size.

Electronic spectra arising from the intraconfigurational d-d (ligand field) transitions and ligand to metal charge-transfer (LMCT) transitions were investigated by calculating one-electron orbital transition energies and deriving the relations between these energies and those of the spectroscopic multiplets. Experimental spectra in the near IR to near UV of several FeOOH and Fe_2O_3 minerals are obtained and compared with the results of theoretical calculations. The results give a consistent band assignment scheme and confirm the accuracy of the electronic structure calculations. The energies of LMCT transitions are of particular interest insofar as these transitions give rise to photochemical reactions between Fe-Mn oxides and organic molecules in natural waters. The calculations show that LMCT transitions in iron(III) and manganese(IV) oxides occur well into the near-ultraviolet. The lowest energy LMCT transition of manganese(IV) oxides is at 4.3 eV. The lowest energy LMCT transition in iron(III) oxides occurs at 4.7 eV. The strong optical absorption in the visible region observed in the spectra of iron(III) oxides results from ligand field transitions which are intensified by the magnetic coupling of next-nearest neighbor Fe atoms in the crystal structure. An additional electronic transition corresponding to the simultaneous excitation two magnetically-coupled Fe^{3+} cations is found at 480-530 nm in the spectra of the Fe_2O_3 and FeOOH minerals. The electronic structure calculations show that the ligand field theory parameter 10Dq for octahedrally coordinated Fe and Mn cations increases in the order $Mn^{2+} < Fe^{2+} < Fe^{3+} < Mn^{3+} < Mn^{4+}$. Calculated values for 10Dq are in very good agreement with those obtained from experimental spectra.

The molecular orbital calculations show that chemical bonds in iron and manganese oxides are not ionic and can have appreciable covalency depending on the formal oxidation state of the transition metal cation. The covalency of the metal-oxygen bond in octahedral coordination polyhedra is found to increase in the order $Mn^{2+} < Fe^{2+} < Fe^{3+} < Mn^{3+} < Mn^{4+}$. This trend in covalency among the different clusters is consistent with the observed geochemical behavior of iron and manganese. The calculated values for the ligand field theory parameter 10Dq and the energy of the lowest LMCT transition parallel the trend in covalency and show how electronic spectra can give information on chemical bonding in minerals.

The spin-unrestricted calculations show that covalency reduces the electronic spin (magnetic moment) of the Fe or Mn cations and induce a net spin on the oxygen ligands. The relative decrease in the Fe^{3+} magnetic moment in the different Fe^{3+} coordination polyhedra agree with both neutron diffraction studies and trends in the magnetic hyperfine field at the Fe nuecleus measured by Mossbauer spectroscopy. The spin-transfer by covalency (spin-polarization of the ligands) results in the superexchange interaction responsible for antiferromagnetism. Electronic structure calculations on a $(FeO_4(OH)_2)^{7-}$ cluster show that superexchange between hydroxyl-bridged Fe^{3+} cations will be weaker than that between oxo-bridged Fe^{3+} cations.

The nature of intervalence charge-transfer and electron delocalization in mixed valence iron oxides and silicates is investigated from a calculation of the electronic structure of a mixed-valence $(Fe_2O_{10})^{15-}$ dimer cluster. Here, the β-spin Fe^{2+} t_{2g} electron is found to be localized to its parent cation center which, in turn, implies that electron delocalization in mixed-valence minerals occurs through the motion of small polarons (hopping of localized electrons) and not by the formation of metal-metal bonds. Approximate energies of optical intervalence charge transfer energies are in reasonable agreement with experiment and are found to result from a $Fe^{2+}(t_{2g}^{\beta}) \rightarrow Fe^{3+}(e_g^{\beta})$ electronic excitation.

Thesis Supervisor: Roger G. Burns
Title: Professor of Mineralogy and Geochemistry

ACKNOWLEDGEMENTS

First I would like to thank my advisor, Roger Burns, not only for supporting me but also for pointing out many interesting problems and giving me unrestricted freedom in my research. Second, I wish to thank Keith Johnson (Dept. of Materials Science, MIT) for helpful discussions and much encouragement. The bulk of the work presented in this thesis is an application of the theoretical technique (SCF-Xα-SW method) developed by Professor Johnson. I would also like to thank Jack Tossell (Dept. of Chemistry, University of Maryland) for initial guidance, and Paco Leon for helpful discussions, regarding the use of the computer programs and other practical problems. Discussions with R. Frankel, H. Hartmann, G. Rossman, and T.D. Waite furthered my interest in the geochemistry of iron and I hope that some of the results presented in this work may be of value to them.

Finally I would like to thank my wife for her patience and all of my family for their encouragement.

This work was funded by NSF Grant no. EAR 8313585 (to study the electronic structures of Fe and Mn oxides) and NASA Grant no. NSG 7604 awarded to R.G. Burns.

TABLE OF CONTENTS

ABSTRACT 2

ACKNOWLEDGEMENTS 4

PREFACE 8

CHAPTER 1: Introduction

Overview 11

Quantum chemical aspects of Fe-Mn oxide mineralogy 12

Scope and Purpose of Investigation 16

References 21

CHAPTER 2: Models for the electronic structures of minerals and the theory of the SCF-Xα-SW method

The Hartree-Fock method for atoms and the Xα approximation . . 24

Models for the electronic structures of solids 28

Theory of the SCF-Xα-SW method 35

References 46

CHAPTER 3: The electronic structures of Mn^{2+}, Mn^{3+} and Mn^{4+} coordination sites in manganese oxides

Abstract 49

Introduction 50

Parameters of Calculation 51

Calculated molecular orbitals 53

Electronic spectra of Mn oxides 59

Applications to the crystal chemistry of Mn oxides. 68

Conclusions 75

References 77

CHAPTER 4: The electronic structures of Fe^{2+} and Fe^{3+} coordination sites in iron oxides

Abstract 82

Introduction 83

Parameters of calculations 85

Electronic structure of octahedral $(FeO_6)^{9-}$ and $(FeO_6)^{10-}$. . . 89

Electronic structure of tetrahedral $(FeO_4)^{5-}$ 98

The electronic structure of trigonal $(FeO_6)^{9-}$ 101

Electronic spectra of iron oxides and related minerals 103

Comparison with experimental spectra 117

Applications to the physical properties and crystal chemistry of iron oxides 127

Comparison with other calculations 136

Conclusions 137

References 139

CHAPTER 5: Electronic Structure of trans $(FeO_4(OH)_2)^{7-}$ coordination polyhedra

Abstract 145

Introduction 146

Cluster Geometries and Input Parameters 149

Calculated Molecular Orbitals 149

Applications to the Spectra of Fe^{3+} oxides and oxide hydroxides 156

Relation of Chemical Bonding to Physical Properties of Fe Oxides and Oxide Hydroxides 158

Conclusions 161

References 162

CHAPTER 6: Electronic Spectra of Iron Oxides and Oxide Hydroxides in the Near-IR to Near-UV

Abstract 164

Introduction 165

Experimental 172

Results and Discussion 174

Conclusions 184

References 186

CHAPTER 7: The electronic structure of the mixed-valence dimer $(Fe_2O_{10})^{15-}$; application to metal-metal charge transfer

Abstract 190

Introduction 191

Cluster Geometry and Input Parameters 195

Results and Discussion 197

Conclusions 204

References 205

CHAPTER 8: Overview of Results and Areas of Future Investigation . . . 207

APPENDIX 1: The Electronic Structures of Co^{3+} Coordination Sites in Fe-Mn Oxides: Application to the Uptake of Co in Marine Ferromanganese Nodules. 219

APPENDIX 2: Spectral Characteristics of the Iron Oxides with Application to the Martian Bright Region Mineralogy (reprinted from: The Journal of Geophysical Research, 87, 10169-10180,1982) 233

PREFACE

A few comments regarding the text are in order. In chapter 1, I give a brief outline of those aspects of the geochemistry of iron and manganese that are inherently quantum chemical in nature. From this quantum chemical perspective I argue that information regarding the electronic structures of iron and manganese oxides should lead to a number of geochemical applications in addition to being of fundamental interest. In chapter 2, I present a brief discussion of the more important theoretical topics which will form the basis of the approach used in subsequent chapters. Chapters 3,4,5,6 and 7 are written to be essentially self-contained manuscripts for publication. This has the shortcoming, however, of some degree of redundancy and repetition of material. For example, the essential features regarding the electronic structures of FeO_6 and MnO_6 polyhedra are the same. Hence, the discussions regarding the nature of the molecular orbitals in MnO_6 (chapter 3) and FeO_6 (chapter 4) clusters are very similar. Also the theoretical aspects of the optical (ligand field and ligand to metal charge-transfer) spectra of Fe^{3+} oxides and silicates are discussed in both chapters 4 and 6. The emphases in the two chapters are somewhat different, however. In chapters 3,4,5 and 7, I apply one or more cluster calculations to a variety of problems. Perhaps a more effective approach would be to dedicate each chapter to one problem or physical property (e.g. spectra or magnetism) and show how the different cluster calculations provide insight on that problem. The approach used here, however, is that usually found in the literature of applied quantum chemistry and is also the most convenient (for me, at least).

A few notes regarding energy units should also be made. All of the

molecular orbital energies are expressed in electron volts. This is the energy required to move an electron through an electrical potential of 1 volt. 1 eV is equivalent to 23.0609 kcal/mole. Electronic spectroscopic transition energies are characteristically expressed in reciprocal centimeters or wavenumbers (cm^{-1}), which, in turn, are obtained from the reciprocal of the wavelength. In subsequent chapters, however, spectroscopic transition energies are given in kiloKaisers or kK; 1 kK = 1000 cm^{-1}. The relation between electron volts and wavenumbers is 1 eV = 8.066×10^3 cm^{-1} = 8.066 kK.

CHAPTER 1:

Introduction

Overview

Oxides and silicates of iron and manganese are major components of marine sediments and other low-temperature geochemical environments. Moreover, both Fe and Mn oxides have been proposed to also occur in the surface mineralogy of Mars. The geochemistry of Fe and Mn is fairly complex. Both metals can exist in different oxidation states under Earth-surface conditions. This allows them, and their different oxide and silicate phases, to participate in a variety of redox equilibria in natural waters. Both iron and manganese oxides can occur as colloidal phases in natural waters and sediments which, in turn, result in a complex variety of surface chemical reactions. The latter range from the adsorption of other transition metal cations (e.g. Co, Ni) to sunlight-induced photo-oxidation of organic molecules. An important aspect of these minerals is that their electronic structures contain partially-occupied Fe or Mn 3d orbitals; this, in turn, is responsible for many aspects of their geochemistry and physical properties.

Quantum-Chemical Aspects of Fe-Mn Oxide Mineralogy

Chemical Bonding and Geochemistry

Phases such as iron and manganese oxides have traditionally been thought of as being ionic. This is certainly a poor approximation and cannot account for much of their crystal chemistries and physical properties. For example, the structures of several important manganese(IV) oxides (e.g. todorokite, psilomelene) would seem unlikely within the context of Pauling's rules for ionic solids. The different oxidation states of Fe and Mn show a wide range of solubility and, hence, geochemical mobility. This indicates differences in the Lewis acid behavior of these oxidation

Table 1.1: Important Fe^{3+} and Fe^{2+} Oxides and Oxide Hydroxide Minerals

Mineral	Formula	Structure Type	Comments
Hematite	α-Fe_2O_3	corundum	Antiferromagnetic, T_N = 958°K
Maghemite	γ-Fe_2O_3	defect Spinel	Ferrimagnetic, T_N > 725°K
Magnetite	Fe_3O_4	inverse Spinel	Metallic at T > 120°K, ferrimagnetic with T_N = 848°K
Wustite	FeO	rock salt	Unstable at Earth's surface
Goethite	α-FeOOH	diaspore	Antiferromagnetic with T_N = 393°K
Akaganeite	β-FeOOH	hollandite	Antiferromagnetic
Lepidocrocite	γ-FeOOH	boehmite	Paramagnetic, T_N = 73°K
Feroxyhyte	δ-FeOOH	disorded brucite	Ferrimagnetic, T_N > 400°K
Ferrihydrite	$xFe_2O_3 \cdot yH_2O$	unknown	Variable stoichiometry and magnetic properties
"Green Rust"	(Fe^{3+},Fe^{2+}) (O,OH,Cl,SO_4)	unknown	Mixed Valence, color due to IVCT, unstable

Table 1.2: Important Mn^{4+}, Mn^{3+} and Mn^{2+} Oxides and Oxide Hydroxides

Mineral	Formula	Structure Type
	Chain Structures	
pyrolusite	β-MnO_2	rutile
ramsdellite	MnO_2	ramsdellite
nsutite	$(Mn^{4+}, Mn^{3+}, Mn^{2+})(O,OH)_2$	pyrolusite + ramsdellite domains
groutite	α-MnOOH	ramsdellite
manganite	γ-MnOOH	distorted rutile
	Tunnel Structures	
hollandite	$(Ba,K)_{1-2}Mn_8O_{16}\cdot xH_2O$	double chains of MnO_6 octahedra linked to give 2x2 tunnels
romanechite (psilomelane)	$(Ba,K,Mn,Co)_2Mn_5O_{10}\cdot xH_2O$	treble and double chains of MnO_6 octahedra linked to give 3x2 tunnel structure
todorokite	$(Ca,Na,K,Ba,Mn)_2Mn_5O_{12}\cdot xH_2O$	
	Layer Structures	
Birnessite	$(Ca,Na)(Mn^{2+},Mg)Mn_6O_{14}\cdot xH_2O$	
Buserite	unknown	
Vernadite (δ-MnO_2)	unknown	

states which, in turn, implies variations in the covalencies of the metal-ligand bonds. Iron(III) and manganese(IV) oxides form several isostructural phases yet the surface chemistries of these phases are quite different: iron oxides tend to absorb anionic species while manganese(IV) oxides tend to absorb cationic species. Such differences undoubtably reflect the electronic structures and nature of chemical bonds at the surfaces of these minerals. An understanding of chemical bonds in minerals is of interest in that it can provide insight on geochemical trends and crystal structures. Moreover, the interpretation of data such as Mossbauer spectra of iron oxides requires recognizing the partial-covalent nature of the Fe-O bond.

Electronic Transitions and Spectra

All minerals exhibit electronic transitions in the high energy regime investigated by X-ray emission, absorption and photoelectron spectroscopy. In iron and manganese oxides and silicates, however, the low energy, partially occupied, 3d orbitals allows these minerals to also exhibit electronic transitions in the near-infrared, visible and near-ultraviolet energy regions. Within this range of energies occur the intraconfigurational transitions between the 3d orbitals ("ligand field transitions") and ligand to metal charge-transfer (LMCT) transitions. The characteristic energies of ligand field and LMCT transitions imply that these transitions can be activated by sunlight. A consequence of sunlight activated electronic transitions in Fe-Mn oxides and silicates is the possibility of photochemical reactions between these minerals and dissolved species in natural waters. For example, Waite (1983) has shown how colloidal iron oxides can, in the presence of sunlight, oxidize different

carboxylic acids to release soluble Fe^{2+}. Sunda et al. (1983) found that Mn(IV) humic acid complexes in seawater undergo a sunlight-induced charge transfer transition resulting in the formation of soluble Mn(II) in the photic zone of the oceanic water column. These reactions imply that the geochemical cycles of iron and manganese are coupled to that of carbon. Moreover, several investigators (e.g. Bauer, 1978; Hartman, 1975) have proposed that photoreduction of CO_2 by ferrous silicates in the Precambrian was the source of early organic molecules leading to the chemical evolution of life. An understanding of the mechanisms of such photochemical reactions requires information on the nature and energies of LMCT and similar transitions. Information on the electronic structures of Fe and Mn oxides, therefore, is expected to not only provide such geochemical models with a greater theoretical foundation, but also point to additional photochemical processes which may be important in low-temperature geochemistry.

Apart from ligand field and LMCT transitions, minerals which contain cations in more than one oxidation state can exhibit intervalence charge-transfer transitions. This is the optical excitation of an electron from a state localized on one cation center to a state localized on an adjacent cation. The most common intervalence charge-transfer (IVCT) transition is $Fe^{2+} \rightarrow Fe^{3+}$. This phenomenom gives rise to the intense colors and pleochroism observed in glauchophane, hornblende, and vivianite. One example of an iron oxide which exhibits IVCT transitions is the so-called "green rust" phase which occurs as an intermediate during the oxidation of $Fe(OH)_2$. In all of these minerals, the exact nature of IVCT transitions is poorly understood. A related type of phenomenon is thermally-induced

electron delocalization in mixed-valence iron-bearing minerals. This will be discussed below.

In the laboratory, optical spectra of minerals have been of interest insofar as they offer potential methods to investigate cation site occupancies and valence states (Burns, 1970). Ligand field and LMCT electronic transitions involve states associated with the bonding and antibonding interactions in the solid; as such, their energies and intensities can reflect a good deal of crystal chemical information.

A second application of mineral spectroscopy is the investigation of planetary surface mineralogies through remote-sensed reflectance spectra. At present, nearly all of our knowledge regarding the surface mineralogy of Mars, for example, is based on results from remote-sensed reflectance spectra (McCord et al., 1982; Singer et al., 1979). The reflectance spectra of Mars are dominated by features attributable to Fe^{3+} ligand field transitions; however, the present understanding of Fe^{3+} spectra in minerals is rather poor and, as such, it is difficult to derive any precise mineralogical information from these spectra.

Magnetism

One important consequence of covalent bonding, together with the presence of unpaired 3d electrons, is magnetism. Under geochemical conditions, all Mn^{4+} oxides are paramagnetic; iron oxides, however, can be paramagnetic, antiferromagnetic or ferrimagnetic. Magnetic coupling between adjacent Fe cations is presumably through superexchange--that is, the indirect coupling of Fe cations through the intervening oxide or hydroxide anions. The superexchange interaction is determined by the geometries of the metal-ligand bonds and the degree of covalency. The ferrimagnetism of

magnetite, maghemite and hematite-ilmenite is responsible for the magnetic signatures in sediments exploited by paleomagnetic studies. On the other hand, the magnetochemistries of all of the iron oxides are relevant to mineralogy, primarily because the magnetochemistry of a mineral is directly related to its crystal structure and chemical bonding. Apart from being intimately associated with chemical bonding, the magnetic structures of Fe-Mn oxides also can effect their electronic spectra. The spin-forbidden ligand field transitions in Fe^{3+} or Mn^{2+} systems become allowed when the spins on adjacent Fe^{3+} or Mn^{2+} cations are coupled. This effect may sometimes be used to derive additional crystal chemical information from mineral spectra (Rossman, 1975; 1976a; 1976b). Sherman (1983) has shown how the relation between magnetic structure and electronic spectra can be used to define the crystal chemistry of Fe^{3+} in the surface mineralogy of Mars. Another important problem is the interpretation of magnetic hyperfine structure in the Mossbauer spectra of Fe oxides and silicates.

Mechanisms of electron transport

The electronic structures of Fe and Mn oxides also determine their electron transport properties; that is, whether these minerals are metals, semiconductors or insulators. This aspect of rock forming minerals has long been of geophysical interest because of the presumed relations between conductivity and temperature profiles in planetary interiors (e.g. Nitsan and Shankland, 1976). The nature of electron transport in low temperature minerals such as the Fe and Mn oxides should also be of geochemical interest, however, since this affects how these phases can participate in different redox equilibria. Understanding such phenomena requires knowing

the energies and degree of spatial localization of the electronic states near the Fermi energy. A fundamental question regarding the electronic structures of these minerals is whether the Fe or Mn 3d orbitals remain localized to their parent atoms or whether they form delocalized 3d bands resulting from metal-metal bonding.

A related problem is found in metal-metal charge-transfer transitions in mixed-valence transition metal bearing minerals. Thermally-induced delocalization of 3d electrons occurs in several minerals which contain transition metal cations in more than one oxidation state. The most famous example being magnetite (Fe_3O_4). It is not known, however, whether electron delocalization occurs through the "hopping" of localized electrons (small polarons) or through the motion of collective or itinerent electrons in a Fe 3d band.

Scope and Purpose of Investigation

In the chapters which follow, the electronic structures of Fe and Mn oxides will be investigated using molecular orbital calculations on finite atomic clusters which represent Fe or Mn coordination polyhedra. The theoretical rationale for this approach will be discussed in Chapter 2. In subsequent chapters, it will be shown that such a finite cluster approach is quite successful.

The quantum chemistry of Fe and Mn oxides is a broad subject; the major purpose of this investigation is to improve our understanding of the electronic structures of these minerals so that studies of their geochemistry can be approached with a greater theoretical foundation. On the other hand, there are several specific, and related, problems which will be addressed:

1. The first problem, and that which will dominate most chapters, is determining the energies and band assignments of the electronic transitions observed in the spectra of Fe and Mn oxides and silicates. Investigations of this kind are especially needed for Fe-Mn oxides in order to provide a greater theoretical basis for understanding mechanisms of photochemical reactions in geochemical systems and interpreting remote sensed spectra of the Earth and Mars. Nearly all of the electronic transitions which occur in Fe-Mn oxides and silicates are localised on the metal atom and its immediate coordination environment (this aspect of the electronic structures of these minerals will be discussed in Chapter 2). In subsequent chapters, it will be shown that the electronic structures of metal atom coordination polyhedra can give a good description of ligand field and LMCT transition energies in these minerals. In Chapter 3, the electronic spectra of manganese oxides (and silicates) will be treated by comparing theoretical electronic transition energies with existing experimental spectra. In Chapters 4 and 5, the optical spectra of Fe^{3+} oxides will be treated in the same way but in much greater detail; because of the geochemical abundance of ferric iron, electronic transitions of this species dominate both laboratory and remote-sensed spectra of minerals. An understanding of the electronic spectra of Fe^{3+} coordination sites, therefore, is a more pressing concern than that of manganese. In addition, the electronic spectra of Fe^{3+} oxides and silicates are poorly understood. In Chapter 6, experimental results on the optical spectra of Fe^{3+} oxides are presented and compared with the results of molecular orbital calculations.

2. The second problem to be addressed in this investigation is determining the natures of the Fe-O and Mn-O chemical bonds and how they

relate to the crystal chemistry, electronic spectra, and magneto-chemistries of these minerals.

3. The final problem to be addressed is understanding the nature of electron delocalization and intervalence charge-transfer transitions in mixed-valence iron oxides and silicates. These phenomena will be addressed in Chapter 7 where the electronic structure of a mixed-valent $(Fe_2O_{10})^{15-}$ binuclear cluster will be presented. This problem is of fundamental importance insofar as it is intimately related to the existence of localized versus collective electronic states in these minerals.

References

Burns, R.G. (1970) Mineralogical applications of crystal field theory, Cambridge University Press, Cambridge, England.

Burns, R.G. (1981) Intervalence transitions in mixed-valence minerals of iron and titanium, Annual Reviews of Earth and Planetary Science, 9, 345-383.

Bauer, M.E. (1978) Thermodynamics of heterogeneous iron-carbon systems: implications for the terrestrial primitive reducing atomosphere, Chemical Geology, 22, 189-206.

Hartman, H. (1975) Speculations on the origin and evolution of metabolism, Journal of Molecular Evolution, 4, 359-370.

McCord, T.B., R.N. Clark, and R.B. Singer (1982) Mars: near-infrared spectral reflectance of surface regions and compositional implications, Journal of Geophysical Research, 87, 3021-3032.

Nitsan, U., and T.J. Shankland (1976) Optical properties and electronic structures of mantle silicates, Geophysical Journal of the Royal Astronomical Society, 45, 59-87.

Rossman, G.R. (1975) Spectroscopic and magnetic studies of ferric iron hydroxy sulfates: intensification of color in ferric iron clusters bridged by a single hydroxide ion, American Mineralogist, 60, 698-704.

Rossman, G.R. (1976a) Spectroscopic and magnetic studies of ferric iron hydroxy sulphates: the series $Fe(OH)SO_4 \cdot nH_2O$ and the jarosites, American Mineralogist, 61, 398-404.

Rossman, G.R. (1976b) The optical spectroscopic comparison of the ferric iron tetrameric clusters in amarantite and leucophosphite, American Mineralogist, 61, 933-938.

Sherman, D.M. (1983) The effect of local magnetic interactions on the crystal field spectra of Fe^{3+} in minerals, Lunar and Planetary Science XIV,

Singer, R.B., T.B. McCord, R.N. Clark, and J.B. Adams (1979) Mars surface composition from reflectance spectroscopy: a summary, Journal of Geophysical Research, 84, 8415-8426.

Sunda, W.G., S.A. Huntsman, and G.R. Harvey (1983) Photoreduction of manganese oxides in seawater and its geochemical and biological implications, Nature, 301, 234-236.

Waite, T.D. (1983) Photoredox properties of iron in natural waters, Ph.D. dissertation, Massachusetts Institute of Technology.

CHAPTER 2:

Models of Electronic Structure in Minerals and the Theory of the SCF-Xα-SW Method

The Hartree-Fock Method For Atoms

Before discussing specific models for the electronic structures of solids, it is worthwhile to first outline the Hartree-Fock method and the independant electron approximation. This is the basis for nearly all theoretical calculations in quantum chemistry. The Xα (or Hartree-Fock-Slater) method, which will be used in calculations reported here, is best understood within the context of the Hartree-Fock theory; it differs from the latter only in the "exchange potential" (described below).

The Schrodinger equation for an N-electron atom is

$$\left(\frac{-h^2}{2m} \sum \nabla_i^2 - \sum \frac{Ze^2}{r_i} + \sum_{i<j} \frac{e^2}{r_{ij}} \right) \Psi = E\Psi \qquad (2.1)$$

Here, the first summation is the electronic kinetic energy, the second summation is the electron-nuclear attraction, and the third summation is the interelectronic repulsion. Ψ is the multielectronic wavefunction where $\Psi = \Psi(r_1, r_2, \cdots r_N; r_{12}, r_{13} \cdots r_{N-1,N})$ and E is the total energy of the system. The many-body problem is insoluble. The first, and most fundamental, approximation is to assume that Ψ can be represented by a single Slater determinant over "one-electron orbitals":

$$\Psi = \begin{vmatrix} \psi_1(1) & \psi_2(1) & \cdots & \psi_N(1) \\ \psi_1(2) & \psi_2(2) & \cdots & \psi_N(2) \\ \vdots & \vdots & \vdots & \vdots \\ \psi_1(N) & \psi_2(N) & \cdots & \psi_N(N) \end{vmatrix} \qquad (2.2)$$

This is, essentially, the independant electron approximation; it assumes that the electronic motions can be separated and that one can solve for a

a set of "one-electron orbitals". In many cases, a given state of a multielectronic system is, in fact, described by a single Slater determinent. In general, however, the correct solution will be best approximated by a linear combination of Slater determinents; this procedure is referred to as configuration interaction.

In the spin-restricted Hartree-Fock approximation, we set $\psi_i(j) = \phi_i(j)\sigma_i(j)$ where ϕ_i and σ_i are the spatial and spin orbitals; that is, we require the spin-up (α-spin) and spin-down (β-spin) electrons to occupy the same spatial orbitals. This approach is correct for closed-shell systems but for open-shell systems (e.g. transition metals with unpaired electrons) it gives only a crude approximation.

The expectation value for the total energy of the system is given as

$$\langle E \rangle = \frac{\langle \Psi | H | \Psi \rangle}{\langle \Psi | \Psi \rangle} \tag{2.3}$$

Using the variational principle, we can improve the wavefunction by minimizing the total energy with respect to the one electron orbitals. Doing this gives the Hartree-Fock equations:

$$[1/2\nabla^2 + V_C + V_X]\psi_i = \varepsilon_i \psi_i \tag{2.4}$$

The first term in the brackets is the one-electron kinetic energy operator. V_C is the coulomb potential which is given as

$$V_C(r_1) = \frac{-2Z}{r_1} + \sum_j (\psi_j^*(r_2)\psi_j(r_2)(e^2/r_{12})dv_2 \tag{2.5}$$

and describes the electron-nucleus attraction and electron-electron repulsion. The second term, V_X, is the "exchange potential" and is purely quantum mechanical in origin. This is given by

$$V_X(r_1) = \frac{-\sum_{j \| i} \int \psi_i^*(r_1)\psi_j^*(r_2)(e^2/r_{12})\psi_j(r_1)\psi_i(r_2)dv_2}{\psi_i^*(r_1)\psi_i(r_1)} \qquad (2.6)$$

where the summation is over electrons with parallel spin.

The Xα approximation

The Xα approximation is to replace the exchange term in the Hartree-Fock equation by a statistical average given by

$$V_\alpha = -6\alpha[3/8\pi\ \rho(r)]^{1/3} \qquad (2.7)$$

Here $\rho(r)$ is the charge density calculated using the definition

$$\rho(r) = \sum_i n_i\phi_i^*(r)\phi_i(r) \qquad (2.8)$$

and α is an adjustable scaling factor chosen so that the Xα total energy equals that obtained using the Hartree-Fock method.

A useful feature of the Xα approximation is that the exchange potential (equation 3) for spin up electrons can be different from that for spin down electrons. This is done simply by setting the charge-density used in the exchange potential to be that due to only electrons with the same spin. This approach is essential for a realistic treatment of open shell systems (e.g. transition metals with unpaired electrons). If unpaired electrons are present, the exchange potentials, and consequently the spin-up (α-spin) and spin down (β-spin) orbitals and orbital energies, will be different.

In the conventional Hartree-Fock approach, the energy of a spin-orbital ϕ_i, containing n_i electrons, is given by an ionization energy,

$$\varepsilon_i = \langle E(n_i-1)\rangle - \langle E(n_i)\rangle \qquad (2.9)$$

where $\langle E(n_i)\rangle$ is the total energy of the system when the occupancy of orbital ϕ_i is n_i. This is formally known as Koopman's theorem. Note, however, that its derivation assumes that the orbitals remain unchanged during the ionization; this may often be a poor approximation insofar as one expects the orbitals to "relax" about the new electronic configuration of the ionized state. In the Xα formalism, the orbital eigenvalues have a somewhat different meaning: If $\langle E\rangle$ is the total energy of the system, then the orbital eigenvalues ε_i are given by

$$\varepsilon_i = \frac{\partial\langle E(n_i)\rangle}{\partial n_i} \tag{2.10}$$

Accordingly, the physical nature of the Xα orbital eigenvalues is similar to the notion of "orbital electronegativity".

To evaluate the energy required for a transition between two states one could calculate the total energy of the system in each state and take the difference. Numerically, this would be very inefficient; electronic transition energies are on the order of a few electron volts while total energies are on the order of 10^4-10^5 electron volts. Slater (1974), however, has shown that one may accurately evaluate the difference between the Xα total energies of two states of a system by using the "transition state" concept. The transition state is defined as having orbital occupancies midway between those found in the initial and final states. Given the transition state configuration, it can be shown that the energy difference between the initial and final states of the system is given by

$$\Delta E = \langle E\rangle_A - \langle E\rangle_B \simeq \sum_i \{n_A(i)-n_B(i)\}\varepsilon_{ts}(i) \tag{2.11}$$

where $n_A(i)$ and $n_B(i)$ are the occupancies of orbital i in the states A and

B, respectively, and $\varepsilon_{ts}(i)$ is the energy of orbital i in the transition state with occupancy

$$n_{ts}(i) = \{n_A(i) + n_B(i)\}/2 \qquad (2.12)$$

One important advantage of the transition state procedure is that it takes into account any orbital relaxation which occurs during the transition.

Models for the Electronic Structures of Solids

Localized electron models

The simplest approach to the electronic structures of solids is the classical electrostatic or ionic bonding model. Here, the solid is viewed as a collection of ions held together by their electrostatic interaction. If this is the case, then the electronic states of the solid can be obtained from the atomic wavefunctions of the free ions. Perturbations on the atomic wavefunctions may result from the interaction between an ion and its immediate neighbors. An example of such a situation is the splitting of the 3d orbitals of transition metals by the non-spherical crystal field created by the neighboring anions. The electrostatic, or ionic, models generally fail to give any quantitative description of the physical properties and spectra of Fe-Mn oxides. Important phenomena such as electron transport and magnetism are beyond the scope of any model invoking completely localized electrons. Still, the ionic bonding description, and its extension using crystal field theory, provide a convenient reference point for the descriptions of electrons in solids.

Collective electron models

At the opposite extreme from the localized electron models are the collective electron or Bloch-Wilson band theories. Here, the electronic

states are delocalized throughout the crystal. The extreme case of the collective electron models is the free electron model. Here, the electrons in the solid are viewed as an ideal electron gas which obeys Fermi statistics. The free electron model has to be modified, however, to account for diffraction of the free electrons by the periodic potential of the crystal lattice. This gives the "nearly-free electron model".

At the level of sophistication of the nearly-free electron model, one already obtains the notion of a band gap or a range of forbidden energies which separate the different energy bands. This, in turn, predicts that solids can be either insulators, metals or semiconductors depending on where the Fermi energy lies relative to the band gap.

The Bloch-Wilson band theory, as it has been traditionally applied, fails to give a correct description of transition metal oxides and, indeed, nearly all minerals. Specifically, it predicts that Fe and Mn oxides should be metals where, instead, they are semiconductors with appreciable (>1 eV) activation energies. A great deal of theoretical work has been directed towards understanding the failure of band theory when applied to transition metal oxides. One reason for its failure lies in the effect of electron correlations; that is, the coulombic electronic interaction which correlates the electron motion.

One component of the "correlation energy" is the repulsion of electrons with opposite spins occupying the same orbital. In the spin-restricted Hartree-Fock approach the one-electron orbitals are of the form

$$\psi(1) = \phi(1)\sigma(1)$$

where $\phi(1)$ is the spatial component and $\sigma(1)$ is the spin component of the one-electron orbital. The spin-up and spin-down electrons are forced to have the same spatial orbitals. If this restriction is relaxed, we can

then take into account some the the "exchange correlation energy". Note that the exchange energy is significant; it is the physical basis of Hund's rules regarding the ground state configuration of an open shell system. The effect of the exchange energy is to split the previously twofold degenerate $\psi(1)$ orbital into spin-up and spin-down suborbitals with different energies. The more stable of the two will be that having the majority spin.

The effect of the exchange splitting on the electronic band structure of a solid is to introduce an additional energy gap. Consider MnO_2 in a ferromagnetic state: Here, the t_{2g} Mn 3d band would be half-full; in a spin-restricted description MnO_2 should, therefore, be a metal. If the exchange splitting is taken into account, however, the t_{2g} band will be split into α-spin and β-spin subbands. The α-spin band would be completely full leading to insulating or semiconducting behavior. The band structure of antiferromagnetic MnO_2 would be somewhat more complex. Here, we have two sublattices A and B which are antiferromagnetically coupled. This gives two α-spin t_{2g} bands with different energies and two β-spin t_{2g} bands with different energies. If the A sublattice is α-spin and the B sublattice is β-spin, then the A α-spin and B β-spin t_{2g} bands would be completely full. It follow that antiferromagnetic MnO_2 would also be an insulator or semiconductor. The band gap would correspond to the exchange splitting of the t_{2g} band. A similar reasoning can be applied to antiferromagetic MnO. Wilson (1968) has shown that spin-unrestricted band structure calculations give a correct description of this system.

Above its Neel temperature, MnO_2 is paramagnetic. The band structure of this system can be used to illustrate an important principle regarding the electronic structures of transition metal oxides and minerals. It has

been traditional among solid-state physicists to regard to band structure of a paramagnetic system as being the same as that obtained using a spin-restricted description; that is, in the paramagnetic state, the exchange splittings of the energy bands disappear. Accordingly, paramagnetic MnO_2 should be a metal. This viewpoint, however, is incorrect. The interactions giving rise to the exchange splittings are primarily between electrons localized on the same atom. These interactions persist above the magnetic transition temperature of the solid. Hence, even in the paramagnetic state, each atom has a definite magnetic moment due to the local exchange potential. These moments are all nearly independant of one another so that the translational periodicity of the solid breaks down. This being the case, the use of Bloch wavefunctions to describe the system is probably incorrect.

Band theory also fails, however, even when the effects of exchange correlation are not relavent. For example, FeO, in either a ferromagnetic or antiferromagnetic state, should be a metal since the six d-electrons donated by each Fe^{2+} cations give a partially-filled α-or β-spin d-band. To understand why FeO is a semiconductor, we have to invoke localized electrons. A metallic state of FeO would require the existence of ionic configurations such as $Fe^{+}Fe^{3+}$ to occur while the d-electrons move through the conduction band. These ionic configurations are much higher in energy than the ground $Fe^{2+}Fe^{2+}$ configuration. The problem is that the Bloch wavefunctions mix in states corresponding to these high-energy ionic configurations. For this reason, the use of Bloch states does not give a correct description of the ground state of the system. This same problem is well-known by quantum chemists from molecular orbital studies of the H_2 molecule.

Apart from the failures of band theory to give a correct description of transition metal oxides and silicates, there are also several practical objections to the use of Bloch wave functions to describe the electronic structures of solids. First, band theory is a reciprocal space representation of electronic structure. This is conceptually awkward and often cannot give a clear picture of chemical bonding in solids. Second, localized phenomena such as "excitons" (localized electronic transitions) must be treated using Wannier functions. These are infinite sums of Bloch states and, as such are computationally difficult to deal with. Finally, Bloch's theorem requires that we have a perfectly periodic potential (i.e. an ideal crystal lattice). Although this is often a reasonable approximation to the actual nature of a solid, there are many cases where this approach is not applicable. For example, Fe-Mn oxides are often either amorphous or full of structural imperfections and defects. Such aspects of Fe-Mn oxides are beyond the scope of band theory. It is interesting to note, however, that the physical properties and electronic structures of amorphous Fe-Mn oxides are quite similar to their crystalline counterparts. This is evidenced by similarities in electronic spectra and quantities related to magnetism (e.g. Curie or Neel temperatures, magnetic moments). The reason for this is that the electronic states giving rise to these phenomena are essentially localized and, as such, do not depend on the long-range crystal structure of the mineral. Hence, Bloch's theorem, although correct, does not seem to have very many significant physical consequences for oxides and silicates.

Historically, solid state physics began with a purely collective-electron description of solids. Phenomena due to localized electrons have been treated by perturbations on the collective electron states. An

alternative approach would be to start with localized electron states which can then be perturbed to allow for collective electron behavior. This, in effect, can be done using the "cluster molecular orbital method".

Molecular Orbital Approach

In the cluster molecular orbital method, the electronic structure of the solid is approximated by that of a finite cluster of atoms which represents some basic entity of the crystal structure (usually not the unit cell). The simplest atomic cluster one might use for transition metal oxides would a metal cation surrounded by its immediate anion coordination environment. A finite atomic cluster has point-group, rather than space-group, symmetry so that Bloch wave functions would not be used. Instead, the one-electron wavefunctions would be molecular orbitals. This, by itself, has several advantages. First, the use of molecular orbitals rather than Bloch wavefunctions gives a real-space and, hence, a chemical bonding description of electronic structure. Second, a finite cluster starts with a more localized electron description. For many solids--oxide and silicate minerals in particular--this is a better "zeroth order" description than that obtained using Bloch states. It is very simple to "perturb" the localized electron states to allow for collective electrons; this is done by simply increasing the size of the cluster.

The finite cluster molecular orbital approach to the electronic structures of solids has an historical precident in ligand field theory. It is well known that the d-d electronic transitions in transition metal oxides and silicates can be understood by using only wavefunctions which have the point group symmetry of the transition metal's coordination environment. In ligand field theory (unlike the electrostatic crystal field theory) the 3d-type wavefunctions are modified to account for some

d-electron delocalization onto the ligands by covalency. The success of ligand field theory shows that the 3d state electronic spectra can by completely understood given the electronic structure of a simple MO_6 or MO_4 coordination polyhedron.

The electronic structure of a MO_6 or MO_4 coordination polyhedron, however, will also allow us to go well beyond the ligand field theory description. Unlike ligand field theory (which treats only the d-type electronic states), molecular orbital theory describes all of the different orbitals in a coordination site. This is necessary for understanding electronic transitions other than the d-d type ligand field transitions. Examples include the O 2p → M 3d (ligand to metal charge-transfer) and M 3d → M 4s interband transitions. High energy X-ray spectra (e.g. X-ray emission and photoelectron spectra) can be completely understood within the context of the molecular orbitals of a simple coordination polyhedron. This approach is, in fact, done and with considerable success. Molecular orbital theory also goes beyond ligand field theory in that it describes the nature of the metal-ligand chemical bonds and whether they are best described as covalent or ionic. This is important for understanding phenomena such as magnetism and the stability of a transition metal cation in a given coordination environment. In this regard, the molecular orbital approach is completely general in that both highly ionic and highly covalent systems can be treated.

Unlike band theory, the cluster molecular orbital approach allows for localized electronic states. Unlike the ionic bonding models and ligand field theory, however, the cluster molecular orbital approach also allows for "collective" electronic states. Although true Bloch states can only be achieved using an infinitely large cluster, the states which give

rise to metallic behavior in solids can be accurately treated using clusters only of sufficient size to allow for the spatial degree of electron delocalization in the solid. Finite cluster calculations on metals, in fact, are found to give accurate descriptions of their density-of-state profiles and, hence, their band structures. The only difference is that the finite cluster will have a finite number of descrete energy levels while the solid will have an infinite number of k-states forming a continuum. For some solids, the electronic structure of an appropriate finite cluster is a completely rigorous representation of their band structures. These are solids whose space groups are symmorphic--that is, space groups which can be factored into pure rotational and translational subgroups (space groups with no glide planes or screw axes fall into this catagory). Provided that the finite cluster has the full symmetry of the rotational subgroup, its electronic structure will incorporate exactly the band structure at the center of the Broulloin zone.

There are a large variety of computational molecular orbital methods that could be applied to clusters in solids. These range from the very primitive Extended Huckel Theory (EHT) to the sophisticated ab-initio techniques. The computational method that will be used here is the Self-Consistent field Xα Scattered Wave method. This is an "ab initio" technique insofar as it is based on first-principles yet the term "ab initio" is generally applied to methods based on the Hartree-Fock approximation.

Theory of the SCF-Xα-SW Method

The theory behind the Xα scattered-wave method has been reviewed in a number of works (Johnson and Smith, 1973; Johnson, 1973; Slater, 1974) and

will only be outlined here.

The Muffin-Tin approximation

The atomic cluster or molecule is partitioned into a set of spheres each of which is centered about a particular atom. Within each of these atomic spheres, the one-electron Schrodinger equation

$$[1/2\nabla^2 + V_C + V_X]\phi_i = \varepsilon_i\phi_i \tag{2.13}$$

is solved for the orbitals ϕ_i and their energies ε_i. In (1), V_C and V_X are the coulomb and exchange potentials, respectively. These are expressed in terms of the electronic charge density ρ given by

$$\rho = \sum(i) n_i \phi_i^* \phi_i \tag{2.14}$$

where n_i is the occupancy of orbital i. From the charge density the coulomb potential is evaluated using electrostatic theory (solving Poisson's equation). This gives (Rosch, 1977)

$$V_C(r) = -\frac{2Z}{r} + \frac{1}{r}\int_0^r 4\pi r'^2 \rho(r')dr' + \int_r^\infty 4\pi r'\rho(r')dr' \tag{2.15}$$

The exchange potential is evaluated using Slater's Xα approximation (Slater, 1974)

$$V_X = -6\alpha\,[3/4\pi\ \rho(r)]^{1/3} \tag{2.16}$$

After the individual atomic potentials are calculated to self consistency, they are superimposed to give an initial molecular potential. The coulomb potential within each atom is then

$$V_C(r_j) = V_C^j(r_j) + \sum_{i\neq j} V_C^i(r_i) \tag{2.17}$$

with an analogous expression for the exchange potential. Within each of the atomic spheres, the new potential is spherically averaged to give a radial

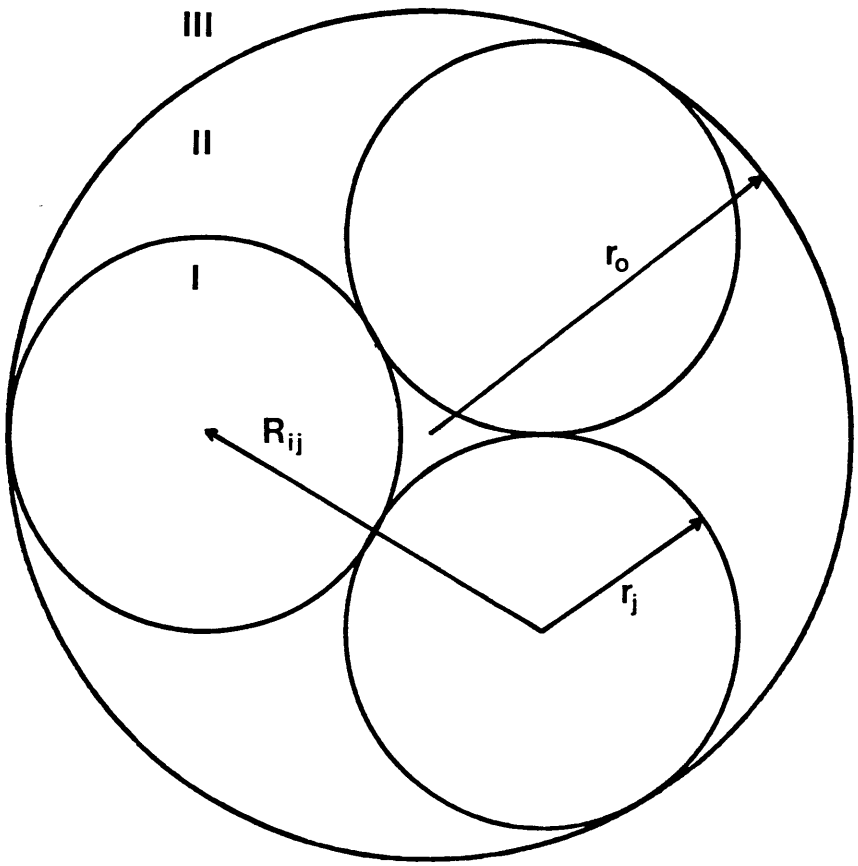


Figure 2.1: Muffin-tin partitioning of a three-atom molecule.

potential appropriate for that atomic region. Since we are then only concerned with the spherically symmetric terms in (2.17) and in the anologous expression for the exchange potential, we can use the spherical-harmonic expansion theorems to write

$$V(r_i) = \frac{1}{2R_{ij}r_i} \int_{|R_{ij}-r_i|}^{R_{ij}+r_i} r'V(r')dr' \qquad (2.18)$$

Hence, the superimposed potentials can be expressed with respect to a single atomic center.

In the interatomic region, the superimposed atomic potentials are volume averaged to give a simple constant potential. Finally, a potential for the extra-molecular region is obtained by spherically averaging the potential within the outer sphere.

For each region of the cluster, the Schrodinger equation (using the appropriate potential) is solved. The solutions are matched at the sphere boundaries using multiple-scattered wave theory and the result is then used to derive a new molecular potential. The process is repeated iteratively until a self-consistent result is obtained.

The multiple-scattered wave method

The multiple-scattered wave method will first be outlined neglecting the Outer Sphere. Within each of the atomic spheres, the radial equation is

$$\left(-\frac{1}{r^2}\frac{d}{dr}r^2\frac{d}{dr} + \frac{\ell(\ell+1)}{r^2} + V_j(r) - \kappa^2\right) R_\ell^j(\kappa;r) = 0 \qquad (2.19)$$

where $r = r_j$ or the distance from the center of the atomic sphere, $V_j(r)$ is the spherically symmetric potential in the atomic sphere and $\kappa^2=\varepsilon$ the orbital energy. The solutions within each atom are then of the form

$$\psi^j(r) = \sum_L C_L^j R_\ell^j(\kappa;r)Y_L(r) \qquad (2.20)$$

where the C_L^j are coefficients to be determined (see below) and Y_L are the spherical harmonic functions (L implies the two quantum numbers ℓ and m).

The solutions in region II are best understood by first considering the solution for a truncated atomic sphere with radius b_j. Here, the potential is such that $V = V(r)$ for $r < b_j$ and $V = V_{II}$ (a constant) for $r > b_j$. The boundary conditions require that $R(\kappa;r=0) = 0$ and $R(\kappa;r\to\infty) = 0$. The solution within the atomic sphere is given by (1); the solution outside the sphere can be expressed as a sum of spherical Hankel functions of the first kind if $\varepsilon < V_{II}$ (κ is imaginary) or spherical Nuemann functions if $\varepsilon > V_{II}$ (κ is real). That is,

$$\psi_{II}^j(r) = \sum_L A_L \, f_\ell(\kappa r) Y_L(\vec{r}) \tag{2.21}$$

where

$f_\ell(\kappa r) = h_\ell^{(1)}(\kappa r)$ (spherical hankel function) if $E<V_{II}$

or $f_\ell(\kappa r) = n_\ell(\kappa r)$ (spherical Nuemann function) if $E>V_{II}$

For the intersphere region of the molecule, therefore, we take the solution to be a superposition of the individual atomic $\Psi_{II}^j(r_j)$ solutions. Hence, for the molecule,

$$\psi_{II}(r) = \sum_j \sum_L A_L^j \, f_\ell(\kappa r_j) Y_L(\vec{r_j}) \tag{2.22}$$

Now, to obtain the molecular orbitals, we must solve for the coefficients A^j and C^j. This is done by satisfying the boundary conditions that the solutions and their first-derivatives be continuous across the sphere boundaries. To do this, we require that at each sphere boundary the Wronskian be zero:

$$[\psi_I^j, \psi_{II}] = \psi_I^j \left(\frac{d\psi_{II}}{dr_j}\right)_{r_j=b_j} - \psi_{II} \left(\frac{d\psi_I}{dr_j}\right)_{r_j=b_j} = 0 \tag{2.23}$$

At this point we note that substituting equations (2.20) and (2.22) into (2.23) will give a set of simultaneous equations for the A^j_L and C^j_L coefficients. This set of equations will have a non-trivial solution if the corresponding determinent has a zero. This is the secular determinent of the problem. What is done, therefore, is to search for values of κ which yield a zero of the determinent; these κ values are then the eigenvalues (orbital energies) of the problem. Upon finding an eigenvalue, the coefficients and, hence, the wavefunctions can be evaluated.

One problem with using equation (2.23) to evaluate the elements of the secular determinent is that the intersphere solution is given in terms of all of the atomic centers (eq. (2.22)). In order to evaluate the expression in equation (2.23) and, hence, the elements of the secular determinent, we must express ψ_{II} in terms of only one atomic center. This can be done using the expansion theorems of Johnson (1973). For example, consider two atomic centers j=1 and j=2. We can express the spherical Hankel function centered at atom 2 in terms of the coordinates relative to atom 1:

$$h_\ell^{(1)}(\kappa r_2)Y_{\ell m}(r_2) =$$

$$\sum_{\ell' m' L} 4\pi(-1)^{\ell'+\ell} I_L(\ell' m';\ell m)\, h_L^{(1)}(\kappa R_{12})Y_{L,m'-m}(R_{12})i^{-\ell}j_\ell(\kappa r_1)Y_{\ell m}(r_1) \qquad (2.24)$$

Here, $I_L(\ell' m';\ell m)$ are the "Gaunt coefficients" which are defined by

$$I_L(\ell' m';\ell m) = \int Y_{L,m-m'}(r)Y^*_{\ell m}(r)Y_{\ell' m'}(r)d\Omega \qquad (2.25)$$

Analogous expansion theorems exist which can be used to express spherical bessel and nuemann functions about different atomic centers.

Note that the familiar approximation of molecular orbitals as linear

combinations of atomic orbitals (LCAO) is not used. The conceptual utility of this approach is retained in the multiple-scattered wave method, however, since the solutions in each region of the cluster are expressed as a summation of functions with definite angular momenta centered at individual atomic sites (partial waves).

If an outer sphere is used, this is treated almost as though it were an additional atom in the cluster. Within the outer sphere, the solution for region II becomes

$$\psi_{II}(r) = \sum_j \sum_L A_L^j f_\ell(\kappa r_j) \vec{Y}_L(r_j) + \sum_L B^o j_\ell(\kappa r_o) Y_L(r_o) \qquad (2.26)$$

where the second term is the contribution to the intersphere wavefunction from the outer sphere. The solution outside the outer sphere (region III) is of the form

$$\psi_{III}(r) = \sum_L D_L^o R_\ell^o(\kappa;r) Y_L(r) \qquad (2.27)$$

Requiring continuity of the wavefunction and its first derivative at the I-II and II-III boundaries yields an anologous set of simultaneous equations for the A, B, C and D coefficients which, in turn, defines the secular determinent for the problem.

A simple example: the H_2^+ molecule

The muffin-tin partitioning of the H_2^+ molecule is shown in Fig 2.2. Here, we will assume that only ℓ=0 partial waves are needed in the solution. Chemically, this is equivalent to saying that only the H 1s orbitals are involved in bonding. This will make the scattered wave equations quite simple. The solutions in each region of the cluster are then ($E<V_{II}$):

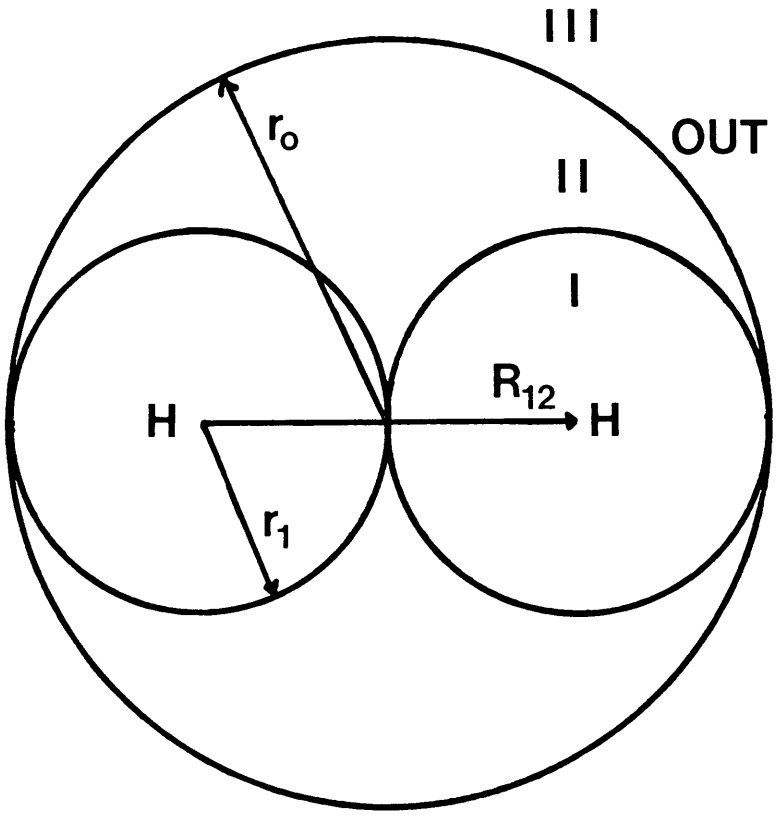


Figure 2.2: Muffin-tin partitioning scheme for H_2^+.

$$\psi_I = C_0 R_0(\kappa;r_1) \tag{2.28}$$

$$\psi_{II} = B_0 j_0(\kappa r_0) + A_0 h_0(i\kappa r_1) + A_0 h_0(i\kappa r_2) \tag{2.29}$$

$$\psi_{III} = D_0 R_0^{out}(\kappa;r_0) \tag{2.30}$$

Using the expansion theorems of Johnson (1973), we can express the solution in region II with respect to either the center of the molecule (that is, in terms of r_{out}) or the center of a particular atom (e.g. in terms of r_1). The particular expansion theorems needed take the form

$$j_0(\kappa r_0) = j_0(\kappa R_1) j_0(\kappa r_1) \tag{2.31}$$

$$h_0(i\kappa r_1) = h_0(i\kappa R_1) j_0(\kappa r_0) \tag{2.32}$$

$$h_0(i\kappa r_2) = h_0(i\kappa R_{12}) j_0(\kappa r_1) \tag{2.33}$$

Hence, the region II solution can be written

$$\psi_{II}(\kappa;r_0) = B_0 j_0(\kappa r_0) + A_0\{h_0(i\kappa R_1) j_0(\kappa r_0) + h_0(i\kappa R_{12}) j_0(\kappa R_1) j_0(\kappa r_0)\}$$

or as

$$\psi_{II}(\kappa;r_1) = B_0 j_0(\kappa R_1) j_0(\kappa r_1) + A_0\{h_0(i\kappa R_{12}) j_0(\kappa r_1) + h_0(i\kappa r_1)\}$$

Now we require continuity of the wave function and its first-derivative at the I-II and II-III boundaries. For ease of notation, let

$$f(r_0) = h_0(i\kappa R_1) j_0(\kappa r_0) + h_0(i\kappa R_{12}) j_0(\kappa R_1) j_0(\kappa r_0)$$

and

$$g(r_1) = h_0(i\kappa R_{12}) j_0(\kappa r_1) + h_0(i\kappa r_1)$$

Then the II-III boundary condition (at $r_0 = b$) gives

$$B_0[R_0^0(\kappa;b),\ j_0(\kappa b)] + A_0[R_0^0(\kappa;b),\ f(b)] = 0$$

while the I-II boundary condition (at $r_1 = a$) gives

$$B_0[R_0^1(\kappa;a),\ j_0(\kappa R_1)j_0(\kappa a)] + A_0[R_0^1(\kappa;a),\ g(a)] = 0$$

Hence, we have two simultaneous homogeneous equations for A and B. There exist a nontrivial (A and B ≠ 0) solution only if the corresponding determinent has a zero. Since it is a 2 × 2 determinent, there will be two roots (eigenvalues) and two linearly independent solutions for A and B (eigenvectors). These two solutions correspond to the bonding and antibonding molecular orbitals of the H_2^+ molecule.

Other aspects of the theory

Empirically it is found that the wavefunctions and their energies are significantly improved if the atomic spheres are allowed to overlap (Salahub et al., 1976; Norman, 1976). This can be qualitatively understood by noting that such overlap will decrease the volume of the interatomic region. In this region, the potential is constant and the wavefunctions are delocalized partial waves. Although this feature simplifies the computation, it is often a poor approximation to the actual physical situation. Any procedure which minimizes the intersphere contribution should improve the resulting wavefunction. The standard method used at present is that of Norman (1976). Here, the radii of the atomic spheres are chosen so as to enclose the atomic number of electrons of the free atoms. The resulting sphere radii are then scaled to optimize the virial theorem ratio (-2T/V where T is the kinetic and V is the potential energy of the molecule). This approach gives sphere overlaps of about 20% between metal and ligand atoms.

The highly charged atomic clusters used to model coordination sites in minerals should include the stabilizing effect of the crystal potential.

This is done approximately using a "Watson sphere" potential. The Watson sphere has a charge q and radius b; within each of the atomic and inter-sphere regions, the potential due to the watson sphere is $V = -q^2/b$. The contribution of the Watson sphere to the potential associated with the outer sphere, however, is given by

$$V = -q^2/b \qquad r \leq b$$

$$V = -q^2/r \qquad r > b$$

One may also use an "inner Watson sphere" so that one has separate watson sphere potentials for the atomic-intersphere and outer sphere regions.

References

Burns, R.G. (1970) Mineralogical applications of crystal field theory, Cambridge University Press, Cambridge, England.

Johnson, K.H. (1973) Scattered wave theory of the chemical bond, Adv. Quantum Chem., 7, 143-185.

Johnson, K.H., and F.C. Smith (1972) Chemical bonding of a molecular transition metal ion in a crystalline environment, Phys. Rev. B., 831-843.

Mattheiss, L.F. (1972a) Electronic structure of the 3d transition metal monoxides, I: Energy band results, Phys. Rev. B., 5, 290-306.

Mattheiss, L.F. (1972b) Electronic structure of the 3d transition metal monoxides, II: Energy band results, Phys. Rev. B., 5, 306-315.

Norman, J.G. (1976) Non-empirical versus emperical choices for overlapping sphere radii ratios in SCF-Xα-SW calculations on ClO_4^- and SO_2, Molecular Physics, 31, 1191-198.

Rosch, N. (197?) The SCF-Xα Scattered wave method with applications to molecules and surfaces, in Electrons in Finite and Infinite structures NATO Advanced Study Institute Series B24, P. Phariseau and L. Scheire (eds.), Plenum Press, New York.

Salahub, D.R., R.P. Messmer and K.H. Johnson (1976) Ionization potentials and bond lengths for CO, N_2 and F_2 using the SCF-Xα-SW method: a study of the effects of overlapping spheres, Molecular Physics, 31, 529-534.

Schwarz, K. (1972) Optimization of the statistical exchange parameter α for the free ions H through Nb, Physical Review B, 5, 2466-2468.

Slater, J.C. (1974) The self consistent field for molecules and solids: Quantum theory of molecules and solids, Volume 4, McGraw-Hill, San Francisco, 1-583.

Wilson, T.M. (1968) Spin polarized energy bands in the antiferromagnetic MnO, Int. J. Quantum Chem., 2S, 269.

CHAPTER 3:

The Electronic Structures of Mn^{2+}, Mn^{3+}, and Mn^{4+} Coordination Sites in Manganese Oxide Minerals*

*Published in American Mineralogist, in press.

Abstract

Molecular orbital calculations, using the Xα scattered wave method, were done for the clusters $(MnO_6)^{10-}$, $(MnO_6)^{9-}$, and $(MnO_6)^{8-}$ corresponding to Mn^{2+}, Mn^{3+}, and Mn^{4+} in octahedral coordination with O^{2-}. Bond lengths representative of those observed in manganese oxides were chosen and O_h symmetry was used for each cluster.

The calculated orbital energies and charge distributions are used to describe the nature of chemical bonding in manganese oxides. Spectroscopic transition energies are calculated and these are compared with experimental optical, x-ray emission and photoelectron (ESCA) spectra of manganese oxides. The agreement between the calculated and experimental spectroscopic transition energies is fairly good and indicates that isolated clusters can be used to model the localized aspects of the electronic structure of manganese oxide minerals.

The electronic structure of these clusters can also be related to the crystal chemistry of the manganese oxides. In spite of radius ratio considerations, Mn^{4+} is found to be considerably more stable in octahedral rather than tetrahedral coordination. This is demonstrated by comparing the electronic structure of MnO_6^{8-} with that of a tetrahedral $(MnO_4)^{4-}$ cluster. A large degree of covalency in the $(MnO_6)^{8-}$ cluster is consistent with the strong Lewis acidity of Mn^{4+}. In contrast, the bonding in $(MnO_6)^{10-}$ is mostly ionic. The calculated exchange splittings of the crystal field orbitals show that low-spin Mn^{2+} should not exist even under high-pressure, but that low spin Mn^{3+} may substitute for Mn^{4+} in manganese(IV) oxides.

Introduction

In natural environments manganese occurs in the Mn(II), Mn(III) and Mn(IV) oxidation states. All three valences form a large number of oxide minerals, ranging from the simple phases manganosite (MnO), partridgite (Mn_2O_3) and pyrolusite (MnO_2) to complex mixed-valence oxides such as birnessite ($(Ca,Na)(Mn^{2+}, Mn^{4+})_7\ O_{14}.3H_2O$) and todorokite ($(Na,Ca,K,Ba,Mn^{2+})_2\ Mn_5O_{12}.3H_2O$) (see, for example, Burns and Burns, 1977; 1979).

In the crystal structures of the manganese oxides, manganese cations are octahedrally coordinated by oxygen anions; the resulting MnO_6 polyhedra are linked by either edge or corner sharing to form infinite chain, sheet, and three-dimensional units. The presence of shared edges allows for cation-cation interactions. Goodenough (1960, 1971), however, has shown that in most of the manganese oxides, these interactions are very weak and that the Mn 3d-electrons are essentially localized to their parent cation and its immediate coordination environment. Accordingly, the electronic structures of these minerals should be fairly well approximated by those of simple MnO_6^{n-} clusters.

In this paper, the results of molecular orbital calculations (using the Xα scattered wave method) on such MnO_6 clusters are presented. Calculations were done for $(MnO_6)^{10-}$, $(MnO_6)^{9-}$ and $(MnO_6)^{8-}$ corresponding to manganese in the 2+, 3+ and 4+ oxidation states, respectively. The calculated molecular orbital energies and charge distributions will be used to describe the nature of chemical bonding in manganese oxides. The calculated orbital energies will then be compared with existing spectroscopic data (x-ray emission, ESCA and optical spectra). Finally, the results will be applied

to the crystal chemistry of these minerals. In addition to being of direct application to manganese oxide mineralogy, the calculations will also serve to demonstrate the effect of metal atom oxidation state on bonding in coordination sites in minerals.

Cluster Geometries and Input Parameters

For all three clusters, octahedral (O_h) symmetry was used. In the structures of manganese oxides, however, the point group symmetries of the MnO_6 clusters are usually much lower (e.g., C_{2v}). Nevertheless, as demon-strated in chapter 4 for iron oxides, small polyhedral distortions are expected to have only a small effect on orbital energies and charge distributions; hence, the use of O_h symmetry should be a good approximation. Still, calculations on clusters of lower symmetry are desired and will undoubtedly be done for Mn oxides as specific examples warrant investigation. For a recent example, Kai et al. (1980) have calculated the electronic structure of $(MnO_6)^{9-}$ using C_{2v} and D_{4h} symmetry. These results were used to interpret the optical absorption spectrum of Mn^{3+} in andalusite.

In the octahedral clusters investigated here, the Mn^{2+}-O, Mn^{3+}-O and Mn^{4+}-O bond lengths are 2.21Å, 2.04Å and 1.88Å, respectively. These values are representative of those observed in the manganese oxides.

Sphere radii were chosen using the procedure of Norman (1976). In each cluster, partial waves up to ℓ=2 were used for manganese, ℓ=1 were used for oxygen, and ℓ=4 were used for the Outer sphere. The sphere radii used in each cluster calculation, together with the resulting virial theorem ratio, are given in Table 3.1.

Table 3.1: Parameters used in Cluster Calculations.

	$(MnO_6)^{8-}$	$(MnO_6)^{9-}$	$(MnO_6)^{10-}$
Sphere Radii			
Mn	1.100	1.195	1.284
O	0.904	0.905	1.372
Out	2.784	2.945	3.582
Bond Length	1.880	2.040	2.210
-T/V	1.008	1.008	1.006

Calculated Molecular Orbitals

General.

The calculated molecular orbital diagrams of the three clusters are illustrated in Figure 3.1. Note that the energies of both the spin-up and spin-down forms of each orbital are indicated. The energy levels shown are those of the valence, crystal field, and low energy conduction band molecular orbitals, which in turn are derived from the manganese 3d, 4s, 4p and the oxygen 2p atomic orbitals. Each molecular orbital is labelled according to its associated irreducible representation of the O_h point group. The core molecular orbitals (not shown) are essentially the manganese 1s, 2s, 2p, 3s, and 3p and the oxygen 1s atomic orbitals. They are at a much lower energy, do not participate in bonding, and are localized on either the Mn or O atoms. The core states are of interest, however, in the interpretation of x-ray emission and ESCA spectra of Mn-oxides and will be discussed below.

Valence Band Orbitals

The valence orbitals of t_{1u} symmetry are nominally composed of Mn 4p and O 2p character. Both the $5t_{1u}$ and $6t_{1u}$ orbitals, however, have essentially no metal atom character, indicating that the Mn 4p orbitals are not involved in bonding. The t_{2u} and t_{1g} orbitals are completely non-bonding since they have no symmetry equivalent on the metal atom.

The orbitals of greatest interest are those with both metal and ligand characters. These are the valence orbitals of e_g, t_{2g} and a_{1g} symmetries, the atomic compositions of which are given in Table 3.2. The most important bonding orbitals are the σ-bonding $2e_g$ and the π-bonding $1t_{2g}$. Both of these orbitals are composed of manganese 3d and oxygen 2p atomic orbitals. With

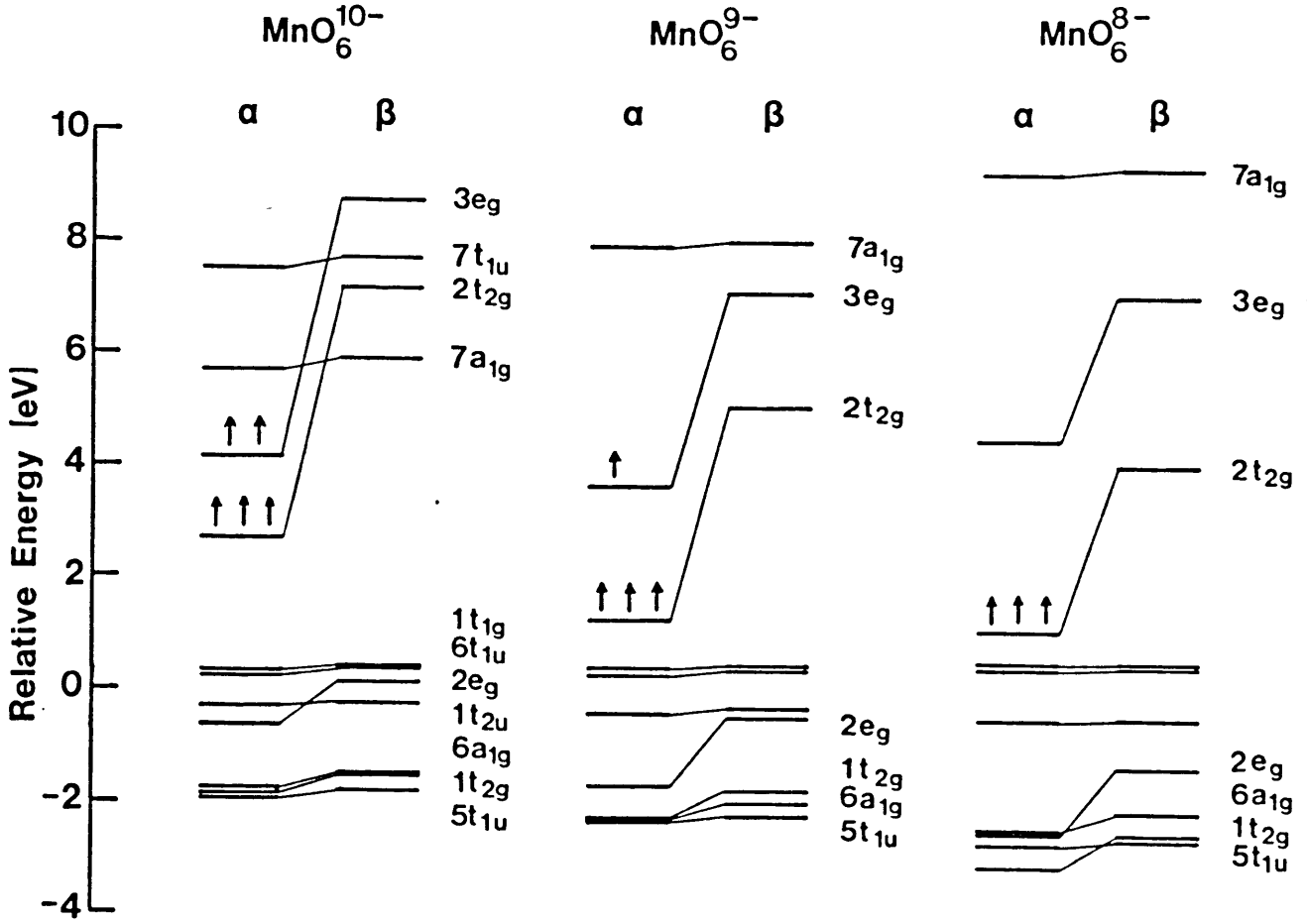


Figure 3.1: Molecular orbital diagrams for the Mn^{2+}, Mn^{3+} and Mn^{4+} octahedral coordination polyhedra, showing orbitals falling within the O(2p), Mn(3d), Mn(4s) and Mn(4p) bands. The orbital energies have been scaled relative to the non-bonding $1t_{1g}$, $1t_{2u}$ and $6t_{1u}$ orbital energies. The number of electrons in the highest occupied molecular orbitals are indicated by the arrow symbols. The α and β symbols indicate spin-up and spin-down orbitals, respectively.

Table 3.2: Orbital Compositions in the 3 Clusters

	MnO_6^{10-}			MnO_6^{9-}			MnO_6^{8-}		
	%Mn	%O	%Int	%Mn	%O	%Int	%Mn	%O	%Int
$3e_g\downarrow$	80	13	6	80	18	1	71	27	2
$3e_g\uparrow$	73	25	1	56	39	4	52	43	4
$2t_{2g}\downarrow$	56	21	23	84	8	8	82	10	8
$2t_{2g}\uparrow$	86	8	6	73	18	8	67	22	10
$2e_g\downarrow$	7	90	2	17	64	17	26	59	13
$2e_g\uparrow$	24	75	1	43	43	13	46	43	10
$1t_{2g}\downarrow$	2	73	24	5	57	36	10	56	33
$1t_{2g}\uparrow$	7	69	23	21	46	32	27	43	29
$6a1g\downarrow$	8	76	16	8	57	34	8	62	30
$6a1g\uparrow$	10	75	15	10	57	33	8	61	29

increasing oxidation state of the manganese atom, these orbitals become more bonding in character insofar as they donate more electron density to the Mn atom and become more stable. The spatial nature of these two orbitals can be seen in Figures 3.2 and 3.3 which show the wave function contours for the $2e_g$ spin up σ-bonding and $1t_{2g}$ spin up π-bonding molecular orbitals of the $(MnO_6)^{8-}$ cluster. The σ-bonds (Figs. 3.2a and 3.2b) can be pictured as lobes of the Mn $d(x^2-y^2)$ and $d(3z^2-r^2)$ atomic orbitals pointing directly at the oxygen p-orbitals while the π-bonds (Fig. 3.3) result from overlap of Mn d(xy),d(yz) and d(xz) orbitals with O 2p-orbitals directed perpendicular to the metal-ligand internuclear vector. The $2e_g$ σ-bonds are strongly directional in character while the $1t_{2g}$ π-bonds are rather delocalized over the three metal-ligand planes. Finally, the σ-bonding $6a_{1g}$ is an important bonding orbital in the MnO_6^{10-} cluster but is of lesser relative importance in the $(MnO_6)^{9-}$ and $(MnO_6)^{8-}$ clusters. This orbital is composed of the Mn 4s and O 2p orbitals.

Crystal Field Orbitals.

The $2t_{2g}$ and $3e_g$ orbitals correspond to the one-electron crystal field states. In the pure ionic bonding description used by crystal field theory these orbitals are the Mn 3d atomic orbitals which have lost their degeneracy by electrostatic interaction with the surrounding anions: the $2t_{2g}$ orbital stabilized by 4Dq and the $3e_g$ orbital destabiliized by 6Dq. In the molecular orbital description, the $2t_{2g}$ and $3e_g$ crystal field orbitals are the corresponding antibonding versions of the $1t_{2g}$ and $2e_g$ bonding orbitals. Note that as the metal atom character of the bonding $1t_{2g}$ and $2e_g$ orbitals increases, the ligand character of the anti-bonding $2t_{2g}$ and $3e_g$ orbitals increases accordingly. Hence, as the $1t_{2g}$ and $2e_g$ orbitals become

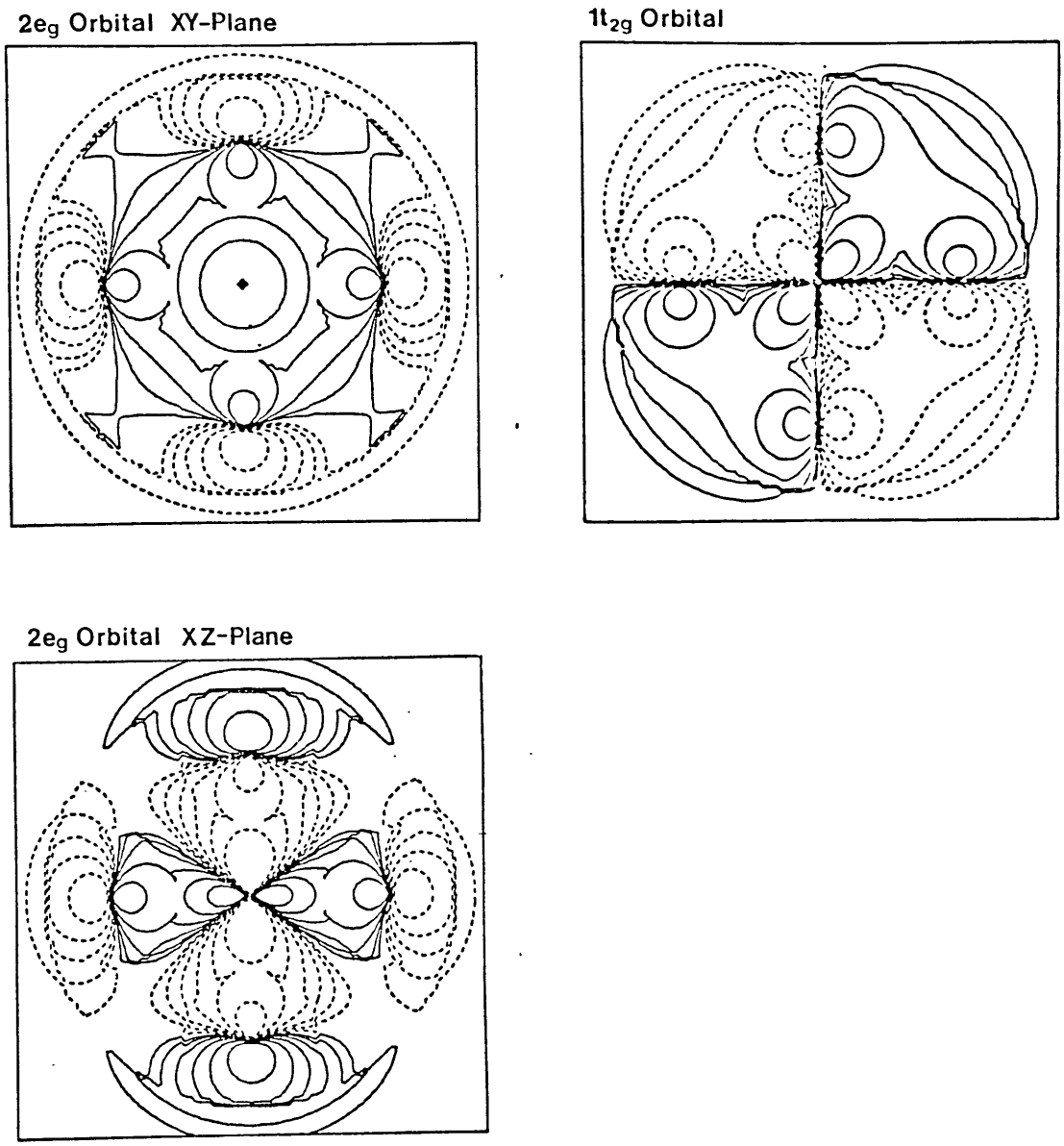


Figure 3.2: Wave function contours for the 2eg sigma bonding orbital in the Mn^{4+} centered MnO_6^{8-} cluster. Solid lines indicate the wave function is negative while dashed lines indicate positive values. Contour intervals are given at 0.005, 0.01, 0.02, 0.04, 0.08, and 0.16.

Figure 3.3 : Wave function contours for the π-bonding spin-up $1t_{2g}$ orbital in MnO_6^{8-}. Contour intervals are as in Figure 2.

more bonding in character, the $2t_{2g}$ and $3e_g$ crystal field orbitals become more antibonding. In spite of their antibonding nature, the average energy of the crystal field orbitals, relative to the O 2p valence band orbitals, decreases with increasing oxidation state of the manganese atom. Since these orbitals are mostly manganese in character, their increasing stability is a conseqence of the increasing electronegativity of the manganese atom. This has important consequences on the ligand to metal charge-transfer spectra of manganese oxides and will be discussed below.

As expected, the crystal field splitting (i.e., the energy separation between the $3e_g$ and $2t_{2g}$ crystal field orbitals) increases with the formal oxidation state of the manganese cation. This is a consequence of two factors: first, an increased electrostatic interaction between the manganese cation and the oxygen anions, and, more importantly, an increased degree of e_g σ-bonding relative to t_{2g} π-bonding in the clusters.

Conduction Band Orbitals.

The energy levels labelled $7a_{1g}$ and $7t_{1u}$ in Figure 3.1 are those of the lowest energy conduction band orbitals. In the molecular orbital description, these are the σ-antibonding versions of the $6a_{1g}$ and the $6t_{1u}$ bonding orbitals. In an extremely localized or ionic description, these orbitals correspond to the manganese 4s and 4p atomic orbitals. Their calculated atomic compositions (not given), however, show that they are delocalized over the oxygen, interatomic and extra-molecular regions.

Orbital Exchange Splittings

As noted previously, when using a spin unrestricted formalism the presence of unpaired electrons will give rise to two different potentials: one for spin up, and one for spin down electrons. In accordance with Hund's

rules, electrons with spin up (taken to be the majority spin) are lower in energy than those with spin down. The most extreme case is Mn^{2+} with five unpaired electrons; the resulting energy difference between spin up and spin down states of the partially filled orbitals (the exchange splitting) is quite large. Since the unpaired electrons in each cluster are localized on the metal atom center, the molecular orbitals with the most metal atom character exhibit the greater exchange splittings.

Electronic Spectra of Manganese Oxides

General

The calculated results can be verified by comparing the theoretical orbital energies with existing x-ray emission, ESCA and optical spectra of manganese oxides. The calculated orbital energies can also be used to interpret electronic spectra when band assignments are uncertain.

It is important to recognize, however, that the Xα scattered wave calculations, like all molecular orbital methods, are done using a one-electron formalism. Spectroscopic transitions, however, are between multielectronic wave functions (spectroscopic states). As a consequence of interelectronic repulsion, a given electronic configuration over several one electron orbitals can generate several multielectronic states (see, for example, Lever, 1968). For example, the ground state electronic configuration of Mn^{4+} in $(MnO_6)^{8-}$ is $(2t_{2g}^{\alpha})^3$. This configuration gives the multielectronic state $^4A_{2g}$. However, the excited state configuration $(t_{2g}^{\alpha})^2(e_g^{\alpha})^1$ yields the two states $^4T_{2g}$ and $^4T_{1g}$. Hence, the energy of the one-electron transition $2t_{2g} \rightarrow 3e_g$ corresponds to a weighted average of the energies of the spectroscopic transitions $^4A_{2g} \rightarrow {}^4T_{2g}$ and $^4A_{2g} \rightarrow {}^4T_{1g}$. As a second example, the excited state configuration $(2t_{2g}^{\alpha})^2(2t_{2g}^{\beta})$ of

$(MnO_6)^{8-}$ gives the states $^2E_g + {}^2T_{2g} + {}^2T_{1g}$. Hence, the energy of the one-electron transition $2t_{2g}^{\alpha} \rightarrow 2t_{2g}^{\beta}$ corresponds to an average energy for the spin-forbidden spectroscopic transitions $^4A_{2g} \rightarrow {}^2E_g$, $^4A_{2g} \rightarrow {}^2T_{2g}$, and $^4A_{2g} \rightarrow {}^2T_{1g}$. In some cases, an electronic transition between two one-electron orbitals corresponds to a unique transition between two multielectronic spectroscopic states. An example is the $2t_{2g}^{\alpha} \rightarrow 3e_g^{\alpha}$ transition in $(MnO_6)^{9-}$; this corresponds exactly to the $^5E_g \rightarrow {}^5T_{2g}$ spectroscopic transition. Such cases provide an opportunity for direct comparison between calculated and experimental results.

Optical Spectra

Transitions between the crystal field orbitals occur in the near-ultraviolet, visible and near-infrared spectral regions. Apart from transitions to higher energy crystal field states, two additional types of transitions occur in the near-ultraviolet: ligand to metal charge transfer and metal to conduction band transitions. Ligand to metal charge-transfer transitions are between the non-bonding ligand orbitals and the metal crystal field orbitals. With reference to the molecular orbitals in Figure 3.1 these are the $6t_{1u} \rightarrow 2t_{2g}$ and $1t_{2u} \rightarrow 2t_{2g}$ transitions. The $1t_{1g} \rightarrow 2t_{2g}$ transition is Laporte forbidden. Metal to conduction band transitions, however, are from the $2t_{2g}$ and $3e_g$ crystal field orbitals (localized on the metal atom) to the $7a_{1g}$ and $7t_{1u}$ conduction band states. Because these transitions may be Laporte allowed, absorption bands are of much greater intensity than those due to crystal field transitions, and often result in an absorption edge in the visible region spectra of transition metal-bearing minerals.

Several investigations have been made of the spectra of Mn^{2+} in oxides and silicates. Pratt and Coelho (1959) obtained the optical spectrum of MnO

and estimated values for the ligand field parameters, but these were later revised by the high resolution spectrum of MnO obtained by Huffman et al. (1969). Keester and White (1968) present spectra of Mn^{2+} in a number of minerals. The ground state d^5 electronic configuration gives rise to the ^6S Russell-Saunders term which in turn, transforms to the $^6A_1$ spectroscopic state in the crystal field. The excited state d-electron configurations which result from promoting a d-electron to one of the spin down d-orbitals, however, give rise to several quartet Russell-Saunders terms. Each of these is split into several states in the crystal field. Hence, a one-electron orbital scheme can provide only the crudest description of the crystal field spectra arising from a high-spin d^5 system. The visible and near-infrared spectrum of Mn^{2+} in octahedral coordination consists of the $^6A_1 \rightarrow {}^4T_1$, $^6A_1 \rightarrow {}^4T_2$ and $^6A_1 \rightarrow {}^4E, {}^4A$ transitions. The first two transitions are of the set which arise from the $3e_g^{\alpha} \rightarrow 2t_{2g}^{\beta}$ one-electron transition. The $^6A_1 \rightarrow {}^4E$, $^4A_1$ and higher energy transitions arise from the $2t_{2g}^{\alpha} \rightarrow 2t_{2g}^{\beta}$ and $3e_g^{\alpha} \rightarrow 3e_g^{\beta}$ one-electron transitions. In particular, these two "spin-flip" transitions give rise to the quartet states whose energies are independant of 10Dq in the Tunabe-Sugano or Orgal diagram for a high-spin d^5 system. One approach to relating the one-electron orbital energies of the $(MnO_6)^{10-}$ calculation with experimental spectra is to calculate the ligand field parameter $10D_q$. Ligand field theory, however, is cast in a spin-restricted formalism. Hence, a spin-restricted Xα calculation must be done to evaluate ligand field parameters (the correct relation between ligand field theory and the Xα approach is presented by Sambe and Felton, 1976). From such a calculation, the crystal field splitting is found to be 10,900 cm^{-1}; this is in good agreement with the best experimental value of 10,100 cm^{-1} for MnO (Huffman et al., 1969).

Messick et al. (1972) have obtained the near-ultraviolet spectrum of MnO. Transition state calculations were done for the lowest energy absorption features and are compared with the experimental results in Table 3.3. The calculated results are in good agreement with experimental absorption band energies, yet the band assignments given here are somewhat different. Messick et al. (1972) assigned most of the features between 4.5 and 7.0 eV to transitions from the valence and crystal field bands to the conduction band. Other transitions, based on their temperature dependance, were assigned as metal-metal charge-transfer (i.e. $2Mn^{2+} \rightarrow Mn^{+} + Mn^{3+}$). No features were assigned as ligand to metal charge-transfer. The calculated results, however, indicate that the first ligand to metal charge-transfer transition is at a very high energy (7.0 ev). At lower energies, but still well into the ultraviolet, are the O 2p to conduction band and the metal to conduction band transitions.

Optical absorption spectra are useful for the identification of Mn^{3+} cations in oxides and silicates (Burns, 1970). The calculated energy for the $^5E_g \rightarrow {}^5T_{2g}$ crystal field transition in the $(MnO_6)^{9-}$ cluster is 19,520 cm^{-1}. This also corresponds to the 10Dq parameter of ligand field theory. In most Mn^{3+}-bearing minerals the local coordination environment is distorted to tetragonal (D_{4h}) symmetry by the Jahn-Teller effect. There has been some confusion as to the definition of 10Dq in non-cubic symmetries and hence the 10Dq values reported for Mn^{3+} in epidote (Burns and Strens, 1967), manganophyllite (Burns, 1970) and andalusite (Halenius, 1978; Kai et al., 1980) do not correspond to the cubic crystal field value of 10Dq. In D_{4h} symmetry, the cubic crystal field parameter 10Dq corresponds to the $^5B_{1g} \rightarrow {}^5B_{2g}$ spectroscopic transition energy (see, for example, Konig and Kremer, 1977). From the spectra of Mn^{3+} in epidote (Burns and Strens,

One-Electron Transition	E(calc.)*	Corresponding Spectral Transitions**	References
$(MnO_6)^{8-}$			
$1t_{2u}^{\beta} \rightarrow 2t_{2g}^{\beta}$	5.17	$O^{2-} \rightarrow$ M CT	
$6t_{1u}^{\beta} \rightarrow 2t_{2g\beta}$	4.32	$O^{2-} \rightarrow$ M CT (ca. 4.3)	1
$2t_{2g}^{\alpha} \rightarrow 3e_g^{\alpha}$	3.33	$^4A_2 \rightarrow {}^4T_2$ (2.64), $^4T_1$	1
$2t_{2g}^{\alpha} \rightarrow 2t_{2g}^{\beta}$	2.95	$^4A_2 \rightarrow {}^2E$, $^2T_1$, $^2T_2$	
$(MnO_6)^{9-}$			
$1t_{2u}^{\beta} \rightarrow 2t_{2g}^{\beta}$	6.27	$O^{2-} \rightarrow$ M CT	
$6t_{1u}^{\beta} \rightarrow 2t_{2g}^{\beta}$	5.55	$O^{2-} \rightarrow$ M CT	
$6t_{1u}^{\alpha} \rightarrow 3e_g^{\alpha}$	4.65	$O^{2-} \rightarrow$ M CT (4.09,4.2,4.5)	2
$2t_{2g}^{\alpha} \rightarrow 3e_g^{\alpha}$	2.42	$^5E \rightarrow {}^5T_2$ (2.25-2.73)	3,4,5
$2t_{2g}^{\alpha} \rightarrow 2t_{2g}^{\beta}$	3.42		
$(MnO_6)^{10-}$			
$6t_{1u}^{\beta} \rightarrow 2t_{2g}^{\beta}$	7.00	$O^{2-} \rightarrow$ M CT (7.2, 6.9)	6
$1t_{1g}^{\alpha} \rightarrow 7t_{1u}^{\alpha}$	5.80	VB $\rightarrow$ CB (5.7)	6
$2t_{2g}^{\alpha} \rightarrow 7t_{1u\alpha}$	5.17	CF $\rightarrow$ CB (5.4?)	6

*Energies in eV (1 eV = 8.066×10^3 cm^{-1}). **Observed spectral features given in parentheses. References: 1. Geschwind et al.(1962); 2. Langer and Abu-Eid (1979); 3. Burns and Strens (1967); 4. Burns (1970); 5. Halenius (1978); 6. Messick et al. (1972).

1967), manganophyllite (Burns, 1970) and andalusite (Halenius, 1978) the cubic 10Dq values are therefore found to be 18,170 cm^{-1}, 19,050 cm^{-1} and 22,000 cm^{-1}, respectively. Hence, the value calculated for the MnO_6^{9-} cluster is reasonable. McClure (1962), however, has obtained a 10Dq value of 19,470 cm^{-1} for Mn^{3+} in corundum; since the Mn^{3+}-O bond length in this phase is expected to be much shorter than the 2.04 A used in this calculation, it appears that the value of 10Dq obtained here may be too high. On the other hand, the 10Dq value of the Mn^{3+} aquo-complex is 21,000 cm^{-1} (Orgel, 1966).

The only near-ultraviolet spectral data for Mn^{3+} in minerals, from which one may obtain ligand-to-metal charge-transfer energies, is the spectrum of piemontite obtained by Langer and Abu-Eid (1977). Strong bands were observed at 33,000 and 34,000 cm^{-1}. These can be assigned as being derived from the $4t_{1u} \rightarrow 3e_g$ transition which is calculated to be at 4.6 eV (37,000 cm^{-1}) in the $(MnO_6)^{9-}$ cluster. Calculated values for other spectral band energies are given in Table 3.3.

The spectrum of Mn^{4+} in corundum has been obtained by Geschwind et al.(1962). As noted previously, the one-electron orbital transition $2t_{2g}^{\alpha} \rightarrow 3e_g^{\alpha}$ in $(MnO_6)^{8-}$ corresponds to the two spectroscopic transitions $^4A_2 \rightarrow {}^4T_2$ and $^4A_2 \rightarrow {}^4T_1$. In the spectrum of Mn^{4+} in corundum, however, only the $^4A_2 \rightarrow {}^4T_2$ transition was observed and its energy was 21,300 cm^{-1}. The energy calculated for the one-electron orbital transition $2t_{2g}^{\alpha} \rightarrow 3e_g^{\alpha}$ is 26,860 cm^{-1}. Since this corresponds to an average of the two spectroscopic transition energies, it is in qualitative agreement with experiment. Finally, the energy of the first ligand to metal charge-transfer transition was estimated to be about 35,000 cm^{-1}. This agrees with the calculated value of 34,850 cm^{-1} for the $4t_{1u} \rightarrow 2t_{2g}$ ligand to metal charge transfer

transition. The calculated energies for the remaining ligand to metal charge-transfer and crystal field orbital transitions of $(MnO_6)^{8-}$ are given in Table 3.3.

The energies of the ligand to metal charge-transfer and metal to conduction band transitions in the three clusters correlate with the relative oxidation and reduction potentials of the three valences of manganese (e.g. Huheey,1978). In the $(MnO_6)^{10-}$ cluster, the first metal to conduction band transition is much lower in energy than the first ligand to metal charge-transfer transition; likewise the oxidation of Mn^{2+} to Mn^{3+} requires less energy than the reduction of Mn^{2+} to Mn^{+}. In the $(MnO_6)^{8-}$ cluster however, the first ligand to metal charge transfer transitions are much lower in energy than the first metal to conduction band transitions; likewise the reduction of Mn^{4+} to Mn^{3+} is more energetically favorable than the oxidation of Mn^{4+} to Mn^{5+}. An intermediate situation is provided by $(MnO_6)^{9-}$ where the two types of transitions are of similar energies.

X-Ray Emission Spectra

When an electron from a 1s core orbital has been photoejected, transitions from the higher energy occupied orbitals to the 1s orbital occur. The emitted photons accompanying the relaxation give rise to the K spectrum. For first row transition metals, the transitions of greatest interest are those that originate from the n = 3 atomic orbitals (M-shell) since these are strongly influenced by the oxidation state and local coordination environment of the metal atom. The transitions of the type $3p_{3/2}$, $3p_{1/2}$, 3d etc. → 1s define the K_β spectrum. The main peak in the K_β spectrum results from the Mn 3p→Mn 1s transition and is designated $K_{\beta 1}$. In addition to the $K_{\beta 1}$ transition, several addition peaks are observed. The

$K_{\beta 5}$ peak is due to transitions which are nominally of the type Mn3d, O2p → Mn1s. The satellite lines Kβ'' and Kβ''' are attributed to O2s → Mn1s and Mn4p (conduction band) → Mn 1s transitions, respectively. By analogy with the K spectrum, the L spectrum results from transitions to the n = 2 atomic levels (i.e. 2s and 2p levels). The 2p level is split by spin-orbit coupling into the $2p_{1/2}$ and $2p_{3/2}$ states. Hence, in first-row transition metals, two allowed transitions are present: $3d \rightarrow 2p_{1/2}$ ($L\beta_1$) and $3d \rightarrow 2p_{3/2}$ ($L\alpha_{1,2}$).

The Kβ and Lα, Lβ spectra of MnO and MnO_2 were calculated using the transition state formalism. These results are presented in Table 3.4 and compared with experimental values (Koster and Mendel, 1970; Tsutsumi et al., 1976; Wood and Urch, 1976). The agreement between theory and experiment is good for the case of MnO although the Kβ energies may be overestimated for the case of MnO_2. The results can also be used to interpret the Kβ spectra of MnO, Mn_2O_3 and MnO_2 phases. The assignment of Kβ" (Koster and Mendel, 1970) or "peak A" (Tsutsumi et al., 1976) to the O2s → Mn1s crossover transition seems to be correct. Similarly, the assignment of Kβ''' to a transition of an excited electron in the Mn 4p ($7t_{1u}$) orbital to the Mn 1s orbital (Koster and Mendel, 1970) seems reasonable. An additional satellite peak, labelled Kβ', was attributed by Koster and Mendel (1970) to a discrete energy loss process whereby a $K\beta_1$ photon excites a Mn 3d electron into the $7t_{1u}$ conduction band. Based on the ground state energies, this does not appear to be correct. Tsutsumi et al. (1976) attribute this feature to exchange splitting of the $K\beta_1$ peak.

X-Ray Photoelectron Spectra (ESCA)

Valence region photoelectron spectra of MnO, Mn_2O_3 and Mn_3O_4 have been investigated. A low resolution spectral profile encompassing the Mn 3d,O 2p

Table 3.4: Experimental and Calculated Kβ and Lα Spectra of MnO and MnO_2

Band	Transition	MnO		MnO_2		Ref
		E (exp)	E (calc)	E (exp)	E (calc	
$K\beta_1$	Mn 3p → 1s	6491.8	6495.1	6490.0	6495.1	1,2
Kβ''	O 2s → 1s	~6521.0	6520.0	6521.0	6528.5	1
$K\beta_5$	$5t_{1u}$ → 1s	6533.2	6532.8	6534.7	6541.0	1,2,3
Kβ'''	$7t_{1u}$ → 1s	~6549.8	6549.5	6549.8		1
Lα	$2t_{2g}$ → 2p	643.	643.1	643.	643.3	3

1. Koster and Mendel (1970); 2. Tsutsumi et al. (1976); 3. Wood and Urch (1976).

and O 2s valence bands of MnO (Wertheim and Hufner, 1972; Hufner and Wertheim, 1973) showed that the O 2p and O 2s bands are separated by their free ion value of ~ 16eV; this is in agreement with the results obtained here (i.e. the $1t_{1g}$, $^{6}t_{1u}$ (2p) - $1e_g$, t_{1u}, a_{1g} (2s) energy separations). Rao et al. (1979) have obtained fairly high resolution spectra profiling the O 2p and Mn 3d bands in MnO, Mn_2O_3 and Mn_3O_4. In the spectra of both MnO and Mn_2O_3, four peaks were observed and were assigned to be the Mn 3d(eg), Mn 3d(t2g), O 2p(σ) and O 2p(π) bands. The peaks were separated by about 1.5-2.0 eV and, accordingly, are in fairly nice aggreement with the ground state energy level diagrams presented in Figure 3.1. In the spectrum of the mixed-valence phase hausmannite (Mn_3O_4), they were able to easily resolve the Mn^{2+} and Mn^{3+} 3d-bands. These states were found to have the energetic order $Mn^{2+}(e_g)>Mn^{3+}(e_g)>Mn^{2+}(t_{2g})>Mn^{3+}(t_{2g})$. This ordering is in aggreement with the ground state electronic structures of the isolated $MnO_6^{10-}$and MnO_6^{9-}clusters if their orbital energies are related by setting the intersphere potentials to be equal (as in Figure 3.1).

Applications to the Crystal Chemistry of Manganese Oxides

Molecular orbital calculations on finite clusters can be used to assess the stability of a given cation valence state and electronic configuration (e.g. high-spin vs. low spin) in a given coordination environment. Ideally, this information can then be applied to understanding mineral stabilities, cation site occupancies, and the speciation and transport of transition metals in geochemical environments.

Chemical Bonding in Manganese Oxides.

Of fundamental importance is the relative ionic versus covalent nature of the manganese-oxygen bond. Of additional interest is the exact nature of

the covalent interaction. In each of the clusters, electronic charge is donated from the O^{2-} anions to the Mn^{2+}, Mn^{3+} or Mn^{4+} cations. One way to describe the nature of the manganese-oxygen bond in each cluster is to calculate the net amount of electronic charge donated to the manganese center by each of the different types of metal-ligand bonding interactions. For each orbital, however, the relative amount of electronic charge in the atomic versus interatomic regions is a function of the atomic sphere radii used in the calculation. To eliminate the dependance of the bonding description on the sphere radii, it is necessary to partition the intersphere electronic charge among the manganese and oxygen atomic regions. A reasonable way of doing this is according to the ratio of manganese to oxygen atomic sphere charges. This was done for each orbital and the calculated net amount of electronic charge donated to the manganese center by the different types of orbital interactions is presented in Table 3.5.

By summing the amount of electronic charge donated by each type of orbital interaction, one may calculate a relative degree of covalancy of the bonding in each cluster. The calculations show that the bonding in manganese(IV) oxides is mostly covalent. The strong covalency of the Mn^{4+}-O bond is also in aggreement with the strong Lewis acidity of Mn^{4+} in aqueous environments. In contrast, the bonding in the Mn^{2+} cluster is mostly ionic; this is in agreement with the tendency for Mn^{2+} to act as a weak Lewis acid and as an exchangable cation in sedimentary environments.

It can be seen that in the Mn^{3+} and Mn^{4+} clusters most of the metal-ligand interaction is through the e_g σ-type bonds (Mn 3d -O 2p overlap). There is also an appreciable degree of π-type bonding interaction as well. Since the former bond type is quite directional, it is expected that the stabilities of these cations in oxides should have a strong

Table 3.5: Electronic charge donated to Mn centers by each type of orbital interaction.

	$(MnO_6)^{10-}$	$(MnO_6)^{9-}$	$(MnO_6)^{8-}$
$e_g(\sigma)$	-0.124	-0.986	-1.624
$t_{2g}(\pi)$	-0.096	-0.549	-0.831
$a_{1g}(\sigma)$	-0.213	-0.271	-0.228
$t_{1u}(\sigma)$	-0.156	-0.272	-0.261
$\sum q =$	-0.589	-2.078	-2.945
% Covalency	29.5	69.3	73.6

dependance on coordination site geometry. Molecular orbital calculations on MnO_6^{9-} and MnO_6^{8-} clusters using different site geometries might therefore be of interest. In contrast, most of the metal-ligand interaction in the MnO_6^{10-} cluster results from the spherically symmetric a_{1g} σ-type interaction and the spatially diffuse t_{1u} interaction. This situation, togeather with the fairly ionic nature of the Mn^{2+}-O bond, suggests that the stability of a Mn^{2+} cations should exhibit a weaker dependance on its coordination geometry.

Octahedral versus Tetrahedral Coordination.

In the crystal structures of the manganese(IV) oxides, the Mn^{4+} cations are only in octahedral coordination (Burns and Burns, 1977; 1979). The ionic radius of Mn^{4+} (Shannon and Prewitt, 1969), however, is less than or equal to that of several cations which often occur in tetrahedral coordination (e.g. Al^{3+}, Fe^{3+}, and even Mn^{2+}). Crystal field theory explains the greater stability of octahedrally coordinated Mn^{4+} since a d^3 transition metal cation will have an octahedral site preference energy of $38/45\Delta_{oct}$ (where Δ is the crystal field splitting and it is assumed that $\Delta_{tet} = 4/9\Delta_{oct}$). Given the calculated crystal field splitting of the d-orbitals in the $(MnO_6)^{8-}$ cluster, the octahedral site preference energy is found to be 2.79 eV. This is an extremely large value and it accounts well for the absence of tetrahedrally coordinated Mn^{4+} in minerals.

Although crystal field theory has been quite successful when applied to the crystal chemistry of the transition metals (Burns, 1970), its physical basis is unfounded. A more physically correct approach is molecular orbital theory. To apply molecular orbital theory to understanding the stability of octahedrally coordinated Mn^{4+} in oxide minerals, a calculation was done for a tetrahedral $(MnO_4)^{4-}$ cluster. The bond length is taken to be the sum of

the Shannon and Prewitt (1969) ionic radii for fourfold-coordinated Mn^{4+} and twofold-coordinated O^{2-}. The resulting molecular orbital diagram is compared with that of the octahedral $(MnO_6)^{8-}$ cluster in Figure 3.4. In the molecular orbital formalism, the notion of octahedral site preference energy is somewhat complicated; still, several differences between the two clusters are apparent. Relative to the top of the oxygen 2p valence band (the t_1 orbital in T_d symmetry and the t_{1g} orbital in O_h symmetry), the occupied Mn^{4+} crystal field orbitals are less stable in the tetrahedral cluster. Moreover, in T_d symmetry one electron must occupy the least stable $5t_2$ orbital which is σ-antibonding. Finally, the bonding molecular orbitals in the $(MnO_6)^{8-}$ cluster are more stable (by about 1 eV) than the analogous orbitals in the $(MnO_4)^{4-}$ cluster. This is probably due to an increased delocalization of the valence orbital electrons in the larger $(MnO_6)^{8-}$ cluster. The molecular orbital approach shows that Mn^{4+} is more stable in octahedral coordination although it is somewhat ambiguous how one may define an octahedral site preference energy.

High- versus Low-spin Mn^{2+} and Mn^{3+}.

Transition metals with more than three electrons can exist in both high spin and low spin states in octahedral coordination. The two spin states of a transition metal cation have different ionic radii (Shannon and Prewitt, 1969) and, hence, different crystal-chemical behavior. The spin-unrestricted calculations can provide insight into the stability of the high-spin relative to the low-spin configuration in a given coordination environment. As noted previously, the calculations show that both Mn^{2+} and Mn^{3+} are in high-spin configurations at the metal-ligand bond distance used for the $(MnO_6)^{10-}$ and $(MnO_6)^{9-}$ clusters. The exchange splitting of the Mn^{2+} crystal field orbitals (Figure 3.1) is quite large (4.5 eV); this indicates that the

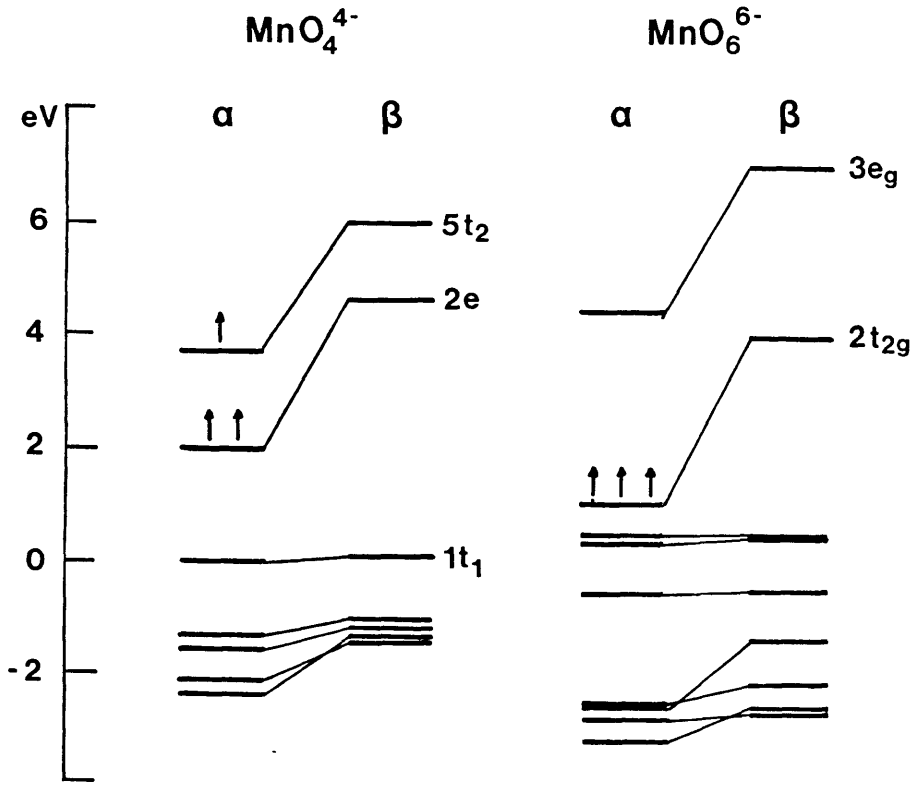


Figure 3.4: Molecular orbital diagram for tetrahedrally-coordinated Mn^{4+} (R=1.74 Å) compared with that for octahedrally-coordinated Mn^{4+}.

high-spin configuration $(t_{2g}^{\alpha})^3(e_g^{\alpha})^2$ of Mn^{2+} is much more stable than the low-spin configuration $(t_{2g}^{\alpha})^3(t_{2g}^{\beta})^2$. It is known that with increasing pressure transition metals may undergo a high spin to low-spin transition. Such a transition of Fe^{2+} is inferred to occur in the Earth's mantle (Fyfe, 1960; Strens, 1969; Burns, 1970). The electronic structure of the MnO_6^{10-} cluster, however, implies that a high-spin to low-spin transition of Mn^{2+} is unlikely, and that Mn^{2+} in the Earth's mantle is in the high-spin state.

In contrast, the smaller exchange splitting of the $2t_{2g}$ orbital and the larger crystal field splitting in the $(MnO_6)^{9-}$ cluster suggest that a high-spin to low-spin transition of Mn^{3+} can occur. When the Mn-O distance in the $(MnO_6)^{9-}$ cluster is decreased from 2.04 to 1.88 A, the low-spin configuration is found to be the most stable; this suggests that low-spin Mn^{3+} may substitute for Mn^{4+} in the manganese(IV) oxides, the ionic radii of Mn^{4+} and low-spin Mn^{3+} being fairly similar (Shannon and Prewitt, 1969). It should be noted, however, that Mn^{3+} distorts its coordination environment via the Jahn-Teller effect and that the resulting tetragonal distortion will stabilize the high-spin configuration. Spin-unrestricted calculations on $(MnO_6)^{9-}$ clusters with D_{4h} symmetry should therefore be done to investigate this problem.

Stability of Mn^{3+} cations in oxides.

The Mn^{3+} ion is often unstable and frequently disproportionates to Mn^{2+} and Mn^{3+} ions (Stumm and Morgan, 1970; Huheey, 1978; Cotton and Wilkinson, 1980) . The molecular orbital diagrams in Figure 3.1 suggest that the stability of the $(MnO_6)^{9-}$ cluster is approximately midway between that of the $(MnO_6)^{10-}$ and $(MnO_6)^{8-}$ clusters. Hence, in oxides, the energy required for the disproportionation of two Mn^{3+} ions should be quite low. Following

Tossell (1978), one may perform a transition state calculation for the disproportionation of two $(MnO_6)^{9-}$ clusters to a $(MnO_6)^{8-}$ and a $(MnO_6)^{10-}$ cluster as follows: 0.5 electrons are removed from the 3eg orbital of the $(MnO_6)^{10-}$ cluster and added to the 3eg orbital of the $(MnO_6)^{8-}$ cluster. The orbital energies of the two isolated clusters can be placed on the same scale by equating their constant intersphere potentials. The resulting energy difference between the $(MnO_6)^{8-}$ and $(MnO_6)^{10-}$ 3eg orbitals would correspond to the energy required for the disproportionation. This is found to be less than 0.25 eV. This approach, however, neglects the electrostatic component of the cluster energies. Moreover, the Mn^{3+} cation will stabilize itself by inducing a tetragonal distortion of its coordination environment. Still, the calculations seem to be qualitatively consistent with the known chemical behavior of Mn^{3+} and suggest that one may relate trends in redox chemistry with theoretical valence orbital energies.

Conclusions

The agreement between the calculated results and experimental spectra of manganese oxides demonstrates that isolated clusters can be used to model chemical bonding in these minerals.

As the formal oxidation state of the manganese atom increases, the Mn-O bond becomes more covalent, the crystal field splitting increases and the exchange splitting of the d-orbitals decreases. The covalent nature of the bonding in the $(MnO_6)^{8-}$ cluster explains the low solubilities of manganese(IV) oxides in solutions where strong complexing agents are absent. In contrast, the ionic nature of the bonding in the MnO_6^{10-}cluster is in agreement with the higher solubility of Mn^{2+} in aqueous solutions and the ability of Mn^{2+} to act as an exchangeable cation in complex oxides.

In terms of crystal field theory, the large crystal field splitting in the $(MnO_6)^{8-}$ cluster explains the absence of tetrahedrally coordinated Mn^{4+} in minerals. In terms of molecular orbital theory, a comparison of the calculated electronic structures of octahedral MnO_6^{8-} and tetrahedral $(MnO_4)^{4-}$ clusters indicates that Mn^{4+} is much less stable in tetrahedral coordination.

Because the bonding in the $(MnO_6)^{10-}$ cluster is mostly ionic, the Mn^{2+} 3d-orbital electrons are strongly localized on the metal atom. Since there are five unpaired electrons, this gives rise to a large exchange splitting of the crystal field orbitals. This, in turn, indicates that a high-spin to low-spin transition of Mn^{2+} in oxides and silicates at high pressure is unlikely.

Finally, the calculations are in qualitative agreement with the tendancy for Mn^{3+} cations to disproportionate. In addition, it is found that at the Mn-O bond distances found in the manganese(IV) oxides, Mn^{3+} is in a low-spin configuration. This suggests that low-spin Mn^{3+} may substitute for Mn^{4+} in manganese oxides.

References

Burns, R. G. (1970) Mineralogical Applications of Crystal Field Theory, Cambridge Universtiy Press: London.

Burns, R. G. and Burns, V. M. (1979) Manganese oxides. In R. G. Burns, Ed., Marine Minerals, Chapter 1, p. 1-46, Mineralogical Society of America, Washington, DC.

Burns, R. G. and Burns, V. M. (1977) Mineralogy of manganese nodules. In G. P. Glasby, Ed., Marine Manganese Deposits, Chapter 7, p. 185-248. Elsevier, New York.

Burns, R.G. and Strens, R.G.J. (1967) Structural interpretation of the polarized absorption spectra of Al-Fe-Mn-Cr epidotes, Mineralogical Magazine, 36, 204-206.

Cotton, F. A. and Wilkinson, G. (1980) Advanced Inorganic Chemistry, 4th edition, John Wiley and Sons, New York.

Geschwind, S., Kislink, P., Klein, M.P., Remeika, J.P., and D.L. Wood (1962) Sharp-line fluorescence, electron paramagnetic resonance and thermoluminescence of Mn^{4+} in αAl_2O_3, Physical Review, 126, 1684-1686.

Fyfe, W.S. (1960) The possibiliy of d-electron coupling in olivine at high pressure, Geochimica Cosmochimica Acta, 19, 141-143.

Goodenough, J.B. (1960) Direct cation-cation interactions in several oxides, Physical Review, 117, 1442-1451.

Goodenough, J.B. (1971) Metallic oxides, Progress in Solid State Chemistry, 5, 145-399.

Halenius, U. (1978) A spectroscopic investigation of manganian andalusite, Canadian Mineralogist, 16, 567-575.

Huffman, D. R., Wild, R. L. and Shinmei, M. (1969) Optical absorption spectra of crystal field transition in MnO. The Journal of Chemical Physics, 50, 4092-4094.

Hufner, S., and Wertheim, G.K. (1973) X-ray photoelectron band structure of some transition metal compounds, Physical Review B, 8, 4857-4867.

Huheey, J. E. (1978) Inorganic Chemistry, 2nd edition, Harper and Row, New York.

Kai, A. T., Larsson, S. and Halenius, U. (1980) The electronic structure and absorption spectrum of MnO_6^{9-} octahedra in manganoan andalusite. Physics and Chemistry of Minerals, 6, 77-84.

Keester, A. S. and White, W. B. (1968) Crystal field spectra and chemical bonding in manganese minerals. In Papers and Proceedings of the Fifth General Meeting, International Mineralogical Association, 1966, p. 22-35. Mineralogical Society, London.

Konig, E., and Kremer, S. (1977) Ligand Field Energy Diagrams, Plenum Press, New York.

Koster, A. S. and Mendel, H. (1970) X-ray K emission spectra and energy levels of compounds of 3d-transition metals-I Oxides. Journal of Physics and Chemistry of Solids, 31, 2511-2522.

Langer, K. and Abu-Eid, R.M. (1977) Measurement of the polarized absorption spectra of synthetic transitio metal-bearing microcrystals in the spectral range 44,000-4,000 cm^{-1}. Physics and Chemistry of Minerals, 1,

Lever, A. P. B. (1968) Inorganic Electron Spectroscopy, Elsevier: Amsterdam.

McClure, D.S. (1962) Optical spectra of transition metal ions in corundum, Journal of Chemical Physics, 36, 2757-2779.

Messick, L., Walker, W. C. and Glosser, R. (1972) Direct and temperature modulated reflectance spectra of MnO, CoO and NiO. Physical Review B, 6, 3941-3949.

Norman, J.G. (1976) Non-empirical versus empirical choices for overlapping sphere radii rations in SCF-Xα-SW calculations on ClO_4^- and SO_2, Molecular Physics, 31, 1191-1198.

Pratt, G. W. J. and R. Coehlo (1959) Optical absorption of CoO and MnO above and below the Neel temperature. Physical Review, 116, 281-286.

Rao, C. N. R., Sarma, D. D., Vasidevan, S., and Hegde, M. S. (1979) Study of transition metal oxides by photoelectron spectroscopy. Proceedings of the Royal Society of London A, 367, 239-252.

Sambe H., and Felton, R.H. (1976) Connection between the Xα method and ligand field theory, International Journal of Quantum Chemistry Symposium, 10, 155-158.

Schwarz, K. (1972) Optimization of the statistical exchange parameter α for the free atoms H through Nb, Physical Review B, 5, 2466-2468.

Shannon, R.D. and Prewitt, C.T. (1969) Effective ionic radii in Oxides and Fluorides, Acta Crystallographica, B25, 925-946.

Strens, R.G.J. (1969) The nature and geophysical importance of spin pairing in minerals of iron(II), in The Application of Modern Physics to the Earth and Planetary Interiors, Wiley-Interscience, London.

Stumm, W. and Morgan, J.J. (1970) Aquatic Chemistry. John Wiley and Sons, New York, 1-583.

Tsutsumi, K., Nakamori, H. and Ichikawa, K. (1976) X-ray Mn K emission spectra of manganese oxides and manganates. Physical Review B, 13, 929-933.

Wertheim G.K. and Hufner, S. (1972) X-ray photoemission band structure of some transition metal oxides, Physical Review Letters, 28, 1028-1031.

Wood, P. R. and Urch, D. S. (1976) Valence band x-ray emission spectra of manganese in various oxidation states. Journal of the Chemical Society, Dalton Transactions, 2472-2476.

CHAPTER 4:

The Electronic Structures of Fe^{2+} and Fe^{3+} Coordination Sites in Iron Oxides

*Submitted to: Physics and Chemistry of Minerals

Abstract

The electronic structures of Fe^{3+} coordination sites in hematite, maghemite and wustite are investigated using self-consistent field Xα scattered-wave (SCF-Xα-SW) molecular orbital calculations on octahedral $(FeO_6)^{9-}$ and $(FeO_6)^{10-}$ clusters, a trigonally distorted $(FeO_6)^{9-}$ cluster, and a tetrahedral $(FeO_4)^{5-}$ cluster. These calculations are also applicable to the electronic structures of other iron oxides and silicates. The overlapping sphere approach to the SCF-Xα-SW formalism is used and is found to give more accurate results than previous calculations on these systems.

Multiplet theory is used to relate the one-electron molecular orbital energies to the ligand field spectra of Fe^{3+} and Fe^{2+} cations in oxides. Calculated energies of ligand to metal charge transfer transitions agree with experimental data and are used to interpret the near-UV spectra of iron oxides and silicates.

The calculated wavefunctions show that chemical bonds in both Fe^{2+} and Fe^{3+} oxides are fairly covalent. Moreover, the Fe-O bond has a strong spin polarization. The latter result is used to show how superexchange and the main features of the magnetic structures of iron(III) oxides are predicted from simple $(FeO_6)^{9-}$ and $(FeO_4)^{5-}$ cluster calculations. The spatial character of the $(FeO_6)^{9-}$ wavefunctions show that iron(III) oxides are p-type semiconductors.

Introduction

Oxides and silicates of trivalent iron are major phases in the surface mineralogy of the Earth and Mars. Many aspects of the geochemistry and physics of these minerals, however, are associated with their partially occupied Fe 3d orbitals and, as such, can only be understood within the context of quantum chemistry. Several current problems in geochemistry warrent an improved understanding of the electronic structures of iron oxides and silicates. Examples include understanding the mechanisms of photochemical reactions between colloidal iron oxides and organic molecules in natural waters and interpreting the remote-sensed reflectance spectra of the surface mineralogy of Mars.

As noted in Chapter 2, the electronic wavefunctions of a solid must be invariant under the space group of symmetry operations defined by its crystal structure. Accordingly, a complete description of the electronic structure of a mineral must be derived using the Bloch wave functions of band theory. An alternative approach is to use what may be referred to as the cluster molecular orbital method. In this method, the electronic structure of a solid is approximated by that of a finite atomic cluster which represents a basic structural entity of the crystal. The usefulness of this approximation will depend on the spatial extent of atomic interactions in the solid relative to the size of the atomic cluster being used. For the iron oxides, the simplest cluster consists of an iron atom surrounded by its immediate coordination environment. Such a cluster will allow a treatment of the localized electronic states in iron oxides and, hence, could be used to understand electronic spectra, Mossbauer isomer shifts, magnetic hyperfine splittings, and the nature of the Fe-O bond. The electronic structure of an

isolated Fe^{3+} or Fe^{2+} coordination polyhedron, moreover, can even provide some insight on phenomena resulting from more long-range atomic interactions. These include magnetic exchange interactions and mechanisms of intrinsic semiconduction.

The first application of the cluster molecular orbital method to the electronic structure of Fe^{2+} and Fe^{3+} oxides was that of Tossell et al. (1973; 1974). In that study, molecular orbital calculations using the self-consistent field Xα scattered-wave (SCF-Xα-SW) method, were done for octahedral $(FeO_6)^{9-}$ and $(FeO_6)^{10-}$ clusters ; the resulting energy levels were used to interpret the electronic spectra (X-ray emission, ESCA and optical) of hematite and wustite. SCF-Xα-SW calculations of the electronic structure of a tetrahedral $(FeO_4)^{5-}$ cluster were later done (Tossell, 1978) for the interpretation of the electronic spectra of tetrahedrally coordinated Fe^{3+} in magnetite. Other SCF-Xα-SW calculations on $(FeO_4)^{5-}$ clusters were done by Tang Kai et al. (1980) to interpret Mossbauer isomer shifts of Fe^{3+}. Marathe and Traututwein (1983), using simple extended Huckel calculations on $(FeO_6)^{9-}$ clusters, have interpreted not only isomer shifts but also quadrupole and magnetic hyperfine splittings in the Mossbauer spectra of iron oxides. To date, few accurate calculations have been done which incorporate the distorted geometries found in most Fe^{2+} or Fe^{3+} coordination sites in minerals.

Since the original investigation of Tossell et al. (1973), several improvements to the SCF-Xα-SW method have been developed, among them the use of overlapping atomic spheres rather than the pure "muffin-tin" approximation to the molecular potential. In addition, new experimental data and theoretical insights on the electronic spectra of iron oxides and other ferric minerals have been obtained.

The purpose of this chapter is to present new calculations of the electronic structure of the octahedral $(FeO_6)^{9-}$, $(FeO_6)^{10-}$ and tetrahedral $(FeO_4)^{5-}$ clusters using the improvements in the SCF-Xα-SW method, to extend the $(FeO_6)^{9-}$ cluster calculations to include the trigonally distorted site geometry in hematite, and to place these results in the context of some of the recent spectroscopic investigations of iron oxides and silicates. Regarding the last objective, the relation between the calculated one-electron molecular orbitals and the multiplet state energies investigated spectroscopically will be derived using multiplet theory. It will be shown how the 10Dq, B and C parameters of ligand field theory relate to the theoretical one-electron orbital energies. These results can then be used to give insight on how chemical bonds affect the optical spectra of iron bearing minerals. Finally, the calculated molecular orbital wavefunctions will be used to describe the nature of chemical bonding in iron oxides. These results will then be used to relate chemical bonding to the physical properties (magnetism, electrical conductivity) and crystal chemistry of iron oxides and related minerals.

Cluster Geometries and Input Parameters

The geometries of the clusters are shown in Figure 4.1. The bond lengths and input parameters for each cluster are given in Table 4.1. The octahedral $(FeO_6)^{10-}$ cluster is modeled after the Fe^{2+} coordination site in wustite (FeO). The octahedral $(FeO_6)^{9-}$ and tetrahedral $(FeO_4)^{5-}$ clusters are modeled after the coordination sites of Fe^{3+} in maghemite (γ-Fe_2O_3) and magnetite (Fe_3O_4). The crystal structure of magnetite is that of an inverse spinel. The structure of maghemite is similar except that vacancies in the tetrahedral A and octahedral B sites give a tetragonal superstructure. The

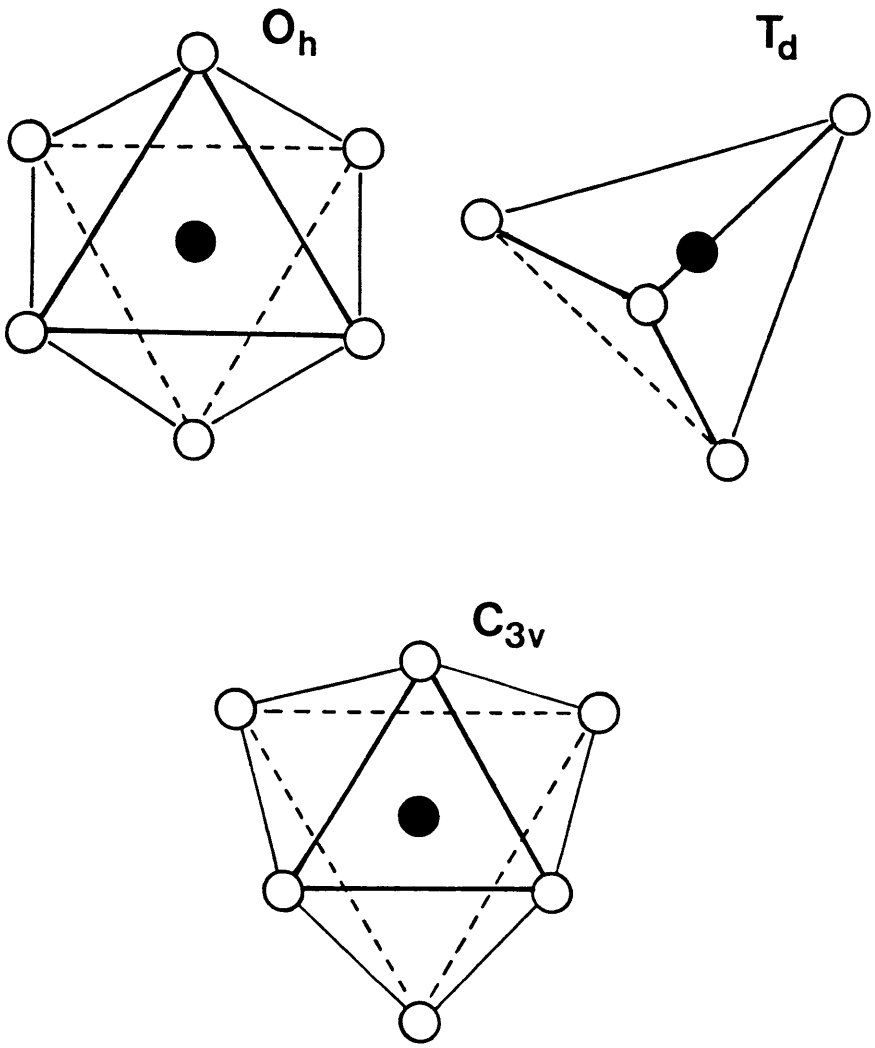


Figure 4.1: Geometries of FeO_6 and FeO_4 clusters. The cubic octahedral (point group O_h) and tetrahedral (point group T_d) are used to model the coordination sites of Fe^{3+} in Fe_3O_4 and γ-Fe_2O_3. The trigonally-distorted FeO_6 cluster (point group C_{3v}) approximates the geometry of the Fe^{3+} coordination site in α-Fe_2O_3.

coordination sites in both minerals are of nearly ideal cubic geometry; there is a small trigonal distortion of the octahedral B sites but this was neglected here. Bond lengths were taken from the data of Fasiska (1967).

The fourth cluster was used to approximate the coordination site of Fe^{3+} in hematite (α-Fe_2O_3). This iron oxide has the corundum structure: pairs of face sharing FeO_6 polyhedra occur along the c-axis; these dimers, in turn, share edges and corners with each other to form sheets of FeO_6 polyhedra in the plane perpendicular to the c-axis. Because of the face-sharing arrangement, the FeO_6 coordination polyhedra have a strong trigonal distortion. One may view each Fe^{3+} center as sandwiched between two triatomic clusters of O^{2-} anions; in the smaller O_3 cluster the oxygen atoms are only 2.67 A apart while in the larger O_3 cluster they are 3.035 A apart. The two O_3 clusters are slightly kinked with respect to each other. This lowers the point group symmetry of the FeO_6 polyhedron from C_{3v} to C_3. However, to simplify the SCF-Xα-SW calculation, this further descent in symmetry was not incorporated into the cluster geometry used here. The Fe-O and O-O bond lengths used for this cluster were determined from the crystal structure data of Blake et al. (1966).

The sphere radii were chosen using the criterion of Norman (1976) and allowing the Fe and O atomic spheres to overlap by about 20%. The resulting virial-theorem ratio T/V (where T and V are the kinetic and potential energies, respectively) is about 2.002 for each cluster. The electrostatic potential of the crystal is approximated by an "inner Watson sphere" (centered about the origin and passing through the oxygen nuclei) and an outer Watson sphere (coincident with the outer sphere). This approach simply allows for different constant potentials to be added to the regions inside and outside of the outer sphere. However, the use of different

Table 4.1: Parameters Used in Cluster Calculations

Cluster	Point Group	Sphere Radii (A)	Bond lengths (A)
$(FeO_6)^{9-}$	O_h	Fe = 1.186	Fe-O = 2.05
		O = 1.245	O-O = 2.899
		Out = 3.295	
$(FeO_6)^{10-}$	O_h	Fe =	Fe-O = 2.165
		O =	O-O = 3.055
		Out =	
$(FeO_4)^{5-}$	T_d	Fe = 1.110	Fe-O = 1.865
		O = 1.117	O-O = 3.046
		Out = 2.982	
$(FeO_6)^{9-}$	C_{3v}	Fe = 1.169	Fe-O(1) = 1.945
		O(1) = 1.248	Fe-O(2) = 2.116
		O(2) = 1.305	O(1)-O(1) = 3.035
		Out = 3.342	O(2)-O(2) = 2.669
			O(1)-O(2) = 2.830

Watson sphere potentials for the atomic-interatomic and outer sphere regions does not appear to have much effect on the results since most of the orbitals have only a small outer-sphere component.

Partial waves with angular momentum quantum numbers $l = 1$ for the oxygen atoms, $l = 2$ for the iron atoms, and $l = 3$ for the outer spheres were used; that is, for the oxygen atoms only s and p orbitals were included while s, p, and d orbitals were included for the iron atoms. Unlike the LCAO Hartree-Fock methods, the SCF-Xα-SW approach does not have the problems associated with choosing between "minimal" or "extended" basis sets. The "basis set" used here is essentially complete within the context of the approximation.

The α values for the atomic regions are those given by Schwarz (1972) while the α values used for the interatomic regions and outer spheres are taken to be the valence-electron weighted average of the atomic values.

Electronic Structure of Octahedral $(FeO_6)^{9-}$ and $(FeO_6)^{10-}$

The calculated molecular orbital diagram for the octahedral $(FeO_6)^{10-}$ cluster is shown in its spin-unrestricted form in Figure 4.2. The corresponding diagram for the $(FeO_6)^{9-}$ cluster is shown in Figure 4.3. Each of the orbitals is labelled according to its corresponding irreducible representation of the O_h point group. The energy levels shown are those which fall within the O 2p and Fe 3d bands. These are the orbitals which determine most of the electronic properties of the octahedral Fe^{3+} or Fe^{2+} coordination site. As in other transition metal oxide clusters (e.g. the manganese oxides discussed in chapter 3), the metal 3s, 3p and oxygen 2s atomic orbitals retain their localized nature in the cluster and are completly non-bonding. Tables 4.2 and 4.3 give the composition of the

orbitals shown in Figures 4.2 and 4.3 in terms of the percent intersphere, Fe atomic and O atomic regions. From its atomic composition, the nature of each orbital can be described.

O 2p Valence Band Orbitals

Within this set are the orbitals responsible for the Fe-O chemical bond. The $1t_{1g}$, $1t_{2u}$, and, to a lesser extent, $6t_{1u}$ orbitals, however, are non-bonding in character. The other orbitals within the O 2p valence band set are bonding in character and may be pictured as resulting from the overlap of the O 2p atomic orbitals with either the Fe 3d, 4s or 4p atomic orbitals. The t_{1u} type O 2p orbital combinations overlap with the Fe 4p orbital. The resulting $5t_{1u}$ molecular orbital is quite delocalized, probably because the Fe 4p atomic orbital has a large radial extent. The a_{1g} type O 2p orbital combinations overlap with the Fe 4s atomic orbital to give the σ-bonding $3a_{1g}$ orbital. The t_{2g} and e_g type O 2p orbital combinations overlap with the Fe 3d orbitals. The most important bonding orbital is the $2e_g$ which corresponds to a σ-type Fe 3d -O 2p bonding interaction. Of next importance is the $1t_{2g}$ orbital which corresponds to a π-type Fe 3d - O 2p bonding interaction. In contrast to the picture given by most inorganic chemistry texts, there is a large degree of π-bonding in Fe^{3+} cluster. Wave function contours for the $2e_g$ and $1t_{2g}$ bonding orbitals in the $(FeO_6)^{9-}$ cluster are shown in Figure 4.4.

Fe 3d band orbitals

The orbitals labelled $2t_{2g}$ and $3e_g$ are the antibonding versions of the $1t_{2g}$ and $2e_g$ bonding molecular orbitals. The $2t_{2g}$ and $3e_g$ orbitals are mostly Fe 3d in character (Tables 4.2 and 4.3) and localized on the metal atom. Wave function contours for these orbitals in the Fe^{3+} cluster are shown in Figure 4.5. Although these orbitals tend to be localized to the Fe

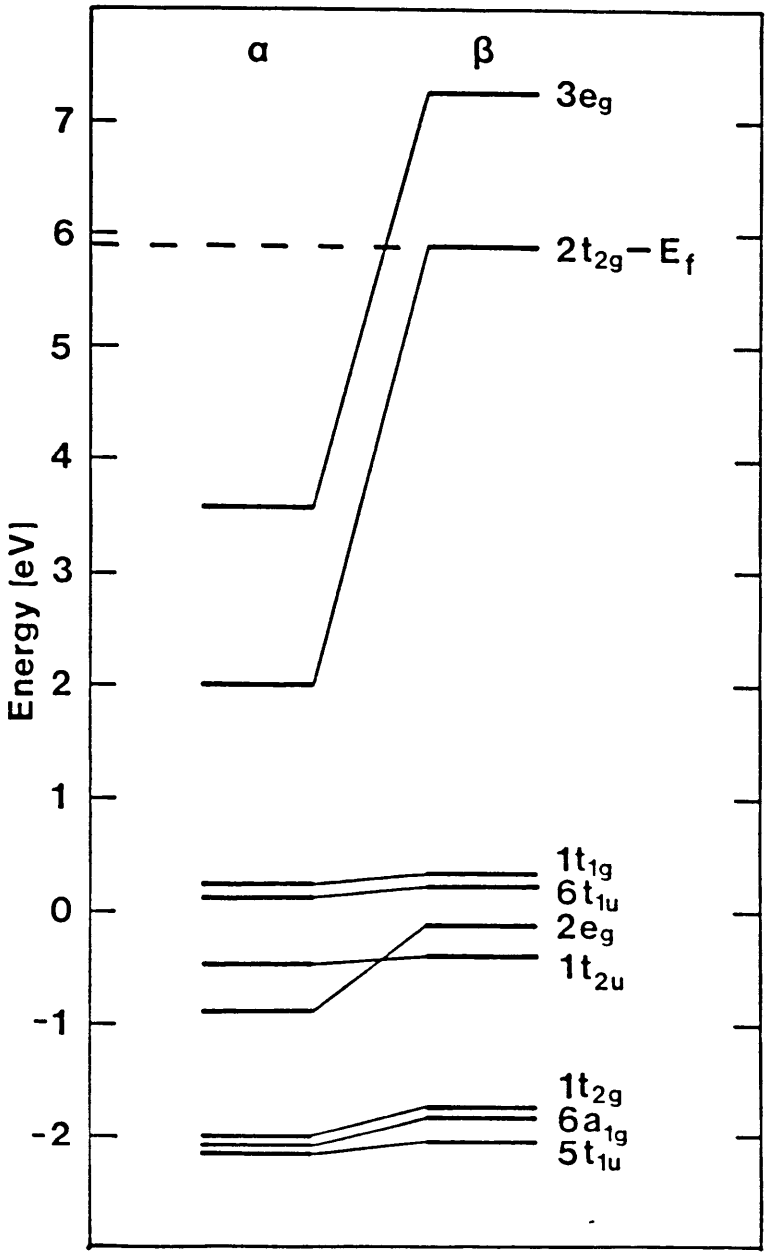


Figure 4.2: Molecular orbital diagram of $(FeO_6)^{10-}$ in a spin-unrestricted description. The symbols α and β refer to spin-up and spin-down electron orbitals, respectively. E_f refers to the Fermi-level, below which all orbitals are occupied; the $2t_{2g}^{\beta}$ orbital at the Fermi energy is occupied by one electron. The orbitals shown are those which fall within the Fe 3d band (antibonding) and the O 2p band (bonding and non-bonding).

Table 4.2: Orbital Compositions in the $(FeO_6)^{10-}$ Cluster.

	Energy (eV)	%Fe	%O	%Int.		Energy (eV)	%Fe	%O	%Int.
	Spin-Up Orbitals					Spin-Down Orbitals			
$3e_g^*$ (2)	3.57	69	29	1	$3e_g^*$ (0)	7.24	84	13	3
$2t_{2g}^*$(3)	2.03	86	9	5	$2t_{2g}^*$(1)	5.87	85	7	8
$1t_{1g}$ (3)	0.23	0	92	8	$1t_{1g}$ (3)	0.32	0	92	8
$6t_{1u}$ (3)	0.11	2	91	7	$6t_{1u}$ (3)	0.23	2	92	7
$1t_{2u}$ (3)	-0.49	0	85	15	2eg (2)	-0.14	11	86	4
$2e_g$ (2)	-0.87	30	68	3	$1t_{2u}$ (3)	-0.40	0	85	15
$1t_{2g}$ (3)	-2.00	9	67	24	$1t_{2g}$ (3)	-1.76	3	72	24
$6a_{1g}$ (1)	-2.08	10	74	16	$6a_{1g}$ (1)	-1.83	9	75	16
$5t_{1u}$ (3)	-2.15	3	71	26	$5t_{1u}$ (3)	-2.05	2	72	26

The numbers in parentheses give the orbital occupancies. Orbitals with an asterisk are antibonding.

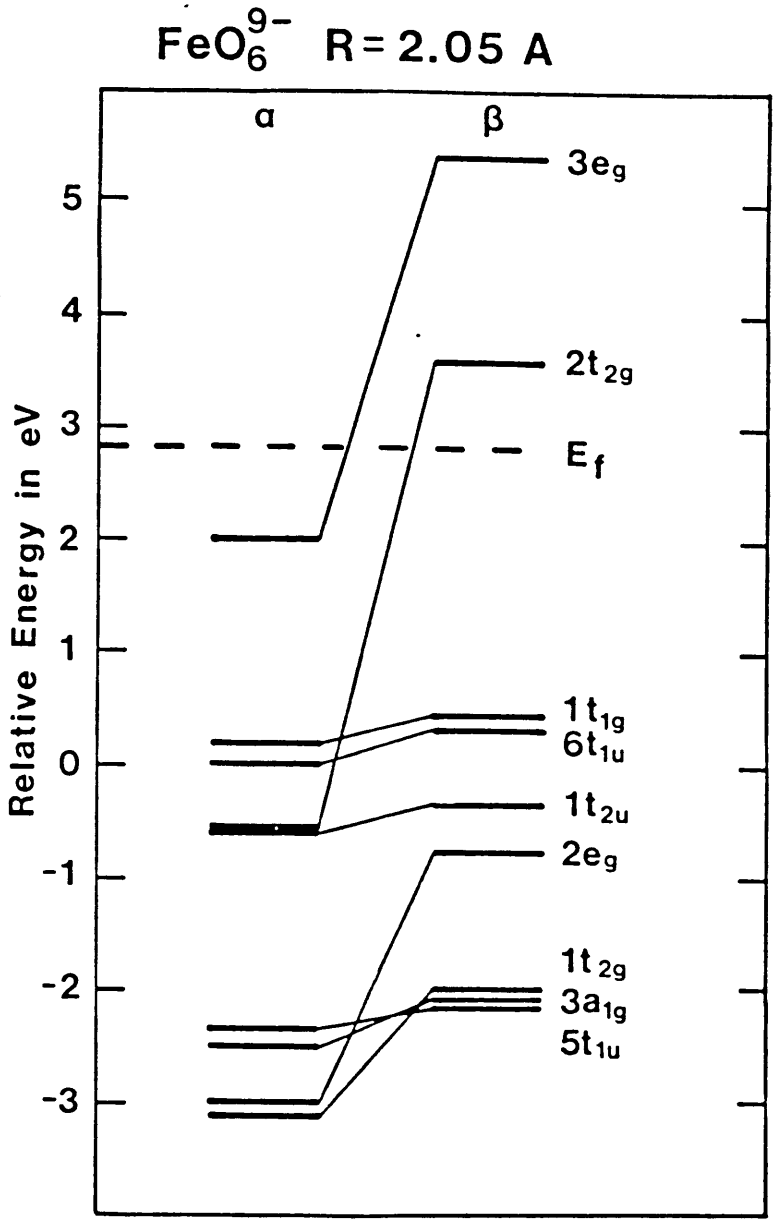


Figure 4.3: Molecular orbital diagram for the Fe^{3+} centered $(FeO_6)^{9-}$ cluster with O_h symmetry.

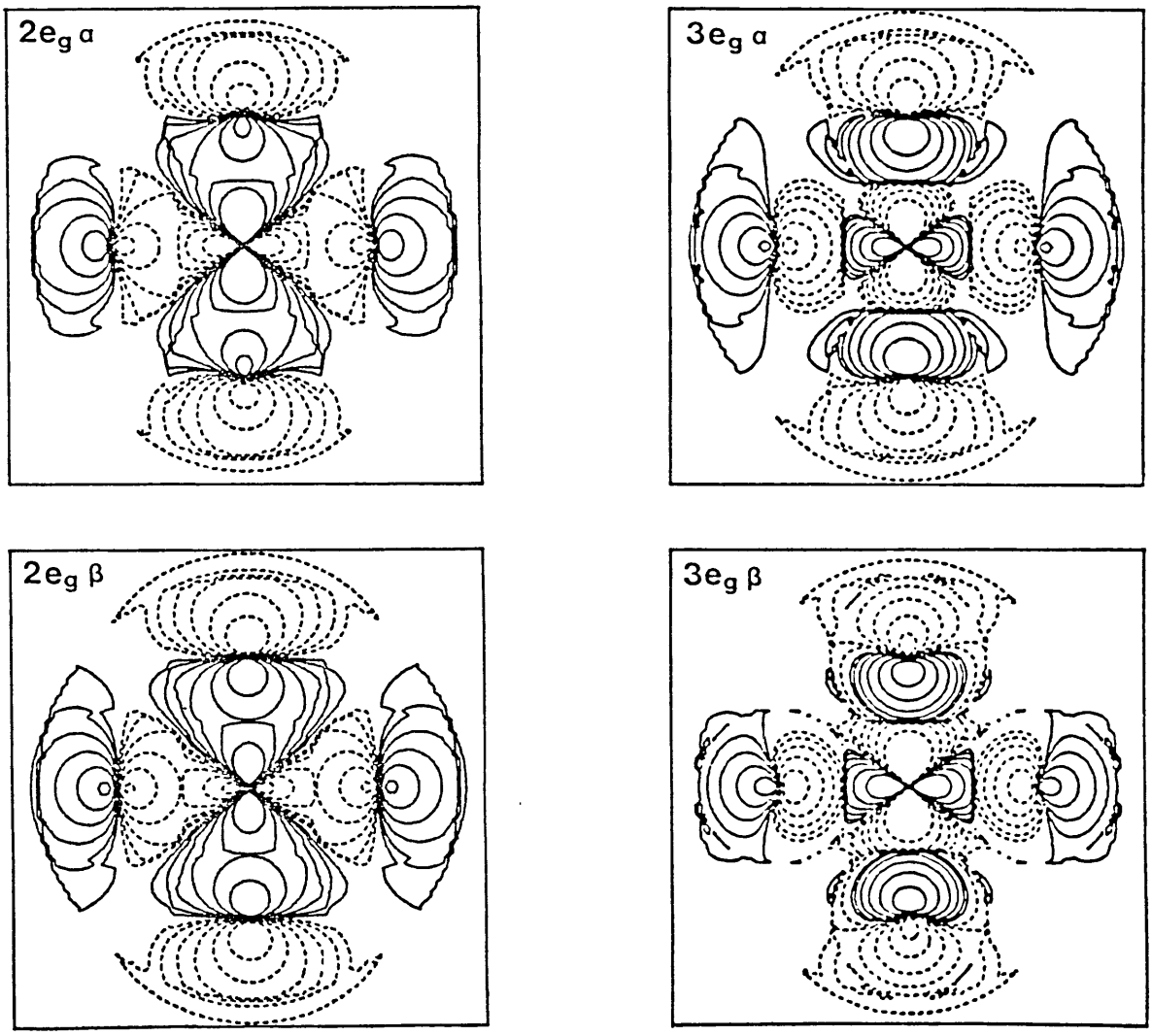


Figure 4.4: Wave function contours for the $2e_g$ bonding and $3e_g$ antibonding orbitals of the $(FeO_6)^{9-}$ cluster in the zx or zy plane. The orbitals may be viewed as consisting of the Fe $3d(z^2-r^2)$ atomic orbital and a linear combination of O 2p orbitals. Contour intervals are at 0.005, 0.01, 0.02, 0.04, 0.08 and 0.16. Solid and dashed contours indicate positive and negative values of the wave function, respectively.

Table 4.3: Orbital Compositions in the $(FeO_6)^{9-}$ Cluster.

	Energy (eV)	%Fe	%O	%Int.		Energy (eV)	%Fe	%O	%Int.
	Spin-Up Orbitals					Spin-Down Orbitals			
$7t_{1u}^*(0)$	8.11	1	32	59	$7t_{1u}^*(0)$	8.25	1	32	59
$4a_{1g}^*(0)$	5.80	0	20	72	$4a_{1g}^*(0)$	5.89	0	20	72
$3e_g^*$ (2)	2.01	35	61	4	$3e_g^*$ (0)	5.44	75	24	1
$1t_{1g}$ (3)	0.20	0	92	8	$2t_{2g}^*(0)$	3.58	86	7	6
$6t_{1u}$ (3)	0.01	2	89	8	$1t_{1g}$ (3)	0.44	0	91	8
$2t_{2g}^*(3)$	-0.56	48	40	12	$6t_{1u}$ (3)	0.29	2	89	8
$1t_{2u}$ (3)	-0.58	0	86	14	$1t_{2u}$ (3)	-0.36	0	85	14
$5t_{1u}$ (3)	-2.36	3	68	29	2eg (2)	-0.77	23	73	3
$3a_{1g}$ (1)	-2.50	11	75	14	$1t_{2g}$ (3)	-2.00	7	69	23
$2e_g$ (2)	-2.98	64	35	0	$3a_{1g}$ (1)	-2.09	9	75	15
$1t_{2g}$ (3)	-3.12	49	38	15	$3t_{1u}$ (3)	-2.14	2	68	29

The numbers in parentheses give the orbital occupancies. Orbitals with an asterisk are antibonding.

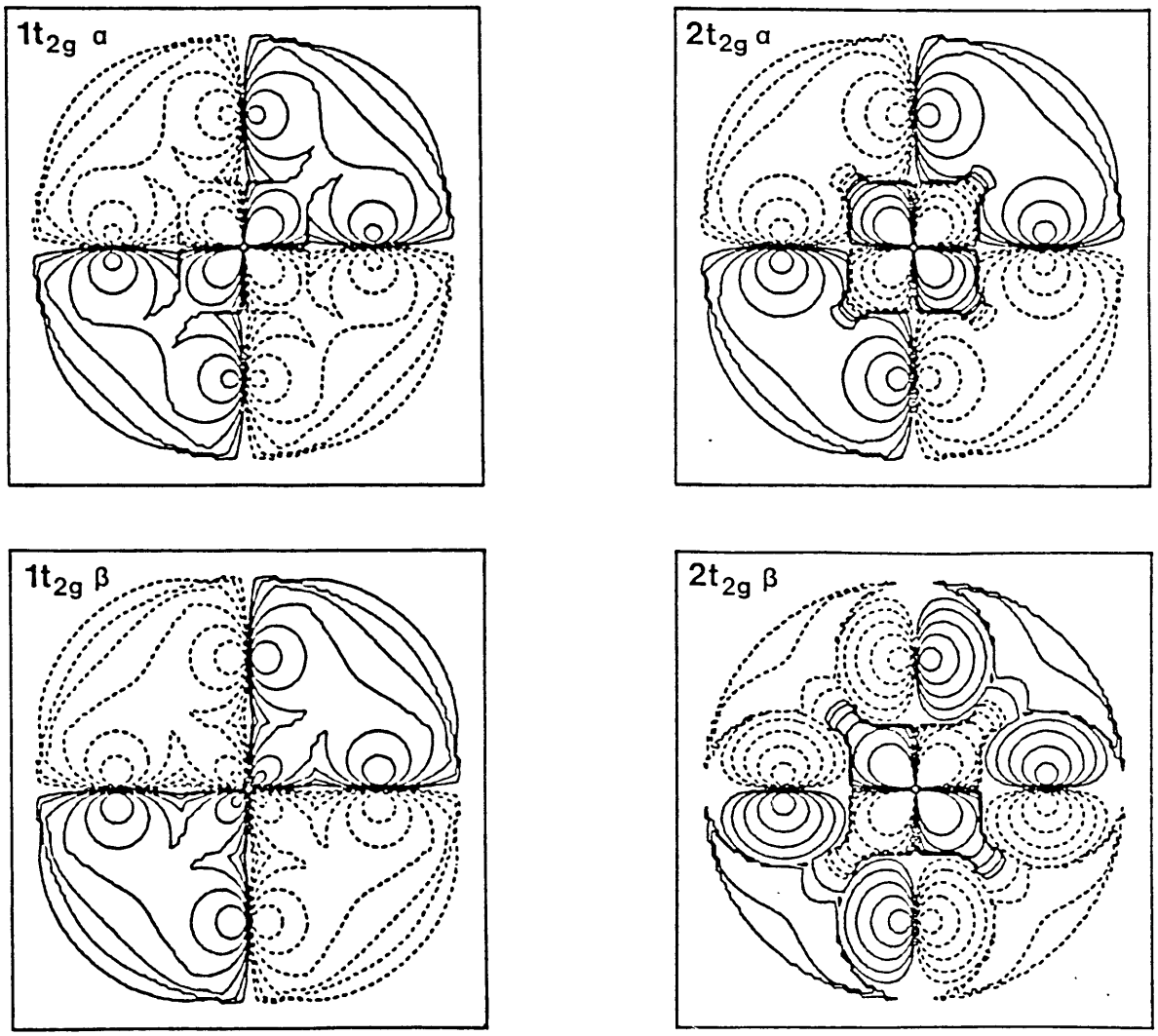


Figure 4.5: Wave function contours for the $1t_{2g}$ bonding and $2t_{2g}$ antibonding orbitals in the $(FeO_6)^{9-}$ cluster. These orbitals consist of the Fe 3d(xy), 3d(xz) or 3d(yz) atomic orbitals and a linear combination of O 2p orbitals. Contour intervals are as in Figure 4.4.

center, they also have a large spin polarization; that is, the spin-up or α-spin orbitals are much less localized than the spin-down or β-spin orbitals. This has some implications for the nature of charge carriers associated with intrinsic semiconduction in iron oxides and will be discussed below. In the spin-unrestricted picture, the $2t_{2g}$ and $3e_g$ orbitals have a large (ca. 3.9-4.1 eV) exchange splitting due to the unpaired Fe 3d electrons.

In the extreme limit of electrostatic crystal field theory, the $2t_{2g}$ and $3e_g$ orbitals are the Fe 3d atomic orbitals which have lost their degeneracy by interaction with the octahedral crystal field. In the more general ligand field theory, these orbitals correspond to the one-electron ligand field states. The molecular orbital and ligand field theory descriptions can be more precisely related. The energy separation between the $2t_{2g}$ and $3e_g$ orbitals in the spin-restricted picture can be equated with the ligand field theory parameter 10Dq provided the correct electronic configuration is used (Sambe and Felton, 1976). Moreover (as discussed below), the exchange splittings of these orbitals are directly proportional to the Racah B and C parameters of ligand field theory.

Fe 4s,4p band orbitals

The $7t_{1u}$ and $4a_{1g}$ orbitals correspond to the Fe 4p and Fe 4s atomic orbitals. They are not indicated in Figures 4.2 or 4.3 but their energies in the $(FeO6)^{9-}$ cluster are given in Table 4.3. Their calculated charge densities, however, show that they are strongly delocalized over the oxygen, intersphere and extramolecular regions. In the molecular orbital description, the $7t_{1u}$ and $4a_{1g}$ orbitals are the antibonding versions of the $3t_{1u}$ and $3a_{1g}$ bonding orbitals.

Electronic Structure of Tetrahedral $(FeO_4)^{5-}$

The spin-unrestricted molecular orbital diagram for the $(FeO_4)^{5-}$ cluster, corresponding to Fe^{3+} in tetrahedral coordination, is shown in Figure 4.6. Again, only the orbitals falling within the O 2p and Fe 3d bands are shown. The compositions of the orbitals shown in Figure 4.6 are given in Table 4.4.

O 2p valence band orbitals.

The non-bonding O 2p orbital combinations in the tetrahedral cluster are those of t_1 symmetry. The rest of the orbitals within the O 2p valence band are bonding in character. The molecular orbitals of t_2 symmetry correspond to both σ- and π-bonding interactions between the O 2p orbitals and the Fe 3d or Fe 4p atomic orbitals. In particular, the $3t_2$ orbital corresponds to Fe 3d - O 2p σ-bonding while the $4t_2$ orbital corresponds to Fe 4p - O 2p σ- and π-bonding. The molecular orbital of e symmetry is the main π-bonding interaction between the Fe 3d and O 2p orbitals. Finally, the $3a_1$ orbital is the O 2p - Fe 4s σ-bonding interaction.

Fe 3d band orbitals.

The 2e and $5t_2$ orbitals are the antibonding versions of the 1e and $3t_2$ bonding molecular orbitals. From Table 4.4, these orbitals are found to be mostly Fe 3d in character and tend to be localized on the Fe center. Although allowed by symmetry, there is no Fe 4p character in these orbitals. As with the $2t_{2g}$ and $3e_g$ orbitals of the $(FeO_6)^{9-}$ cluster, the 2e and $5t_2$ orbitals of the $(FeO_4)^{5-}$ cluster correspond to the e and t_2 one-electron states of ligand-field theory. In the tetrahedral cluster we also find a strong spin polarization such that the α-spin 2e and $5t_2$ orbitals are much less localized to the Fe center than are their β-spin counterparts.

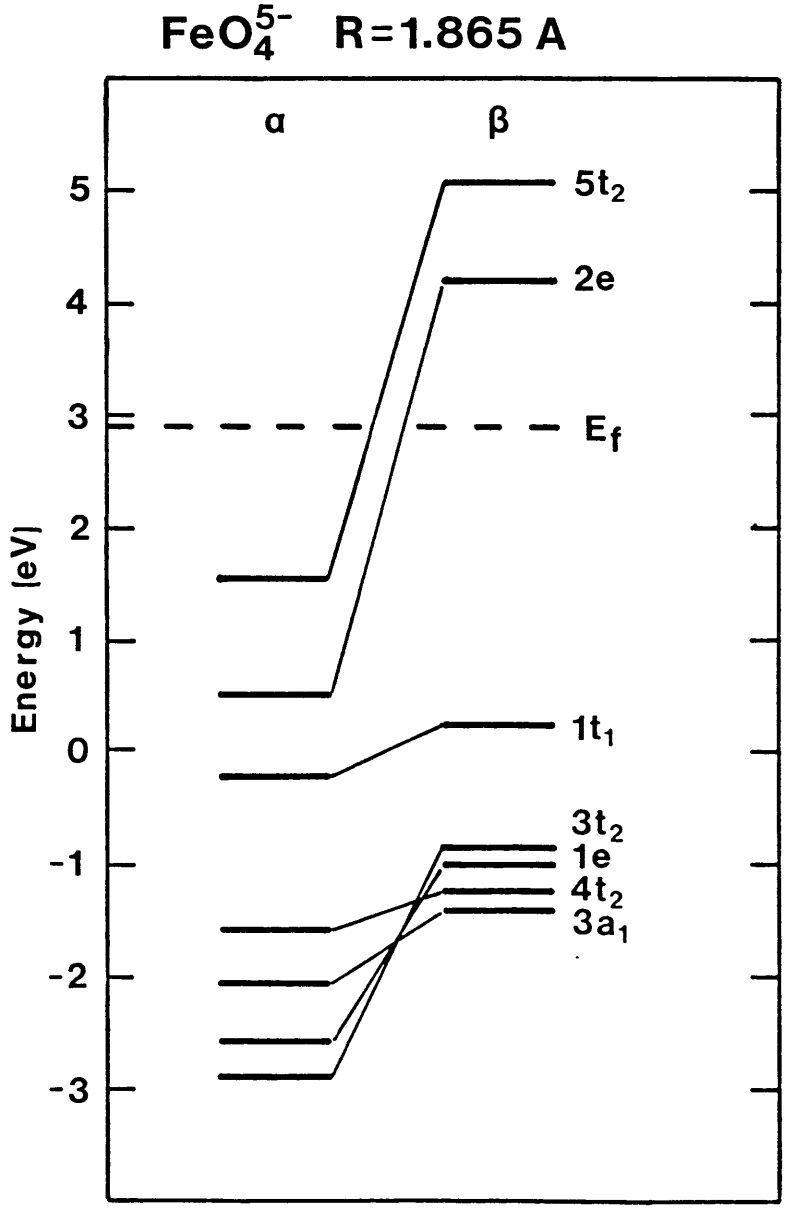


Figure 4.6: Molecular orbital diagram for the tetrahedral $(FeO_4)^{5-}$ cluster showing the orbitals which fall within the Fe(3d) bands (antibonding) and the O(2p) valence band (bonding and non-bonding). E_f is the Fermi energy, below which all orbitals are occupied. The Fe-O bond length in this cluster is 1.865 A.

Table 4.4: Orbital Compositions in the $(FeO_4)^{5-}$ Cluster.

	Energy (eV)	%Fe	%O	%Int.		Energy (eV)	%Fe	%O	%Int.
	Spin-Up Orbitals					Spin-Down Orbitals			
$4a_1^*$(0)	6.53	1	17	71	$4a_1^*$(0)	6.90	1	17	71
$5t_2^*$(3)	1.64	41	50	9	$5t_2^*$(0)	5.08	70	20	10
$2e^*$ (2)	0.53	44	46	10	$2e^*$ (0)	4.19	81	12	7
$1t_1$ (3)	-0.24	0	85	14	$1t_1$ (3)	0.24	0	86	13
$4t_2$ (3)	-1.65	3	64	33	$3t_2$ (3)	-0.86	21	68	10
$3a_1$ (1)	-2.06	11	71	18	1e (2)	-1.03	11	68	20
1e (2)	-2.57	52	35	13	$4t_2$ (3)	-1.25	3	63	34
$3t_2$ (3)	-2.88	55	40	4	$3a_1$ (1)	-1.43	9	70	21

Values in parentheses are the occupancies of the orbitals. For orbitals whose charge distribution does not sum to 100%, the remaining charge is located outside the outer sphere.

Fe 4s band orbitals.

The $4a_1^*$ orbital is the antibonding version of the $3a_1$ bonding orbital. The former also corresponds to the Fe 4s atomic orbital but is found to be strongly delocalized over the oxygen, interatomic, and extra-molecular regions. The energy of this orbital is given in Table 4.4. At an even higher energy is the $6t_2$ orbital which corresponds to the Fe 4p atomic orbital and the antibonding version of the $4t_2$ bonding orbital. The energy of the $6t_2$ orbital was not calculated, however.

The Electronic Structure of Trigonal $(FeO_6)^{9-}$

Figure 4.7 shows the spin-unrestricted electronic structure of the trigonally distorted $(FeO_6)^{9-}$ cluster used to approximate the coordination polyhedron of Fe^{3+} in hematite and minerals with related structures (for example, ilmenite and Fe^{3+} in Al_2O_3). Relative to the octahedral $(FeO_6)^{9-}$ cluster discussed previously, the descent in symmetry to C_{3v} splits the triply degenerate orbitals into twofold-degenerate e and singly degenerate a_1 or a_2 orbitals. The splitting of the orbitals due to the trigonal field in hematite is small, however, and as such, the electronic structures of the octahedral and trigonally distorted clusters are fairly similar.

The orbitals labelled $1a_2$, 7e, $8a_1$, 8e, $2a_2$, and 9e are all primarily O 2p non-bonding orbitals. Formally, the $1a_2$ and 7e orbitals result from splitting of the $1t_{1g}$ orbital, the $8a_1$ and 8e result from the splitting of the $6t_{1u}$ orbital, and the 7e and $1a_2$ result from the splitting of the $1t_{2u}$ orbital. These relations among the orbitals are only a convenience, however, because the the $1t_{2u}$, $6t_{1u}$ and $1t_{1g}$ non-bonding orbitals of the octahedral $(FeO_6)^{9-}$ cluster clearly mix with one another upon going from O_h

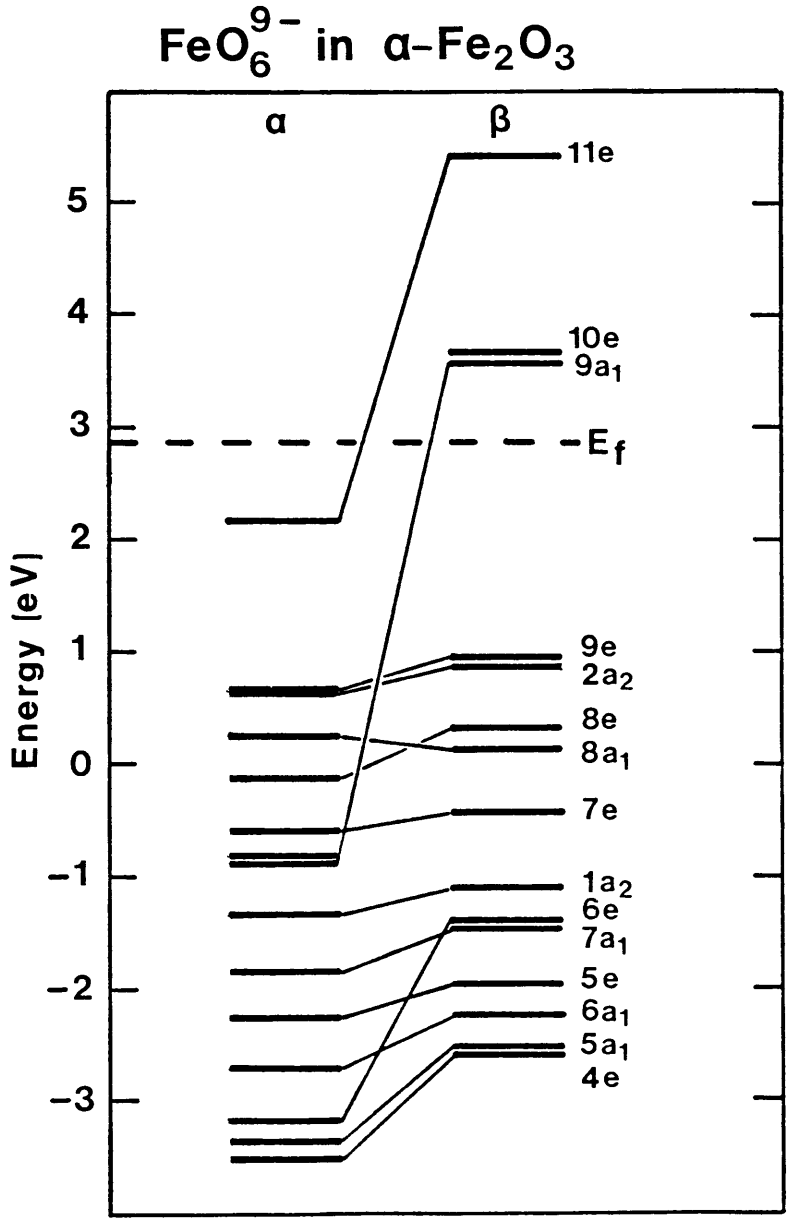


Figure 4.7: Molecular orbital diagram for the trigonally distorted $(FeO_6)^{9-}$ cluster (C_{3v} point group symmetry) used to approximate the coordination site of Fe^{3+} in hematite and other corundum structure oxides.

to C_{3v} symmetry. Hence, for example, the $1a_2$ and $2a_2$ orbitals each result from both the $1t_{1g}$ and $1t_{2u}$ orbitals of the octahedral $(FeO_6)^{9-}$ cluster.

The width of the O 2p non-bonding orbital set (about 2 eV) is much greater than that found in the octahedral $(FeO_6)^{9-}$ cluster. This broadening, in part, results from the trigonal site distortion. The latter forces the O(2) oxygens to be only 2.67 A apart which, in turn, increases their repulsive O-O interaction. This raises the energies of the O(2) oxygen 2p orbitals and, as such, the highest energy non-bonding orbitals (9e, and $2a_2$) are completely localised on the O(2) oxygens. On the other hand, the trigonal site distortion forces the O(1) oxygens to be farther apart with an O(1)-O(1) bond distance of 3.3 A. This decreases the O(1)-O(1) repulsive interaction and stablizes the O(1) oxygen 2p orbitals. Accordingly, the lowest energy O 2p non-bonding orbital ($1a_2$) is localised on the O(1) oxygens.

Electronic Transitions in Iron(III) Oxides and Silicates

General.

The near-infrared, visible and near-ultraviolet spectra of iron oxides consist of several types of electronic transitions: First, there are the transitions between the different multiplet states arising from the different Fe 3d configurations. These states are usually described using ligand field theory; the Tanabe-Sugano diagram for both octahedral and tetrahedral Fe^{3+} is shown in Figure 4.8. Second, there are the ligand to metal charge-transfer (LMCT) transitions. These are excitations from the O 2p valence band orbitals (mostly ligand character) to the Fe 3d crystal field type orbitals (mostly metal atom character). These transitions are most easily understood within the context of molecular orbital theory. At

somewhat higher energies than the LMCT transitions are the transitions from the Fe 3d-type orbitals to the Fe 4s- and 4p-type orbitals. These will be referred to as metal-to-conduction band (MCB) transitions. Finally, there are transitions which arise from Fe^{3+}-Fe^{3+} pair interactions; these will be discussed in more detail below.

The optical spectra of Fe^{3+} systems have been poorly understood. Often, the different ligand field states shown in Figure 4.8 are obscured by the higher energy LMCT transitions. An additional source of complexity in the spectra of Fe^{3+} systems, however, is the effect of Fe-O-Fe superexchange interactions on the Fe 3d intraconfigurational (ligand field type) transitions. Note that all of the transitions from the $^6A_1$ ground state to the excited states involve a two-fold change in spin-multiplicity. As such, all of these transitions are spin-forbidden and one would expect their intensities to be very small. In the spectra of iron oxides and a number of other minerals, however, the nominally spin-forbidden Fe^{3+} ligand field transitions are found instead to be quite intense. The apparent relaxation of the spin selection rule results from the magnetic coupling of second-nearest-neighbor Fe^{3+} cations in the crystal structure (Ferguson et al., 1966; Krebs and Maisch, 1971; Lohr, 1972; Rossman, 1975). In the presence of Fe^{3+}-Fe^{3+} coupling, localized excitations involving a change in spin-multiplicity can occur provided that the net spin of the coupled pair remains unchanged. Because of the strong intensification of the Fe^{3+} ligand-field transitions by Fe^{3+}-Fe^{3+} pair interactions, it is often difficult to distinguish these transitions from the ligand to metal charge-transfer bands. Assignments of features to LMCT transitions based on their intensities should be viewed with caution.

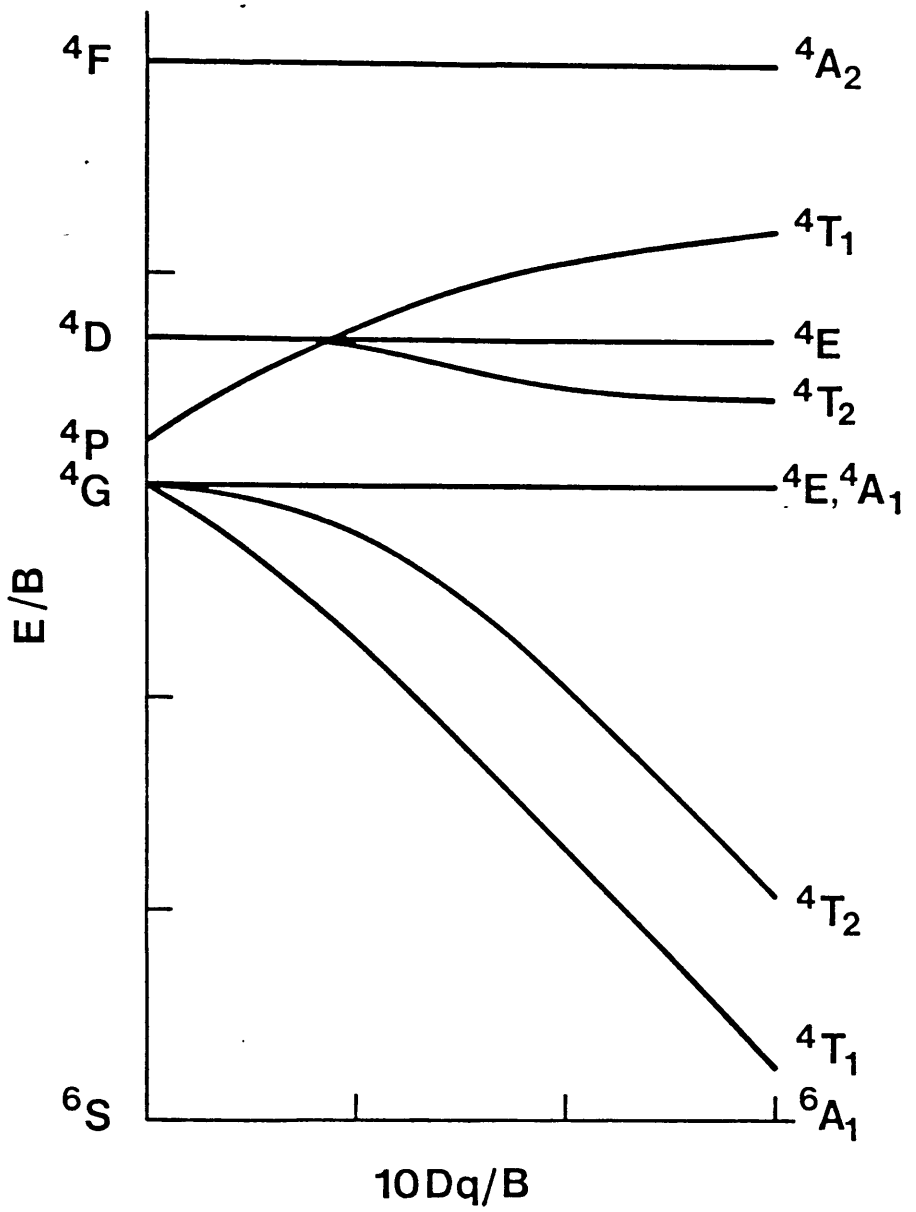


Figure 4.8: Tanabe-Sugano diagram for high-spin Fe^{3+} in either octahedral or tetrahedral coordination. Relative state energies were calculated using the expressions given in Lever (1968) and assuming C/B = 4.0. The doublet (S = 1/2) states are not shown since they are not observed in the spectra of Fe^{3+} solids and complexes.

To complicate matters further, the Fe^{3+}-Fe^{3+} pair interactions allow for a new type of electronic transition, namely, the simultaneous excitation of two Fe^{3+} centers by a single photon. These excitations give rise to additional absorption features at energies given by the sum of two simple Fe^{3+} ligand field transitions. Such transitions have been invoked by Ferguson and Fielding (1972) to account for several features in the spectra of Fe^{3+} in Al_2O_3.

Multiplet theory for Fe^{3+} crystal field states.

Because the electronic structures of the clusters are obtained in a one-electron orbital formalism, all that can be directly calculated are the energies of transitions between one-electron orbitals. The ligand field transitions indicated in Figure 4.8 are derived from the one-electron orbital transitions between the $2t_{2g}$ and $3e_g$ orbitals (see Fig. 4.3). The energies of the latter were calculated using the transition-state formalism and are given in Table 4.5. To use these calculated one-electron orbital transition energies for the interpretation of the spectra of iron oxides, it is first necessary to show how the one-electron orbitals are related to the ligand field states (or multiplets) given in Figure 4.8. The relations between the one-electron orbital energies and the energies of the different multiplets arising from the Fe^{3+} d^5 configurations can be derived using multiplet theory (Slater, 1968; 1974).

The spectroscopic states or multiplets shown in Figure 4.8 are composed of linear combinations of Slater determinents over the five Fe 3d type orbitals. For example, denoting the three $2t_{2g}$ orbitals by ξ, η, and ζ and the two $3e_g$ orbitals by u and v, the Ms = 5/2 state of the $^6A_{1g}(^6S)$ multiplet is simply

$$|^6A_{1g}(^6S),\ M_S=5/2\rangle = |\xi\eta\zeta uv| \qquad (4.1)$$

Table 4.5: Calculated Optical spectra of Fe^{3+} oxides.

One-electron Transition	Energy (kK)	Corresponding Spectroscopic Transitions	Comments
$(FeO_6)^{9-}$ O_h			
$6t_{1u}^{\beta} \rightarrow 3e_g^{\beta}$	51.9	$^6A_{1g} \rightarrow {}^6T_{1u}, {}^6T_{2u}$	LMCT
$3e_g^{\alpha} \rightarrow 7t_{1u}^{\alpha}$	50.9	$6A1g \rightarrow {}^6T_{1u}, {}^6T_{2u}$	MCB
$1t_{2u}^{\beta} \rightarrow 2t_{2g}^{\beta}$	43.6	$^6A_{1g} \rightarrow {}^6A_{1u}, {}^6E_u, {}^6T_{1u}, {}^6T_{2u}$	LMCT
$6t_{1u}^{\beta} \rightarrow 2t_{2g}^{\beta}$	38.1	$^6A_{1g} \rightarrow {}^6A_{2u}, {}^6E_u, {}^6T_{1u}, {}^6T_{2u}$	LMCT
$3e_g^{\alpha} \rightarrow 4a_{1g}^{\alpha}$	32.7	$^6A_{1g} \rightarrow {}^6E_g$	MCB (Forbidden)
$2t_{2g}^{\alpha} \rightarrow 2t_{2g}^{\beta}$	29.3	$^6A_{1g} \rightarrow {}^4E_g, {}^4A_{1g}(^4G), {}^4T_{2g}(^4D),$	Ligand Field
$3e_g^{\alpha} \rightarrow 3e_g^{\beta}$	25.4	$^4E_g(^4D), {}^4T_{1g}(^4P), {}^4A_{2g}(^4F)$	
$3e_g^{\alpha} \rightarrow 2t_{2g}^{\beta}$	11.1	$^6A_{1g} \rightarrow {}^4T_{1g}(^4G), {}^4T_{2g}(^4G)$	Ligand Field
$(FeO_4)^{5-}$			
$1t_1^{\beta} \rightarrow 2e^{\beta}$	40.4	$^6A_1 \rightarrow {}^6T_1, {}^6T_2$	LMCT
$2e^{\alpha} \rightarrow 2e^{\beta}$	26.0	$^6A_1 \rightarrow {}^4E, {}^4A_1(^4G), {}^4T_2(^4D),$	Ligand Field
$5t_2^{\alpha} \rightarrow 5t_2^{\beta}$	23.0	$^4E(^4D), {}^4T_1(^4P), {}^4A_2(^4F)$	
$2e^{\alpha} \rightarrow 5t_2^{\beta}$	16.2	$^6A_1 \rightarrow {}^4T_1(^4G), {}^4T_2(^4G)$	Ligand Field

but the $M_S = 3/2$ state of the $^4A_{1g}(^4G)$ multiplet is

$$|^4A_{1g}(^4G),\ M_S=3/2\rangle = -(2/15)^{1/2}\{|\xi\eta\bar{\zeta}uv| + |\xi\eta\zeta\bar{u}v| + |\xi\eta\zeta u\bar{v}|\} + (3/10)^{1/2}\{|\xi\eta\zeta uv\overline{|} + |\xi\eta\zeta uv|\overline{|}\} \quad (4.2)$$

where the bar indicates a spin-down or β-spin orbital.

Using the transition-state formalism, the energy required for a transition between one-electron orbitals corresponds to the energy difference between the ground and resulting excited state electronic configurations. The energy of an electronic configuration over one-electron orbitals corresponds to the average energy of all the Slater determinents that are consistent with that electronic configuration. In order to evaluate the energies of the multiplet states of the system, we must be able to find the energies of individual Slater determinents over the Fe 3d orbitals. This, in general, cannot be done. On the other hand, we can always find the average energy of several Slater determinents, depending on the chosen electronic configuration, and this can be related to the average energy of the multiplets that are constructed from those Slater determinents.

The following discussion will be based on Fe^{3+} in octahedral coordination; the results for Fe^{3+} in tetrahedral coordination follow directly. The ground state configuration of octahedrally coordinated Fe^{3+} in the spin-restricted picture is $t_{2g}^3e_g^2$. Now, the energy of the $(2t_{2g})^3(3e_g)^2$ configuration corresponds to the average energy of all the Slater determinants resulting from this configuration. By taking the direct product of all the occupied one-electron orbitals, we find that these Slater determinents must combine to give the multiplet states:

$$^6A_1(^6S) + {}^4E(^4G) + {}^4A_1(^4G) + {}^4E(^4D) + {}^4A_2(^4F) + {}^4T_1(^4P) + {}^4T_2(^4D) + \text{doublet states} \quad (4.3)$$

The energy of the $(2t_{2g})^3(3e_g)^2$ configuration corresponds to the average energy of all of these multiplets. Unfortunately, these multiplets span most of the excited states of Fe^{3+} given in Figure 4.8. As such, the spin-restricted one-electron orbitals provide only the crudest description of the ligand field states of high-spin Fe^{3+}.

A spin-unrestricted calculation, however, allows us to set up a configuration with a given value of the magnetic spin quantum number M_S. This gives us much more information since the energy of such a configuration corresponds to the average energy of only the Slater determinents resulting from that configuration which have that value of M_S. This energy, in turn, corresponds to the average energy of the multiplets with components that can be constructed with these Slater determinents (that is, the multiplets whose spin quantum number S is greater than or equal to M_S). In other words, the energy of a configuration with a given M_S corresponds to the average energy of the multiplets arising from that configuration that have $S \geq M_S$. First, we wish to find the energy of the ground $^6A_1$ multiplet. The $M_S = 5/2$ component of this multiplet is the only state which arises from the $t_{2g}{}^3e_g{}^2$ configuration with $M_S = 5/2$ (that is, the spin unrestricted configuration $(2t_{2g}{}^\alpha)^3(3e_g{}^\alpha)^2$). Hence, the energy of the $^6A_1$ multiplet can be directly equated with the energy of this spin-unrestricted configuration.

Next, we wish to find the energies of the quartet multiplets arising from the $t_{2g}{}^3e_g{}^2$ configuration. The $M_S = 3/2$ components of these multiplets, together with the $M_S = 3/2$ component of the $^6A_1$ multiplet, arise

from the $t_{2g}^3e_g^2$ configurations that have $M_S = 3/2$--namely, the $(2t_{2g}^{\alpha})^2(3e_g^{\alpha})^2(2t_{2g}^{\beta})^1$ and $(2t_{2g}^{\alpha})^3(3e_g^{\alpha})^1(3e_g^{\beta})^1$ spin-unrestricted configurations. There are thirteen Slater determinents with $M_S = 3/2$ arising from the $t_{2g}^3e_g^2$ configuration. The energy of the $(2t_{2g}^{\alpha})^2(3e_g^{\alpha})^2(2t_{2g}^{\beta})^1$ configuration corresponds to the average energy of nine of these determinents while the energy of the $(2t_{2g}^{\alpha})^3(3e_g^{\alpha})^1(3e_g^{\beta})^1$ configuration corresponds to the average energy of the remaining four determinents. Hence, the average energy of all the Ms = 3/2 determinental wavefunctions associated with the $(2t_{2g})^3(3e_g)^2$ configuration is given by

$$\langle E(M_S = 3/2)\rangle = (1/13)(9\langle E_1\rangle + 4\langle E_2\rangle) \qquad (4.4)$$

where $\langle E_1\rangle$ and $\langle E_2\rangle$ are the energies of the $(2t_{2g}^{\alpha})^2(3e_g^{\alpha})^2(2t_{2g}^{\beta})^1$ and $(2t_{2g}^{\alpha})^3(3e_g^{\alpha})^1(3e_g^{\beta})^1$ configurations, respectively. By the diagonal sum rule, $\langle E(M_S = 3/2)\rangle$ also corresponds to the average energy of all multiplets associated with the $(2t_{2g})^3(3e_g)^2$ configuration which have an $M_S = 3/2$ component. These are the $^6A_1$ and the quartet multiplets given above. Now we are able to calculate the average energy difference between the quartet states that arise from the $(2t_{2g})^3(3e_g)^2$ configuration and the ground $^6A_{1g}$ state: From the above relation, the total energy of all the $M_S = 3/2$ determinental wavefunctions is $9\langle E_1\rangle + 4\langle E_2\rangle$. This corresponds to the total energy of all the multiplet states which have an $M_S = 3/2$ component. Of these, there are 12 quartet states and 1 hextet state. Hence,

$$12\langle E(S=3/2)\rangle + \langle E(S=5/2)\rangle = 9\langle E_1\rangle + 4\langle E_2\rangle \qquad (4.5)$$

Rearranging gives,

$$\langle E(S=3/2)\rangle - \langle E(S=5/2)\rangle = (3/4)\{\langle E_1\rangle - \langle E(S=5/2)\rangle\} + (1/3)\{\langle E_2\rangle - \langle E(S=5/2)\rangle \qquad (4.6)$$

The quantities $\{\langle E_1\rangle - \langle E(S=5/2)\rangle\}$ and $\{\langle E_2\rangle - \langle E(S=5/2)\rangle\}$ can be readily evaluated using the transition state procedure: $\{\langle E_1\rangle - \langle E(S=5/2)\rangle\}$ and $\{\langle E_2\rangle - \langle E(S=5/2)\rangle\}$ correspond to the energies of the $2t_{2g}^{\alpha} \rightarrow 2t_{2g}^{\beta}$ and $3e_g^{\alpha} \rightarrow 3e_g^{\beta}$ one-electron orbital transitions. From the $(FeO_6)^{9-}$ cluster calculation, the $2t_{2g}^{\alpha} \rightarrow 2t_{2g}^{\beta}$ and $3e_g^{\alpha} \rightarrow 3e_g^{\beta}$ one-electron orbital transitions are calculated to have energies of 29.3 and 25.4 kK, respectively (Table 4.5). Hence, the average energy of the ^4E, $^4A_1(^4G)$, $^4T_2(^4D)$, $^4E(^4D)$, $^4T_1(^4P)$ and $^4A_2(^4F)$ states, relative to the $^6A_1(^4G)$ state, is 30.4 kK. For the $(FeO_4)^{5-}$ cluster, the theoretical barycenter energy of the quartet states arising from the $(e)^2(t_2)^3$ configuration is 25.9 kK.

Finally we consider the quartet multiplets arising from the excited state one-electron orbital configuration $t_{2g}^4e_g^1$ of $(FeO_6)^{9-}$. The direct product of these one-electron orbitals (again, considering only the different spin-multiplicities allowed by the Pauli principle) gives the multiplets

$$^4T_1(^4G) + {}^4T_2(^4G) + 2(^2T_1) + 2(^2T_2) + {}^2A_1 + {}^2A_2 + 2(^2E) \qquad (4.7)$$

(The doublet states are not shown in Figure 4.7). As before, the energy of the $t_{2g}^4e_g^1$ configuration corresponds to the average energy of all these multiplets. We can go to the spin-unrestricted calculation, however, and find the average energies of only those multiplets which have a component of a given M_s. We are interested only in the quartet multiplets since these are the only ones observed experimentally. Hence, we are only interested in the Ms = 3/2 $t_{2g}^4e_g^1$ configuration, $(2t_{2g}^{\alpha})^3(3e_g^{\alpha})^1(2t_{2g}^{\beta})^1$. The energy of this configuration is the average energy of the $^4T_{1g}(^4G)$ and $^4T_{2g}(^4G)$ multiplets. Hence, the average energy of the $^6A_{1g} \rightarrow {}^4T_{1g}$ and $^6A_{1g} \rightarrow {}^4T_{2g}$ spectroscopic transitions is given by the difference between the $2t_{2g}^{\beta}$ and

$3e_g^{\alpha}$ orbital energies in the transition state configuration $(2t_{2g}^{\alpha})^3(3e_g^{\alpha})^{1.5}(2t_{2g}^{\beta})^{0.5}$. This is calculated to be 11.13 kK. From the $(FeO_4)^{5-}$ cluster orbital energies, the average energy of the $^6A_1 \rightarrow {}^4T_1$ and $^6A_1 \rightarrow {}^4T_2$ transitions of tetrahedrally coordinated Fe^{3+} is calculated to be 16.2 kK.

Estimation of Fe^{3+} Ligand Field Theory Parameters.

The meaning of the ligand field theory parameter 10Dq in the context of one-electron molecular orbital theory has been uncertain. Sambe and Felton (1976) have shown, using the hyper-Hartree-Fock energy functional (Slater, 1974) that 10Dq does have meaning in the context of spin-restricted Xα one-electron molecular orbitals. For the case of the $(FeO_6)^{9-}$ cluster, 10Dq is the $3e_g$-$2t_{2g}$ one-electron orbital energy difference in the spin-restricted configuration $t_{2g}^3e_g^2$. Similarly, for the $(FeO_4)^{5-}$ cluster, 10Dq is the $5t_2$-2e one-electron orbital energy difference in the configuration $(2e)^2(5t_2)^3$. (The relation is not as straightforward for other transtion metal ions.) From the spin-restricted calculation of the octahedral $(FeO_6)^{9-}$ cluster, the parameter 10Dq is calculated to be 15.8 kK. In the trigonally-distorted $(FeO_6)^{9-}$cluster, 10Dq decreases slightly to 15.0 kK. For the tetrahedral $(FeO_4)^{5-}$ cluster, 10Dq is calculated to be 8.23 kK. The ligand field theory expression for the average energy of the $^4T_1(^4G)$ and $^4T_1(^4G)$ states that arise from the $(t_{2g})^4(e_g)^1$ configuration of $(FeO_6)^{9-}$ or the $(t_2)^4(e)^1$ configuration of $(FeO_4)^{5-}$ is (Lever, 1968)

$$E = -10Dq + 14B + 6C \qquad (4.8)$$

(Note that this expression neglects the configuration interaction terms.) This energy was calculated from the one-electron orbital energies to be 11.1 kK in the $(FeO_6)^{9-}$ cluster and 16.2 kK in the $(FeO_4)^{5-}$ cluster. The ligand field theory expression for the approximate average energy of the quartet

states arising from the $(t_{2g})^3(e_g)^2$ configuration of $(FeO_6)^{9-}$ (or the $(e)^2(t_2)^3$ configuration of $(FeO_4)^{5-}$) can be derived from the Tanabe-Sugano expressions for the energies of these states (e.g. Lever, 1968). This gives

$$E = (91/6)B + (17/3)C \qquad (4.9)$$

This was calculated to be 30.4 kK for the $(FeO_6)^{9-}$ cluster and 25.9 kK in the $(FeO_4)^{5-}$ cluster. Given equations (4.8) and (4.9), and the previously calculated values for 10Dq, we might be able to calculate values for the Racah B and C parameters. Unfortunately, the small (20%) relative errors in the theoretical average state energies give very large relative errors in the Racah B and C parameter values. If, instead, we assume that C = 4.7B as in the free-ion, then for the $(FeO_6)^{9-}$ cluster we get B = 727 cm^{-1} from the $(t_{2g})^4(e_g)^1$ configuration (eq. 11) and B = 637 cm^{-1} from the $(t_{2g})^3(e_g)^2$ configuration (eq. 12). Similarly, for the $(FeO_4)^{5-}$ cluster, we get B = 579 cm^{-1} from the $(t_2)^4(e)^1$ configuration and B = 620 cm^{-1} from the $(t_2)^3(e)^2$ configuration.

Ligand to Metal Charge-Transfer Transitions

In the $(FeO_6)^{9-}$ cluster, the lowest energy allowed one-electron LMCT transitions are $6t_{1u}^{\beta} \rightarrow 2t_{2g}^{\beta}$ and $6t_{1u}^{\beta} \rightarrow 3e_g^{\beta}$. The one-electron $6t_{1u}^{\beta} \rightarrow 2t_{2g}^{\beta}$ transition corresponds to a set of spectroscopic transitions $^6A_{1g} \rightarrow {}^6T_{1u}, {}^6A_{2u}, {}^6E_u, {}^6T_{2u}$. Of these, only the $^6A_{1g} \rightarrow {}^6T_{1u}$ transition is allowed by the Laporte (or parity) selection rule. The $6t_{1u}^{\beta} \rightarrow 3e_g^{\beta}$ transition corresponds to two spectroscopic transitions $^6A_{1g} \rightarrow {}^6T_{1u}, {}^6T_{2u}$ and, again, only the $^6A_{1g} \rightarrow {}^6T_{1u}$ is allowed.

We wish to relate the energies of the one-electron LMCT transitions to those of the actual spectroscopic transitions. Here, we shall use an approach similar to that of Verdonck and Vanquickenborne (1976). Consider the transition $6t_{1u}^{\beta} \rightarrow 2t_{2g}^{\beta}$ in $(FeO_6)^{9-}$. The excited state electronic

configuration can be expressed as $(6t_{1u}^{\alpha})^3(6t_{1u}^{\beta})^2(2t_{2g}^{\alpha})^3(2t_{2g}^{\beta})^1(3e_g^{\alpha})^2$. This may be thought of as consisting of a $(6t_{1u}^{\alpha})^3(6t_{1u}^{\beta})^2$ sub-configuration over the ligand nonbonding orbitals and a $(2t_{2g}^{\alpha})^3(2t_{2g}^{\beta})^1(3e_g^{\alpha})^2$ subconfiguration over the Fe 3d type antibonding orbitals. Now the $(6t_{1u}^{\alpha})^3(6t_{1u}^{\beta})^2$ subconfiguration yields the term $^1T_{1u}$. Likewise, the $(2t_{2g}^{\alpha})^3(2t_{2g}^{\beta})^1(3e_g^{\alpha})^2$ subconfiguration yields the term $^5T_{2g}$. The $^6T_{1u}$,$^6A_{2u}$,^6E_u,$^6T_{2u}$ excited states arising from the $6t_{1u}^{\beta} \rightarrow 2t_{2g}^{\beta}$ one-electron transition, therefore, result from the direct product of the $^1T_{1u}$ and $^5T_{2g}$ terms arising from the two subconfigurations. This implies that the spread in energy of the different LMCT excited states ($^6T_{1u}$,$^6A_{2u}$,^6E_u,$^6T_{2u}$) arising from the $6t_{1u}^{\beta} \rightarrow 2t_{2g}^{\beta}$ transition is dependent only on the interelectronic repulsion between the Fe 3d ($2t_{2g}$) and O 2p ($6t_{1u}$) orbital electrons. Intuitively, we expect this repulsion to be small since the ligand-type non-bonding orbitals and the Fe 3d-type antibonding orbitals have very different spatial distributions. Accordingly, the different states arising from the $6t_{1u}^{\beta} \rightarrow 2t_{2g}^{\beta}$ transition should have similar energies. (The same argument can be made for the $6t_{1u}^{\beta} \rightarrow 3e_g^{\beta}$ transition.) This being the case, the energies of the multielectronic LMCT transitions observed experimentally should be close to the energies of the one-electron orbital LMCT transitions. This approximation will probably fail, however, when one is considering transitions from the bonding O 2p valence band orbitals to the Fe 3d band orbitals. This is because of the repulsion between the bonding orbital electrons and Fe 3d band orbital electrons.

It is of interest to consider the effect of trigonal site distortions on the LMCT energies of the $(FeO_6)^{9-}$ clusters. Tossell (1980) calculated the electronic structure of a $(FeO_6)^{9-}$ cluster with C_{2v} symmetry (one O-O

distance shortened) and found that the energy separation between the Fe 3d and O 2p bands was decreased from that found in an octahedral $(FeO_6)^{9-}$ cluster. It was suggested that, in accordance with the smaller energy gap, the LMCT transition energies will also be smaller. In the $(FeO_6)^{9-}$ cluster with C_{3v} symmetry investigated here, we also find a significant decrease in the energy separation between the O 2p and Fe 3d bands. This does not imply, however, that the LMCT transition energies will be smaller. To understand why this is the case, it is worthwhile to digress on the nature of the LMCT excited states in O_h and C_{3v} symmetry.

In O_h symmetry, the $6t_{1u} \rightarrow 2t_{2g}$ transition corresponds to a set of spectroscopic transitions

$$^6A_{1g} \rightarrow {}^6A_{2u},\ {}^6E_u,\ {}^6T_{1u},\ {}^6T_{2u} \qquad (4.10)$$

Upon descent to C_{3v} symmetry, the different states are split to give

$$^6A_1 \rightarrow {}^6A_2,\ {}^6E,\ {}^6A_1,\ {}^6E,\ {}^6A_2,\ {}^6E \qquad (4.11)$$

Similarly the $1t_{2u} \rightarrow 2t_{2g}$ one-electron transition in octahedral symmetry corresponds to a set of spectroscopic transitions

$$^6A_{1g} \rightarrow {}^6A_{1u},\ {}^6E_u,\ {}^6T_{1u},\ {}^6T_{2u} \qquad (4.12)$$

which split in C_{3v} symmetry to give

$$^6A_1 \rightarrow {}^6A_1,\ {}^6E,\ {}^6A_1,\ {}^6E,\ {}^6A_2,\ {}^6E \qquad (4.13)$$

Finally, the $1t_{1g} \rightarrow 2t_{2g}$ transition in O_h symmetry corresponds to the spectroscopic transitions

$$^6A_{1g} \rightarrow {}^6A_{1g},\ {}^6E_g,\ {}^6T_{1g},\ {}^6T_{2g} \qquad (4.14)$$

which split in C_{3v} symmetry to give

$$^6A_1 \rightarrow {}^6A_1,\ {}^6E,\ {}^6A_2,\ {}^6E,\ {}^6A_1,\ {}^6E \qquad (4.15)$$

Now, as noted previously, the $1t_{2u}$, $6t_{1u}$ and $1t_{1g}$ orbitals of the octahedral cluster mix with each other under the trigonal distortion. Consequently, the states in (4.11), (4.13) and (4.15) with the same symmetry also mix with

each other. This being the case, all that can be said precisely is that the average energy of all of the states in (4.11), (4.13) and (4.15) with a given symmetry is given by the average energy of all of the one-electron orbital transitions which give excited state configurations with that symmetry. For example, in the one-electron orbital description of the trigonally-distorted $(FeO_6)^{9-}$ cluster calculated here, the $2a_2 \rightarrow 9a_1$ LMCT type transition, which gives an excited state configuration with $^6A_2$ symmetry, has an energy of only 3.5 eV.This does not imply that there is a spectroscopic $^6A_1 \rightarrow {}^6A_2$ transition with that energy, however; it only implies that there is a Slater determinent with that energy. The true $^6A_2$ LMCT states are made up of linear combinations of several Slater determinents with $^6A_2$ symmetry.

The decreased separation between the Fe 3d and O 2p orbitals in the trigonal $(FeO_6)^{9-}$ cluster, therfore, does not have any immediate physical significance. Other clusters with low symmetry, such as $(FeO_4(OH)_2)^{7-}$ and $(Fe_2O_{10})^{14-}$ discussed in chapters 5 and 6, also show a decreased separation between the O 2p and Fe 3d orbitals. The reason for this is simply that we are able to separate more of the Slater determinents from each other by removing the orbital degeneracies.

Metal to Conduction Band transitions.

In this section, we will briefly consider the transitions from the Fe 3d bands to the Fe 4s and Fe 4p conduction bands. These will be referred to as metal-to-conduction band (MCB) transitions. In the octahedral $(FeO_6)^{9-}$ cluster, the Fe 4s and Fe 4p bands are defined by the $7a_{1g}$ and $7t_{1u}$ orbitals. These orbitals are quite delocalized and, hence, like the lowest energy LMCT transitions, the spread in energies of the multiplet states arising from a given one-electron orbital transition to these orbitals

should be small. The lowest energy MCB transition is the $3e_g^{\alpha} \rightarrow 4a_{1g}^{\alpha}$ which corresponds to the single multielectronic transition $^6A_{1g} \rightarrow {}^6E_g$. The energy of this transition is calculated to be only 32.7 kK. There is no evidence for this transition in the near-UV spectra of Fe^{3+} oxides and silicates, however, probably because it is forbidden by the Laporte selection rule.

In contrast, the $3e_g^{\alpha} \rightarrow 7t_{1u}^{\alpha}$ transition of $(FeO_6)^{9-}$ is allowed by the Laporte selection rule. The energy of this transition is calculated to be 50.9 kK or well into the near-ultraviolet.

It should be noted that the energies calculated for the MCB transitions are probably much less reliable than those for other types of spectroscopic transitions. The $7a_{1g}$ and $7t_{1u}$ orbitals of the $(FeO_6)^{9-}$ cluster have a large outer-sphere component. Accordingly, the potential calculated for electrons in these orbitals is a poor approximation to that in real solids.

Comparison With Experimental Fe^{3+} Spectra

Tables 4.6 and 4.7 give spectral band energies for Fe^{3+} cations in octahedral and tetrahedral coordinations in several oxides and silicates. Spectra of the iron oxide and oxide hydroxide polymorphs, particularly in the near-UV, are few. For comparison with the theoretical results described here, however, the most useful experimental data are spectra of dilute Fe^{3+} cations in oxide host phases. In these systems, spectral bands resulting from Fe^{3+}-Fe^{3+} pair interactions can be more easily identified.

Spectra of Octahedral Fe^{3+}

The most extensively investigated system is Fe^{3+} in Al_2O_3 (Krebs and Maisch, 1971; Ferguson and Fielding, 1972; Lehman and Harder, 1970; Tippins, 1970). These data are perhaps the most reliable of any Fe^{3+} system studied. Spectra of Fe^{3+} in MgO have been investigated by Blazey (1977); these

results are fairly consistent with those for Fe^{3+} in Al_2O_3. The band assignments for these systems (Table 4.6) are in agreement with those of the different investigators.

In addition to the spectra of dilute Fe^{3+} cations in oxide host phases, spectra of two condensed Fe^{3+} phases (hematite and nontronite) are available. The band assignments for Fe^{3+} in nontronite are somewhat different from those of Karickhoff and Bailey (1973); they did not take spectra in the near-infrared and, hence, did not find the $^4T_1(^4G)$ and $^4T_2(^4G)$ bands at 10.6 and 16.1 kK (Singer, 1982). A feature at 19.2 kK was assigned by them to the $^4T_2(^4G)$ band; this feature more likely corresponds to the $^4T_1(^4G)+^4T_1(^4G)$ pair excitation.

In their investigation of the optical spectrum of hematite, Marusak et al. (1980) used the calculated one-electron orbital transition energies obtained by Tossell et al. (1973;1974) to assign spectroscopic features to either "spin-flip" or LMCT transitions. Some of the spectral band assignments given by Marusek et al. (1980), and Tossell et al.(1973) are incorrect; the calculated energies for the one-electron LMCT transitions are too low by about 1.5 -2.0 eV (this work) which led to features due to ligand field transitions being misassigned to LMCT transitions. Moreover, the spectra were interpreted by assigning specific one-electron orbital transitions to spectroscopic absorption features. Actually, for the LMCT transitions this may not be a bad approximation (as discussed previously); in general, however, it is physically incorrect.

From the octahedral $(FeO_6)^{9-}$ cluster calculation, the average energy of the $^6A_1(^6S) \rightarrow {}^4T_1(^4G)$ and $^6A_1(^6S) \rightarrow {}^4T_2(^4G)$ transitions is estimated to be 11.13 kK. This compares favorably with the data for Fe^{3+}:Al_2O_3 and Fe^{3+}:MgO where the average is about 11.9 kK. For other octahedral Fe^{3+}

Table 4.6: Observed electronic transition energies for Fe^{3+} in octahedral coordination sites in oxides and silicates (energies are in kK).

State	$Fe^{3+}:Al_2O_3$	$Fe^{3+}:MgO$	α-Fe_2O_3	Nontronite
$^4T_1(^4G)$	9.45	10.0	11.6	10.6
$^4T_2(^4G)$	14.35	13.5	--	16.1
$^4E,^4A_1(^4G)$	22.27	21.74	23.8	22.5
$^4T_2(^4D)$	25.51	25.12	--	26.0
$^4E(^4D)$	26.8	27.5	26.7	27.2
$^4T_1(^4P)$	32.5	30.97	31.8	--
$^4A_2(^4F)$	--	--	--	--
$6t_{1u}^{\beta} \rightarrow 2t_{2g}^{\beta}$	38.6	35.8	38.9	38.2
$1t_{2u}^{\beta} \rightarrow 2t_{2g}^{\beta}$	--	40.5	44.8(?)	--
$6t_{1u}^{\beta} \rightarrow 3e_g^{\beta}$	51.5	46.2	--	50.0
$3e_g^{\alpha} \rightarrow 7t_{1u}^{\alpha}$	58.1	--	--	--
10Dq	15.27	13.4	15.9	14.2
B	0.65	0.48	0.41	0.67
C	3.16	3.38	3.93	3.12
Reference	1-4	5,6	7	8

1. Krebs and Maisch (1971); 2. Ferguson and Fielding (1971);
3. Lehmann and Harder (1971) 4. Tippins (1970); 5. Blazey (1977);
6. Cheng and Kemp (1971); 7. Marusak et al. (1980);
8. Karickhoff and Bailey (1973)

systems, however, the average energy of these two transitions is somewhat higher; in hematite it is 14 kK while in nontronite it is 13.4 kK.

The average energy of the quartet states arising from the $(2t_{2g})^3(3e_g)^2$ configuration was calculated to be 30.4 kK. This cannot be directly measured experimentally because the high-energy $^4T_1(^4P)$ and $^4A_2(^4F)$ transitions are obscured by the LMCT bands. Still we can estimate an experimental value for the average energy of the quartet states by using the Rachah B and C parameters derived from the spectra and the approximate Tanabe-Sugano expression for the average energy (eq. 13). This gives 28.1 kK for $Fe^{3+}:Al_2O_3$, 27.9 kK for $Fe^{3+}:MgO$, 28.0 kK for Fe^{3+} in nontronite and 27.8 kK for hematite. Considering the approximations involved, these values are in good agreement with the theoretical MO results.

The value for 10Dq in the octahedral $(FeO_6)^{9-}$ cluster was estimated to be 15.8 kK. The Racah B parameter is estimated to be on the order of 0.64-0.73 kK assuming C/B = 4.7. The value for 10Dq is in good agreement with those estimated for the systems in Table 4.6. It is also in good agreement with values obtained from the spectra of goethite (α-FeOOH) and lepidocrocite (γ-FeOOH) obtained by Mao and Bell (1974) and the data presented in Chapter 6. Close agreement between theory and experiment is expected in this case given that calculations on the isoelectronic $(MnO_6)^{10-}$ and comparably covalent $(MnO_6)^{9-}$ clusters, described in chapter 3, also gave accurate values for 10Dq. The crude estimation of the Racah B parameter value is consistent with the experimental estimates. It should be pointed out that, in ligand field theory, the parameters 10Dq, B and C are derived assuming that their values are independant of the electronic configuration. In effect, the assumption is made that the $2t_{2g}$ and $3e_g$ orbitals do not relax during electronic transitions. Since this is not the

case, the experimental values for 10Dq, B and C really represent the average values over all the possible electronic configurations. In the approach used here, the values for 10Dq and B are derived from the $2t_{2g}$ and $3e_g$ orbital energies in a single configuration. The good agreement between the SCF-Xα-SW results for these parameters and the experimental values, therefore, indicate that ligand field theory provides a good approximation for the spectra of Fe^{3+} oxides and silicates.

The lowest energy LMCT transition, $6t_{1u}^{\beta} \rightarrow 2t_{2g}^{\beta}$, is estimated to occur at 38.1 kK. This corresponds nearly exactly with the position of a strong band in the spectra of Fe^{3+}:Al_2O_3, nontronite, and hematite that has also been assigned by the original investigators of these spectra to a LMCT transition. In Fe^{3+}:MgO, this feature is found at a somewhat lower energy (35.8 kK) and may reflect a larger Fe^{3+}-O distance. The agreement between the theoretical energy of this one electron orbital transition and the experimental value of the lowest LMCT transition band energy supports the argument given in the previous section, namely, that the spread in energy of the multiplets arising from the $6t_{1u}^{\beta} \rightarrow 2t_{2g}^{\beta}$ transition ($^6A_{2u}$, ^6E_u, $^6T_{1u}$ and $^6T_{2u}$) is small enough not to perturb their energies.

The next LMCT transition, $1t_{2u}^{\beta} \rightarrow 2t_{2g}^{\beta}$, corresponds to a set of transitions $^6A_{1g} \rightarrow {}^6A_{1u}, {}^6E_u, {}^6T_{1u}, {}^6T_{2u}$ which are calculated to have an average energy of 43.6 kK. Although the $^6A_{1u} \rightarrow {}^6T_{1u}$ transition is Laporte-allowed, it apparently has a fairly low intensity since no feature is resolved at the energy in the spectra of Fe^{3+}:Al_2O_3 and nontronite. This band may be obscured by the presumeably more intense $^6A_{1g} \rightarrow {}^6T_{1u}$ transition that arises from the $6t_{1u}^{\beta} \rightarrow 2t_{2g}^{\beta}$ one-electron orbital transition. A feature at 44.8 kK in the spectrum of hematite may correspond to the $1t_{2u}^{\beta} \rightarrow 2t_{2g}^{\beta}$ set or it may simply be an instrumental artifact

resulting from the cutoff of the UV detector.

The next higher energy LMCT transitions are the $^6A_{1g} \rightarrow {}^6T_{1u}, {}^6T_{2u}$ that arise from the $6t_{1u}^{\beta} \rightarrow 3e_g^{\beta}$ one-electron orbital transition. The energy of the latter is calculated to be 51.9 kK. This energy corresponds to that of a feature at 51.5 and 50.0 kK in the spectra of $Fe^{3+}:Al_2O_3$ and nontronite, respectively, and may also correspond to the band at 46.1 kK in the spectra of Fe^{3+}:MgO. In the spectra of these systems, this band is considerably more intense than that associated with the $6t_{1u}^{\beta} \rightarrow 2t_{2g}^{\beta}$ transition. This may be explained, in part, by noting that the $6t_{1u}^{\beta} \rightarrow 2t_{2g}^{\beta}$ transition corresponds to four spectroscopic transitions $^6A_{1g} \rightarrow {}^6A_{2u}, {}^6E_u, {}^6T_{1u}, {}^6T_{2u}$ with only the $^6A_{1g} \rightarrow {}^6T_{1u}$ allowed while the $6t_{1u}^{\beta} \rightarrow 3e_g^{\beta}$ transition corresponds to only two spectroscopic transitions $^6A_{1g} \rightarrow {}^6T_{1u}, {}^6T_{2u}$ with the $^6A_{1g} \rightarrow {}^6T_{1u}$ transition being allowed. As such, we can observe one-half of the transitions associated with the $6t_{1u}^{\beta} \rightarrow 3e_g^{\beta}$ transition but only one-fourth of the transitions associated with the $6t_{1u}^{\beta} \rightarrow 2t_{2g}^{\beta}$ transition. Note that the $3e_g^{\alpha} \rightarrow 7t_{1u}^{\alpha}$ MCB transition was estimated to have an energy of 50.9 kK. Hence, this transition might also account for the 50-51 kK band observed in Fe^{3+} spectra. However, finite cluster calculations can grossly underestimate MCB transition energies and as such the calculated $3e_g^{\alpha} \rightarrow 7t_{1u}^{\alpha}$ energy is probably unreliable. Instead, the intense feature at 58.3 kK in the spectrum of $Fe^{3+}:Al_2O_3$ probably corresponds to this transition.

Spectra of Tetrahedral Fe^{3+}

The data for tetrahedrally coordinated Fe^{3+} in $LiAlO_2$ (Waychunas and Rossman, 1983) is quite useful since the mean Fe-O bond length in this system was determined by EXAFS to be 1.82 A. This is fairly similar to the bond distance in the $(FeO_4)^{5-}$ cluster calculation presented here (1.865 A). Waychunas and Rossman (1983) did not assign any of the absorption bands in

their optical spectra of Fe^{3+} in $LiAlO_2$. According to Lehmann (1970), Fe^{3+} in low-quartz occupies the tetrahedral interstitial site. Lehmann (1970) assigned the 18.7 and 20.2 kk features in the Fe^{3+}:SiO_2 spectrum to the $^6A_1 \rightarrow {}^4T_1(^4G)$ and $^4T_2(^4G)$ transitions, respectively. Likewise, Karickhoff and Bailey (1973) assigned the 19.0 and 20.5 kk features in the spectra of tetrahedral Fe^{3+} in phlogopite to these transitions. The band assignments given here differ in that these two features are assigned to split components of the $^4T_2(^4G)$ state. Both the $^4T_1(^4G)$ and $^4T_2(^4G)$ states are usually split by the dynamic Jahn-Teller effect. The revised assignment scheme presented here is in closer agreement with the data of Waychunas and Rossman (1983) and, as will be shown below, with the $(FeO_4)^{5-}$ cluster calculation.

The average energy of the $^4T_1(^4G)$ and $^4T_2(^4G)$ transitions of the tetrahedral $(FeO_4)^{5-}$ cluster was calculated to be 16.2 kK. This argues against the assignments given by Lehmann (1970) and Karickhoff and Bailey (1973) for the $^4T_1(^4G)$ and $^4T_2(^4G)$ bands. The calculated average energy is in reasonable agreement with the data for Fe^{3+}:$LiAlO_2$ if the band assignment given in Table 4.7 is used.

The average energy of the quartet states arising from the $(2e)^2(5t_2)^3$ configuration was calculated to be 25.9 kK. Using the band assignments and the resulting values for B and C, the experimental average energy is estimated to be 26.7 kK for Fe^{3+}:$LiAlO_2$, 27.8 for Fe^{3+} in orthoclase, 28.1 kK for Fe^{3+}:SiO_2 and 27.6 kK for Fe^{3+} in phlogopite. The agreement between theory and experiment is fairly good for Fe^{3+}:$LiAlO_2$ where the Fe-O bond lengths are known to be fairly similar to those of the $(FeO_4)^{5-}$ cluster. As will be discussed below, the $(FeO_4)^{5-}$ cluster calculation indicates that the effective spin on the Fe atom is smaller in the $(FeO_4)^{5-}$

Table 4.7: Observed electronic transition energies in tetrahedral Fe^{3+} coordination sites in oxides and silicates

State	Fe^{3+}:$LiAlO_2$	Fe^{3+}:SiO_2	Orthoclase	Phlogopite
$^4T_1(^4G)$	14.5,16.3	--	--	--
$^4T_2(^4G)$	18.5,19.6	18.7,20.2	20.7	19.0,20.5
$^4E,^4A_1(^4G)$	21.6	22.5	22.7	22.6
$^4T_2(^4D)$	22.3	24.8	24.8	24.4
$^4E(^4D)$	25.6	27.3	26.5	26.3
$^4T_1(^4P)$	--	--	--	--
$^4A_2(^4F)$	--	--	--	--
LMCT	--	40.7	--	--
LMCT or MCB	--	51.1	--	47.2
10Dq	8.35			
B	0.57	0.69	0.55	0.53
C	3.18	3.13	3.43	3.46
Reference	1	2	3	4

1.Waychunas and Rossman (1983); 2. Lehmann (1970); 3. Manning (1970); 4. Karickhoff and Bailey (1973)

cluster than in the $(FeO_6)^{9-}$ cluster. A smaller effective spin should result in a decreased exchange splitting of the Fe 3d orbitals, as is the case. In accordance with the decreased exchange splittings, the average energy of the quartet states in the $(FeO_4)^{5-}$ cluster should also be smaller, as was calculated. The experimental data indicate that this picture is qualitatively correct but, on the other hand, the calculations seem to exaggerate the magnitude of the effect.

The value for 10Dq in $(FeO_4)^{5-}$ was estimated to be 8.23 kK using the approach of Sambe and Felton (1976). If the energy of the $^4T_1(^4G)$ state is taken to be the average energy of the 14.5 and 16.3 kK bands, then the experimental value for 10Dq is estimated to be 8.35 kK. This value also predicts the $^4T_2(^4G)$ band energy with the expected accuracy. The close agreement between the SCF-Xα-SW and experimental values for 10Dq lends further support for the band assignments given in Table 4.7.

The lowest energy LMCT transition of the $(FeO_4)^{5-}$ cluster is the $1t_1^{\beta} \rightarrow 2e^{\beta}$ which was calculated to have an energy of 40.4 kK. This agrees well with the spectrum of Fe^{3+}:SiO_2 where the first LMCT band is observed at 40.7 kK. No feature near 40 kK is found in the spectrum of Fe^{3+} in phlogopite but a broad shoulder at 35.7 kK in one sample was observed by Karickhoff and Bailey (1973). This feature was assigned by Faye (1968) to $Fe^{3+} \rightarrow Al^{3+}$ charge-transfer. More likely, it corresponds to the $1t_{1\beta} \rightarrow 2e^{\beta}$ LMCT transition. Bands observed at 51.5 kK and 47.2 kK in the spectra of Fe^{3+}:SiO_2 and Fe^{3+} in phlogopite, respectively, can be readily assigned to the $1t_1^{\beta} \rightarrow 5t_2^{\beta}$ transition.

The lowest energy LMCT transitions of octahedrally- and tetrahedrally-coordinated Fe^{3+} occur well into the near-ultraviolet. Although the tails of these transitions contribute to some of the absorption

by Fe^{3+} in the visible region, they are not responsible for the visible region absorption edge observed in the spectra of Fe^{3+} oxides and silicates. Spectra of isolated Fe^{3+} centers in solids or mononuclear complexes show only weak absorbance in the visible region (e.g. Lehmann, 1970; Rossman, 1975); indeed, such systems are nearly colorless. In systems where Fe^{3+} centers are magnetically coupled with each other, however, the characteristic visible region absorption edge is present. Hence, most of the visible region absorption in iron oxides and silicates is due to ligand field transitions which have been intensified by Fe-O-Fe superexchange interactions. The pair excitations, not addressed here but discussed in chapter 5, may also contribute to the visible region absorption edge.

Spectra of Fe^{2+} Cations in Oxides

The electronic spectra of Fe^{2+} cations in oxides will be treated briefly. The lowest energy one-electron orbital transition in $(FeO_6)^{10-}$ is $2t_{2g}{}^{\beta} \rightarrow 3e_g{}^{\beta}$. This corresponds exactly with the spectroscopic transition $^5T_2 \rightarrow {}^5E$ and its energy is equal to the ligand field theory parameter 10Dq. The energy of the $2t_{2g}{}^{\beta} \rightarrow 3e_g{}^{\beta}$ transition is calculated to be 11.13 kK, in reasonable agreement with the $^5T_2 \rightarrow {}^5E$ energy observed in Fe^{2+} in MgO (Blazey, 1977) and numerous Fe^{2+} bearing silicates (Burns, 1970). All other ligand field transitions of octahedrally coordinated Fe^{2+} are spin-forbidden and the relations between the one-electron orbital energies and those of the other ligand field states are complex. The multiplet theory approach used in the previous section for Fe^{3+} was based on the strong field approximation (Lever, 1968); this is probably less reliable for Fe^{2+}.

The lowest energy LMCT transition in $(FeO_6)^{10-}$ is $6t_{1u}{}^{\beta} \rightarrow 2t_{2g}{}^{\beta}$. The energy of this transition is calculated to be 53.7 kK, in very good

agreement with that observed for a strong band in the spectra of Fe^{2+} bearing olivine and pyroxene (Nitsan and Shankland, 1976). Note that the energy of the first LMCT transition in Fe^{2+} oxides and silicates is much greater than that for Fe^{3+} oxides. This is to be expected and is due to the lower formal oxidation state, and hence, optical electronegativity of Fe^{2+}. The same result was found for the LMCT transition energies in Mn^{2+}, Mn^{3+} and Mn^{4+} oxides discussed in chapter 3.

Applications to the Physical Properties and Crystal Chemistry of Iron Oxides

Ionic vs. Covalent Bonding

By the nature of the Fe-O chemical bond, electronic charge is donated to the Fe^{3+} center by the O^{2-} anion coordination environment; that is, the Fe-O bond is partially covalent. Covalency, however, is not a quantum mechanical observable and, as such, it is not possible to give a quantitative measure of covalency without invoking an arbitrary scheme for partitioning the electronic charge among the atoms. The results of the SCF-Xα-SW calculations give the electronic charge within each of the atomic spheres and within the interatomic region. One approach to partitioning the electronic charge among the atoms is to partition the interatomic charge of a given orbital according to the ratio of the atomic charges of the orbital. The results of this procedure for the Fe^{3+} clusters are given in Table 4.8 which shows the net electronic charge (number of electrons) of each spin donated to the different Fe^{3+} centers by each type of orbital interaction. Analogous results for the $(FeO_6)^{10-}$ cluster are given in Table 4.9. The results show that, in each cluster, the Fe-O bond is fairly covalent; the charge on the Fe^{3+} center is reduced to about 40% of its hypothetical ionic value of +3. Likewise, the Fe^{2+} center in $(FeO_6)^{10-}$ has a charge of about

Table 4.8: Net Charge Donated to Fe Atoms by Each Type of Orbital Interaction.

	$(FeO_6)^{9-}$ O_h			$(FeO_6)^{9-}$ C_{3v}			$(FeO_4)^{5-}$ T_d	
	α-Spin	β-Spin		α-Spin	β-Spin		α-Spin	β-Spin
$e_g(\sigma)$	-0.009	-0.474						
$t_{2g}(\pi)$	-0.365	-0.273				e	-0.173	-0.276
t_{1u}	-0.191	-0.150	e	-0.374	-0.763	t_2	-0.182	-0.837
$a_{1g}(\sigma)$	-0.128	-0.106	a_1	-0.292	-0.280	a_1	-0.134	-0.114
Total	-0.693	-1.003		-0.666	-1.043		-0.489	-1.227
Net Charge on Fe	+1.304			+1.291			+1.284	
Net Spin on Fe	4.69 α-spin			4.623 α-spin			4.260	

Table 4.9: Charge Donated to Fe^{2+} Cation in $(FeO_6)^{10-}$ by Each Type of Orbital Interaction.

	α-Spin	β-Spin
$e_g(\sigma)$	-0.006	-0.227
$t_{2g}(\pi)$	-0.071	-0.044
t_{1u}	-0.186	-0.146
$a_{1g}(\sigma)$	-0.119	-0.107
Total	-0.382	-0.524

Net Charge on Fe = +1.094

Net Spin on Fe = 3.858 μ_B

55% of its hypothetical ionic value. The Fe^{3+}-O bond should be more covalent than the Fe^{2+}-O bond since the smaller, more highly charged Fe^{3+} cation has a greater electron affinity. Note that the covalency of the Fe-O bond is essentially the same in the octahedral, tetrahedral, and trigonally-distorted octahedral clusters. On the other hand, the nature of the Fe-O covalency, in particular its spin-polarization, differs appreciably among the clusters. The effect of covalency on the spin-population (and effective magnetic moment) at the Fe^{3+} site can be related to the magnetic structures of Fe^{3+} oxides; this will be discussed below.

The bonding in the trigonally distorted $(FeO_6)^{9-}$ cluster is interesting insofar as there are two different oxygen sites. The Fe-O(2) bond is somewhat more covalent than the Fe-O(1) bond. This is contrary to what one might expect given that the Fe-O(2) bond length (2.117 A) is considerably greater than the Fe-O(1) bond length (1.950 A). Apparently, the strong repulsive interactions across the short (2.669 A) O(2)-O(2) bonds promote the Fe-O(2) bonding interaction. (One might argue that the covalency of the Fe-O(2) bond is greater than that of the Fe-O(1) bond because the atomic sphere radius of the O(2) atom is greater than that of the O(1) atom. This does not appear to be the case since the atomic sphere overlap of the Fe-O(2) bond is much smaller than that of the Fe-O(1) bond.)

The electronic structures of MnO_6 clusters corresponding to Mn^{2+}, Mn^{3+} and Mn^{4+} coordination sites in manganese oxides were discussed in chapter 3 and several points of comparison with the FeO_6 cluster calculations are worth noting. The Mn^{2+} centered $(MnO_6)^{10-}$ cluster is isoelectronic with the $(FeO_6)^{9-}$ cluster. The bonding in the $(MnO_6)^{10-}$ cluster is found to be much more ionic than in $(FeO_6)^{9-}$, in accordance with the expected smaller polarizing ability of the Mn^{2+} ion. Because of the smaller degree of

covalency in the Mn^{2+} cluster, the extent of 3d electron delocalization onto the ligands in $(MnO_6)^{10-}$ is smaller than in $(FeO_6)^{9-}$. This results in the exchange splittings of the Mn^{2+} 3d type orbitals being somewhat greater than those of the Fe^{3+} 3d type orbitals. Optical spectra indicate that this is indeed the case; in oxides and silicates, the Racah B and C parameters for Mn^{2+} ions are greater than those for Fe^{3+} ions (Manning, 1970).

Fe^{3+} and Mn^{4+} oxides exhibit similar mineralogical and geochemical behaviors. The crystal structures of several Mn^{4+} oxides are isostructural with certain Fe^{3+} oxide hydroxides. On the other hand, Mn^{4+} oxides can form a number of structures not found among the Fe^{3+} oxides and oxide hydroxides. The bonding in Mn^{4+} oxides is more covalent than that in Fe^{3+} oxides. Using the same charge-partitioning scheme as that outlined above, the effective charge on the Mn^{4+} center in the $(MnO_6)^{8-}$ cluster was found to be smaller than that of Fe^{3+} in the $(FeO_6)^{9-}$ cluster (+1.06 vs. +1.3, see Tables 3.5 and 4.7). The smaller effective charge of the Mn^{4+} center in oxides may explain why the manganese (IV) oxides show a greater structural diversity than that of the iron (III) oxides. Unlike Fe^{3+}, Mn^{4+} can form a number of layer-structured oxides (e.g. birnessite, lithiophorite, chalcophanite and buserite). These structures require MnO_6 polyhedra to share edges with 5 or even 6 adjacent polyhedra and as such are not energetically favorable in the context of Pauling's rules for ionic solids.

Magnetism in Iron Oxides

An important aspect of the Fe-O chemical bond is its spin polarization. In the $(FeO_6)^{9-}$ cluster, the α-spin $3e_g$ and $2t_{2g}$ antibonding orbitals are occupied. This tends to cancel out much of the α-spin $1t_{2g}$ and $2e_g$ Fe-O bonding interaction. At the same time, the β-spin antibonding orbitals are unoccupied. Consequently, most of the net electronic charge donated to the

Fe^{3+} center by the O^{2-} anions is of β-spin character (see Table 4.7). This leaves the oxygen atoms with a net α-spin excess. The oxygen atoms will therefore favor donating α-spin electronic charge to any other Fe^{3+} centers to which they are bonded. This can be done only if the antibonding orbitals localized on these Fe^{3+} centers are occupied by β-spin electrons; that is, if these Fe^{3+} centers are antiferromagnetically coupled to the first Fe^{3+} center. It follows, therefore, that the spin-polarized calculations on simple $(FeO_6)^{9-}$ clusters predict the occurence of the antiferromagnetic superexchange interaction observed in Fe^{3+} oxides and silicates. The same result follows from the nature of the bonding in the $(FeO_4)^{5-}$ cluster.

We can apply these concepts to the magnetic structures of iron oxides. In spinel-structure oxides such as magnetite or maghemite, Fe atoms in the octahedral B sites are coupled antiferromagnetically with Fe atoms in the tetrahedral A sites. This forces the B site cations to be ferromagnetically coupled to each other. Such a magnetic structure implies that the A-B site antiferromagnetic coupling is stronger than the B-B site antiferromagnetic coupling. The results given in Table 4.7 show that the net electronic spin at the tetrahedral Fe^{3+} center is much smaller than that at an octahedral Fe^{3+} center. Hence, the electronic spin of an O^{2-} anion is polarized stronger by the A-site Fe^{3+} center than by the B-site Fe^{3+} center. This, in turn, results in the Fe(A)-O-Fe(B) antiferromagnetic interaction being stronger than the Fe(B)-O-Fe(B) antiferromagnetic interaction. Note, however, that in the mixed-valence oxide magnetite, ferromagnetic coupling between the B-site Fe^{2+} and Fe^{3+} cations should also be promoted by the double-exchange mechanism (Goodenough, 1971).

The magnetic structure of hematite is such that the Fe^{3+} ions are antiferromagnetically coupled across the shared faces along the c-axis but

ferromagnetically coupled within the basal planes perpendicular to the c-axis. Within the basal planes, FeO_6 polyhedra share edges and corners. This magnetic structure follows if the antiferromagnetic interaction between face-sharing FeO_6 polyhedra is stronger than that between edge- and corner-sharing FeO_6 polyhedra. In the context of the simple FeO_6 clusters, one might expect the face-sharing antiferromagnetic interaction to be stronger than the edge-or corner-sharing antiferromagnetic interaction simply because face-sharing FeO_6 polyhedra have three ligands in common while edge-or corner-sharing FeO6 polyhedra have only two, or one, ligands in common. Although this may be the case, we also find, in the trigonally-distorted $(FeO_6)^{9-}$ cluster, that the Fe^{3+} ion induces a greater α-spin population on the O(2) site than it does on the O(1) site. Hence, the Fe-O(2)-Fe antiferromagnetic interaction will be stronger than the Fe-O(1)-Fe antiferromagnetic interaction. Since the O(2) oxygens are those which bridge the face-sharing $(FeO_6)^{9-}$ polyhedra, it follows that the face-sharing $(FeO_6)^{9-}$ coordination sites will be antiferromagnetically coupled to one another. In short, the strong Fe-O(2)-Fe antiferromagnetic interaction is promoted by the trigonal distortion of the Fe coordination site in hematite. Note also that we need not invoke any metal-metal interaction across the shared face to account for the magnetic structure.

The theoretical discussion of the relation between chemical bonding and magnetism presented here can be addressed by results of polarized neutron diffraction (Tofield, 1975;1976) studies on Fe^{3+} coordination sites in oxides. Rakhecha and Satya Murthy (1978) have investigated the magnetic moment of the tetrahedral Fe^{3+} site in magnetite (Fe_3O_4). The observed reduction of the Fe^{3+} magnetic moment from the free ion value is a function of the spatial volume of integration about the Fe^{3+} site but is in

qualitative agreement with that found here. Bonnet et al. (1978) measured the magnetic moments at the octahedral and tetrahedral sites in yttrium iron garnet ($Y_3Fe_5O_{12}$); their results showed that, as found here, the tetrahedral Fe^{3+} moment is smaller than the octahedral Fe^{3+} moment. In both of these systems, the reduction in Fe^{3+} moment is attributed to Fe-O covalency.

Previous $(FeO_6)^{9-}$ and $(FeO_4)^{5-}$ cluster molecular orbital calculations, using the Discrete Variational Method (Xα exchange but with the LCAO approximation), have been done by Byrom et al. (1975). These results also showed that, due to covalency, the magnetic moment of tetrahedrally-coordinated Fe^{3+} is smaller than that for octahedrally-coordinated Fe^{3+}.

Chemical-bonding and the Mossbauer spectra of iron oxides.

Several aspects of the Fe-O bond that are given in Table 4.7 can be related to the Mossbauer spectra of iron oxides. First, the isomer shifts (relative to metallic iron) of tetrahedrally coordinated Fe^{3+} are generally smaller than those of octahedrally coordinated Fe^{3+}. In γ-Fe_2O_3, for example, the isomer shift of tetrahedral Fe^{3+} is 0.27 mm/sec while that for octahedral Fe^{3+} is 0.41 mm/sec (Goodman, 1982). The isomer shift (relative to metallic iron) decreases with increasing s-electron charge density at the Fe nucleus. From Table 4.7 we find that the net 4s orbital population is greater in the $(FeO_4)^{5-}$ cluster than in the $(FeO_6)^{9-}$ cluster and, accordingly, the s-electron charge density at the nucleus in probably greater in $(FeO_4)^{5-}$ than in $(FeO_6)^{9-}$. Tang Kai et al. (1980) have shown that with decreasing Fe-O distance, the isomer shift in $(FeO_4)^{5-}$ decreases, due to increased Fe-O covalency. This may also explain the decreased isomer shift of tetrahedrally coordinated Fe^{3+} relative to that of octahedrally coordinated Fe^{3+}.

The effective magnetic field at the Fe nucleus is generally smaller in

tetrahedrally-coordinated Fe^{3+} than in octahedrally-coordinated Fe^{3+} (e.g. Gibb, 1976). The magnetic field at the Fe^{3+} nucleus arises only from the Fermi contact interaction and, as such, should be dependant upon the net effective spin at the Fe site. In agreement with the trend observed in the Mossbauer spectra, the net α-spin density at the Fe site in the $(FeO_4)^{5-}$ cluster is calculated to be smaller than that in the $(FeO_6)^{9-}$ clusters. Note, however, that the calculations probably exaggerate the difference in spin densities.

Note that the a_{1g} orbital population in $(FeO_6)^{10-}$ is not very different from that in $(FeO_6)^{9-}$. Isomer shifts for Fe^{2+}, however, are much greater than those for Fe^{3+} in oxides and silicates. The difference in Fe^{2+} and Fe^{3+} isomer shifts are not, to first order, due to differences in 4s orbital covalencies but instead result from the presence of the sixth d-electron in Fe^{2+}. The latter shields the Fe s-electrons from the nucleus resulting in a larger isomer shift than that observed for Fe^{3+} with only five d-electrons (Marfunin, 1979).

Electronic Properties

The calculated molecular orbital energies show that Fe^{3+} oxides are semiconductors. For iron oxides with only octahedrally coordinated Fe^{3+}, the lowest-energy band gap, in the one-electron orbital sense, is the $3e_g^{\alpha}$-$2t_{2g}^{\beta}$ orbital separation. The electronic transition between these two one-electron orbitals corresponds to the $^6A_1(^6S) \rightarrow {}^4T_{1g}(^4G)$ and $^6A_1(^6S) \rightarrow {}^4T_2(^4G)$ ligand field-type transitions. Photoconductivity measurements of hematite (Marusek et al., 1980) show peaks at energies corresponding to these transitions. Conductivity arising from this one-electron orbital transition suggests that the Fe 3d orbitals form a narrow d-band. The wavefunction contours shown in Figures 3 and 4 indicate

that the β-spin Fe 3d orbitals are quite localized; on the other hand, the α-spin Fe 3d orbitals are quite delocalized. Most likely, therfore, charge-transport occurs in the α-spin Fe 3d band. This, in turn, requires that charge transport is by hole conduction; that is, iron oxides are p-type semiconductors when exhibiting intrinsic semiconduction activated by visible light. Experimental evidence in this regard is reviewed by Goodenough (1971) and Shuey (1975). In natural minerals, however, the presence of impurities will, of course, result in extrinsic semiconduction which may be either p- or n-type.

Comparison with other Calculations

The results presented here give much more reasonable values for the ligand field and LMCT transition energies of Fe^{2+} and Fe^{3+} oxides than those obtained by Tossell et al. (1973; 1974). The major differences between the $(FeO_6)^{9-}$ and $(FeO_4)^{5-}$ results (using overlapping atomic spheres) presented here and the earlier results (using tangent atomic spheres) of Tossell et al.(1973;1974) and Tossell (1978) concern the exchange splittings of the Fe 3d type orbitals, the O 2p -Fe 3d energy separation and the value of the crystal field splitting. The qualitative pictures of the electronic structure of iron oxides are the same in both calculations. In the multiple-scattering method, the potential in the interatomic region is constant. Accordingly, the wave functions in this region are delocalized partial waves. If tangent, rather than overlapping, atomic spheres are used the interatomic volume is increased which, in turn, tends to overdelocalize the molecular orbital wavefunctions. The effect of this delocalization is to decrease the exchange splittings of the orbitals and, hence, decrease the energy of the β-spin Fe 3d type orbitals relative to that of the O 2p

valence band. Hence, the more reasonable exchange splittings of the Fe 3d type orbitals and the improved values of the LMCT energies in the overlapping sphere calculations are a consequence of decreasing the volume of the physically undesireable intersphere region.

Conclusions

The Fe-O chemical bond in Fe^{3+} oxides is found to be fairly covalent. This agrees with the observed Lewis acidity of Fe^{3+} in aqueous systems and also provides a qualitative explanation for the structural diversity of iron oxides. The Fe^{2+}-O chemical bond is somewhat less covalent due to the smaller electron affinity of the Fe^{2+} cation. The spin unrestricted calculations show how the phenonemon of superexchange leading to antiferromagnetism can be easily understood in terms of the nature of the Fe-O chemical bond. The relative magnitudes of the spin-polarizations of the oxygen atoms by Fe^{3+} cations in the different coordination polyhedra investigated provide a qualitative explanation for the magnetic structures of hematite and maghemite.

Calculated energies of electronic transitions observed in the optical spectra of Fe^{3+} and Fe^{2+} oxides and silicates are in good agreement with experimental results. The energy of the first ligand to metal charge transfer transition of octahedrally coordinated Fe^{3+} cations in oxides and silicates is calculated to be about 4.7 eV (38 kK). This is in agreement with spectroscopic data on a wide variety of octahedral Fe^{3+}-oxo complexes and minerals. Moreover, this particular result implies that most of the strong optical absorption in the visible and near-ultraviolet spectra of Fe^{3+} oxides and silicates is due to Fe^{3+} ligand field transitions which have been intensified by Fe^{3+}-Fe^{3+} pair interactions. The lowest energy LMCT

transition of Fe^{2+} oxides and silicates is calculated to occurs near 6.6 eV (53 kK). The larger energy of $O^{2-} \rightarrow Fe^{2+}$ charge-transfer, relative to that of $O^{2-} \rightarrow Fe^{3+}$ charge transfer, is expected and can be attributed to the smaller electron affinity (or "optical electronegativity") of the Fe^{2+} cation.

Using multiplet theory, the diagonal sum rule, and the Tanabe-Sugano expressions of ligand field theory, values of 10Dq and B for Fe^{3+} were calculated from the one-electron orbital energies. The values obtained are in good agreement with those estimated from experimental spectra of iron oxides. An important aspect of the multiplet theory approach is its ability to relate the conceptually useful one-electron orbital picture with experimental spectra. For example, the Racah B and C parameters are shown to be directly proportional to the exchange splittings of the one-electron Fe^{3+} 3d type orbitals (the $2t_{2g}$ and $3e_g$). The exchange splittings of these orbitals are, in turn, a direct function of the spin-down versus spin-up charge density donated to the Fe^{3+} center by the oxygen ligands. Further calculations on other Fe^{3+} and Fe^{2+} centered clusters and comparison with optical spectra are expected to provide more insight on the relation between chemical bonding and electronic spectra of Fe^{3+} minerals and complexes. Examples for oxide hydroxide clusters and mixed valence dimers are described in subsequent chapters.

References

Blake, R.L., R.E. Hessevick, T. Zoltai, and L.W. Finger (1966) Refinement of the hematite structure, American Mineralogist, 51, 123-129.

Blazey, K.W. (1977) Optical absorption of MgO:Fe, Journal of Physics and Chemistry of Solids, 38, 671-675.

Bonnet, M., A. Dela Palme, P. Becker, and H. Fuess (1978) Magnetization density in yttrium iron garnet (YIG), Journal of Magnetism and Magnetic Materials, 7, 23-25.

Burns, R.G. (1970) Mineralogical Applications of Crystal Field Theory, Cambridge University Press, Cambridge.

Byrom, E., A.J. Freeman, and D.E. Ellis (1975) Covalency effects on tetrahedral and octahedral Fe^{3+} sites in YIG: charge and spin densities and neutron form factors, AIP Conference Proceedings 24, Magnetism and Magnetic Materials, 1974, 209-210.

Faye, G.H. (1969) The optical absorption spectrum of tetrahedrally coordinated Fe^{3+} in orthoclase, Canadian Mineralogist, 10, 112-117.

Fasiska, E.J. (1967) Structural aspects of the oxides and oxyhydrates of iron, Corrosion Science, 7, 833-839.

Ferguson, J., H.J. Guggenheim and Y. Tanabe (1966) The effects of exchange interactions in the spectra of octahedral manganese II compounds, Journal of the Physical Society of Japan, 21, 347-354.

Ferguson, J., and P.E. Fielding (1972) The origins of the colours of natural yellow, blue, and green sapphires, Australian Journal of Chemistry, 25, 1371-1385.

Gibb, T.C. (1976) Principles of Mossbauer Spectroscopy, London: Chapman and Hill, 22-43.

Goodenough, J.B. (1971) Metallic Oxides, Progress in solid state chemistry, 5, 145-399.

Goodman, B.A. (1982) Mossbauer Spectroscopy, in, Advances Techniques for Clay Mineral Analysis, J.J. Fripiat (ed.), Amsterdam: Elsevier, 113-137.

Johnson, K.H. (1973) Scattered wave theory of the chemical bond, Advances in Quantum Chemistry, 7, 143-185.

Johnson, K.H., and F.C. Smith Jr.(1972) Chemical bonding of a molecular transition metal ion in a crystalline environment, Physical Review B, 831-843.

Karickhoff, S.W., and G.W. Bailey (1973) Optical absorption spectra of clay minerals. Clays and Clay Minerals, 21, 59-70.

Krebs, J.J. and W.G. Maisch (1971) Exchange effects in the optical absorption spectra of Fe^{3+} in Al_2O_3, Physical Review B, 4, 757-769.

Lehmann, G., (1970) Ligand field and charge transfer spectra in Fe(III)-O complexes, Zeitschrift fur Physikalische Chemie Neue Folge, 72, 279-297.

Lehmann, G., and H. Harder (1970) Optical spectra of di- and trivalent iron in corundum, American Mineralogist, 55, 98-105.

Lever, A.B.P. (1968) Inorganic electronic spectroscopy, Elsevier, Amsterdam.

Lohr, L.L. (1972) Spin-forbidden electronic excitations in transition metal complexes, Coordination Chemistry Reviews, 8, 241-259.

Manning, P.G. (1970) Racah parameters and their relationship to lengths and covalencies of Mn^{2+} and Fe^{3+} oxygen bonds in silicates, Canadian Mineralogist, 10, 677-687.

Mao, H.K., and P.M. Bell (1974) Crystal-field effects of ferric iron in goethite and lepidocrocite: Band assignments and geochemical application at high pressure, Carnegie Institute of Washington Yearbook, 1973, 502-507.

Marathe, V.R., and A. Trautwein (1983) Calculation of charge density, electric field gradient and internal magnetic field at the nuclear site using molecular orbital cluster theory, in, Advances in Mossbauer Spectroscopy, B.V. Thosar (ed.), 398-449.

Marfunin, A.S. (1979) Spectroscopy, Luminescence and Radiation Centers in Minerals, Springer-Verlag, Berlin.

Marusak, L.A., R. Messier and W.B. White (1980) Optical absorption spectrum of hematite, α-Fe_2O_3, near IR to UV, Journal of Physics and Chemistry of Solids, 41, 981-984.

Nitsan, U., and T.J. Shankland (1976) Optical properties and Electronic structure of mantle silicates, Geophysical Journal of the Royal Astronomical Society, 45, 59-87.

Norman, J.G. (1976) Non-empirical versus empirical choices for overlapping sphere radii rations in SCF-Xα-SW calculations on ClO_4^- and SO_2, Molecular Physics, 31, 1191-1198.

Rakhecha, V.C., and N.S. Satya Murthy (1978) Spin-transfer due to covalency for the tetrahedral-site Fe^{3+} ions in Fe_3O_4, Journal of Physics C, 11, 4389-4404.

Rossman, G.R. (1975) Spectroscopic and magnetic studies of ferric iron hydroxy sulphates: intensification of color in ferric iron clusters bridged by a single hydroxide ion, American Mineralogist, 60, 698-704.

Salahub, D.R., R.P. Messmer and K.H. Johnson (1976) Ionization potentials and bond lengths for CO, N_2 and F_2 using the SCF-Xα-SW method: a study of the effect of overlapping spheres, Molecular Physics, 31, 529-534.

Sambe H. and R.H. Felton (1976) Connection between the Xα-method and Ligand field theory, International Journal of Quantum Chemistry Symposium number 10, 155-158.

Schwarz, K. (1972) Optimization of the statistical exchange parameter α for the free ions H through Nb, Physical Review B, 5, 2466-2468.

Shuey, R.T. (1975) Semiconducting Ore Minerals, Amsterdam: Elsevier, 357-370.

Singer, R.B. (1982) Spectral evidence for the mineralogy of the high albedo soils and dusts on Mars, Journal of Geophysical Research, 87, 10159-10168.

Slater, J.C. (1968) Average energy of states of given multiplets in atoms, Physical Review, 165, 655-658.

Slater, J.C. (1974) The Self-Consistent Field Method for Atoms, Molecules, and Solids, McGraw-Hill, New York.

Tang Kai, A., H. Annersten, and T. Ericsson (1980) Molecular orbital (MSXα) calculations of s-electron densities of tetrahedrally coordinated ferric iron: comparison with experimental isomer shifts, Physics and Chemistry of Minerals, 5, 343-349.

Tippins, H.H. (1970) Charge-transfer spectra of transition metal ions in corundum, Physical Review B, 1, 126-135.

Tofield, B.C. (1976) Covalency effects in magnetic interactions, Journal de Physique, 37, C6539-C6569.

Tofield, B.C. (1975) The study of covalency by magnetic neutron scattering, in, Structure and Bonding, 21, 1-88, Springer-Verlag, New York.

Tossell, J.A. (1978) Self-consistent-field-Xα study of one-electron energy levels in Fe_3O_4, Physical Review B, 17, 484-487.

Tossell, J.A. (1980) Electronic structure of dichalcogenide and dipnictide anions, Journal of Physics and Chemistry of Solids, 41, 1047-1052.

Tossell, J.A., D.J. Vaughan, and K.H. Johnson (1973) Electronic structure of ferric iron octahedrally coordinated to oxygen, Nature (London) Physical Science, 244, 42-45.

Tossell, J.A., D.J. Vaughan, and K.H. Johnson (1974) The electronic structure of rutile, wustite and hematite from molecular orbital calculations, American Mineralogist, 59, 319-334.

Verdonck, E., and G. Vanquikenborne (1976) Charge transfer spectra of octahedral transition metal complexes, Inorganica Chimica Acta, 23, 67-76 (1976).

Waychunas, G.A., and G.R. Rossman (1983) Spectroscopic standard for tetrahedrally coordinated ferric iron: γ $LiAlO_2:Fe^{3+}$, Physics and Chemistry of Minerals, 9, 212-215.

CHAPTER 5:

The Electronic Structure of *trans* $(FeO_4(OH)_2)^{7-}$ clusters; Applications to the Spectra and Magnetochemistry of Hydroxyl-Bearing Fe^{3+} Oxides and Silicates

*To be submitted to *Physics and Chemistry of Minerals*.

Abstract

SCF-Xα-SW molecular orbital calculations were done on several trans-$(FeO_4(OH)_2)^{7-}$ clusters to investigate the differences between Fe-O and Fe-OH bonding in hydroxyl-bearing iron oxides and silicates. The Fe-OH bond appears to be much more ionic, and with a smaller spin-polarization, than the Fe-O bond. This explains why Fe-OH-Fe superexchange interactions are much weaker than Fe-O-Fe superexchange. Replacement of oxygens in the Fe^{3+} coordination environment by OH ligands appears to promote the covalency between Fe^{3+} centers and O^{2-}oxygens. This offers an explanation for the decreased magnetic hyperfine fields at the Fe nucleus in FeOOH polymorphs relative to those found in Fe^{3+} oxides.

Introduction

In Chapter 4, the electronic structures of Fe^{3+} cations bonded to O^{2-} anions were investigated. In a variety of Fe^{3+} minerals, however, hydroxyl (OH^-) ligands, in addition to O^{2-} anions are present. The most important examples are in the FeOOH polymorphs and in phyllosilicates.

Experimental investigations of minerals indicate several phenomena resulting from the presence of OH^- ligands. Mossbauer studies on the FeOOH and Fe_2O_3 polymorphs show that, when compared to the pure oxides, the effective magnetic hyperfine field (H_{eff}) at the ^{57}Fe nucleus is decreased when Fe^{3+} cations are bonded to hydroxyl groups (Forsyth et al., 1968). Observed magnetic hyperfine parameters and magnetic data for Fe^{3+} oxides are given in Table 5.1 The angular momentum contribution to the magnetic hyperfine field in high-spin Fe^{3+} is zero and, as such, the only contribution is from the electronic spin. The decreased magnetic hyperfine field indicates that the net spin density at the Fe^{3+} site is decreased. That this decrease in spin density is associated with Fe-OH bonds is also demonstrated in studies of the so-called hydrogoethite (α-FeOOH$\cdot n H_2O$) phase (Gendler et al., 1976). In this system the chemically-bound H_2O molecules are hydrogen-bonded with O^{2-} anions to give Fe-OH bonds. Increases in the H_2O content result in decreasing values of H_{eff}. The mineral ferrihydrite is a poorly crystalline iron oxide hydroxide which shows considerable variation in its stoichiometry and H_2O or OH^- content. There have been numerous Mossbauer studies of ferrihydrite (e.g. Okamoto et al., 1972; Okamoto and Sekizawa, 1979; Murad and Schwertmann, 1980; Coey and Readman, 1973) which also indicate that H_{eff} decreases with increasing H_2O content.

Table 5.1: Magnetic Hyperfine Fields and Curie (or Neel) Temperatures observed for Fe^{3+} oxides and hydroxides

Mineral	Formula*	H_{eff} at 4.2°K (kOe)	T_N or T_C (°K)	References
Hematite	α-Fe_2O_3	517-540	958	1,2
Maghemite	γ-Fe_2O_3	499 (oct. Fe) 488 (tet. Fe)		3
Geothite	α-FeOOH	504	403	4
Akaganeite	β-FeOOH	436-474		5
Lepidocrocite	γ-FeOOH	460	73	6
Feroxyhyte	δ-FeOOH	505,525	420	7
Ferrihydrite		455-508	--	8,9,10

*The true formula for β-FeOOH is $Fe_8(O,OH)_{16}(X,H_2O)_2$ where X = Cl,F; the formula for ferrihydrite is variable.
References: 1. Nakamura and Shimizu (1964); 2. Shirane et al. (1962); 4. Forsyth et al. (1968); 5. Childs et al. (1979); 7. Johnson (1969) 8. Coey and Readman (1973); 9. Okamoto et al.(1972); 10. Mathalone et al.(1970).

In the hydrogoethite phase one finds a correlation between the Neel temperature of the sample and the H_2O content (Gendler et al., 1976). This was interpreted as indicating that protonation of oxygens which bridge adjacent Fe^{3+} centers (that is, to give Fe-OH-Fe rather than Fe-O-Fe bridging) decreases the superexchange interaction between the Fe^{3+} cations. In well-characterized minerals, hydroxo- versus oxo-bridging of adjacent Fe^{3+} cations is found to effect their electronic spectra. As discussed in Chapter 3, the Fe^{3+} ligand field transitions are spin-forbidden if the Fe^{3+} cations occur as isolated parmagnetic centers but become both spin-and laporte allowed if adjacent Fe^{3+} cations are magnetically coupled. The degree of magnetic coupling and, hence, the intensification of the Fe^{3+} ligand field transitions, depends on the strength of the Fe-O-Fe super-exchange interaction. Rossman (1975;1976) has shown that if Fe^{3+} cations are bridged by hydroxyl groups rather than O^{2-}anions, the intensities of the Fe^{3+} ligand field transitions decreases.

To provide insight on these phenomena, the electronic structures of several trans-$(FeO_4(OH)_2)^{7-}$ clusters were calculated using the SCF-Xα-SW method. The results of these calculations will be directed mainly towards understanding the differences between Fe^{3+}-O^{2-} and Fe^{3+}-OH^- chemical bonds and how these differences affect the magnetochemistries of Fe^{3+} oxides and oxyhydroxides. Additional applications to the spectra of Fe^{3+} systems will also be presented.

Cluster Geometries and Input Parameters

Table 5.2 gives the bond-lengths and sphere radii used in the clusters. For all clusters the O-Fe-O bond angle is 90°. Cluster A has D_{4h} symmetry because the Fe-O-H bond angle was set to 180°. The remaining clusters used the more realistic Fe-O-H bond angle of 109.5° and the conformation is such that these clusters have C_{2h} symmetry. For the Fe and O atoms, the standard Schwarz (1972) value of the α parameter was used while, for the H atoms, the spin-polarized value of 0.77627 was used.

The choice of sphere radii for the atoms in these clusters presents a problem. In the previous $(FeO_6)^{9-}$ cluster calculation, Fe and O sphere radii were 1.186 and 1.245 A, respectively. This gave about 20% sphere overlap and very good agreement with experiment. If the hydroxyl oxygen sphere radii in these clusters are taken to be as large as the oxygen sphere radii in the $(FeO_6)^{9-}$ cluster, however, the hydroxyl oxygen sphere will incorporate the H atom nucleus. Consequently, the hydroxyl oxygen sphere radii were scaled-down to prevent the critical overlap.

Calculated Molecular Orbitals

Figure 5.1 presents the MO diagram for the $(FeO_4(OH)_2)^{7-}$ cluster which has the geometry given in column C of Table 5.2. It is best to describe the energy levels in this cluster relative to those found in the octahedral $(FeO_6)^{9-}$ cluster (Figure 4.1). Each of the orbitals in the $(FeO_6)^{9-}$ cluster splits under the descent in symmetry to C_{2h} and, to relate the two sets of orbitals, a correlation table for the O_h, D_{4h} and C_{2h} point groups is given in Table 5.3. In addition to the effect of the descent in symmetry, new orbitals are present in the $(FeO_4(OH)_2)^{7-}$ cluster which result from the O-H chemical bond.

Table 5.2: Input Parameters and Cluster Geometries.

Cluster	A	B	C
Point Group	D_{4h}	C_{2h}	C_{2h}
	Bond Lengths (Angstroms)		
Fe-O	2.05	2.05	2.025
Fe-OH	2.05	2.05	1.985
O-H	1.00	1.00	1.00
∢Fe-O-H	180°	109.5°	109.5°
	Sphere Radii		
Fe	1.214	1.214	1.214
O	1.242	1.242	1.242
O (OH)	0.927	0.927	0.927
H	0.428	0.428	0.428
Outer Sphere	3.291	3.291	3.291

Fe 3d band orbitals

At the top of the MO diagram of Figure 5.1 are the energy levels of the orbitals within the Fe 3d band. The $3e_g$ orbital of the $(FeO_6)^{9-}$ cluster splits under C_{2h} symmetry into the $7b_g$ and $11a_g$ orbitals. As in the $(FeO_6)^{9-}$ cluster, these are the Fe 3d - O 2p σ-antibonding orbitals. The $2t_{2g}$ Fe 3d orbital in the $(FeO_6)^{9-}$ cluster splits into the $10a_g$, $6b_g$, and $9a_g$ orbitals in C_{2h} symmetry and, as in the $(FeO_6)^{9-}$ cluster, these are the Fe 3d - O 2p π-antibonding orbitals.

Note that the splitting of the $3e_g$ orbital under C_{2h} symmetry is quite large (ca. 1.0 eV). This does not imply that the Fe^{3+} spectroscopic states will be split in this fashion, however. As will be shown in the next section, the energy separation between the $7b_g$ and $11a_g$ α-spin orbitals corresponds to the separation between the $^4T_1(^4G)$ and $^4T_2(^4G)$ states observed in the spectra of Fe^{3+} in octahedral coordination. In the octahedral $(FeO_6)^{9-}$ cluster, all we could calculate is the average energy of these states. The cluster investigated here, however, provides a special case in which the energies of these states can be directly calculated. The splitting of the actual Fe 3d spectroscopic states by the non- cubic ligand field environment of the (FeO4(OH)2)7- coordination polyhedron is indicated more by the splitting of the $2t_{2g}$ orbital into the $10a_g$, $6b_g$, and $9a_g$ orbitals. As can be seen in Figure 5.1, this splitting is quite small.

O 2p Band Orbitals

Below the Fe 3d type orbitals is a group of orbitals corresponding to the O 2p atomic orbitals. The resulting O 2p band, however, is split into three distinct groups of orbitals corresponding to the Fe-O, Fe-OH, and O 2p -H 1s bonding interactions. The Fe-O bonding orbitals are themselves split into two groups: one being mostly O 2p non-bonding and lying at the

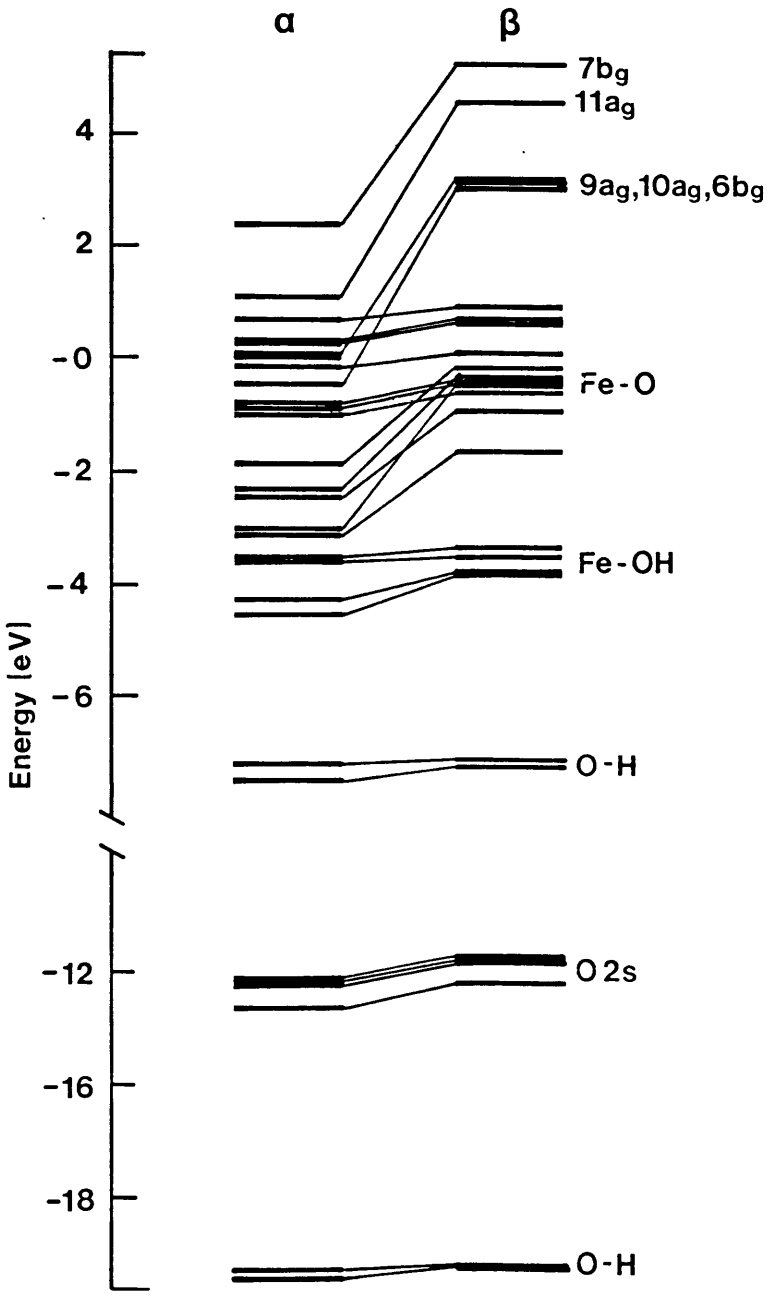


Figure 5.1: Molecular orbital diagram for trans-$(FeO_4(OH)_2)^{7-}$ cluster with geometry C in Table 5.2. The orbitals shown are those which fall within the Fe(3d), O(2p) and O(1s) valence bands (not break in energy scale). E_f is the Fermi energy below which all orbitals are occupied. Note that the orbitals within the O(2p) valence band fall within distinct groups corresponding to Fe-O, Fe-OH and O-H bonding orbitals. The O(2s) valence band is split into two sets corresponding to O^{2-} oxygen non-bonding and OH oxygen O(1s)-H(1s) bonding orbitals.

Table 5.3: Correlation Table for Point Groups O_h, D_{4h} and C_{2h}

O_h	D_{4h}	$C_{2h}(C_2 = C_2'')$
A_{1g}	A_{1g}	A_g
A_{2g}	B_{1g}	B_g
E_g	$A_{1g} + B_{1g}$	$A_g + B_g$
T_{1g}	$A_{2g} + E_g$	$A_g + B_g + B_g$
T_{2g}	$B_{2g} + E_g$	$A_g + A_g + B_g$
A_{1u}	A_{1u}	A_u
A_{2u}	B_{1u}	B_u
E_u	$A_{1u} + B_{1u}$	$A_u + B_u$
T_{1u}	$A_{2u} + E_u$	$A_u + B_u + B_u$
T_{2u}	$B_{2u} + E_u$	$A_u + A_u + B_u$

top of the O 2p valence band and the other being the actual Fe-O bonding orbitals. The non-bonding and bonding sets can be distinguised by the much larger exchange splittings (induced by covalent bonding with the Fe^{3+} center) of the bonding orbitals compared to those of the non-bonding set.

The Fe-OH bonding orbitals are at a lower energy than the Fe-O bonding orbitals; this does not mean that the Fe-OH bond is stronger than the Fe-O bond, however, it simply reflects the greater electronegativity of the hydroxyl oxygens relative to that of the O^{2-} oxygens. Note also that the exchange splittings of the Fe-OH bonding orbitals are much smaller than those of the Fe-O bonding orbitals. As will be discussed below, the calculated charge distributions indicate that the spin-polarization of the O^{2-} oxygens is much greater than that of the hydroxyl groups; this is why the exchange splittings of the two sets of orbitals are so different.

About 2 eV below the Fe-OH bonding orbitals are the orbitals corresponding the the O 2p - H 1s bonding interaction. This does show that the O-H bond is stronger than the Fe-OH bond, as expected.

O 2s Valence Band Orbitals

About 12 eV below the O 2p band are the orbitals corresponding to the O^{2-} and OH^- oxygen 2p atomic orbitals. This set of orbitals is also split into two groups: the higher-energy orbitals are O 2s non-bonding molecular orbitals while the lower energy set correspond to the O 2s - H 1s bonding interaction.

Effect of Fe-O-H bond angle on electronic structure

The electronic structure of the trans-$(FeO_4(OH)_2)^{7-}$ cluster with the Fe-O-H bond angle of 180° is shown in Figure 7.2. The effect of the change in bond angle on the Fe-O bonding and antibonding orbital energies is quite small; the O-H bonding orbitals, however, are stabilized by about 1 eV.

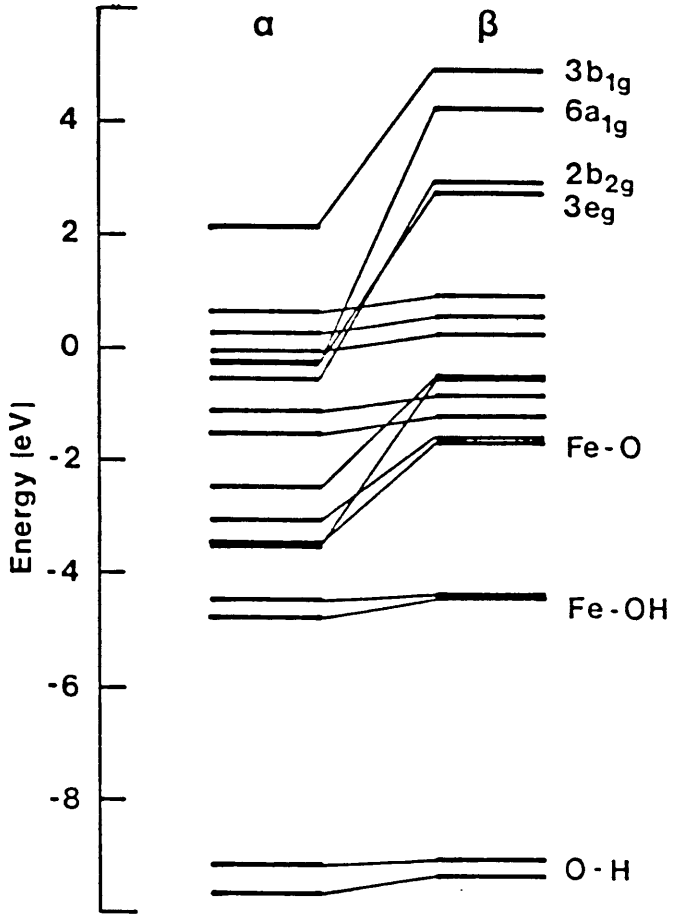


Figure 5.2: Molecular orbital diagram for a trans-$(FeO_4(OH)_2)^{7-}$ cluster with the geometry of column A in Table 5.2; here, the Fe-O-H bond angle is 180°.

Applications to the Spectra of Fe^{3+} Oxides and Oxide Hydroxides

The only aspects of the spectra of Fe^{3+} oxides and oxide hydroxides that will be discussed here are those which can be treated by the $(FeO_4(OH)_2)^{7-}$ clusters but are beyond the scope of the simpler $(FeO_6)^{9-}$ clusters.

Fe^{3+} Ligand Field Spectra in Oxides and Oxide Hydroxides

The lowest energy ligand field transitions of octahedrally coordinated Fe^{3+} are the $^6A_{1g}(^6S) \rightarrow {}^4T_{1g}(^4G)$ and the $^6A_{1g}(^6S) \rightarrow {}^4T_{2g}(^4G)$ transitions. From a one-electron molecular orbital calculation on an octahedral $(FeO_6)^{9-}$ cluster, all that we can calculate is the average energy of these transitions. Upon descent from O_h to D_{4h} symmetry, the $^4T_{1g}$ state splits into $(^4A_{2g} + {}^4E_g{}^a)$ while the $^4T_{2g}$ state splits into $(^4B_{2g} + {}^4E_g{}^b)$. The $^6A_{1g} \rightarrow {}^4A_{2g}$ component of the $^6A_{1g}(^6S) \rightarrow {}^4T_{1g}(^4G)$ transition corresponds exactly with the $3b_{1g}{}^{\alpha} \rightarrow 2b_{2g}{}^{\beta}$ one-electron orbital transition in cluster A (Figure 5.2); likewise, the $^6A_{1g} \rightarrow {}^4B_{2g}$ component of the $^6A_{1g}(^6S) \rightarrow {}^4T_{2g}(^4G)$ transition corresponds exactly with the $6a_{1g}{}^{\alpha} \rightarrow 2b_{2g}{}^{\beta}$ one-electron orbital transition. (The $^6A_{1g} \rightarrow {}^4E_g{}^a$ and $^6A_{1g} \rightarrow {}^4E_g{}^b$ components of the $^6A_{1g} \rightarrow {}^4T_{1g}$ and $^6A_{1g} \rightarrow {}^4T_{1g}$ transitions each correspond to both the $3b_{1g}{}^{\alpha} \rightarrow 3e_g{}^{\beta}$ and the $6a_{1g}{}^{\alpha} \rightarrow 3e_g{}^{\beta}$ one-electron orbital transitions and, hence, their energies cannot be separately calculated.) If, upon going from O_h to D_{4h} symmetry, the splittings of the $^4T_{1g}$ and $^4T_{2g}$ states are small, we can effectively calculate the energies of the $^6A_{1g} \rightarrow {}^4T_{1g}$ and $^6A_{1g} \rightarrow {}^4T_{1g}$ transitions.

Upon further descent to C_{2h} symmetry (Cluster B), we find that the average energy of the $7b_g{}^{\alpha} \rightarrow (10a_g{}^{\beta}, 6b_g{}^{\beta}, 9a_g{}^{\beta})$ one-electron transitions corresponds to the $^6A_{1g} \rightarrow {}^4T_{1g}$ transition energy while the average energy of the $11a_g{}^{\beta} \rightarrow (10a_g{}^{\beta}, 6b_g{}^{\beta}, 9a_g{}^{\beta})$ transitions correspond to the $^6A_{1g} \rightarrow {}^4T_{2g}$

transition energy. Note that the splitting between the $10a_g^{\beta}$, $6b_g^{\beta}$, and $9a_g^{\beta}$ orbitals is quite small and, as such, the calculations correctly predict that the presence of both OH^- and O^{2-} ligands will give only negligable splittings of the $^4T_{1g}$ and $^4T_{2g}$ states of octahedral Fe^{3+} even though the descent in symmetry is quite large. Now, the average energy of the $11a_g^{\alpha} \rightarrow (10a_g^{\beta}, 6b_g^{\beta}, 9a_g^{\beta})$ transitions is calculated to be 15.9 kK; this is in excellent agreement with the observed energy (ca. 15.4 kK) of the $^6A_{1g} \rightarrow {}^4T_{2g}$ transition in Fe^{3+} oxides. The average energy of the $7b_g^{\alpha} \rightarrow (10a_g^{\beta}, 6b_g^{\beta}, 9a_g^{\beta})$ transitions is calculated to be 5.1 kK; this, however, is in poor agreement with the observed energy (10-11 kK) of the $^6A_{1g} \rightarrow {}^4T_{1g}$ transition in Fe^{3+} oxides. It appears that the $7b_g^{\alpha}$ orbital energy is about 0.5 eV to high. Note, however, that the results presented here are consistent with the octahedral $(FeO_6)^{9-}$ cluster calculations. From the latter, the average energy of the $^6A_{1g} \rightarrow {}^4T_{1g}$ and $^6A_{1g} \rightarrow {}^4T_{2g}$ transitions was estimated to be 11.1 kK. Here, the average energy is estimated to be 10.5 kK or nearly the same.

Photoelectron Spectra of Fe^{3+} Oxides and Oxide Hydroxides

Oxygen 1s photoelectron spectra of goethite and lepidocrocite (Asami and Hasimoto, 1977; Hoste et al., 1982) show that in these minerals the O 1s photoelectron peak is split by about 2.0 eV corresponding to O^{2-} and OH^- oxygens. The dehydration studies of Hoste et al. (1982) showed that the hydroxyl oxygen peak has the greater binding energy. These results are in agreement with those obtained here; the 1s orbital energies of the O^{2-} and OH^- oxygens differ by about 2.0 ev and the hydroxyl oxygen 1s orbitals are the more stable. Asami et al. (1977) also obtained valence region photoelectron spectra of goethite and lepidocrocite; these spectra, however, do not differ appreciably from those of hematite and do not show

additional features due to Fe-OH bonding orbitals as might be implied by Figure 5.1. The reason for this is probably that the Fe-OH bonding orbitals are almost entirely OH^- in character and, since the spectra are a really measure of the Fe cross section, the peaks corresponding to these orbitals are very weak.

Relation Between Chemical Bonding and Physical Properties of Fe Oxides and Oxide Hydroxides

In order to describe the nature of the chemical bonds in the $(FeO_4(OH)_2)^{7-}$ cluster, we need to understand how the the electronic charge and spin-density is partitioned among the Fe, O and H atoms. In the SCF-Xα-SW method, this is complicated by the presence of charge in the intersphere and outer sphere regions. A simple, yet crude, approach to correcting for the charge in these regions is simply to renormalize each orbital charge distribution among the Fe, O and H atomic regions. The results of this procedure seem to provide a good qualitative, if not quantitative, description of the system.

The results of this charge-partitioning scheme are presented in Table 5.3. The effective charge and spin-population at the Fe atom are considerably lower in this cluster than in the octahedral and trigonal $(FeO_6)^{9-}$ clusters. In the former clusters, the charge on the Fe atom was estimated to be +1.3 while the net-spin was estimated to be 4.69 μ_B.

The Fe-O and Fe-OH bonding interactions appear to be are quite different. The effective charge on the hydroxyl group is found to be ca. -1.0 while that on the oxide oxygens is about -1.5. As such, the Fe-OH bonding interaction appears to be entirely ionic. What is actually happening is that the charge donated to the Fe atom by the hydroxyl oxygens is

cancelled by delocalization of the Fe 3d electrons onto the latter. Even though the covalent interaction is cancelled, it still induces a small spin-polarization of the hydroxyl oxygens.

The Fe-O covalency in this cluster appears to be greater than that in the $(FeO_6)^{9-}$ clusters discussed in Chapter 4. It appears that the smaller covalency of the Fe-OH bond promotes the Fe-O covalent interaction so that the charge and effective spin on the Fe atom is smaller than if it were bonded to only O^{2-} anions. This is an interesting result in that it offers an explanation for both the decreased hyperfine fields observed in the Mossbauer spectra and the decreased Fe-Fe superexchange interaction in Fe^{3+} oxide hydroxides. In particular, the OH^- ligand is more electronegative than the O^{2-} ligands (here, this shows up also in the greater binding energies of the orbitals associated with the OH^- ligands compared to those associated with the O^{2-} ligands). As such, we expect the Fe-OH bond to be more ionic than the Fe-O bond or, more precisely, we expect each of the O^{2-} ligands to donate more electronic charge to the Fe^{3+} center than that donated by an OH^- ligand. If this described the entire situation, however, it would not explain why the hyperfine field at the Fe nucleus decreases when some of the oxygens in the Fe coordination environment are replaced by hydroxyl groups. Indeed, we would expect the hyperfine field to increase. The electronic structure of the $(FeO_4(OH)_2)^{7-}$ cluster, however, shows that there is a cooperative effect when both OH^- and O^{2-} ligands are present; namely, the ionic Fe-OH interaction promotes the covalency of the Fe-O bond. The latter is spin-polarized so that more β-spin charge is donated to the Fe atom than is α-spin charge and, as such, the hyperfine field at the Fe nucleus decreases.

The difference between the Fe-O and Fe-OH chemical bonds also explains

Table 5.3: Electronic Charge donated to Fe Atom by Each Type of Orbital Interaction.

Orbital	Donated Electronic Charge	
	α-Spin	β-Spin
a_g	-0.403	-0.628
b_g	-0.123	-0.452
a_u	-0.074	-0.066
b_u	-0.141	-0.132
Total Charge	-0.740	-1.278
Net Charge on Fe atom = +0.98		
Net Spin on Fe atom = 4.463 μ_B		

why the Fe-Fe superexchange interaction in a solid is decreased when Fe atoms are bridged by hydroxide, rather than oxide, anions. As discussed previously, the superexchange interaction results from the spin-polarization of the bridging ligands by the metal-ligand chemical bond. In accordance with the more ionic character of the Fe-OH bond relative to that of the Fe-O bond, the spin-polarizability of the OH ligands is much smaller than that of the O^{2-} ligands. Hence, an Fe-OH-Fe superexchange interaction will be weaker than an Fe-O-Fe superexchange interaction, as is observed.

Conclusions

The electronic structure of the $(FeO_2(OH)_4)^{7-}$ clusters show several differences between the Fe-O and Fe-OH chemical bonds. These differences, in turn, can be related to effects observed in the Mossbauer spectra and magnetochemistry of iron(III) oxides and oxide hydroxides. The Fe-OH chemical bond is much less covalent than the Fe-O bond; moreover, the spin-polarizability of the hydroxyl oxygens by the Fe^{3+} cation is much smaller than that of the oxide oxygens. Since superexchange interactions between adjacent Fe atoms results from the spin-polarization of the bridging ligands, it follows that Fe-OH-Fe superexchange will be weaker than Fe-O-Fe superexchange.

Although the Fe-OH bond is more ionic than the Fe-O bond, the hyperfine fields observed in the Mossbauer spectra of FeOOH phases are smaller than those in the Fe_2O_3 polymorphs. A comparison of the chemical bonding in $(FeO_6)^{9-}$ clusters with that in the trans $(FeO_4(OH)_2)^{7-}$ cluster suggests that as the O^{2-} ligands in the Fe^{3+} coordination environment are replaced by hydroxyl groups, the covalent interaction between the Fe^{3+} center and the remaining O^{2-} ligands is enhanced. This, in turn, decreases the effective spin on the Fe atom resulting in a decreased hyperfine field.

References

Asami, K., and K. Hashimoto (1977) The X-ray photo-electron spectra of several oxides of iron and chromium, Corrosion Science, 17, 559-570.

Forsyth, J.B., I.G. Hedley, and C.E. Johnson (1968) The magnetic structure and hyperfine field of goethite (α-FeOOH), Journal of Physics C, 1, 179-188.

Gendler, T.S., R.N. Kuz'min, and T.K. Urazeava (1976) Study of the Mossbauer effect in hydrogoethite, Soviet Physics and Crystallography, 21, 440-444.

Hoste, S., L. Verdonck, and G.P. Van Der Kelen (1982) IR study on the solid state reaction between iron hydroxide and KCN, Bull. Soc. Chim. Belg., 91, 597-604.

Rossman, G.R. (1976) The optical spectroscopic comparison of the ferric iron tetrameric clusters in amarantite and leucophosphite, American Mineralogist, 61, 933-938.

Okamoto, S., and H. Sekizawa (1979) Magnetic properties of amorphous ferric gels, Journal de Physique, C2, 137-139.

Okamoto, S., H. Sekizawa, and S.I. Okamoto (1972) Characterization and phase transformation of amorphous ferric hydroxide, in, Reactivity of Solids, (J.S. Anderson, M.W. Roberts, and F.S. Stone, eds.) Chapman and Hall, London.

CHAPTER 6:

Electronic Spectra of Fe^{3+} Oxides and Oxide Hydroxides in the Near IR to Near UV*

*To be submitted to American Mineralogist

(Coauthor: T.D. Waite)

Abstract

Optical absorption and diffuse reflectance spectra of several Fe_2O_3 and FeOOH polymorphs (hematite, maghemite, goethite, lepidocrocite) in the near-infrared to near-ultraviolet spectral regions (2000-200 nm) are presented. The spectra consist primarily of Fe^{3+} ligand field and ligand to metal charge-transfer transitions. Band assignments were made using ligand field theory and the results of recent SCF-Xα-SW molecular orbital calculations of $(FeO_6)^{9-}$ coordination polyhedra. Values of the ligand field parameters 10Dq, B and C were found to be 14.0-15.9, 0.55-0.61, and 3.4-3.5 kK, respectively. The lowest energy ligand to metal charge-transfer transition is near 40.0 kK, in agreement with the molecular orbital calculations. The Fe^{3+} ligand field transitions are strongly intensified by magnetic coupling of adjacent Fe^{3+} cations. Several additional spectral bands are assigned to "double exciton" processes involving the simultaneous excitation of two Fe^{3+} cations which are magnetically coupled. These results show that the red to yellow colors of these minerals are not due to the LMCT transitions but result from pair excitations and Fe^{3+} ligand field transitions which have been intensified by magnetic coupling of adjacent Fe^{3+} cations.

Introduction

The electronic spectra of iron oxides and oxide hydroxides are directly relevant to several current problems in geochemistry. At present, a great deal of interest in planetary science is directed towards determining the surface mineralogy of Mars using spectroscopic remote sensing techniques (e.g. Singer et al., 1979; Singer, 1982, Sherman et al., 1982). On another front, the electronic transitions which give Fe oxides their optical spectra are also of interest in that they determine the mechanisms of sunlight-induced photochemical reactions between colloidal iron oxides and organic molecules in natural waters (Waite, 1983). Although several of the iron oxides and oxide hydroxides (e.g. hematite and goethite) are among the most common minerals on the Earth's surface, their electronic spectra are poorly known or understood. As will be discussed below, the spectra of Fe^{3+} minerals consist not only of electronic transitions localized to the FeO_6 coordination site (e.g. Fe^{3+} ligand field and $O^{2-} \rightarrow Fe^{3+}$ charge-transfer transitions) but can also exhibit phenomena resulting from the interactions between adjacent Fe^{3+} cations. These latter phenomena make the spectra of condensed Fe^{3+} phases (such as iron oxides) considerably more complex than those of dilute Fe^{3+} cations in a silicate or oxide host phase.

In this chapter, the near-IR to near-UV electronic spectra of hematite (α-Fe_2O_3), maghemite (γ-Fe_2O_3), goethite (α-FeOOH) and lepidocrocite (γ-FeOOH) are presented. Band assignments will be given based on ligand field theory, results of the SCF-Xα-SW molecular orbital calculations presented in chapter 4, and comparison with existing spectra of Fe^{3+} cations in oxides.

Theory of Fe^{3+} Spectra in Minerals

To help clarify the rationale behind the spectral band assignments, it is worthwhile to first review the important theoretical aspects of Fe^{3+} electronic spectra in minerals. Two principle types of electronic transitions occur in the optical spectra of Fe^{3+} minerals. First, there are the Fe^{3+} ligand field transitions. These are transitions between the different states arising from the Fe(3d) electronic configurations and are most easily described by the well-known ligand field (or crystal field) theories. In octahedral coordination, the Fe(3d) atomic orbitals are split into two sets of orbitals labelled t_{2g} and e_g. The t_{2g} and e_g orbital energy separation is the 10Dq ligand field parameter or the crystal field splitting. The t_{2g} and e_g orbitals are each split, in turn, by the exchange energy. The latter is the stabilization of electrons with majority spin (α-spin). The exchange splitting results in two sets of t_{2g} and e_g orbitals, one for the majority spin (spin-up or α-spin) and the other for minority spin (spin-down or β-spin) electrons. The Racah B and C parameters of ligand field theory are, in effect, measures of the exchange splitting of the t_{2g} and e_g orbitals. The ligand field transitions are between the states which arise from the different possible electronic configurations of the t_{2g} and e_g orbitals. In the approximation of ligand field theory, the energies of these states are expressed in terms of the three parameters 10Dq, B and C. The energies of the Fe^{3+} ligand field states as a function of 10Dq (assuming constant B and C) are shown schematically in the Tanabe-Sugano diagram (Figure 6.1). Analytical expressions for these state energies, which will be used to make spectral band assignments, are given in Table 6.1.

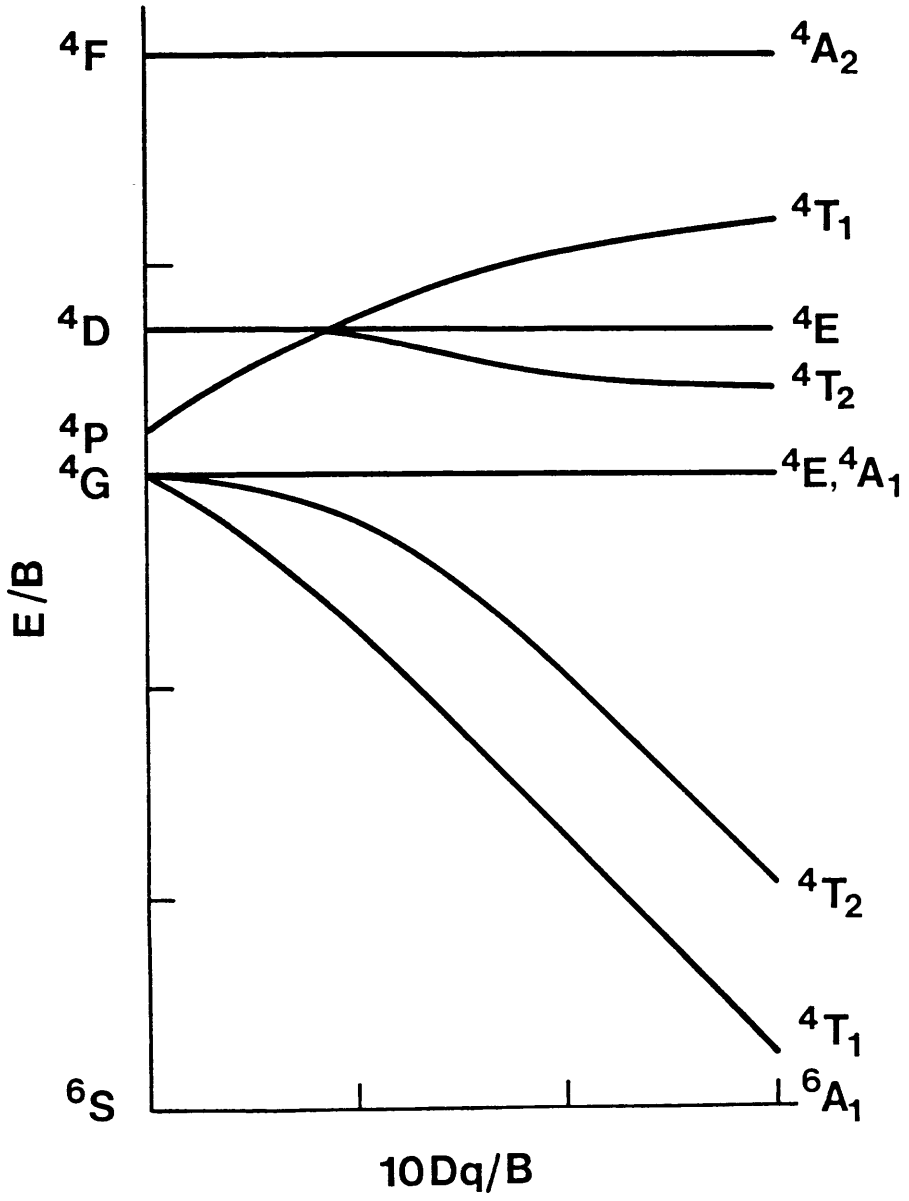


Figure 6.1: Tanabe-Sugano diagram for high-spin Fe^{3+} in either octahedral or tetrahedral coordination. The state energies were calculated using the expressions in Table 6.1 and assuming C/B = 4.0.

Table 6.1: Tanabe-Sugano Expressions for Ligand Field State Energies of Octahedral and Tetrahedral Fe^{3+}.*

State	Configuration	Energy
$^6A_1(^6S)$	$(t_{2g})^3(e_g)^2$	0
$^4T_1(^4G)$	$(t_{2g})^4(e_g)1$	$-10Dq + 10B + 6C - 26B^2/10Dq$
$^4T_1(^4G)$	$(t_{2g})^4(e_g)^1$	$-10Dq + 18B + 6C - 38B^2/10Dq$
$^4E,^4A_1(^4G)$	$(t_{2g})^3(e_g)^2$	$10B + 5C$
$^4T_2(^4D)$	$(t_{2g})^3(e_g)^2$	$13B + 5C + x$
$^4E(^4D)$	$(t_{2g})^3(e_g)^2$	$17B + 5C$
$^4T_1(^4P)$	$(t_{2g})^3(e_g)^2$	$19B + 7C - x$
$^4A_2(^4F)$	$(t_{2g})^3(e_g)^2$	$22B + 7C$

* From Lever (1968). The terms which are quadratic in B describe the configurational interaction and were derived assuming C = 4B. The quantities designated by x in the expressions for the $^4T_2(^4D)$ and $^4T_1(^4P)$ state energies arise from off-diagonal terms in the Tanabe-Sugano matrices; these will be neglected.

The ground $^6A_1(^6S)$ state in Figure 6.1 arises from the ground state $(t_{2g}^{\alpha})^3(e_g^{\alpha})^2$ configuration of high-spin Fe^{3+}. The first possible excited state configuration is $(t_{2g}^{\alpha})^3(e_g^{\alpha})^1(t_{2g}^{\beta})^1$; this configuration gives the $^4T_1(^4G)$ and $^4T_2(^4G)$ states of Figure 6.1. Note that the configuration giving these states contains a singly occupied t_{2g}^{β} orbital. Hence, it is expected that the $^4T_1(^4G)$ and $^4T_2(^4G)$ states will each be split by the dynamic Jahn-Teller effect. The remaining states in Figure 6.1 result from the "spin-flip" configurations $(t_{2g}^{\alpha})^2(e_g^{\alpha})^2(t_{2g}^{\beta})^1$ and $(t_{2g}^{\alpha})^3(e_g^{\alpha})^1(e_g^{\beta})^1$. Note that the energies of these configurations, relative to that of the ground configuration, are not a function of 10Dq but only of the exchange splittings of the t_{2g} and e_g orbitals. The latter are a function of the covalency of the Fe-O bond; as such, the energies of the states arising from these configurations are expected to fairly constant among Fe^{3+} oxides and silicates.

All of the transitions from the ground $^6A_1(^6S)$ state to the excited ligand field states are, in principle, both spin- and parity-forbidden. In a number of Fe^{3+} minerals and binuclear inorganic complexes, however, these transitions become allowed through the magnetic coupling of electronic spins of next-nearest neighbor Fe^{3+} cations in the crystal structure (Ferguson et al., 1966; Krebs and Maisch, 1971; Lohr, 1972). If two Fe^{3+} cations are strongly coupled, one must consider the spectroscopic selection rules for the Fe^{3+}-Fe^{3+} pairs and not those for individual Fe^{3+} centers.

We can obtain a qualitative understanding of the states associated with an Fe-Fe pair by assuming that the coupling between the two Fe centers is via the Heisenberg Hamiltonian:

$$H = J\, S_a \cdot S_b \qquad (6.1)$$

Here, S_a and S_b are the electronic spins of the two Fe^{3+} cations and J is the Heisenberg exchange integral. Application of this Hamiltonian as a perturbation to the ligand field states of the uncoupled Fe^{3+} cations yields a set of states for the pair with energies given by

$$E = J/2[S(S+1) - S_a(S_a+1) - S_b(S_b+1)] \quad (6.2)$$

where S is the net spin of the pair with values $|S_a+S_b|$, $|S_a+S_b-1|$,..., $|S_a-S_b|$. If both Fe^{3+} cations are in their ground $^6A_1$ states, then $S_a=S_b=5/2$; the resulting pair-states derived by coupling the two Fe^{3+} cations will have S = 0,1,2,3,4, and 5. Now, if one of the Fe^{3+} cations in the pair is excited to a quartet ligand field state, then S_a = 3/2 and S_b = 5/2; the two Fe^{3+} cations would therefore couple to give a set of pair states with S = 1,2,3, and 4. Transitions from S = 1,2,3, and 4 states in the $Fe^{3+}(^6A_1)$-$Fe^{3+}(^6A_1)$ pair-state manifold to the states in the excited-single-ion pair-state manifold can, therefore, occur with $\Delta S = 0$ and be spin-allowed. The relative energies of the states in the ground and excited-single-ion pair-state manifolds are shown in Figure 6.2.

An additional phenomenon resulting from the magnetic coupling of adjacent Fe^{3+} cations is the presence of new absorption features corresponding to the simultaneous excitation of two Fe^{3+} centers (Schugar et al., 1972). These features occur at energies given approximately by the sum of two single ion Fe^{3+} ligand field transitions and are often referred to as "double exciton processes". Several absorption bands in the spectrum of Fe^{3+} cations in Al_2O_3 have been demonstrated by Ferguson and Fielding (1972) to result from these Fe^{3+}-Fe^{3+} pair excitations. These transitions are also spin-allowed: if both Fe^{3+} cations are excited to a quartet ligand field state so that $S_a = S_b$ =3/2, the pair states resulting from coupling the two

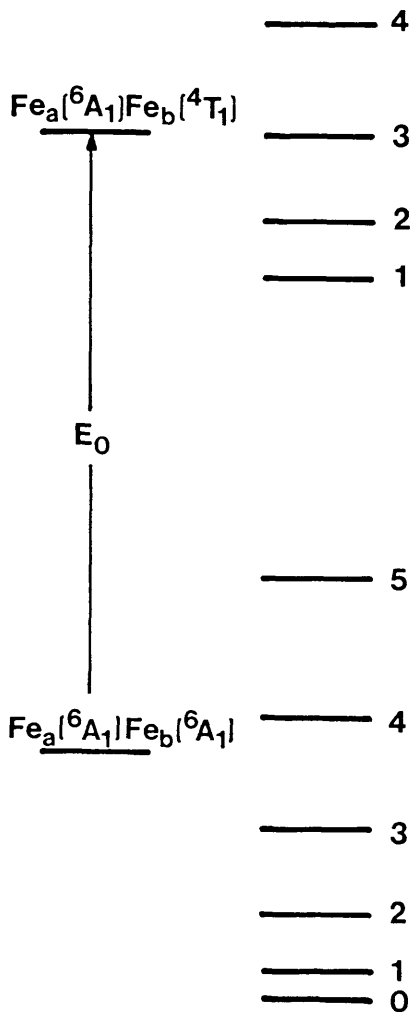


Figure 6.2: States of a Fe^{3+}-Fe^{3+} pair assuming the Fe^{3+} cations are coupled by the Heisenberg Hamiltonian $H = J\ S_a \cdot S_b$. Here, J is the exchange integral, S_a and S_b are the net spins on Fe atoms a and b, E_0 is the energy difference between the ground $^6A_1$ state and a quartet state of an isolated, uncoupled Fe^{3+} cation. The numbers next to each level indicate the spin S of the pair state.

Fe^{3+} cations will have S values of 0,1,2, and 3. Transitions to these pair states can therefore occur from the S=0,1,2, and 3 states in the $Fe^{3+}(^6A_1)$-$Fe^{3+}(^6A_1)$ ground state manifold. The relative energies of the double exciton states, relative to those of the ground and single-ion-excited-state manifolds, are shown in Figure 6.2.

At energies higher than most of the ligand field transitions are the ligand to metal charge-transfer (LMCT) transitions. These are most easily described in terms of molecular orbital theory. The molecular orbital diagram for a $(FeO_6)^{9-}$ coordination polyhedron is shown in Figure 4.1. The lowest energy LMCT transitions are from non-bonding molecular orbitals (labelled $1t_{2u}$, $6t_{1u}$, and $1t_{1g}$ in Figure 4.2) localized on the oxygen atoms to the antibonding t_{2g} Fe(3d) orbitals. As discussed in chapter 4, the energies of the $6t_{1u} \rightarrow 2t_{2g}$ and $1t_{2u} \rightarrow 2t_{2g}$ transitions are calculated to be 38.1 kK and 43.6 kK, respectively. Bands near these energies are observed in the spectra of several Fe^{3+} phyllosilicates (Chen et al., 1979; Karickhoff and Bailey, 1973), Fe^{3+}-oxo complexes (Lehman, 1970) and Fe^{3+} in Al_2O_3 (Tippins, 1970) and were also assigned to LMCT transitions. In the iron oxides, therefore, LMCT bands should be present near these energies.

Experimental

Except for hematite, all of the Fe_2O_3 and FeOOH samples were synthesized. The identity and purity of each sample was confirmed using powder X-ray diffraction and Mossbauer spectroscopy.

Lepidocrocite samples were prepared by areal oxidation of a 10^{-2} M Fe(II) solution which was buffered to pH 6.5-7.5.

The maghemite sample was synthesized by thermal dehydration of lepidocrocite. The product is a dark-brown magnetic powder. The 298°K

Mossbauer spectrum of the sample used in this investigation showed a six-line hyperfine spectrum collapsing to a quadrupole doublet. This indicates that the mean particle size in this sample is sufficiently small to cause superparamagnetism. Small particle sizes are also indicated by the X-ray diffraction pattern where only the seven most intense lines for γ-Fe_2O_3 were observed and these were fairly broad and diffuse.

Visible and near-ultraviolet absorption spectra were obtained using a Beckman model 25 spectrophotometer. Samples were dispersed in distilled water (pH = 4) using a sonifier and diluted to give a colloidal suspension of about 10μM FeOOH or 5μM Fe_2O_3. The spectra were obtained using a 5 cm length cell.

Diffuse reflectance spectra in the visible and near-infrared were obtained using a Cary 17 spectrophotometer with an integrating sphere diffuse reflectance accessory. The integrating sphere was coated with MgO and the spectra were referenced against MgO. For easier comparison with the visible and near-ultraviolet absorption spectra, the reflectance spectra were converted to the Kebulka-Munk remission function defined by

$$F(R) = (1-R)^2/2R = k/s \qquad (6.3)$$

where R is the reflectance, k is the absorption coefficient and s is the scattering coefficient. Assuming that the scattering coefficient has only a small variation with wavelength over the range of interest, the shapes of the remission function and the actual absorption spectrum over that wavelength range should be identical.

Results and Discussion

Figure 6.3 shows the visible and near-infrared diffuse reflectance spectra of the different iron oxides and oxide hydroxides. Near-UV and visible region absorption spectra of these minerals are shown in Figure 6.4.

The visible and near ultraviolet spectra of goethite, lepidocrocite, and maghemite are all quite similar and, except for small differences in band energies, qualitatively resemble the spectrum of the Fe^{3+} phyllosilicate nontronite investigated by Karickhoff and Bailey (1973). The shape of the hematite spectrum is quite different from those of the other iron oxides; the band energies in the hematite spectrum, however, are essentially the same. The primary difference between the hematite spectrum and the others is that a band at 430 nm in the hematite spectrum is quite intense while the analogous band in the spectra of maghemite and the FeOOH phases occurs only as an inflection. The reason for this will be discussed below. Note that the hematite spectrum obtained here is quite similar to the polarized absorption spectrum of a hematite thin film obtained by Marusek et al. (1980). The band energies in the two spectra, however, are somewhat different. This may be due to particle scattering in our spectrum or simply a dependance of the observed hematite band energies with polarization direction in the single-crystal absorption spectrum.

In the near infrared and visible regions, all of the spectra are characterised by the presence of two prominant absorption bands near 640 nm (15 kK) and 900 nm (11 kK). These features can readily be assigned to the $^6A_1(^6S) \rightarrow {}^4T_2(^4G)$ and $^6A_1(^6S) \rightarrow {}^4T_1(^4G)$ ligand field transitions of Fe^{3+}, respectively. Analogous features were observed in the polarized absorption spectra of goethite and lepidocrocite single crystals obtained by

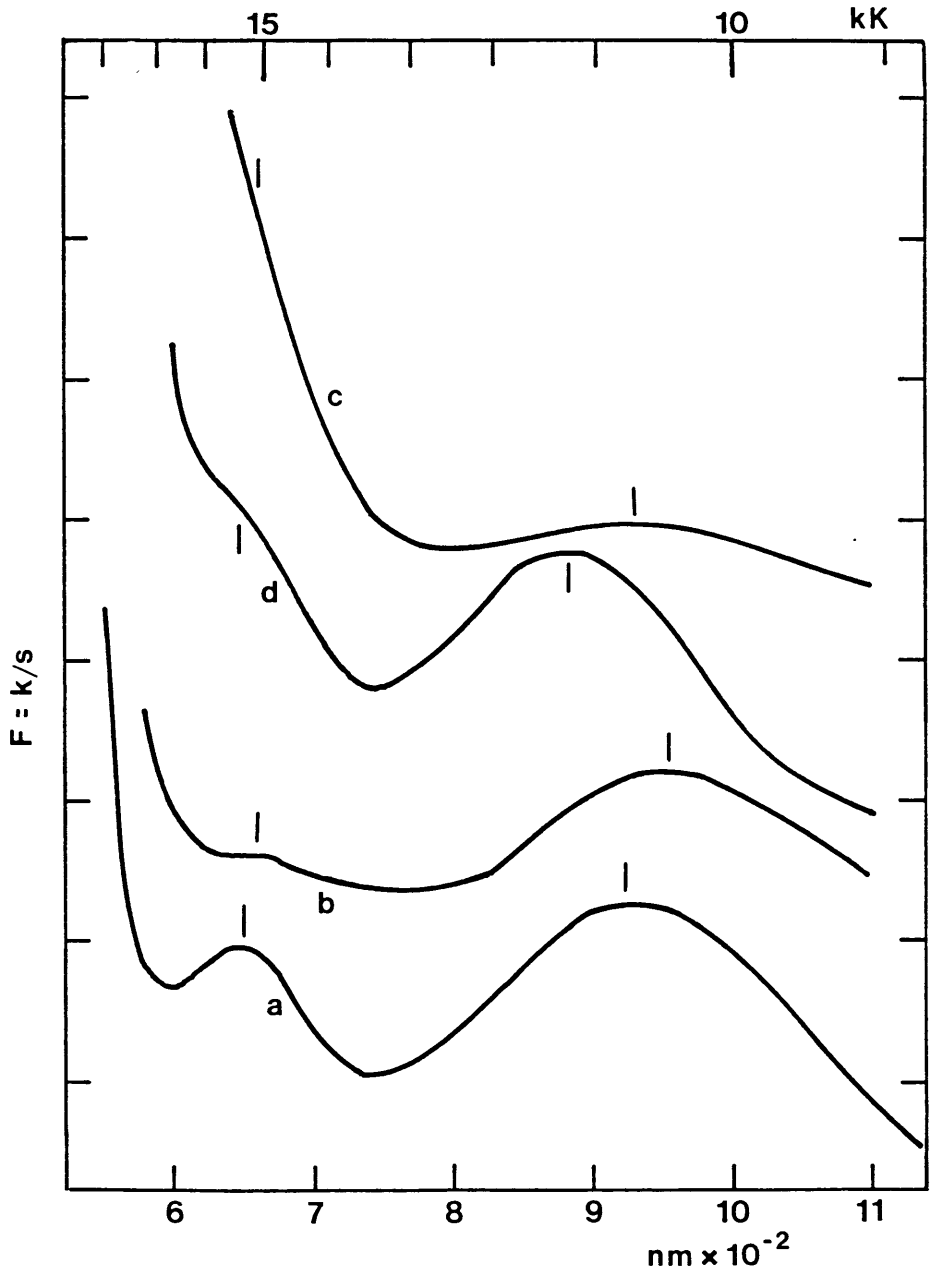


Figure 6.3: Kebulka-Munk remission function (Equation 6.1) of (a) goethite (b) lepidocrocite (c) maghemite and (d) hematite) in the visible and near-infrared regions obtained from diffuse reflectance spectra. The vertical bars indicate band positions. The band near 900 nm corresponds to the $^6A_1 \rightarrow {}^4T_1(^4G)$ transition while the band near 640 nm corresponds to the $^6A_1 \rightarrow {}^4T_2(^4G)$ transition. The steep absorption edge in the visible region gives these minerals their yellow to red colors and results primarily from higher energy ligand field transitions which have been intensified by magnetic coupling of adjacent Fe^{3+} cations.

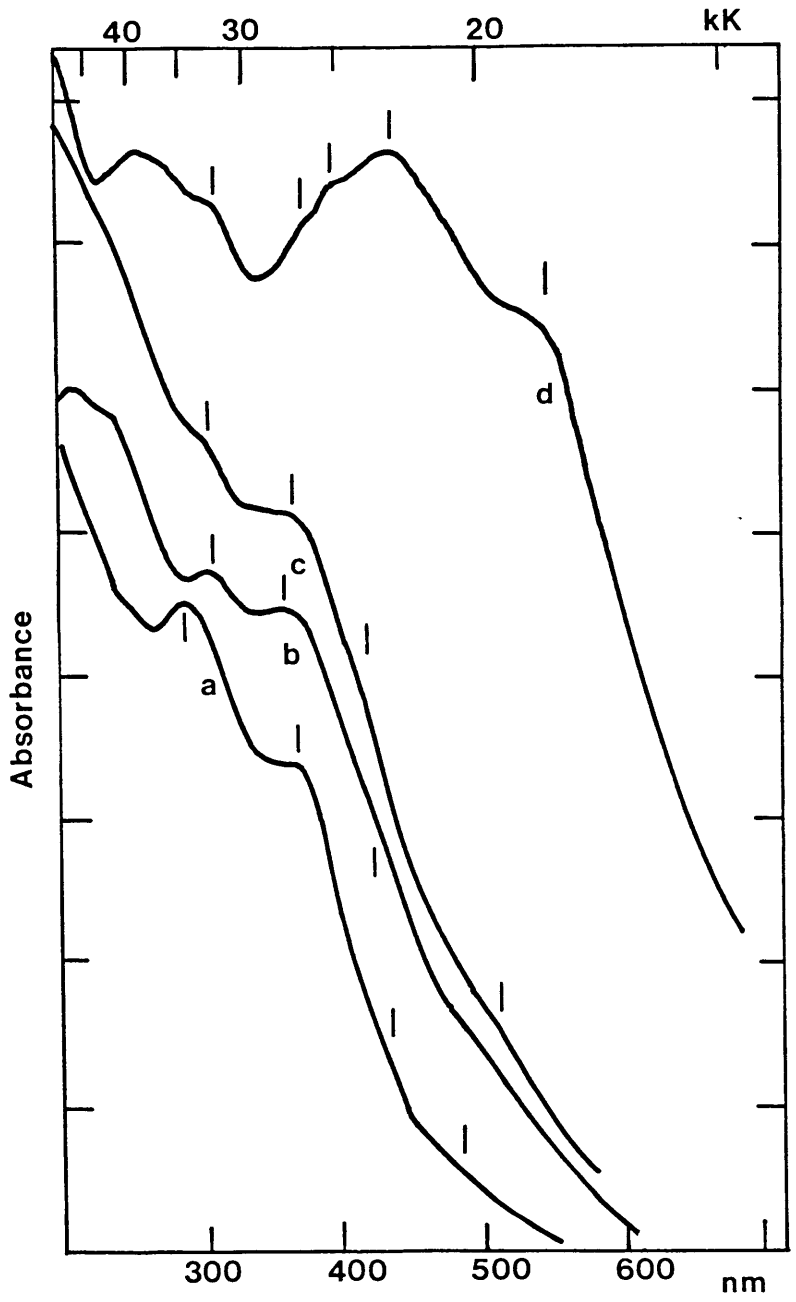


Figure 6.4: Visible and near-ultraviolet absorption spectra of (a) goethite (b) lepidocrocite (c) maghemite and (d) hematite. Absorption bands near 430, 360-380, and 290-310 nm correspond to the $^6A_1 \rightarrow {}^4E, {}^4A_1({}^4G)$, $^6A_1 \rightarrow {}^4E({}^4D)$, and $^6A_1 \rightarrow {}^4T_1({}^4P)$ ligand field transitions of Fe^{3+}. A feature near 485-500 nm is assigned to the $^6A_1 + {}^6A_1 \rightarrow {}^4T_1 + {}^4T_1$ excitation of an Fe-Fe pair. Higher energy features, at wavelengths below 270 nm, are assigned to LMCT transitions.

Mao and Bell (1974). In the latter spectra, the splitting of the $^4T_2(^4G)$ band by the dynamic Jahn-Teller effect is quite evident; here, however, this phenomenon is unresolved.

In principle, maghemite should contain some tetrahedrally-coordinated Fe^{3+}; in the sample investigated here, however, the absorption bands can be accounted for by considering only transitions of octahedrally coordinated Fe^{3+}. The reason for this may be that the $^6A_1 \rightarrow {}^4T_1(^4G)$ and $^6A_1 \rightarrow {}^4T_2(^4G)$ transitions of tetrahedral Fe^{3+} are much weaker than those of octahedral Fe^{3+} and, hence, cannot be observed in Figure 6.3. In chapter 4 it was argued that the $^6A_1 \rightarrow {}^4T_1(^4G)$ and $^6A_1 \rightarrow {}^4T_2(^4G)$ transtions of tetrahedral Fe^{3+} should occur near 15.0 and 19.5 kK. Interference from such bands may explain why the $^6A_1 \rightarrow {}^4T_2(^4G)$ transition of octahedral Fe^{3+} (near 15.0 kK) is so poorly-resolved in the spectrum of γ-Fe_2O_3.

Additional spectral bands at wavelengths shorter than 600 nm are present in the diffuse reflectance spectra of all of the iron oxides and oxide hydroxides yet, because these transitions are so much more intense than the 640 and 900 nm bands, they give only a steep absorption edge. The visible region absorption spectra show two bands near 480-500 nm and 430 nm. The 480-500 nm band appears as a strong, reasonably well-defined feature in the spectrum of hematite. In the spectra of the other phases, however, the 480-500 nm band is much weaker and gives only a slope change or small poorly-resolved peak. The 430 nm band is very strong and well-defined in hematite but gives only a perceptible shoulder in the spectra of the other minerals. The energy of the 430 nm feature corresponds to that of the $^6A_1(^6S) \rightarrow {}^4E,{}^4A_1$ ligand field transition; the latter is about 22-23 kK in the spectra of a wide variety of Fe^{3+} oxides, silicates, sulphates and phosphates. (e.g. Lehmann, 1970; Manning, 1967; Manning, 1970). Given this

assignment, the 500 nm band remains unaccounted for. This feature is absent in the spectra of minerals in which Fe^{3+} cations are not magnetically coupled suggesting that it results from the simultaneous excitation of coupled Fe^{3+} ions. The lowest energy "double exciton" or pair excitation should occur near 480-500nm and is the $^6A_1 + {}^6A_1 \rightarrow {}^4T_1(^4G) + {}^4T_1(^4G)$ transition. An analogous spectral band is found in Fe^{3+} doped Al_2O_3 (Ferguson and Fielding, 1972) and was also assigned to the pair excitation process. A second possible assignment for this band is that it is a split component (via the dynamic Jahn-Teller effect) of the $^4T_2(^4G)$ band. Such an assignment would imply a splitting of ~5 kK, however, which seems unlikely.

The 20 kK absorption band that is assigned to the $^6A_1 + {}^6A_1 \rightarrow {}^4T_1(^4G) + {}^4T_1(^4G)$ double exciton process is at an energy somewhat less than twice that of the single ion $^6A_1 \rightarrow {}^4T_1(^4G)$ transition (note that the latter is more correctly designated as the $^6A_1 + {}^6A_1 \rightarrow {}^4T_1(^4G) + {}^6A_1$ "exciton + magnon" transition). One might expect that the energy of a double exciton process would be given exactly by the sum of the energies of the component single ion transitions. The discrepency can be explained with reference to the energy level diagram of Figure 6.2. For example, the energy required for the transition between the ground and excited pair states with S = 2 in the $^6A_1 + {}^6A_1 \rightarrow {}^4T_1(^4G) + {}^6A_1$ exciton + magnon process, is found, using equation 6.2, to be

$$E_1 = E_0 + (23/4)J_1 - (13/4)J_2 \qquad (6.4)$$

Here, E_0 is the true energy of the $^6A_1 \rightarrow {}^4T_1(^4G)$ transition of a single, uncoupled, Fe^{3+} cation; J_1 is the exchange integral between two Fe^{3+} cations that are in the $^6A_1$ state; and J_2 is the exchange integral between an Fe^{3+} cation in the $^6A_1$ state and an Fe^{3+} cation in the $^4T_1(^4G)$ state. On the

other hand, the energy required for the $^6A_1 + {}^6A_1 \rightarrow {}^4T_1(^4G) + {}^4T_1(^4G)$ double exciton transition (S = 2 states only) is

$$E_2 = 2E_0 + (23/4)J_1 - (3/4)J_3 \qquad (6.5)$$

where J_3 is the exchange integral between two Fe^{3+} cations that are in the $^4T_1$ state. The difference between $2E_1$ and E_2 is then

$$\Delta E = (23/4)J_1 - (26/4)J_2 + (3/4)J_3 \qquad (6.6)$$

If J_1, J_2 and J_3 are either very small or nearly equal, then ΔE would close to zero. This is probably the case in the binuclear Fe-EDTA complex investigated by Schugar et al.(1970) where the double exciton band energies were almost exactly equal to the sum of the component single ion transition energies. This may also be the case in the spectrum of lepidocrocite investigated here since the energy of the $^6A_1 + {}^6A_1 \rightarrow {}^4T_1(^4G) + {}^4T_1(^4G)$ band is very close to twice that of the $^6A_1 + {}^6A_1 \rightarrow {}^4T_1(4G) + {}^6A_1$ band. In the spectra of hematite and maghemite, however, ΔE is about 2.0-3.0 kK. One explanation for the large values of ΔE is that in maghemite and hematite, and probably also goethite, the coupling between the $^6A_1$ and $^4T_1$ states is ferromagnetic ($J_2 < 0$) while the $^6A_1$-$^6A_1$ and $^4T_1$-$^4T_1$ couplings are antiferromagnetic ($J_1, J_2 > 0$). If the absolute magnitudes of J_1, J_2 and J_3 are roughly the same, then a value of ΔE of 1.0-2.0 kK would imply that the magnitudes of the J integrals are on the order of 75 - 150 cm^{-1}; such values are quite reasonable for these minerals.

The strong, well-defined band at 360-380 nm is at an energy characteristic of the $^6A_1 \rightarrow {}^4E(^4D)$ transition. The $^6A_1 \rightarrow {}^4T_2(^4D)$ transition is of similar energy and it appears that in these spectra the two transitions are unresolved. The characteristic energies of the $^4E(^4D)$ and

$^4T_2(^4D)$ states imply that in the absorption spectra they would only be separated by about 20 nm. In the spectrum of hematite, however, the two transitions appear to be resolved. A very strong band near 290-310 nm is tentatively assigned to the $^6A_1 \rightarrow {}^4T_1(^4P)$ ligand field transition. There are several alternative assignments for this band, however. The first is to the pair excitation $^6A_1 + {}^6A_1 \rightarrow {}^4T_1(^4G) + {}^4E,{}^4A_1(^4G)$; this is predicted to have an energy 33.8-34.2 kK. A second alternative assignment is the pair excitation $^6A_1 + {}^6A_1 \rightarrow {}^4T_2 + {}^4T_2$ which should have an energy near 30.8 kK. The observed peak may, in fact, be a composite of these three transitions.

Note that the visible to near-ultraviolet spectrum of maghemite is quite similar to that of the FeOOH phases even though the former should contain some tetrahedrally-coordinated Fe^{3+}. The higher energy, and nominally field independant, ligand field states of tetrahedrally coordinated Fe^{3+} have energies which are similar to the analogous states of octahedrally coordinated Fe^{3+}. As such, band attributable to Fe^{3+} in octahedral and tetrahedral coordination may not be resolved in Figure 6.4.

At wavelengths shorter than about 270 nm, there are several broad bands which can readily be assigned to LMCT transitions. The energies of these absorption bands are similar to those of analogous bands in other Fe^{3+} oxides, silicates and inorganic complexes involving Fe-O bonds (e.g. Karickhoff and Bailey, 1973; Tippins, 1970; Lehman, 1970). In most of the spectra reported here, the LMCT bands are rather ill-defined. This is most-likely due to increased light scattering at shorter wavelengths.

The observed band energies and their assignments are summarized in Table 6.2. From the $^6A_1 \rightarrow {}^4T_1(^4G)$, $^6A_1 \rightarrow {}^4E,{}^4A_1(^4G)$, and $^6A_1 \rightarrow {}^4E(^4D)$ transition energies and the Tanabe-Sugano equations (Table 6.1), we can calculate values for the ligand field theory parameters 10Dq, B and C and

Table 6.2: Energies and Assignments of Bands Observed in Fe_2O_3 and FeOOH Spectra

Transition	Observed (and Calculated*) Spectral Band Energies (kK)			
	α-Fe_2O_3	α-FeOOH	γ-Fe_2O_3	γ-FeOOH
$^6A_1 \rightarrow {}^4T_1(^4G)$	11.3 (11.3)	10.9 (10.9)	10.7 (10.7)	10.4 (10.4)
$\rightarrow {}^4T_2(^4G)$	15.4 (15.4)	15.4 (15.3)	~15. (14.9)	15.4 (15.2)
$2(^6A_1) \rightarrow 2(^4T_1(^4G))$	18.9 (~22.6)	20.8 (~21.8)	19.6 (~21.4)	20.6 (~20.8)
$^6A_1 \rightarrow {}^4E, {}^4A_1(^4G)$	22.5 (22.5)	~23. (23.3)	~23. (23.1)	~23. (23.5)
$\rightarrow {}^4T_2(^4D)$	24.7 (24.1)	-- (25.1)	-- (24.8)	-- (25.3)
$\rightarrow {}^4E(^4D)$	26.3 (26.3)	27.4 (27.4)	27.0 (27.0)	27.8 (27.8)
$\rightarrow {}^4T_1(^4P)$	31.3 (34.1)	35.0 (35.6)	31.7 (35.2)	32.8 (36.0)
$6t_{1u} \rightarrow 2t_{2g}$ (LMCT)	37.0	40.0	40.0	41.7
$1t_{2u} \rightarrow 2t_{2g}$ (LMCT)	--	44.4	--	47.6
10Dq	14.0	15.32	15.41	15.95
B	0.54	0.59	0.56	0.61
C	3.41	3.49	3.51	3.47

use these to predict the energies of the remaining transitions. The values for 10Dq, B and C , together with the predicted band energies, are summarized in Table 6.2. The predicted energies of the pair excitation bands are obtained assuming that they are equal to the sum of the two ligand field transition energies. As discussed previously, this may sometimes be only a rough approximation.

The values for 10Dq, B, and C are physically quite reasonable and are similar to those obtained in other Fe^{3+} oxygen systems. The values for 10Dq agree with that obtained from the SCF-Xα-SW calculation on an $(FeO_6)^{9-}$ cluster (chapter 4). The energy of the $^6A_1 \rightarrow {}^4T_2(^4G)$ band is predicted quite accurately. Finally, the energies of the LMCT transitions are in good agreement with the energies obtained from the $(FeO_6)^{9-}$ molecular orbital calculations. These considerations support the overall band assignments given in Table 6.2. Note, however, that the predicted energy of the $^4T_1(^4P)$ band is in rather poor agreement with that observed. This is to be expected: First, the energy of this excited state is most likely depressed by configurational interaction with the LMCT excited states with T_1 symmetry. Second, the Tanabe-Sugano expression used to calculate this state energy is only approximate. Third, as mentioned above, the observed band may instead be due to the $^6A_1 + {}^6A_1 \rightarrow {}^4T_1(^4G) + {}^4E, {}^4A_1(^4G)$ and $^6A_1 + {}^6A_1 \rightarrow {}^4T_2 + {}^4T_2$ double exciton processes.

The $(FeO_6)^{9-}$ molecular orbital calculations cannot predict the energies of the individual ligand field transitions. Such calculations can, however, estimate the average energy of the ligand field states that arise from a given electronic configuration. The calculation on the $(FeO_6)^{9-}$ cluster described in chapter 4 estimates that the average energy of the quartet states arising from the $(t_{2g})^3(e_g)^2$ configuration is 30.5 kK. We

cannot directly estimate the average energy of these states from the spectra because the energy of the $^4A_2(^4F)$ state is unknown. Using the values for B and C, however, we can estimate the average energy of these states using the Tanabe-Sugano expressions for the state energies (Table 6.1). This gives 27.5, 28.3, 28.4 and 28.9 kK for hematite, goethite, maghemite, and lepidocrocite, respectively. These are in good agreement with the theoretical result and add further support both to the band assignment scheme and to the reliability of the molecular orbital calculations.

A rather different, but at first glance reasonable, band assignment scheme would be to assign the 20.6, 23.5, and 27.8 kK bands to the $^6A_1 \rightarrow {}^4E,{}^4A_1(^4G)$, $^6A_1 \rightarrow {}^4T_2(^4D)$, and $^6A_1 \rightarrow {}^4E(^4D)$ transitions, respectively. This scheme, however, gives an unrealistically small value for 10Dq (~9 kK) and B values which are greater than the Fe^{3+} free ion value. Also, the resulting 10Dq, B and C values give a poor prediction of the $^6A_1 \rightarrow {}^4T_2(^4G)$ state energy.

Given the assignments of the bands at wavelengths greater than 270 nm to Fe^{3+} ligand field and pair excitation processes, it is significant that their intensities are comparable to those of the LMCT bands. In the iron oxides and oxide hydroxides, the spin and Laporte selection rules for the Fe^{3+} ligand field transitions are relaxed by the magnetic coupling of adjacent Fe^{3+} cations. This magnetic coupling occurs via the superexchange interaction which, in turn, results from the spin polarization of the Fe-O chemical bond. All of these minerals have FeO_6 coordination polyhedra in edge- and corner-sharing arrangements which allow relatively strong magnetic coupling via superexchange interactions. In hematite, however, FeO_6 polyhedra are also in face-sharing arrangements. The face-sharing arrangement results in a trigonal distortion of the FeO_6 coordination

polyhedra. The molecular orbital calculations on octahedral and trigonally-distorted FeO_6 coordination polyhedra discussed in chapter 4 showed that the trigonal distortion increases the spin-polarization of the oxygens bridging face-sharing FeO_6 polyhedra. This, in turn, implies that the superexchange interaction and, hence, the strength of the magnetic coupling, between face-sharing FeO_6 polyhedra in hematite will be greater than that between the edge-sharing FeO_6 polyhedra in the other oxides and oxide hydroxides. Accordingly, we expect the the Fe^{3+} ligand field transitions in hematite to be more intense than those in the other iron oxides. On the other hand, the strength of the coupling between two Fe^{3+} cations will vary depending on the electronic states of the Fe^{3+} cations; that is, some Fe^{3+} ligand field transitions will be intensified much more so than others. This is why the shape of the hematite spectrum is so different from that of the other iron oxides: the $^6A_1 \rightarrow {}^4E,{}^4A_1({}^4G)$ transition in hematite is strongly intensified by the greater degree of Fe^{3+}-Fe^{3+} coupling. The pair excitation feature near 500 nm is also much stronger. The most noticeable effect of the stronger Fe^{3+}-Fe^{3+} coupling in hematite, relative to the other iron oxides, is that the former is deep red while the latter are pale yellow to brown. Rossman (1975; 1976) has shown how the colors of Fe^{3+} sulphate and phosphate minerals can be directly related to their magnetic structures.

Summary and Conclusions

Near-infrared to near-ultraviolet spectra of Fe(III) oxides and oxide hydroxides show bands due to ligand field and ligand-to-metal charge-transfer transitions whose energies are similar to those found in other Fe(III) oxygen systems. The Fe^{3+} ligand field transitions are strongly

intensified by magnetic coupling of adjacent Fe^{3+} cations in the crystal structures of these minerals. Additional spectral features are attributed to the simultaneous excitation of two Fe^{3+} cations which are magnetically coupled.

From the spectra and the band assignment scheme, values for the ligand field theory parameters 10Dq, B and C were calculated. The parameters are physically reasonable and are able to accurately predict the energies of the Fe^{3+} ligand field transitions. A comparison with the spectral band energies and the results of spin-polarized SCF-Xα-SW molecular orbital calculations on Fe^{3+} coordination sites in oxides shows very good agreement. The theoretical value for 10Dq was calculated to be 15.8 kK; this compares well with the experimental values which range from 14.0 to 15.95 kK. The one-electron molecular orbital calculations estimate that average energy of the quartet ligand field states arising from the $(t_{2g})^3(e_g)^2$ configuration to be 30.5 kK. From the experimental values for B and C, the average energies of these states is estimated to be 27.5 to 29.0 kK, in good agreement with the MO calculations. The SCF-Xα-SW calculations give the energies of the first few ligand to metal charge-transfer transitions to be 38.1 and 43.6 kK. In the iron oxide and oxide hydroxide spectra, these transitions are found at 37.0-41.7 kK and 44.4-47.6 kK.

Taken together, these results show that the ligand to metal charge transfer transitions in Fe^{3+} oxides and silicates occur at energies much higher than those suggested by some previous investigators. The visible region absorption edge, which gives the iron oxides their red to yellow colors, does not result from ligand to metal charge-transfer transitions but is a consequence of very intense Fe^{3+} ligand field and Fe^{3+}-Fe^{3+} pair transitions. Both types of transitions are both Laporte and spin-allowed via the magnetic coupling of adjacent Fe^{3+} cations.

References

Chen, Y., D. Shaked and A. Banin (1979) The role of structural iron in the UV absortion by smecites, Clay Minerals, 14, 93-102.

Ferguson, J., H.J. Guggenheim and Y. Tanabe (1966) The effects of exchange interactions in the spectra of octahedral manganese II compounds, Journal of the Physical Society of Japan, 21, 347-354.

Ferguson, J., and P.E. Fielding (1972) The origins of the colours of natural yellow, blue, and green sapphires, Australian Journal of Chemistry, 25, 1371-1385.

Karickhoff, S.W., and G.W. Bailey (1973) Optical absorption spectra of clay minerals. Clays and Clay Minerals, 21, 59-70.

Krebs, J.J. and W.G. Maisch (1971) Exchange effects in the optical absorption spectra of Fe^{3+} in Al_2O_3, Physical Review B, 4, 757-769.

Lehmann, G., (1970) Ligand field and charge transfer spectra in Fe(III)-O complexes, Zeitschrift fur Physikalische Chemie Neue Folge, 72, 279-297.

Lehmann, G., and H. Harder (1970) Optical spectra of di- and trivalent iron in corundum, American Mineralogist, 55, 98-105.

Lever, A.B.P. (1968) Inorganic electronic spectroscopy, Elsevier, Amsterdam.

Lohr, L.L. (1972) Spin-forbidden electronic excitations in transition metal complexes, Coordination Chemistry Reviews, 8, 241-259.

Manning, P.G. (1967) The optical absorption spectra of some andradites and the identification of the $^6A_1 \rightarrow {}^4A_1, {}^4E$ transition in octahedrally bonded Fe^{3+}, Canadian Journal of Earth Sciences, 4, 1039-1047.

Manning, P.G. (1970) Racah parameters and their relationship to lengths and covalencies of Mn^{2+} and Fe^{3+} oxygen bonds in silicates, Canadian Mineralogist, 10, 677-687.

Mao, H.K., and P.M. Bell (1974) Crystal-field effects of ferric iron in goethite and lepidocrocite: Band assignments and geochemical application at high pressure, Carnegie Institute of Washington Yearbook, 1973, 502-507.

Marusak, L.A., R. Messier and W.B. White (1980) Optical absorption spectrum of hematite, α-Fe_2O_3, near IR to UV, Journal of Physics and Chemistry of Solids, 41, 981-984.

Rossman, G.R. (1975) Spectroscopic and magnetic studies of ferric iron hydroxy sulphates: intensification of color in ferric iron clusters bridged by a single hydroxide ion, American Mineralogist, 60, 698-704.

Rossman, G.R. (1976) Spectroscopic characteristics and magnetic studies of ferric iron hydroxyl sulphates--the sines $Fe(OH)SO_4 \cdot nH_2O$ and the jarosites, American Mineralogist, 61, 398-404.

Schugar, H.J., G.R. Rossman, J. Thibeault, and H.B. Gray (1970) Simultaneous pair electronic excitations in a binuclear iron(III) complex. Chemical Physics Letters, 6, 26-28.

Sherman, D.M. (1984) Electronic structures of Fe^{3+} coordination sites in iron oxides: applications to spectra, bonding, and magnetism. Physics and Chemistry of Minerals (submitted).

Sherman, D.M., R.G. Burns, and V.M. Burns (1982) Spectral characteristics of the iron oxides with application to the Martian bright region mineralogy, Journal of Geophysical Research, 87, 10169-10180.

Singer, R.B. (1982) Spectral evidence for the mineralogy of high albedo soils and dusts on Mars, Journal of Geophysical Research, 87, 10159-10168.

Singer, R.B., T.B. McCord, R.N. Clark, J.B. Adams, and R.L. Huguenin (1979) Mars surface composition from reflectance spectroscopy: a summary, Journal of Geophysical Research, 84, 8415-8426.

Tippins, H.H. (1970) Charge-transfer spectra of transition metal ions in corundum, Physical Review B, 1, 126-135.

Waite, T.D. (1983) Photoredox properties of iron in natural waters, Ph.D. dissertation, Massachusetts Institute of Technology.

CHAPTER 7:

Electronic Structure of the Mixed-Valence Dimer $Fe_2O_{10}^{15-}$: Application to Charge Transfer in Minerals*

*To be submitted to Physics and Chemistry of Minerals

Abstract

To investigate the nature of optically-induced intervalence charge-transfer and electron delocalization in mixed-valence iron oxides and silicates, molecular orbital calculations, using the SCF-Xα-SW method, were done for a mixed-valence $(Fe_2O_{10})^{15-}$ binuclear cluster. The results show that even if Fe^{2+} and Fe^{3+} cations occupy identical coordination sites, the Fe 3d electrons are strongly localized to their parent cations. This implies that electron delocalization in magnetite and other mixed-valence iron oxides and silicates occurs by the motion of small polarons. The optically-induced intervalence charge-transfer transition is found to be a transition from the $Fe^{2+}(t_{2g}{}^{\beta})$ orbital to the $Fe^{3+}(e_g{}^{\beta})$ orbital and is estimated to have an energy of 13.75 kK.

Introduction

A number of minerals, polynuclear inorganic complexes, and biological molecules contain transition metal cations in more than one valence state. The most important mineralogical examples of these systems are mixed valence iron oxides and silicates. The crystal structures of these phases frequently allow adjacent Fe^{2+} and Fe^{3+} cations to interact across shared edges of the octahedral coordination polyhedra. These interactions, in turn, allow for optically-induced intervalence charge transfer transitions (resulting in intense colors and pleochroism) and thermally-induced electron delocalization in the ground electronic state (Hush, 1967; Robin and Day, 1967; Burns et al., 1980; Burns, 1981).

The most famous example of a mixed valence iron mineral is magnetite (Fe_3O_4). This phase is quite common in the earth's crust and has also been suggested to be present on the surface of Mars. The crystal structure of magnetite is that of an inverse spinel; the tetrahedral A sites are occupied by Fe^{3+} cations while the infinite chains of edge-sharing octahedral B sites are occupied by equal numbers of Fe^{2+} and Fe^{3+} cations. Among the B-sites, the Fe cations are ferromagnetically coupled; each Fe cation has five α-spin 3d electrons but each Fe^{2+} cation also has a β-spin electron in the t_{2g} Fe 3d type orbitals. Above 120 K, however, the Fe^{2+} and Fe^{3+} B-site cations are indistinguishable by the Mossbauer effect and only a single hyperfine spectrum, corresponding to iron in an intermediate valence state, is observed. This implies that the Fe^{2+} β-spin electrons are delocalized over the B sites and that the residence time of a β-spin electron at a given site is less than 10^{-8} sec. The most significant effect of the delocalized electrons is the metallic behavior of Fe_3O_4. Other examples of

mixed-valence minerals exhibiting electron delocalization include deerite and ilvaite (Burns et al., 1980; Burns, 1981). Further mineralogical examples undoubtably exist and remain to be discovered.

Robin and Day (1967) devised a classification scheme for mixed valence compounds that is based on the degree of coupling between the two metal atoms. Magnetite falls under class III insofar as there is sufficient coupling between the two valence states to allow for electron delocalization. Most minerals, however, fall under class II; here, different valence states occupy adjacent sites yet there is only weak coupling between the two cations. The weak coupling, however, does allow charge-transfer by optical excitation. These charge-transfer transitions are manifested as strong absorption features near 1.6 eV in the optical spectra of mixed-valence iron minerals. These absorption bands, in turn, give rise to intense blue and green colors. Minerals exhibiting this phenomenon include hornblende, glaucophane and vivianite (Burns et al., 1980; Burns, 1981).

Two different interpretations have been given of the apparent electron delocalization in magnetite and, by extension, other minerals and solids (Goodenough, 1971; Goodenough, 1980; Camphausen, 1972) The first describes the β-spin Fe-3d electron as "itinerant"; that is, its delocalization corresponds to the formation of a delocalized Fe-3d band resulting from direct metal-metal bonding. The alternative interpretation describes the β-spin electron as a "small polaron." Here, the β-spin electron is localized to a particular Fe site but can tunnel from one Fe atom to the next. (This process is often referred to as "electron hopping".) The tunneling process is assisted by vibrational modes (or phonons) which bring

the Fe^{3+} and Fe^{2+} t_{2g}^{β} 3d type orbital energies into coincidence. The dependence of tunneling probability on vibrational modes would explain the temperature dependence of electron delocalization.

A knowledge of the electronic structures of magnetite and other mixed-valence minerals should provide considerable insight as to the nature of optically-induced intervalence charge-transfer transitions and electron delocalization. Several attempts to derive a one-electron energy level scheme for magnetite have been made. Balberg and Pankove (1971), by interpreting their cathodoluminescence spectra of magnetite, inferred that the splitting between the β-spin t_{2g} and e_g Fe(3d) bands (the crystal field splitting) was 2.6 eV; the exchange splittings of the t_{2g} and e_g Fe(3d) bands was assumed to be 6eV. This resulted in an energy level scheme that placed the B-site Fe(3d) α-spin energy levels within the O(2p) band and the B-site Fe(3d) β-spin energy levels within the energy gap between the O(2p) and Fe(4s) bands. The values for the crystal field splitting and the exchange splitting of the Fe(3d) bands used by Balberg and Pankove (1971) were much to large. Camphausen et al. (1972) recognized this and reinterpreted Balberg and Pankove's and other spectroscopic data to obtain a new version of the one-electron energy level scheme in magnetite. In the energy level schemes of Camphausen et al. (1972) and Balberg and Pankove (1971), it was assumed that the B-site Fe^{3+} and Fe^{2+} cations give rise to only one set of Fe(3d) bands.

Tossell (1978) approached the electronic structure of magnetite using the results of early SCF-Xα-SW molecular orbital calculations on $(FeO_6)^{9-}$, $(FeO_6)^{10-}$, and $(FeO_4)^{5-}$ clusters. Here, an energy level scheme for magnetite was devised by superimposing the energy levels of the three

clusters (this was done by assuming the O(2p) non-bonding levels of the clusters had the same energies). This approach automatically results in two sets of Fe(3d) bands resulting from the B-site Fe atoms; the Fe(3d) bands split under the crystal field to give $Fe^{2+}(t_{2g})$, $Fe^{2+}(e_g)$, $Fe^{3+}(t_{2g})$, and $Fe^{3+}(e_g)$ bands. In a spin-unrestricted picture, each of these bands are, in turn, split by the exchange energy. None of these approaches provide any indication of the nature of electron delocalization in magnetite.

In the investigation reported here, the electronic structures of magnetite and other mixed-valence iron oxides are modeled using Self-Consistent Field Xα Scattered Wave (SCF-Xα-SW) molecular orbital calculations on a $(Fe^{2+}Fe^{3+}O_{10})^{15-}$ dimer cluster. The calculated electronic structure will be used to investigate the mechanism of electron delocalization in these minerals and the nature of optically-induced intervalence charge-transfer. The reliability of the SCF-Xα-SW method for transition metal complexes has been well-established in the last decade and it is the only method which can deal with a cluster this large (12 atoms, 147 electrons).

Cluster Geometry and Input Parameters

The $(Fe_2O_{10})^{15-}$ cluster consists of two identical FeO_6 octahedra in an edge-sharing arrangement; its geometry is shown in Figure 7.1. The Fe-O bond length is 2.05 A which is essentially the same as the Fe(B-site)-O bond length in magnetite (2.06 Å). Two possible point group symmetries are possible for this cluster, depending upon whether the metal atoms are equivalent or not. For equivalent Fe atoms, the cluster point group is D_{2h}; for nonequivalent Fe atoms, the point group is C_{2v}. Calculations employing both point groups were done and the physical significance of the use of each of these point groups will be discussed below.

The sphere radii used for the two iron atoms are the same and equal to 1.208 A; the sphere radius used for each of the bridging oxygens is 1.114 A. The remaining oxygen atoms have sphere radii of 0.856 A. Most of the oxygen spheres are tangent to a given Fe atom but the bridging oxygen spheres overlap the Fe atomic spheres by about 5%. Calculations employing overlapping spheres (20%) had difficulty converging (at least in the spin-unrestricted stage). The spin-unrestricted calculation using tangent atomic spheres required about 6 hours of CPU time (30 iterations) on a Honeywell Multics Computer.

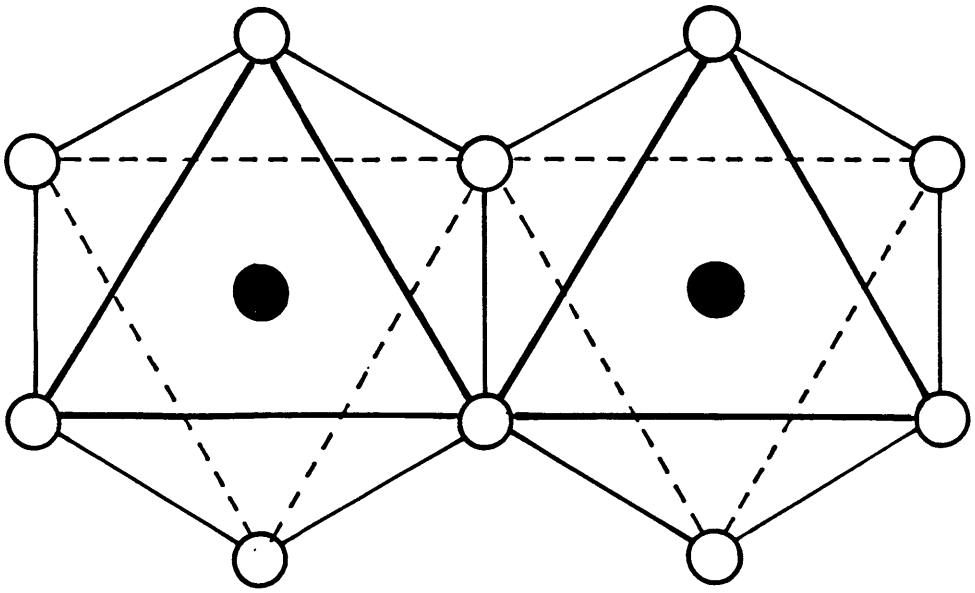


Figure 7.1: Geometry of $(Fe_2O_{10})^{15-}$ cluster.

Results and Discussion

The electronic structure of the $(Fe_2O_{10})^{15-}$ dimer was first calculated using D_{2h} symmetry. Here, both metal atoms are symmetrically equivalent and, accordingly, the fully delocalized model is forced upon the cluster. This constraint was then relaxed by lowering the symmetry to C_{2v}. Finally, the calculation was taken to its full spin-unrestricted form; that is, the exchange potential was modified to account for the different energies of α- versus β-spin electrons in the open shell system. The electronic configuration in the cluster is such that the two Fe centers are ferromagnetically coupled: ten of the Fe 3d electrons are spin-up (α-spin) and one Fe 3d electron is spin-down (β-spin).

The molecular orbital diagram for the cluster calculated using C_{2v} symmetry is shown in Figure 7.2. Here, the orbitals falling within the Fe (3d) and the O(2p) bands are shown. In the C_{2v} (rather than D2h) symmetry, the metal atoms are no longer forced to be equivalent and, in fact, the delocalized D_{2h} solution is found to be unstable: Each of the Fe 3d type orbitals becomes strongly localized to one of the metal atoms in C_{2v} symmetry. Of the occupied orbitals, the most delocalized is that containing the β-spin electron (labelled $21a_1^{\beta}$); still, this orbital has 82% of its electron density at one Fe center and only 10% at the other. (The other 8% is delocalized onto the oxygen atoms due to Fe-O covalency.) Wave function contours for this orbital are shown in Figure 7.3; note that it is actually metal-metal σ-antibonding and that the α-spin orbital is much more delocalized than the β-spin orbital. An important result is that distinct Fe^{2+} and Fe^{3+} centers are present in the dimer; associated with each of these centers is a distinct set of Fe 3d type orbitals. Note that the slight

metal-metal interaction removes the degeneracy of the orbitals within the t_{2g} and e_g sets. This metal-metal interaction is minor except for the Fe^{2+} β-spin e_g set where one of the orbitals is strongly delocalized over the two metal atom centers. In the ground state, however, this orbital is unoccupied.

Note that the unoccupied Fe^{3+} t_{2g}^{β} orbitals lie below the occupied Fe^{2+} t_{2g}^{β} set; this is not physically unreasonable, however: In the Xα formalism, orbital energy differences, as they are in the ground-state electronic configuration, do not correspond to electronic transition energies. During an electronic transition, the orbital energies will relax about the new excited state electronic configuration.* In this case, transfer of the Fe^{2+} t_{2g}^{β} electron to the Fe^{3+} t_{2g}^{β} orbitals would, because of orbital relaxation, result in an identical energy-level diagram as before. Hence, even though the unoccupied Fe^{3+} t_{2g}^{β} orbitals lie below the Fe^{2+} e_g^{α} and Fe^{2+} t_{2g}^{β} orbitals, the electronic configuration given here corresponds to the ground state. This, however, assumes that only integral occupancies are allowed or, equivalently, that the ground state can be represented by a single Slater determinant. However, there is a small degree of metal-metal bonding, and, because of this, the true ground state of the system should be represented as

$$\Psi_1 = \alpha|Fe_a^{2+}Fe_b^{3+}| + (1-\alpha^2)^{1/2}|Fe_a^{3+}Fe_b^{2+}| \qquad (7.1)$$

where α is a measure of the extent of electron delocalization. In the

*Electronic transition energies must be calculated using the "transition-state" approximation (Slater, 1974); here, 0.5 electrons are promoted from the ground-state orbital to the excited state orbital; the system is then reconverged to self consistency using the transition state configuration and the transition energy is taken as the energy difference between the fractionally occupied orbitals.

extreme case where there is a strong degree of metal-metal bonding, $\alpha = 1/\sqrt{2}$; this corresponds to an electronic configuration in which both the Fe^{2+} t_{2g}^{β} an Fe^{3+} t_{2g}^{β} orbitals in Figure 7.2 are each occupied by 0.5 electrons.

Nature of electron delocalization

The absence of any significant metal-metal bonding and the consequent localized nature of the Fe 3d electrons are the most physically important results of the cluster calculation. They imply that electron delocalization in Fe_3O_4 and other mixed-valence iron oxides and silicates is due to "electron hopping" or small polaron motion and not to the formation of itinerant electrons or d-bands. With reference to Figure 7.1, the energy of the Fe^{2+} $t_{2g}^{\beta} \rightarrow Fe^{3+}$ t_{2g}^{β} transition, calculated using the transition-state formalism, is less than 400 cm^{-1} for this cluster (this energy is roughly equal to the width of the $Fe(t_{2g})$ bands). Hence, the t_{2g}^{β} electron will oscillate between the two sites; the frequency of this oscillation will depend on the degree of coupling between the metal atoms. Since this coupling is usually assisted by vibrational modes, the observed electron delocalization will be often be temperature dependant.

Nature of Optical Intervalence Charge-Transfer

The cluster calculation can also be used to show the nature of optical intervalence charge transfer in mixed valence iron-bearing minerals. These transitions are often assigned as $Fe^{2+}(t_{2g}^{\beta}) \rightarrow Fe^{3+}(t_{2g}^{\beta})$. In the cluster treated here, the coordination environments of the two Fe centers are identical and, as noted previously , no energy is required for the $Fe^{2+}(t_{2g}^{\beta}) \rightarrow Fe^{3+}(t_{2g}^{\beta})$ transition. Moreover, considering the results of simple $(FeO_6)^{9-}$ and $(FeO_6)^{10-}$ cluster calculations (e.g. Tossell, 1978),

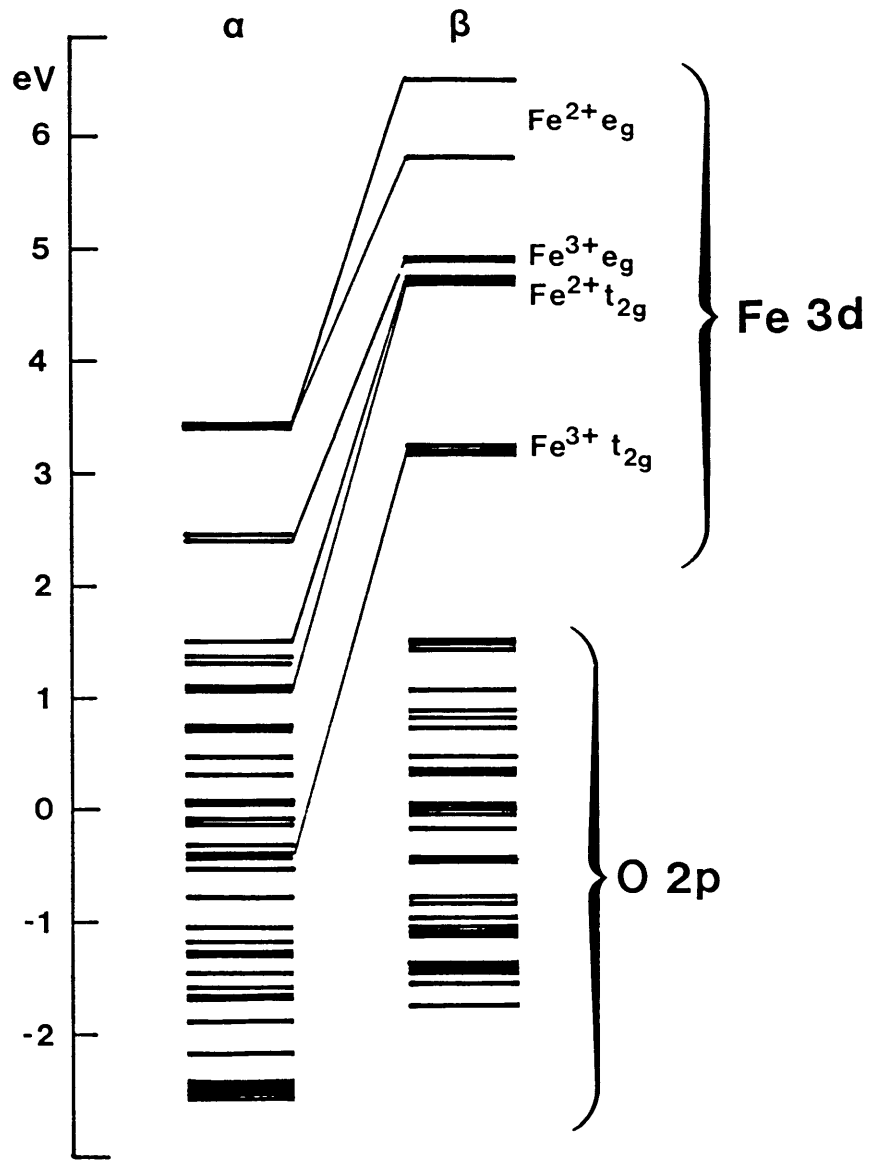
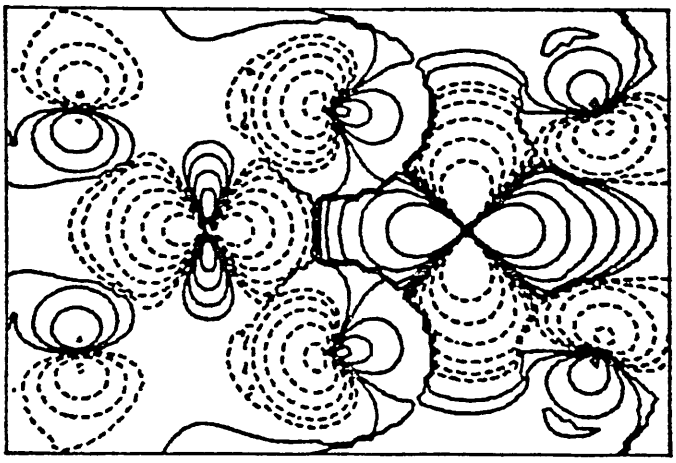


Figure 1: Electronic structure of the $(Fe_2O_{10})^{15-}$ cluster showing the energies of the orbitals within the Fe(3d) and O(2p) bands. Different orbital sets are given for α-spin (spin-up) and β-spin (spin-down) electrons. The orbitals within the Fe(3d) band are labelled according to their corresponding orbitals in a simple FeO_6 cluster. All of the orbitals within the α-spin Fe(3d) set are occupied; the orbitals within the β-spin Fe(3d) set are unoccupied except for the Fe^{2+} t_{2g} set which has one electron.

Table 7.1: Energies and Charges of Fe(3d) orbitals in $(Fe_2O_{10})^{15-}$

Orbital	Energy(eV)	%Fe^{2+}	%Fe^{3+}	%O	%Int
$Fe^{2+}(e_g^{\beta})$ Orbitals:					
$23a_1$ (0)	-18.44	70	0	15	15
$15b_1$ (0)	-19.11	18	16	23	43
$Fe^{3+}(e_g^{\beta})$ Orbitals:					
$22a_1$ (0)	-20.02	5	25	18	52
$14b_1$ (0)	-20.04	2	50	19	29
$Fe^{2+}(t_{2g}^{\beta})$ Orbitals:					
$7a_2$ (0)	-20.18	84	0	5	11
$21a_1$ (1)	-20.19	66	8	6	20
$13b_2$ (0)	-20.19	80	1	7	12
$Fe^{2+}(e_g^{\alpha})$ Orbitals:					
$23a_1$ (1)	-21.45	49	0	38	13
$15b_1$ (1)	-21.53	47	1	39	13
$Fe^{3+}(t_{2g}^{\beta})$ Orbitals:					
$12b_2$ (0)	-21.69	0	78	12	10
$6a_2$ (0)	-21.72	0	81	10	9
$20a_1$ (0)	-21.75	3	77	10	10
$Fe^{3+}(e_g^{\alpha})$ Orbitals:					
$22a_1$ (1)	-22.48	3	29	52	16
$14b_1$ (1)	-22.57	2	30	52	16
$Fe^{2+}(t_{2g}^{\alpha})$ Orbitals:					
$7a_2$ (1)	-23.40	43	0	41	16
$13b_2$ (1)	-23.56	46	0	39	15
$21a_1$ (1)	-23.86	39	0	45	16
$Fe^{3+}(t_{2g}^{\alpha})$ Orbitals:					
$20a_1$ (1)	-25.24	0	24	52	24
$12b_2$ (1)	-25.37	6	27	45	22
$6a_2$ (1)	-25.46	0	19	57	24

$21a_1^{\beta}$



$21a_1^{\alpha}$

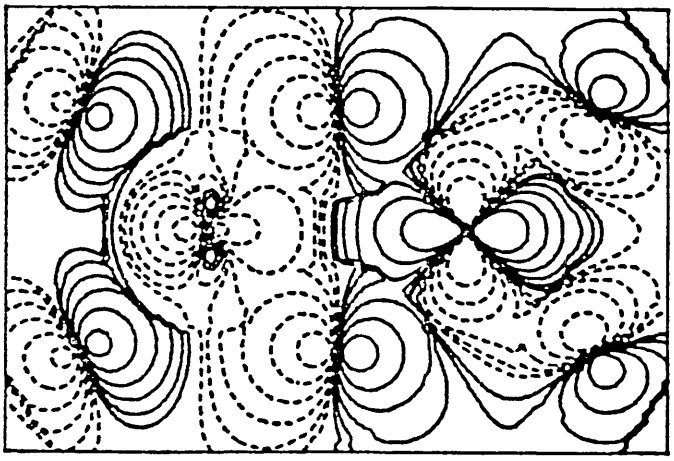


Figure 7.2: Wave function contours for the α- and β-spin $2la_1$ orbitals. The β-spin orbital contains the Fe^{2+} t_{2g}^{β} electron which exhibits thermally-activated electron delocalization in mixed valence Fe oxides. From the wave-function contours, it can be seen that both orbitals are metal-metal σ-antibonding.

one finds that even if the two Fe centers occupy different coordination environments, the energy difference between the Fe^{2+} t_{2g}^{β} and Fe^{3+} t_{2g}^{β} orbitals is to small to account for visible region transitions. With reference to Figure 7.2, however, several transitions will occur at energies comparable to those observed for $Fe^{2+} \rightarrow Fe^{3+}$ charge transfer. The most important is the spin-allowed $Fe^{2+}(t_{2g}^{\beta}) \rightarrow Fe^{3+}(e_g^{\beta})$ transition. Using the transition-state formalism (Slater, 1974) the energy of this transition is estimated to be about 1.71 eV or 13,750 cm^{-1} in the cluster investigated here. This transition energy will vary, depending on the geometries of the individual Fe sites and the Fe-O bond distances. In silicates, $Fe^{2+} \rightarrow Fe^{3+}$ charge transfer transition energies range from 9,700 cm^{-1} to 18,000 cm^{-1} with most values falling near 13,000 cm^{-1} (e.g. Burns et al., 1980). Hence, the calculated energy and band assignment seem reasonable.

Note also that, in addition to the spin allowed transition, there are several spin-forbidden charge transfer transitions. An example is the $Fe^{2+}(e_g^{\alpha}) \rightarrow Fe^{3+}(t_{2g}^{\beta})$. The excited state one-electron configuration, however, will give rise to a large number of multielectronic states and hence the one-electron transition will not correspond to a single multielectronic transition. These transitions may correspond to higher energy absorption features observed in the spectra of mixed-valence Fe minerals. Although such transitions are nominally spin-forbidden, they might be greatly intensified when second nearest neighbor Fe cations are magnetically coupled. Note that, because the cluster calculation presented here appears to underestimate the exchange splittings of the Fe 3d orbitals, the energies of these spin-forbidden charge-transfer transitions cannot be reliably calculated.

Conclusions

The results of this investigation imply that the minority spin electrons in the octahedral B-sites of magnetite are mostly localized to their parent cations. Electron delocalization giving metallic properties to magnetite and other mixed-valence minerals must occur through the motion of small polarons.

The calculated orbital energies, together with the transition state formalism, indicates that optically-induced intervalence charge-transfer absorptions result from the $Fe^{2+}(t_{2g}^{\beta}) \rightarrow Fe^{3+}(e_g^{\beta})$ electronic transition. The latter is estimated to have an energy of 13.8 kK which is in reasonable agreement with experimental data.

References

Balberg, I., and J.I. Pankove (1971) Cathodoluminescence of Magnetite, Physical Review Letters, 27, 1371-1374.

Burns, R. G. (1981) Intervalence transitions in mixed valence minerals of iron and titanium, Ann. Rev. Earth Planet. Sci., 9, 345-383.

Burns, R. G., D. A. Nolet, K. M. Parkin, C. A. McCammon, and K. B. Schwartz (1980) Mixed valence minerals of iron and titanium: correlations of structural, Mossbauer, and electronic spectral data, in Mixed-Valence Compounds, (D. B. Brown, ed.), D. Reidel: Dordrecht, Netherlands, 295-336.

Camphausen, D.L., J.M.D. Coey, and D.K. Chakraverty (1972) One-electron energy levels in Fe_3O_4, Physical Review Letters, 29, 657-660.

Camphausen, D.L. (1972) High temperature Fe_3O_4--a polaronic semiconductor?, Solid State Communications, 11, 99-103.

Goodenough, J. B. (1980) The Verwey transition revisted, in Mixed-Valence Compounds, (D. B. Brown, ed.), D. Reidel: Dordrecht, Netherlands, 413-425.

Goodenough, J. B. (1971) Metallic Oxides, Progress in Solid State Chemistry, 5, 145-399.

Hamilton, W.C. (1958) Neutron diffraction investigation of the 119°K transition in magnetite, Physical Review, 110, 1050-1057.

Hush, N.S. (1967) Intervalence transfer absorption. Part 2. Theoretical considerations and spectroscopic data, Progr. Inorg. Chem., 8, 391-444.

Robin, M. B. and P. Day (1967) Mixed valence chemistry--a survey and classification, Adv. Inorg. Radiochem., 10, 247-422.

Slater, J.C. (1974) The Self-consistent field method for atoms, molecules and solids, McGraw Hill: New York.

Tossell, J.A. (1976) Am. Mineral., 61, 130-144.

Tossell, J.A. (1978) Self-consistent-field-Xα study of one-electron energy levels in Fe_3O_4, Physical Review B, 17, 484-487.

CHAPTER 8:

Overview of Results and Areas of Future Investigation

The close agreement between calculated electronic transition energies in MO_6 and MO_4 clusters and experimentally observed electronic transition energies in minerals indicates that finite cluster molecular orbitals provide good descriptions of the electronic structures of iron and manganese oxides. The reason for this is that both the electronic transitions and chemical bonds in these minerals are localized to the metal atom and its immediate coordination environment. This is of of fundamental significance and begins to explain why the traditional Bloch-Wilson band model approach fails to give an adaquate description of the electronic structures of these minerals.

The characterization of the electronic spectra of iron and manganese oxides is one of the more important practical results of this study. Such information is essential for understanding geochemically-important electronic transitions and in the spectroscopic remote-sensing of the surface mineralogies of the Earth and Mars. Previously, however, the optical spectra of iron(III) oxides and silicates were poorly understood; moreover, there was very little information on the energies of electronic transitions in the manganese(IV) oxides. In this study, it was shown that the LMCT (ligand to metal charge-transfer) transitions in iron and manganese oxides occur at much higher energies (>4.6 eV) than previously supposed by some investigators. Strong absorption bands at energies below 4.6 eV in the spectra of iron(III) oxides and silicates result from cooperative phenomena such as exchange-enhances ligand field transitions and Fe-Fe pair excitations. The black color and opacity of manganese(IV) oxides is not due to LMCT transitions since these occur at energies above 4.5 eV. One possible explanation for the opacity of these minerals is the optical absorption of polarons associated with intervalence charge-transfer,

as in magnetite (Fe_3O_4). The manganese(IV) oxides are characteristically non-stoichiometric and hence electron delocalization via $Mn^{2+} \rightarrow Mn^{4+}$ and $Mn^{3+} \rightarrow Mn^{4+}$ charge transfer should occur.

The energies of electronic transitions between one-electron molecular orbitals give a good approximation to the actual energies of transitions between the multiplet states involved in LMCT transitions. This, in general, is not the case for the ligand field transitions; here, one must use multiplet theory to relate the one-electron orbital energies to those of the ligand field states. In general, one can only obtain the average energy of a set of ligand field multiplet states from the energy of an electronic configuration. Previous molecular orbital studies of Fe^{2+} and Fe^{3+} coordination sites in minerals (Tossell et al., 1973;1974; Vaughen et al., 1974) directly equated transitions between the Fe 3d one-electron orbitals with spectroscopic absorption features and, as such, obtained incorrect results. (To compound the problem, the results were often in fortuitous agreement with experiment.)

Given that the molecular orbital calculations on finite clusters can provide a good description of electronic spectra (at least to the extent possible by one-electron orbitals), it follows that such calculations should also give a good description of the chemical bonds between the metal atom and its immediate coordination environment. Some aspects of chemical bonding in iron and manganese oxides can be inferred from the chemical behavior of these minerals. On the other hand, the results of the molecular orbital calculations presented here place our understanding of such chemical behavior on a greater theoretical foundation. One important result obtained here is that the covalencies of the Fe-O and Mn-O chemical bonds

can be quite large (50-70%) depending on the oxidation state of the metal atom. For this reason, the classical ionic-bonding models that are commonly used in geochemistry often do not give adaquate explanations for the crystal chemistry and structures of iron and manganese oxides. Using the charge-partitioning scheme outlined in previous chapters, the effective charge of the octahedrally-coordinated metal atom in oxides is found to decrease in the order

$$Mn^{2+} > Fe^{3+} > Fe^{2+} > Mn^{4+} > Mn^{3+} \qquad (8.1)$$

The magnitudes of the effective charges on all these cations are fairly similar, however, and range from +1.4 to +1.0. A more interesting trend is the relative degree of covalency of the metal-oxygen bond. The latter is found to increase in the order

$$Mn^{2+} < Fe^{2+} < Fe^{3+} < Mn^{3+} < Mn^{4+} \qquad (8.2)$$

This trend is quite reasonable considering the formal charges and d-orbital electronic configurations of the cations: First, the degree of bond covalency increases with the formal charge of the cation. This is expected since, as its formal charge increases, the ability of the cation to polarize the electron cloud of the ligands increases. Second, for cations with the same formal charge, the metal ligand covalency will vary depending on the d-orbital electronic configuration. In particular, the Fe^{2+}-O bond is more covalent than the Mn^{2+}-O bond because the sixth d-electron of Fe^{2+} occupies the weakly antibonding $2t_{2g}^{\beta}$ orbital; electrons in this orbital poorly screen the Fe nuclear charge and, as such, the Fe^{2+} center has a greater polarizing ability than that of the Mn^{2+} center (an alternative way of stating this is that, to the ligands, Fe^{2+} resembles Fe^{3+} more than Mn^{2+} resembles Mn^{3+}). The Mn^{3+}-O bond is more covalent than the Fe^{3+}-O bond because the strongly σ-antibonding $3e_g^{\alpha}$ orbital in Mn^{3+} is occupied by only

one electron while the same orbital in Fe^{3+} is occupied by two electrons.

The trends in covalencies provide insight on the solubilities and, hence, residence times and geochemical mobilities of iron and manganese cations in natural waters. In the absence of other complexing agents (e.g. organic chelates, Cl^-, HCO_3^-) the dissolution of iron or manganese oxides involves the formation of soluble aquo- or hydroxo-complexes:

$$\text{e.g. } \alpha\text{-FeOOH} + 2H_3O^+ + 4H_2O = Fe(H_2O)_5(OH)^{2+} + 2H_2O \qquad (8.3)$$

Dissolution of the metal oxides or oxide hydroxides, therefore, requires protonation of the structural oxygens. This will happen to the extent that the structural oxygens are Bronsted bases. The basicity of of the oxygens, however, will decrease with increasing covalency of the metal-oxygen bond. This is because the effective negative charge on the oxygens, and hence their proton affinity, will decrease with metal-ligand bond covalency. For this reason, manganese(IV) oxides are much less soluble in aqueous solutions (at a given pH) than are iron(III) oxides. Moreover, the solubilities of the iron and manganese oxides and hydroxides decrease in the order

$$Mn^{2+} > Fe^{2+} > Fe^{3+} > Mn^{4+} \qquad (8.4)$$

which, in turn, parallels the increase in metal-oxygen bond covalency.

The effect of covalency on the Bronsted basicity of the structural oxygens in Fe and Mn oxides also explains some geochemically-important aspects of the surface chemistries of the iron(III) and manganese(IV) oxides. In aqueous systems, the surfaces of oxides consist of terminal $M\text{-}O^{2-}$, $M\text{-}OH^-$ and $M\text{-}OH_2$ groups. At a characteristic pH, the net charge on the surface will be zero; this is referred to as the zero-point of charge and the pH at which it occurs is designated pH_{zpc}. The pH at which the surface charge is zero (pH_{zpc}) for a oxide depends on the relative acidity

or basicity of the surface oxygens. One important feature of the colloidal chemistry of manganese(IV) oxides and that of iron(III) oxides is that their pH_{zpc} values differ considerably (Stumm and Morgan, 1980; Drever, 1982). For iron(III) oxides and oxide hydroxides, the pH_{zpc} is found to be near 6-9 while for manganese(IV) oxides the pH_{zpc} falls near 2. The different pH_{zpc} for the two oxides can be understood by noting that, since the Mn^{4+}-O bond is more covalent than the Fe^{3+}-O bond, the effective negative charge and, hence, basicity of the manganese(IV) oxide surface oxygens will be smaller than that of the surface oxygens on iron(III) oxides and oxide hydroxides. An interesting consequence is that, at a given pH, the surface charge (neglecting the formation of an electrical double layer) on iron(III) oxide will be positive relative to that on a manganese(IV) oxide. This may explain why iron(III) oxides tend to adsorb anionic species while manganese(IV) oxides tend to adsorb cations. This effect also results in some differences in the crystal chemistries of these minerals. For example, the minerals akaganeite (β-FeOOH) and hollandite (MnO_2) have the same tunnel structures (e.g. Burns and Burns, 1979); the tunnels, however, must be stabilized by ions occupying the large channels. In akaganeite, these ions are always anions (Cl^-, SO_4^{2-}) while in hollandite they are cations (usually Ba^{2+}).

An major objective of spectroscopy and quantum chemistry is to understand how chemical bonds affect spectroscopic observables. In mineralogy, this is of particular interest since it may enable electronic spectra of minerals to provide a greater amount of crystal chemical information. Several trends between chemical bonding and spectroscopic observables can be seen from the cluster calculations presented in this study. First, the value of the ligand field theory parameter 10Dq for

octahedrally-coordinated cations is found to increase in the order:

$$Mn^{2+} < Fe^{2+} < Fe^{3+} < Mn^{3+} < Mn^{4+} \qquad (8.6)$$

This trend is found to parallel the degree of metal-oxygen covalency but not the effective charge on the metal atom. The increase in 10Dq with covalency can be explained by noting that 10Dq is a measure of the energy difference between the e_g σ-antibonding and t_{2g} π-antibonding orbitals. Since e_g σ-bonding is usually much more important than t_{2g} π-bonding, an increase in the bond strength (and, presumably, bond covalency) will increase the energy of the e_g σ-antibonding orbitals more than it will increase the energy of the t_{2g} π-antibonding orbitals. The net effect will be an increase in 10Dq. In the crystal field theory, increases in 10Dq result from increased electrostatic interaction with the ligands. Since increasing the bond-strength via covalent interactions also increases 10Dq, we may have an explanation why crystal field field theory has been so succesful in predicting crystal chemical trends (Burns, 1970) even though the chemical bonds in transition metal oxides and silicates are only partially ionic.

Covalency should also be related to the energies of the LMCT transitions. In the octahedral clusters, the $6t_{1u}^{\beta} \rightarrow 2t_{2g}^{\beta}$ transition energies decrease in the order:

$$Mn^{2+} > Fe^{2+} > Mn^{3+} > Fe^{3+} > Mn^{4+} \qquad (8.7)$$

Except for Mn^{3+} or Fe^{3+} this trend also parallels the increase in bond covalency. If we instead consider the energies of the lowest energy LMCT transition in each cluster, then the trend correctly follows that of covalency. A decrease in LMCT transition energy with increasing bond covalency is expected and recalls some of the fundamental notions of chemical bonding. In particular, the covalency of the metal-ligand bond will increase as the electronegativity difference between the metal and

ligand atoms decreases. At the same time, the smaller the electronegativity difference, the smaller the energy required for charge-transfer.

Finally, we can summarize how chemical bonds in iron(III) oxides and oxide hydroxides can be related to the Mossbauer spectra and magnetochemistries of these minerals. In chapter 4 it was shown that the spin-polarization of the Fe-O chemical bond results in the superexchange interaction responsible for antiferromagnetism. The degree of spin-polarization of the oxygens by the iron atoms in tetrahedral, octahedral, and trigonally-distorted octahedral coordination sites correlates with the magnetic structures of several iron(III) oxides. As shown in chapter 5, the spin polarizability of OH^--ligands is smaller than that of O^{2-}-ligands. This explains why superexchange via Fe-OH-Fe bridging is weaker than superexchange via Fe-O-Fe bridging. In passing, we can relate this concept to the electronic spectra of iron(III) oxides, oxide hydroxides and silicates. The Fe^{3+} ligand-field transitions in these minerals are intensified by magnetic coupling of adjacent Fe^{3+} cations. Hydroxyl- rather than oxo-bridging of Fe^{3+} cations lowers the strength of the Fe^{3+}-Fe^{3+} magnetic coupling which, in turn, lowers the intensities of the Fe^{3+} ligand field transitions. For this reason, the iron oxide hydroxides (e.g. goethite, lepidocrocite) are yellow to orange while the iron oxides (hematite, maghemite) are deep red.

The spin-polarization of the Fe^{3+}-O chemical bond affects the spin-population at the Fe^{3+} cation. Variations in the Fe^{3+} spin result in variations in the magnetic hyperfine field at the ^{57}Fe nucleus observed in Mossbauer spectroscopy. The effective spin of Fe^{3+} is calculated to decrease upon going from octahedral to tetrahedral coordination with oxygen. This agrees with the observation that the magnetic hyperfine

field for tetrahedrally coordinated Fe^{3+} (488 kOe) is smaller than that for octahedrally coordinated Fe^{3+} (499) in γ-Fe_2O_3. The magnetic hyperfine field is also found to decrease if Fe^{3+} cations are bonded to hydroxyl groups. This observation is explained by the calculated electronic structure of the trans-$(FeO_4(OH)_2)^{7-}$ cluster. In the latter, the $3e_g^{\alpha}$ electrons are delocalized onto the OH ligands; this, in turn, promotes the Fe-O^{2-} covalency by removing electrons from the antibonding orbital. Both effects serve to decrease the effective spin on the Fe atom. Understanding how chemical bonds affect the magnetochemistries and Mossbauer spectra of iron oxides and silicates is of geochemical importance since both Mossbauer spectroscopy and magnetic measurements are used to characterize the complex and poorly-crystalline mineralogies found in marine ferromanganese nodules, sediments, and low-temperature alteration assemblages. The results presented here are only preliminary and a great deal of additional work in this regard remains to be done.

Future Areas of Investigation

Even if we restrict ourselves to the iron and manganese oxides, the application of quantum mechanics to geochemistry is an open-ended subject. In view of the results obtained in this study, however, two problems are of particular interest and their investigation should yield interesting results:

1. Further calculations on mixed-valence dimers containing Fe^{2+}-Fe^{3+} pairs should be done in order to determine the effects of site geometry and bond distances on intervalence charge-transfer transitions and electron delocalization. The results of such investigations would be far reaching insofar as the mixed valence clusters are models for inner-sphere electron

transfer processes. In addition to iron oxide clusters, calculations on Mn^{2+}-Mn^{3+}, Mn^{3+}-Mn^{4+} and Mn^{2+}-Mn^{4+} clusters would be of interest to help understand electron delocalization and redox reactions in manganese oxides.

2. Calculations on oxo-and hydroxo-bridged Fe^{3+}-Fe^{3+} dimers can shed insight on the magnetic coupling interactions between Fe^{3+} cations. From such calculations, one may evaluate the sign and magnitude of the Heisenberg exchange integral J (using the transition state formalism) and determine how it varies with cluster geometry and the nature of the bridging ligands.

3. Calculations on Fe and Mn coordination polyhedra containing Cl^-, H_2O, S^{2-} and OH^- ligands are of interest to investigate how electronic structure and chemical bonding can be related to the speciation of Fe and Mn cations in natural waters and hydrothermal solutions.

4. Experimental investigations on the electronic spectra of manganese oxides are needed. Although the spectrum of MnO has been well-studied, this is not true for manganese(III) and manganese(IV) oxides.

References

Burns, R.G. (1970) Mineralogical Applications of Crystal Field Theory, Cambridge University Press, Cambridge.

Burns, R.G. and V.M. Burns (1979) Manganese Oxides, in, Marine Minerals, (R.G. Burns, ed.), Mineralogical Society of America, Washington D.C.

Drever, J.I. (1982) The Geochemistry of Natural Waters, Prentice-Hall, Engelwood Cliffs, New Jersey.

Stumm, W.S. and J.J. Morgan (1982) Aquatic Chemistry, John Wiley and Sons, New York.

Tossell, J.A., D.J. Vaughan, and K.H. Johnson (1974) The electronic structures of rutile, wustite and hematite from molecular orbital calculations, American Mineralogist, 59, 319-334.

Vaughan, D.J., J.A. Tossell, and K.H. Johnson (1974) The bonding of ferrous iron to sulphur and oxygen in tetrahedral coordination: a comparitive study using SCF-X -SW molecular orbital calculations, Geochimica et Cosmochimica Acta, 38, 993-1005.

APPENDIX 1:

The Electronic Structures of Co^{3+} Coordination sites in Fe-Mn Oxides: Application to the Uptake of Co in Marine Ferromanganese Nodules

Abstract

The electronic structures of $(CoO_6)^{9-}$ clusters were calculated using the SCF-Xα-SW molecular orbital method. $(CoO_6)^{9-}$ clusters with cobalt-oxygen distances of 2.005Å and 1.905Å were used to model the range of coordination environments of Co^{3+} in iron(III) and manganese(IV) oxides, respectively.

The results show that, when the Co-O distance is increased from 1.905 to 2.005 A, Co^{3+} goes from the the low-spin to the high-spin state. The low-spin to high-spin transition of Co^{3+} is predicted to occur at Co-O distance of 1.96 A. Hence, although only low-spin Co^{3+} should occur in manganese(IV) oxides, both low- and high-spin Co^{3+} may coexist in thermal equilibrium in iron(III) oxides. The uptake of soluble high-spin Co^{3+} in iron(III) oxides may explain the observed Fe-Co correlations observed in marine ferromanganese nodules. The possibility of different spin states of Co^{3+} in the iron and manganese oxides suggest that photoelectron spectra could be used to investigate the uptake and partitioning of Co in ferromanganese nodule mineralogies. Previous arguments, based on crystal field theory, regarding the relative stability of Co^{3+} in manganese versus iron oxides are evaluated in the context of MO theory. High spin Co^{3+} in iron(III) oxides is strongly stabilized by a large exchange energy. A higher stability of low spin Co^{3+} must be due to a greater electrostatic stabilization energy.

Introduction

The uptake of Co in marine ferromanganese nodules has received considerable attention (e.g. Burns, 1976; Murray and Brewer, 1977; Arrhenius et al., 1979; Glasby and Thiyssen, 1982; Halbach et al., 1982) and is one of comparitively few geochemical processes which have been addressed using models of chemical bonding (Burns, 1976) and spectroscopy (Murray and Dillard, 1979). Marine ferromanganese nodules consist of complex intergrowths of manganese(IV) oxides (10A manganite or todorookite, 7A manganite or birnessite, and vernadite or δ-MnO_2) and iron(III) oxide hydroxides (see Burns and Burns, 1979). A major point of uncertainty is which of these phases are responsible for the uptake of Co^{3+} in ferromanganese nodules. Inter-element relations show both Co-Mn and Co-Fe correlations in ferromanganese nodules (Arrhenius et al., 1979; Halbach et al., 1982) suggesting that Co can be taken up into both the manganese(IV) oxide and iron(III) oxide phases.

The crystal chemistry of cobalt is fairly complex. Within the range of geochemical conditions at the Earth's surface, two different oxidation states of cobalt are possible (Co(III) and Co(II)). Murray and Dillard (1979) have shown, using core-level photoelectron spectroscopy, that Co adsorbed on the surface of manganese(IV) oxides is in the Co^{3+} oxidation state. The oxidation of Co^{2+} and Co^{3+} is attributed to the electric field at the oxide surface which raises the activity of Co^{2+}. Presumably, the same effect will occur on the surface of an iron(III) oxide hydroxide. On the other hand, Co^{3+} can exist in either the high-spin state (with a Co 3d configuration $t_{2g}^4e_g^2$) or in the low-spin state (with a Co 3d configuration of $t_{2g}^6e_g^0$). The high- and low-spin states of Co^{3+} have ionic radii of

0.61 and 0.53Å, respectively (Shannon and Prewitt, 1969). Because of their different ionic radii, the two spin states of Co^{3+} are expected to exhibit different crystal-chemical trends. One important feature is that the ionic radius of low-spin Co^{3+} is nearly the same as that of Mn^{4+} (0.54 A) while the ionic radius of high-spin Co^{3+} is very close to that of Fe^{3+} (0.65 A). One might, therefore, argue that high-spin Co^{3+} is taken up into the iron(III) oxide phases while low-spin Co^{3+} is taken up into the manganese(IV) oxides. This, essentially, is what was suggested be Halbach et al.(1982). Burns (1976), however, used crystal field theory to argue that low spin Co^{3+} is the most stable spin-state. This is supported by the observation that nearly all Co^{3+} complexes are low-spin. It follows that because the ionic radius of low-spin Co^{3+}(0.53Å) is nearly identical to that of Mn^{4+} (0.54Å), Co^{3+} should substitute for Mn^{4+} and be taken up in the MnO_2 phases and not in the ferric oxyhydroxides.

In the model of electrostatic crystal field theory, the Co 3d orbitals are split into a t_{2g} set with energy -4Dq and an e_g set with energy +6Dq. Low-spin Co^{3+}, with an electronic configuration of $t_{2g}^6e_g^0$, would therefore be stabilized by -24Dq while high-spin Co^{3+}, with an electronic configuration of $t_{2g}^4e_g^2$, would be stabilized by only -4Dq. On the other hand, one must also consider the "pairing energy" resulting from the repulsion of electrons occupying the same orbital. The stabilization energy for low-spin Co^{3+} in then -24Dq + 4P while that for high-spin Co^{3+} is -4Dq + P where P is the pairing energy. Crystal field theory cannot be used to predict which spin-state is the more stable without information on the relative values of P and 10Dq. In general, P is on the order of 10Dq. Hence, it is not clear, even in the context of crystal field theory, that low-spin Co^{3+} is more stable than high-spin Co^{3+}. We can solve this problem

either by spectroscopic measurement of 10Dq and P or by estimating analogous parameters using accurate theoretical calculations.

The purpose of this investigation is to determine the electronic structure and the nature of chemical bonding of Co^{3+} in the coordination sites of iron and manganese oxide phases. The approach used is the molecular orbital cluster method: the Co^{3+} coordination sites are modelled by $(CoO_6)^{9-}$ clusters whose electronic structures are obtained using the self-consistent field Xα-scattered-wave (SCF-Xα-SW) method. Using the calculated electronic orbitals and orbital energies, the factors affecting the stabilities of the $(CoO_6)^{9-}$ clusters will be investigated as will potentially useful spectroscopic transitions that can be applied to understanding the uptake of Co^{3+} in marine ferromanganese nodules.

Electronic Structure of $(CoO_6)^{9-}$

Molecular orbitals diagrams for the two $(CoO_6)^{9-}$ clusters are given in Figure 1. The orbitals shown are those which fall within the O 2p valence band and the Co 3d band. These are the orbitals which determine most of the chemical properties and stabilities of the two clusters insofar as they comprise the bonding and occupied-antibonding molecular orbitals. The $(CoO_6)^{9-}$ cluster with a Co-O distance of 2.005Å is found to have the high-spin (Ms = 2) configuration in its ground state. Because there are four more spin-up than spin-down electrons in this configuration, the electrons with spin-up will experience a different interelectronic potential than that for electrons with spin-down. This gives rise to two different sets of orbitals and orbital energies, as indicated in Figure 1. The energy difference between the spin-up and spin-down versions of an orbital is the "exchange splitting." The exchange splitting of the orbitals serves to

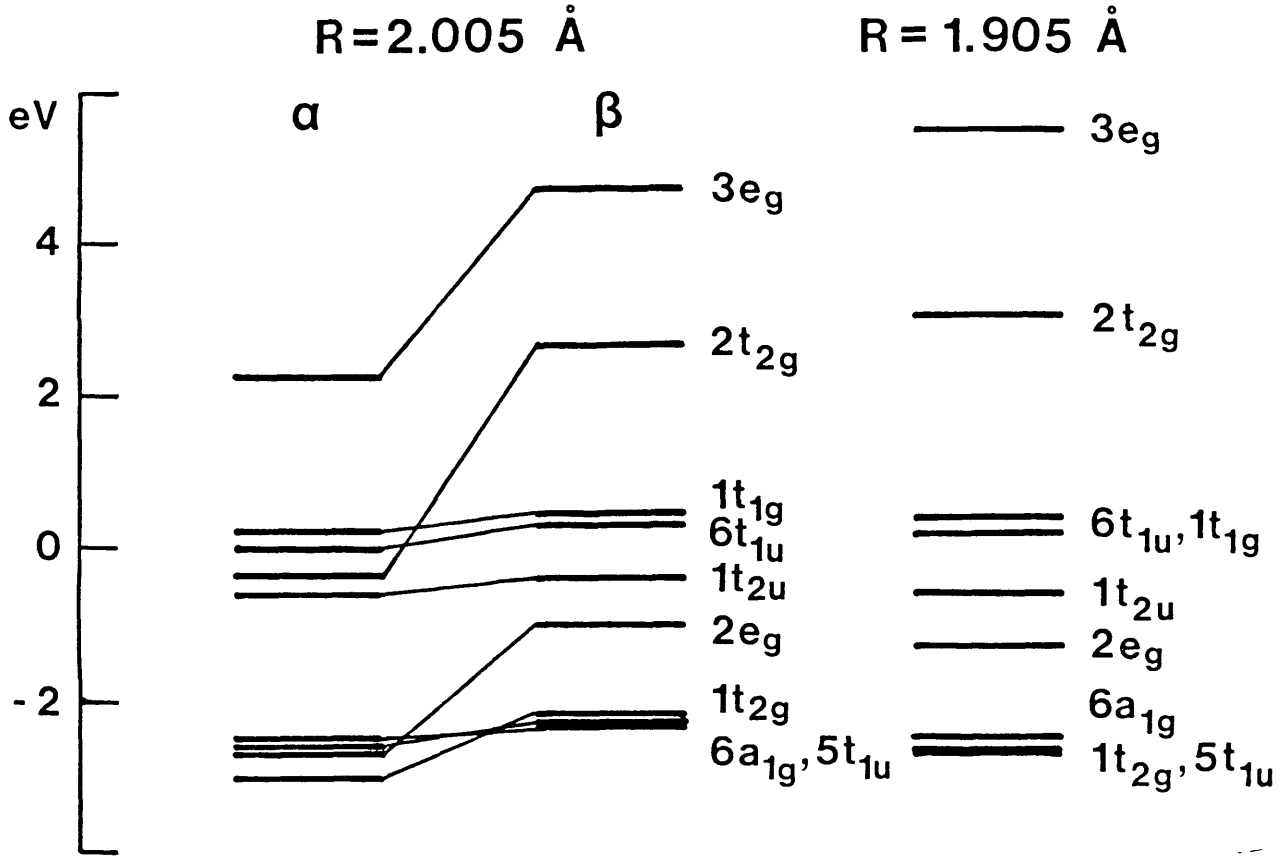


Figure 1: Calculated molecular orbital diagrams for $(CoO_6)^{9-}$ clusters with Co-O bond lengths of 1.905 and 2.005 A. At the larger bond length, the Co^{3+} ion is in the high-spin state with four unpaired electrons. The latter induce a spin-polarization of the molecular orbitals.

stabilize the majority spin electrons, in accordance with Hund's rules. In contrast, the $(CoO_6)^{9-}$ cluster with a Co-O distance of 1.905Å is found to have the low-spin (Ms = 0) configuration in its ground state. In this state, the numbers of spin-up and spin-down electrons are equal and both types of electrons experience the same potential. As such, there is no spin-polarization and no exchange stabilization energy. Note that the different spin states occuring at the different Co-O distances is consistent with the Shannon and Prewitt ionic radii for high- and low-spin Co^{3+}.

The orbitals shown in Figure 1 are labelled according to their associated irreducible representations of the O_h point group. The orbitals may be pictured as resulting from the overlap of O 2p atomic orbitals with the Co 3d, 4s and 4p atomic orbitals. The t_{2g} and e_g orbitals are π and σ-interactions, respectively, between the Co 3d and O 2p orbitals. The t_{1u} orbitals are σ,π-interactions between the Co 4p and the O 2p orbitals. The a_{1g} orbital is the Co 4s - O 2p σ-bonding interaction. Finally, the t_{1g} and t_{2u} orbitals are non-bonding combinations of O 2p atomic orbitals.

The $2t_{2g}$ and $3e_g$ orbitals are the antibonding versions of the $1t_{2g}$ and $2e_g$ bonding orbitals. If there were no Co-O covalency, the $2t_{2g}$ and $3e_g$ would be the pure Co 3d atomic orbitals or the "crystal field orbitals." The exchange splittings of these orbitals can be related to the "pairing energy" of crystal field theory. The crystal field theory parameter Δ or 10Dq is the $3e_g$ - $2t_{2g}$ orbital energy separation in the spin-restricted configuration $2t_{2g}^{3.5}\ e_g^{2.5}$.

The nature of the Co-O bond.

In the $(CoO_6)^{9-}$ clusters, electronic charge is donated to the Co^{3+} centers by the O^{2-} anions. The net number of electrons donated to the Co^{3+} center by each type of orbital interaction is given in Table 1. In both

Table 1: Electronic Charge Donated to Co atoms in $(CoO_6)^{9-}$ Clusters

	High-Spin Co^{3+} R(Co-O) = 2.005 A		Low-Spin Co^{3+} R(Co-O) = 1.905 A
	α-Spin	β-Spin	
t_{2g} (π)	-0.290	-0.250	-0.184
e_g (σ)	-0.020	-0.619	-1.160
a_{1g} (σ)	-0.126	-0.116	-0.205
t_{1u} (σ,π)	-0.215	-0.215	-0.293
Total Charge	-0.651	-1.200	-1.842
Net Co Charge	+1.185		+1.158

clusters, the effective charge on the Co atom is estimated to be about +1.2. Note, therefore, that the degree of covalency in each cluster is about the same. On the other hand, the nature of the Co-O covalent interaction is quite different in each cluster. In the larger $(CoO_6)^{9-}$ cluster (R(Co-O) = 2.005), the Co 4s - O 2p (-bonds of a_{1g} symmetry) and Co 4p - O 2p (, -bonds of t_{1u} symmetry) interactions account for about half of the Co - O bonding covalency. There is also a substantial (0.54 electrons) amount of charge donated to the Co center by the Co 3d - O 2p -bonding (t_{2g}) interaction. In the smaller $(CoO_6)^{9-}$ cluster (R(Co-O) = 1.905), however, most of the electronic charge donated to the Co atom is through the Co 3d - O 2p -bonding (e_g) interaction. Hence the bonding in the low-spin $(CoO_6)^9$ cluster is much more directional. This illusrates an interesting aspect of chemical bonding that appears to be applicable to a variety of other systems; namely, that different orbital interactions are important over different metal-ligand bond distances. The Co 4s and 4p orbitals have a larger radial extent than the Co 3d orbital. Accordingly, the Co 4s-O 2p and Co 4p-O 2p bonding interactions are important when the Co-O bond distance is large. At smaller Co-O bond distances, however, the more short-range Co 3d-O 2p -bonding interaction dominates. Note, however, that the Co(3d)-O(2p) e_g -bonding interaction is strongly promoted by the high-spin to low-spin transition since the latter depopulates the $3e_g$ -antibonding orbitals.

The high-spin $(CoO_6)^{9-}$ cluster is isoelectronic to the high-spin Fe^{2+} centered $(FeO_6)^{10-}$ cluster. Comparing the electronic structures of these clusters to each other may shed some insight as to why Co^{3+} is much less stable to a high-spin to low-spin transition than is Fe^{2+}. Because the formal charge of the Co^{3+} cation is greater than that of the Fe^{2+} cation,

the Co-O bond is more covalent than the Fe-O bond. The greater covalency increases the delocalization of the $2t_{2g}$ electrons onto the ligands which, in turn, decreases the exchange splitting of the $2t_{2g}$ orbitals in $(CoO_6)^{9-}$ relative to that found in $(FeO_6)^{10-}$. In the Co cluster, the $2t_{2g}$ exchange splitting is 2.95 eV while in an Fe cluster (chapter 4) it is found to be 3.84 eV. Because the Co-O bond is more covalent than the Fe-O bond, there is more e_g σ-bonding in $(CoO_6)^{9-}$ than in $(FeO_6)^{10-}$. The e_g σ-bonding interaction raises the energy of the $3e_g$ σ-antibonding orbitals and, hence, increases the $3e_g$-$2t_{2g}$ orbital separation. The latter energy difference can be related to the 10Dq parameter of crystal field theory. The two effects of covalency serve to give a much smaller energy separation between the $3e_g^{\alpha}$ and $2t_{2g}^{\beta}$ orbitals in high-spin $(CoO_6)^{9-}$ (0.4 eV) than that found in high-spin $(FeO_6)^{10-}$ (2.3 eV); since the high-spin to low-spin transition involves promoting the two $3e_g^{\alpha}$ electrons to the $2t_{2g}^{\beta}$ orbital, the stability of high-spin Co^{3+} relative to low-spin Co^{3+} is much smaller than the stability of high-spin Fe^{2+} relative to low-spin Fe^{2+}.

Application to the uptake of Co in marine ferromanganese nodules

High-spin Co^{3+} should be very soluble in iron(III) oxides given that its ionic radius is similar to that of Fe^{3+}. On the other hand, low-spin Co^{3+} should be more soluble in manganese(IV) oxides than in iron(III) oxides since its ionic radius is similar to that of Mn^{4+}. With this in mind, it appears that the main factor governing the uptake and partitioning of Co^{3+} in ferromanganese nodules is the relative stability of high- versus low-spin Co^{3+}.

The $(CoO_6)^9$ molecular orbital diagrams given in Figure 1 show that, relative to the O 2p non-bonding orbitals, the high-spin $(CoO_6)^9$ cluster is strongly stabilized by the exchange energy. In the context of the simple cluster approach, one would expect the high spin $(CoO_6)^9$ cluster to be the stable ground-state when considering the orbital energies relative to those of the non-bonding orbitals. The low-spin $(CoO_6)^9$ cluster, however, is also stabilized by the greater electrostatic energy resulting from the shorter Co-O bond. Since nearly all Co^{3+} complexes are low-spin, the gain in the electrostatic stabilization energy resulting from the decrease in the bond length must usually be greater than the loss in the exchange stabilization energy; moreover, it is this electrostatic component to the total energy which must be responsible for the greater stability of low-spin Co^{3+} over high-spin Co^{3+}.

An interesting possibility arises, however, if the exchange stabilization energy of high-spin $(CoO_6)^9$ is comparable to the electrostaic stabilization energy of low-spin $(CoO_6)^9$. This situation might allow for the possibility of both high-spin and low-spin Co^{3+} to exist in oxides under the PT conditions of marine sediments. Several lines of experimental evidence suggest that this may be the case. Chanavas et al. (1971) found, using crystal structure data, that Co_2O_3 is in the high-spin state at one atmosphere pressure. Madhusudan et al. (1980) investigated the magnetic susceptibilities of $Ln[CoO_3]$ (where Ln = Pr, Nd, Tb, Dy, and Yb) and found that these phases exhibit low-spin → high-spin transitions of Co^{3+} over the temperature range 200° → 800°K; hence, several of these phases contained high-spin Co^{3+} at STP. It was also found that the spin-state transition

temperature increased with decreasing unit cell volume (as governed by the size of the rare-earth ion). This, in turn, supports the notion that the electrostatic component of the total energy is what controls the relative stabilities of high- and low-spin Co^{3+}.

The relative stability of high- versus low-spin Co^{3+} in iron(III) oxides is difficult to predic since the Co^{3+}-O bond length for Co sites in iron(III) oxides is unknown. For high-spin Co^{3+} in iron oxides, the Co-O bond length should be near 2.00 A. For low-spin Co^{3+} in iron oxides, the Co-O bond length will be between 1.905 and 1.96 A. Above 1.96 A, Co^{3+} is predicted to undergo a low-spin to high-spin transition. Given that a fairly small change in bond length will induce a low-spin to high-spin transition, it seems plausible that both high-spin and low-spin Co^{3+} may coexist in thermal equilibrium in iron(III) oxides. One possible explanation, therefore, for the observed Co-Fe correlations in ferromanganese nodules is that high-spin Co^{3+}, in addition to low-spin Co^{3+}, is substituting for Fe^{3+} in the FeOOH phases. One way to investigate whether this occurs is through x-ray photoelectron or ESCA spectroscopy. Generally, however, valence states of Co are distinguished by the multiplet splitting of the Co 3s line and the $2p_{1/2}$ - $2p_{3/2}$ separation. It is always assumed that Co^{3+} is in the low-spin state so that no multiplet splitting of the 3s line will be present. The observation of 3s multiplet splittings are taken to indicate Co^{2+} which is always high-spin. Using this approach, high-spin Co^{3+}, if present, would be incorrectly assigned to be Co^{2+}.

One other explanation for the observed Co-Fe correlations is that Co might enter the FeOOH phase as Co^{2+} with charge balance being maintained by protonating an O^{2-} anion for each Co^{2+} cation.

References

Chenavas, J., J. C. Joubert, and M. Marezio (1971) Low-spin→high spin state transition in high pressure cobalt sesquioxide. Solid State Communications, 9, 1057-1060.

Murray, J. W. and J. G. Dillard (1979) The oxidation of Co^{2+} adsorbed on manganese dioxide. Geochimica et Cosmochimica Acta, 43, 781-787.

Murray, J. W. and P. G. Brewer (1977) Mechanisms of removal of manganese, iron, and other trace metals from sea water. In G. P. Glasby, ed., Marine Manganese Deposts, Elsevier: Amsterdam, 291-325.

Glasby, G. P. and T. Thyssen (1982) Control of the mineralogy and composition of marine manganese nodules by the supply of divalent transition metal ions. Nues Jharbuch Mineral....?, 145, 291-307.

Burns, R. G. (1976) The uptake of cobalt into ferromanganese nodules, soils, and synthetic manganese(IV) oxides. Geochimica et Cosmochimica Acta, 40, 90-102.

Halbach, P., R. Giovanoli, and D. von Borstel (1982) Geochemical processes controlling the relationship between Co, Mn, and Fe in early diagenetic deep-sea nodules. Earth and Planetary Science Letters, 60, 226-236.

JOURNAL OF GEOPHYSICAL RESEARCH, VOL. 87, NO. B12, PAGES 10,169-10,180, NOVEMBER 30, 1982

SPECTRAL CHARACTERISTICS OF THE IRON OXIDES WITH APPLICATION TO THE MARTIAN BRIGHT REGION MINERALOGY

David M. Sherman, Roger G. Burns, and Virginia Mee Burns

Department of Earth and Planetary Sciences, Massachusetts Institute of Technology
Cambridge, Massachusetts 02139

Abstract. In an effort to determine the nature and significance of the iron oxide mineralogy on Mars, reflectance spectra of eight polymorphs of FeOOH and Fe_2O_3 are presented together with additional data on these materials. The Kebulka-Munk theory is used to qualitatively constrain the effect of other components that might interfere with iron oxide absorption features. Although the wavelength range 0.4-1.0 μm is potentially the most diagnostic spectral region for delineating the iron oxide phases, the effect of temperature complicates the identification of a given Fe^{3+} phase based on the position of the $^6A_1 \rightarrow {}^4T_1$ absorption feature. The Fe^{3+} crystal field transitions are spin forbidden, but most of the iron oxide polymorphs exhibit anomalously intense crystal field absorption features resulting from magnetic coupling between adjacent FeO_6 octahedra. The resulting deviations from observed remote sensed reflectance spectra of Mars may provide a basis for the exclusion of many iron oxide phases as significant components of the Martian Fe^{3+} mineralogy. Comparison with the visible region spectra of Martian bright regions suggest that the predominant Fe^{3+}-bearing phase may be a magnetically disordered material. Possible candidates include amorphous gels, some ferric sulphates, and other minerals in which Fe^{3+} ions in the crystal structure are not magnetically coupled.

Introduction

The red color of Mars has long been attributed to the occurrence of iron oxides on its surface [for example, Sagan et al., 1965; Hovis, 1965; Binder and Jones, 1972]. On the earth, a number of polymorphs of FeOOH and Fe_2O_3 are known (Table 1), and considerable controversy has arisen over which, if any, of these phases are present in the Martian soil. Because each of these phases has a distinctive formation pathway both in the laboratory and in the natural environment, knowledge of the predominant iron oxide phase present on Mars could provide considerable insight into the geochemical processes occurring on the planet's surface.

The Viking X ray fluorescence experiment [Toulmin, et al., 1977] demonstrated that the iron contents in the soil at the two Viking Lander sites are very high (ca. 18 wt % as Fe_2O_3). The Viking magnetic properties experiment demonstrated the presence of between 1 and 7% magnetic material in the soil at the Viking lander sites [Hargraves et al., 1979]. This was interpreted to be maghemite, although other minerals (magnetite, feroxyhyte, and perhaps ferrihydrite) are just as likely to be present within the available constraints. Confirmation that a sizable fraction of the regolith iron is in the ferric state is provided by earth-based remote sensed spectra of the Martian bright and dark regions [McCord and Adams, 1969; Singer et al., 1979]. Figure 1 is an average spectrum of the Martian bright regions [Singer, et al., 1979]. The spectra of Mars characteristically exhibit several features attributable to Fe^{3+} crystal field transitions: a weak absorption feature centered at about 0.87 μm ($^6A_1 \rightarrow {}^4T_1$), a slope change near 0.64 μm ($^6A_1 \rightarrow {}^4T_2$), and a second slope change at about 0.53 μm ($^6A_1 \rightarrow {}^4E$, $^4A_1$). The latter two features are superimposed on a low energy oxygen to metal charge transfer absorption edge which is typical of ferric-bearing minerals. To date, however, the number of mineralogical data that have been extracted from the earth-based remote sensed spectra of Mars has been limited. Much of this is attributable to the small data base available for relevant Martian candidate materials. We hope to diminish this gap by providing spectra of several iron oxide polymorphs together with some interpretations on the relationships between the structure, the magnetochemistry, and the spectral characteristics of the different phases. In addition, the effect of temperature on the Fe^{3+} crystal field spectra is examined since this has significant effects on the position of the absorption features and may complicate the identification of a given Fe^{3+} phase based on the spectral band positions.

For purposes of later discussion, it is worthwhile to outline the theory of diffuse reflectance [Wendlendt and Hecht, 1966; Kortum, 1969]. The spectra shown in this study are measurements of the directional-hemispherical reflectance obtained using an integrating sphere. As such, the Kebulka-Munk theory should be an adequate formalism for making qualitative arguments. Clark and Roush [1982], however, have discussed the shortcomings of Kebulka-Munk theory when applied to vigorous quantitative interpretation of planetary spectra. For an infinitely thick layer (> 2 mm) the diffuse reflectance is given by

$$R = \frac{(1-(k/(k+2s))^{1/2}}{(1+(k/(k+2s))^{1/2}}$$

where k is the absorption coefficient and s is the scattering coefficient. The absorption coefficient is the same quantity occurring in the Beer-Lambert law $T = e^{-kd}$ where T is the transmittance and d is the path length. We define the optical depth as being 1/k, i.e., the layer thickness required for the transmittance to

Copyright 1982 by the American Geophysical Union.

Paper number 2B0592.
0148-0227/82/002B-0592$05.00

TABLE 1. Information for Selected Iron Oxides and Oxide Hydroxides

	Formula	Crystal Class (Space Group)	Cell Parameters (A)	Structure Type	Magnetic Data*
Magnetite	Fe_3O_4	cubic (Fd3m)	a_o = 8.391	spinel	ferrimagnetic; T_c = 848°K; J_s = 92.5 emu/g
Hematite	α-Fe_2O_3	hexagonal (R3c)	a_o = 5.04; c_o = 13.77	corundum	antiferromagnetic; T_N = 958°K
Maghemite	γ-Fe_2O_3	cubic ($P4_132$) or tetragonal ($P4_1$)	a_o = 8.32 or a_o = 8.34; c_o = 25.02	defect spinel	ferrimagnetic; T_c > 725°K; J_s = 81.5 emu/g
Goethite	α-FeOOH	orthorhombic (Pbnm)	a_o = 4.65; b_o = 10.02; c_o = 3.04	diaspore (ramsdellite)	antiferromagnetic; T_N = 393°K
Akaganeite	β-FeOOH	tetragonal (I4/m)	a_o = 10.48; c_o = 3.028	hollandite	weakly ferrimagnetic-paramagnetic; T_c = 290-300°K
Lepidocrocite	γ-FeOOH	orthorhombic (Amam)	a_o = 3.88; b_o = 12.54; c_o = 3.07	boehmite	paramagnetic; T_N = 73°K
Feroxyhyte	δ-FeOOH	hexagonal	a_o = 2.93; c_o = 4.60	disordered brucite	antiferromagnetic-ferrimagnetic; T_c > 400°K; J_s = 5-25 emu/g
Ferrihydrite	$5Fe_2O_3.9H_2O$ or $Fe_2O_3.2FeOOH.2{\cdot}6H_2O$	hexagonal	a_o = 5.08; c_o = 9.4	unknown	antiferromagnetic-ferrimagnetic; T_N ≈ 450°K
Amakinite	$Fe(OH)_2$	hexagonal P3m1	a_o = 3.46; c_o = 4.85	brucite	paramagnetic

* Magnetic state at room temperature; T_N, T_c are Neel and Curie temperatures; J_s are saturation magnetizations.

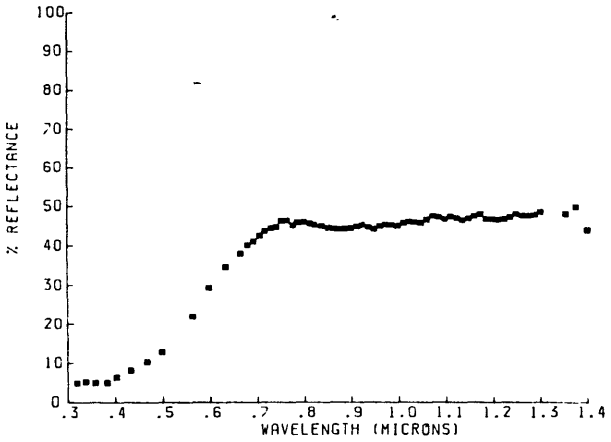


Fig. 1. Average bright region spectrum of Mars [Singer et al., 1979]. Fe^{3+} features are the absorption edge below 0.7 μm, the $^6A_1 \rightarrow {}^4T_1$ band at 0.87 μm, the $^6A_1 \rightarrow {}^4T_2$ slope change at ca. 0.63 μm and the $^6A_1 \rightarrow {}^4A_1$, ^4E slope change at about 0.5 μm.

be reduced by a factor e. The scattering coefficient is a function of the physical state of the material and varies with particle size and may also be a function of wavelength. In general, $s \propto 1/d_{rms}$ where d_{rms} is the mean particle size.

A useful quantity is the Kebulka-Munk function defined as

$$F(R) = \frac{(1-R)^2}{2R} = \frac{k}{s}$$

Using this quantity, one may relate reflectance spectra to transmittance measurements [e.g., Mao and Bell, 1974; Marusak et al., 1979].

Experimental

Both natural and synthetic samples were used, and when appropriate, synthesis procedures are described below. Identities of samples were confirmed using X ray diffraction techniques. Additional characterization was achieved using Mossbauer spectroscopy at 298°K and 77°K, transmission electron microscopy, and single area electron diffraction. Reflectance spectra were obtained using a Cary 17 spectrophotometer with a diffuse reflectance accessory utilizing an integrating sphere. Spectra were referenced against a reflectance standard of smoked MgO in a hermetically sealed holder [Osborne et al., 1978]. Spectrally matched Pyrex slides covered both the MgO standard and the sample holders. The usable working range was from 0.35 to 2.15 μm with a reproducibility better than 1.0%. A 500-W tungsten lamp was used which heated the interior of the integrating sphere to 30°C. As such, 'room temperature' spectra refer to this temperature. Low temperature spectra were obtained by mounting the sample in a copper jacket-cold finger assembly which was placed in a tank of liquid nitrogen. The equilibration temperature of the sample using this apparatus was -10°C.

Results and Discussion

Characteristics of Specific Polymorphs

Goethite (α-FeOOH). Goethite forms under a wide range of conditions. In general, it results from the slow oxidation of Fe^{2+} or the slow hydrolysis of Fe^{3+} in dilute solutions (see, for example, Murray [1979]; Chukhrov et al. [1973a]). Apparently, these conditions are necessary to give an ordered arrangement of Fe^{3+} and OH^- ions in the crystal structure which consists of double chains of edge sharing $[FeO_6]$ octahedra extending along the c axis. Each $[FeO_6]$ octahedron shares edges with four adjacent octahedra and shares corners through bridging oxygens with two $[FeO_6]$ octahedra belonging respectively to overlying and underlying double chains. Some representative spectra of synthetic and natural goethite samples are shown in Figure 2. The synthetic samples exhibit the $^6A_1 \rightarrow {}^4T_1$ band at 0.93 μm while the natural samples show this band centered at 0.91 μm. The $^6A_1 \rightarrow {}^4T_1$ and $^6A_1 \rightarrow {}^4A_1$, ^4E bands are fairly well separated in the spectrum of goethite, and it is usually possible to resolve a well-defined $^6A_1 \rightarrow {}^4T_2$ feature centered at 0.64 μm. Sample α-2, which was recovered from a deep sea Antarctic fracture zone dredge haul, however, contains about 10 wt % SiO_2, and this may be responsible for the absence of a well-defined $^6A_1 \rightarrow {}^4T_2$ band. Both α-1 and α-2 gave sharp, well-defined X ray powder diffraction patterns, indicating that they are well crystallized. The Transmission Electron Microscopy (TEM) study showed no distinct morphology, but uniform grain size. Other goethite samples we have studied indicate that the presence of a well-defined $^6A_1 \rightarrow {}^4T_2$ band is independent of the crystallinity of the material.

Hematite (α-Fe_2O_3). In terrestrial supergene systems, hematite forms by the transformation of ferrihydrite [Chukhrov et al., 1976]. It is also a product of the oxidation of most ferromagnesian silicate minerals during the weathering of basalts [Haggarty, 1976]. At elevated temperatures, goethite will dehydrate to hematite, but this transformation is kinetically unfeasible at, or below, 298°K [Langmuir, 1971; Chukhrov et al., 1976]. Figure 3 is the spectra of hematite samples H-1 and H-2. H-1 is a

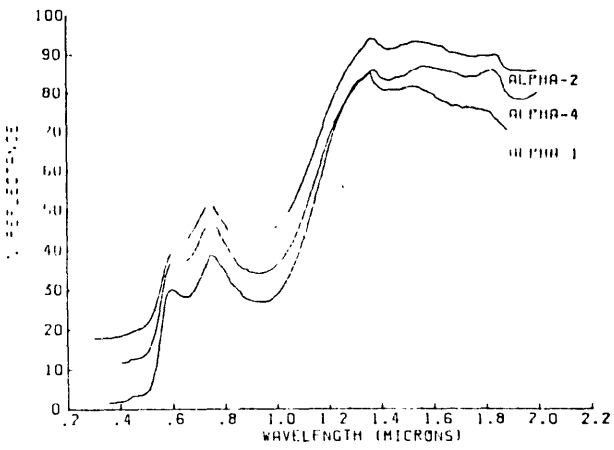


Fig. 2. Diffuse reflectance spectra of natural and synthetic goethites.

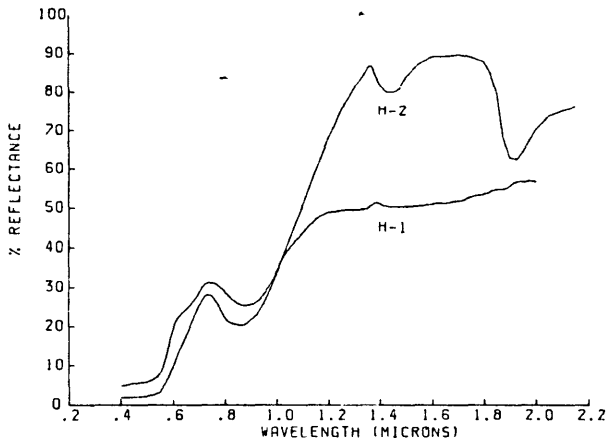


Fig. 3. Diffuse reflectance spectra of natural and synthetic hematites. Sample H-1 is from Cumberland Moor, England. Sample H-2 was synthesized by thermal dehydration of goethite sample Alpha-4.

natural sample from Cumberland Moor, England, while H-2 was prepared by thermal dehydration of goethite sample α-4. Both samples yield six-line hyperfine patterns in their Mossbauer spectra at 298°K indicating a crystallite size >> 130 Å [Suzdalev, 1971]. The $^6A_1 \rightarrow {}^4T_1$ band is centered at 0.88 μm in sample H-1 and at 0.86 μm in sample H-2. The $^6A_1 \rightarrow {}^4T_2$ feature is a slope change on the visible region absorption edge. The reflectance is nearly flat from the UV to about 0.53 μm because of the intense $^6A_1 \rightarrow {}^4A_1$, ^4E feature. The presence of adsorbed water is evidenced in sample H-2 by the hydroxyl bands at 1.4 and 1.9 μm.

Akaganeite (β-FeOOH). Akaganeite results from hydrolysis of Fe^{3+} in Cl^- and F^- bearing solutions; its formation requires one of these ions to be present [Murray, 1979]. The reflectance spectrum of a synthetic akaganeite is shown in Figure 4. This sample was prepared by hydrolysis of $FeCl_3$ at 60°C. The $^6A_1 \rightarrow {}^4T_1$ band is centered at 0.908 μm and is very well defined. The other crystal field bands appear as slope changes on the absorption edge. The X ray and electron diffraction data together with examination by transmission electron microscopy showed that these samples are very well crystallized rods that are uniform in size, about 1500 Å long, which is typical of akaganeite.

Lepidocrocite (γ-FeOOH). Lepidocrocite, the orange polymorph of FeOOH, forms via the moderately fast oxidation of Fe^{2+} in neutral to slightly basic solutions to give green rusts and green solution complexes which undergo further oxidation to give either lepidocrocite or magnetite [Bernal, et al., 1959]. The reflectance spectrum of a synthetic lepidocrocite is shown in Figure 5. The $^6A_1 \rightarrow {}^4T_1$ band is centered at 0.96 μm and a fairly well defined $^6A_1 \rightarrow {}^4T_2$ feature appears at about 0.65 μm. This sample was synthesized by aerial oxidation of a $FeCl_2$ solution at a pH of 6-7. The X ray diffraction pattern of this sample was extremely well-defined, implying a high degree of crystallinity.

Feroxyhyte and δ-FeOOH. The δ-FeOOH phases result from the violent oxidation of $Fe(OH)_2$ (amakinite) in very basic solutions. The naturally occurring δ'-FeOOH (feroxyhyte) results from oxidation under more moderate conditions [Chukhrov et al., 1977; Carlson and Schwertmann, 1980]. By analogy with goethite, the structure of δ-FeOOH is based on a hexagonal close-packed lattice of O^{2-} and OH^- ions, but, unlike goethite, the OH^- and octahedrally coordinated Fe^{3+} ions are disordered so that edge-sharing $[FeO_6]$ arrays are random in δ-FeOOH. The relation between the nonmagnetic, naturally occurring feroxyhyte and the ferrimagnetic δ-FeOOH has not been worked out. It has been shown that the saturization magnetism of the ferrimagnetic δ-FeOOH phase increases dramatically when diamagnetic impurities (Mg^{2+}, Ca^{2+}) are present [Muller et al., 1980]. Sample δ-1 is a synthetic δ-FeOOH produced by oxidizing an $Fe(OH)_2$ precipitate by hydrogen peroxide at pH = 12. The reflectance spectrum of this sample is shown in Figure 6. The $^6A_1 \rightarrow {}^4T_1$ band is centered at 0.88 μm with no well defined $^6A_1 \rightarrow {}^4T_2$ and $^6A_1 \rightarrow {}^4A_1$, ^4E features. The Mossbauer spectrum at 298°K consists of a superparamagnetic doublet indicating a particle size of the order of 50 Å. The TEM study, however, showed that the crystallites formed aggregates as large as 1.5 μm. Sample δ-2 is a natural feroxyhyte from a Red Sea hydrothermal brine deposit. The reflectance spectrum of this sample is also shown in Figure 5. This sample has a substantial amount of halite present which may account for the higher reflectivity in the reflectance spectrum. The Mossbauer spectrum was identical to that of δ-1, yet a weak hyperfine sextet was also detected which may indicate the presence of goethite impurities.

Maghemite (γ-Fe_2O_3). There appear to be several varieties of maghemite (γ-Fe_2O_3); one form is tetragonal while another is cubic [Bernal et al., 1959]. The cubic and tetragonal forms are unstable intermediate phases usually formed during the oxidation of magnetite. A second formation pathway is the thermal dehydration of lepidocrocite. Reflectance spectra of several maghemite samples, both natural and synthetic, are shown in Figure 7. Maghemites M4-A and M4-B were produced by thermal oxidation of a nonstoichiometric (Fisher reagent)

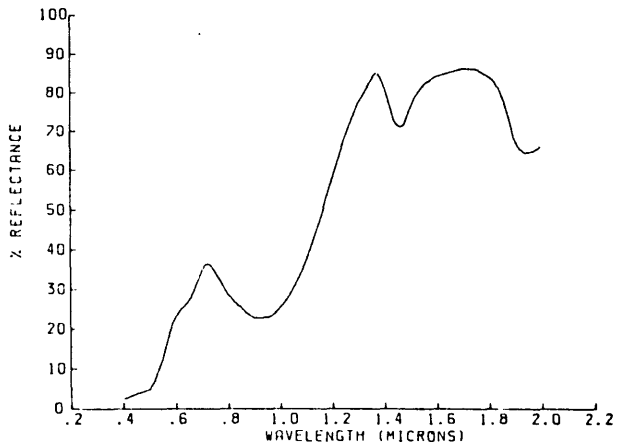


Fig. 4. Diffuse reflectance spectrum of akaganiete.

magnetite [Daniels and Rosencwaig, 1969] for 1 and 5 days, respectively. The 77°K Mossbauer spectra of these samples are identical and show no evidence of a magnetite component [Daniels and Rosencwaig, 1969; Graham et al., 1975]. The X ray patterns confirm the identity of these samples and together with the TEM data indicate that they are well crystallized and occur in clusters of varying particle sizes but most average about 0.58 μm. We attribute the low reflectivity of these samples to the presence of Fe^{2+} and an associated electron delocalization occurring over a finite number of octahedra (i.e., class IIIA intervalence behavior [Robin and Day, 1967]). Note that the more oxidized sample (M-4b) exhibits a higher reflectance. Natural maghemites typically contain Fe^{2+} as 4 to 15% of the total iron [Taylor and Schwertmann, 1974a, b]. An example is sample M-7 which is a natural specimen from the Massachusetts of Technology collection.

All of these samples exhibit a sharp absorption edge with essentially opaque behavior at wavelengths shorter than 0.53 μm. This feature is apparently due to an intense $^6A_1 \rightarrow {}^4A_1$, ^4E band centered near 0.53 μm. The shape and position of the absorption edge were unaffected by the degree of oxidation of the samples and the temperature at which the spectra were taken. Mixing these samples with a nonabsorbing component did not remove the 'band saturation' effect at wavelengths below 0.55 μm. Sample M-5 was produced by thermal dehydration of lepidocrocite and is presumably Fe^{2+} free. This sample was very poorly crystallized and gave only seven very broad lines in the X ray diffraction pattern. The 298°K Mossbauer spectrum showed a hyperfine sextet collapsing to a superparamagnetic doublet--indicative of very fine particle size and poor crystallinity. An apparently identical product was obtained by Giovanoli and Brütsch [1974] by following the same synthesis procedure. The reflectance spectrum shows a very high reflectivity in the near infrared with a fairly well defined $^6A_1 \rightarrow {}^4T_1$ feature centered at 0.93 μm. The spectral characteristics in the visible region are very similar to the magnetite oxidation products (M-4A and M-4B). The water band at 1.9 μm is due to chemically adsorbed water associated with the

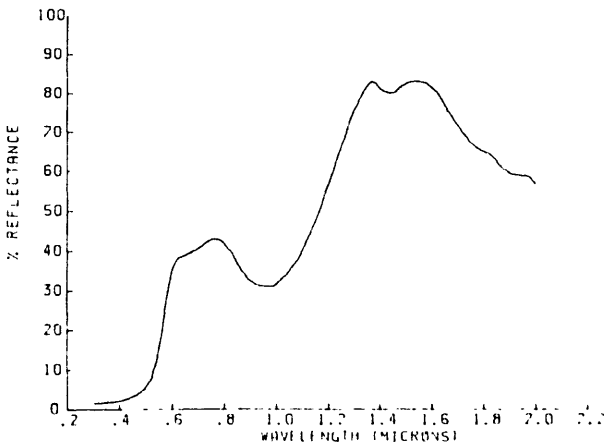


Fig. 5. Diffuse reflectance spectrum of lepidocrocite.

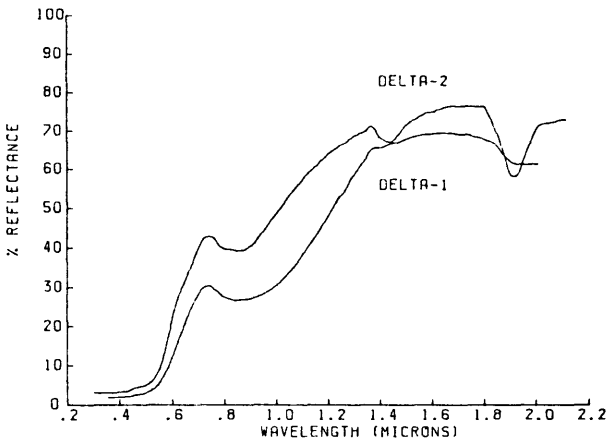


Fig. 6. Diffuse reflectance spectra of δ-FeOOH (sample delta-1). Sample delta 2 is a natural material recovered from a Red Sea metalliferous brine deposit.

ultrafine particle size. We attempted to synthesize an additional 'maghemite' by aerial oxidation of fresh colloidal magnetite. This sample had a diffraction pattern identical to sample M-5 yet the reflectance spectrum (not shown) resembles those of samples M-4A and M-4B.

In summary, the variations in the near infrared spectra of maghemite samples are attributable to electron delocalization associated with incomplete oxidation. The visible region spectral characteristics are fairly constant and appear to be independent of the crystallinity of the material.

Ferrihydrite. Ferrihydrite is similar, if not identical, to the synthetic, X ray amorphous iron hydroxide phase discussed by Towe and Bradley [1967]. Ferrihydrite is not truly amorphous in a crystallographic sense, yet because of its poor crystallinity and frequent ultrafine particle size (<50 Å) the material may give few, if any, diffraction lines. Although the crystal structure of ferrihydrite is unknown, it appears to contain OH^- ions [Russell, 1979] and octahedral Fe^{3+} ions randomly distributed in a hexagonal close-packed oxygen lattice [Okamoto et al., 1972]. Of interest is the observation that coprecipitation of divalent ions with ferrihydrite may yield a ferrimagnetic product [Okamoto and Okamoto, 1977]. The reflectance spectra of two synthetic ferrihydrites are shown in Figure 8. Sample F-1 gave no detectable X ray diffraction pattern after a 24 hour exposure using FeKα radiation. This material exhibits a very similar spectrum to that given by Evans and Adams [1980] and is referred to as an iron hydroxide gel. The $^6A_1 \rightarrow {}^4T_1$ band is centered at about 0.91 μm with no evidence of the other crystal field transitions. Sample F-2 was produced by rapid oxidation of Fe^{2+} at pH = 3-5. This material gave X ray diffraction lines at 1.5 and 2.6 Å. In the reflectance spectrum the $^6A_1 \rightarrow {}^4A_1$, ^4E band is evident at about 0.5 μm while the $^6A_1 \rightarrow {}^4T_1$ is centered at about 0.87 μm.

In terrestrial systems, ferrihydrite is generally formed by the rapid oxidation of weakly complexed Fe^{2+} by iron bacteria [Chukhrov et al., 1973a,b]. Ferrihydrite is the principle iron

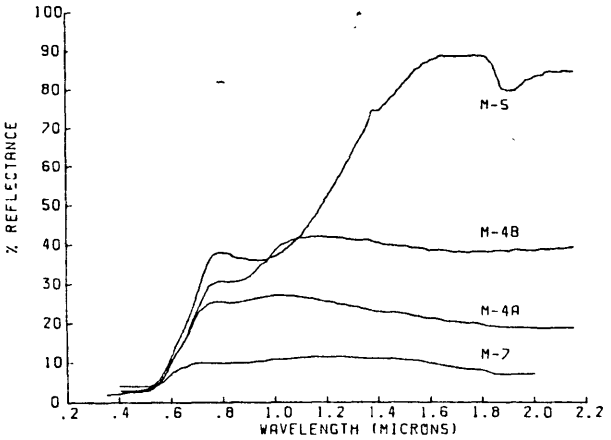


Fig. 7. Diffuse reflectance spectra of natural and synthetic maghemites. The variation in the near infrared reflectance is attributed to electron delocalization associated with incomplete oxidation.

oxide phase resulting from the biogenic alteration of lichen-covered basaltic rocks in Hawaii [Jackson and Keller, 1970]. Abiogenic formation also occurs when acidic $FeSO_4$ solutions are rapidly neutralized by $CaCO_3$ [Chukhrov et al., 1976]. The formation of ferrihydrite is catalyzed by the presence of silica which, in addition, prevents recrystallization and strongly inhibits the transformation of ferrihydrite to hematite or goethite [Carlson and Schwertmann, 1981]. The latter authors have shown that natural and synthetic ferrihydrites formed in the presence of SiO_2 have Si-O-Fe vibrational features in the infrared spectra indicating SiO_2 as a structural constituent. The role of silica in the stabilization of ferrihydrite could imply the existence of a number of naturally occurring iron-silica materials with variable degrees of structural order. Figure 9 shows the reflectance spectrum of a synthetic 'iron silica gel.' This material was prepared by the addition of $FeCl_3$ to a basic (pH = 13) silica saturated solution. The spectrum exhibits a higher reflectance overall (in part, owing to the silica dilution effect), and the $^6A_1 \rightarrow {}^4T_2$ and $^6A_1 \rightarrow {}^4A_1$, ^4E features are very weak. The $^6A_1 \rightarrow {}^4T_1$ band is centered at about 0.91 μm. The Mossbauer spectrum of this material gave only a paramagnetic doublet. Whether this material is a magnetically disordered phase or a colloidal dispersion of superparamagnetic crystallites in the silica matrix is uncertain.

Low temperature spectra. We know of no previous attempts to determine the spectra of iron oxide phases at low temperatures. We have obtained spectra of several phases at -10°C (268°K). These are shown in Figure 10. Although this temperature is well above the range on present-day surfaces of Mars, the low T spectra serve to illustrate the temperature dependence of the position and intensity of the Fe^{3+} crystal field bands. Note that the room temperature spectra were run at 36°C (314°K) and the difference between room and low temperature spectra reflects a temperature decrease of 46°C. The broad $^6A_1 \rightarrow {}^4T_1$ band exhibits a fairly pronounced shift (0.03 μm) to shorter wavelengths while the more narrow $^6A_1 \rightarrow {}^4T_2$ and $^6A_1 \rightarrow {}^4A_1$, ^4E transitions show little change in position. The $^6A_1 \rightarrow {}^4T_1$ band shifted from 0.88 to 0.85 μm in feroxyhyte, from 0.88 to 0.84 μm in hematite, and from 0.93 to 0.90 μm in goethite. The positions of $^6A_1 \rightarrow {}^4T_2$ and $^6A_1 \rightarrow {}^4A_1$, ^4E features were unaffected, as were the position and slope of the absorption edge in the visible region. As a consequence of the shift in the position of the $^6A_1 \rightarrow {}^4T_1$ band, the position of the local reflectance maximum near 0.75 μm also shifted to shorter wavelengths. The temperature dependence of the band position is due to depopulation of the excited vibrational states in the ground ($^6A_1$) electronic state. Transitions from excited vibrational states ('hot bands'), which occur at the long wavelength side of the band maximum, are lowered in intensity with a consequent shift of the band maximum.

Application to Mars

All of the reflectance spectra of the pure iron oxide phases exhibit several deviations from the earth-based remote sensing spectra of both the Martian bright and dark regions. First, the reflectance of the iron oxides continues to rise in the near infrared, reaching a maximum reflectance of about 0.8 (except in the case of Fe^{2+}-bearing maghemite). Second, the slope of the absorption edge from the UV to 0.75 μm has a pronounced slope change at about 0.53 μm due to the intense $^6A_1 \rightarrow {}^4A_1$, ^4E crystal field band. For several phases, this crystal field band is intense enough to cause a flat opaque behavior up to about 0.51 μm. The spectra of pure goethite samples, and to a lesser extent γ-FeOOH, exhibit a very well defined $^6A_1 \rightarrow {}^4T_2$ feature at 0.68 μm. This feature appears as a subtle slope change in the spectra of Mars. Finally, the intensity (or contrast) of the band near 0.9 μm is significantly greater in the iron oxide spectra than in the spectra of the Martian bright regions.

The high reflectance of iron oxides in the near infrared (1.3-2.2 μm) implies that these phases are weakly absorbing in this spectral region. As such, these materials will behave as spectrally neutral components relative to any phase which has higher absorption coefficient in this wavelength range. Of course, the ferric

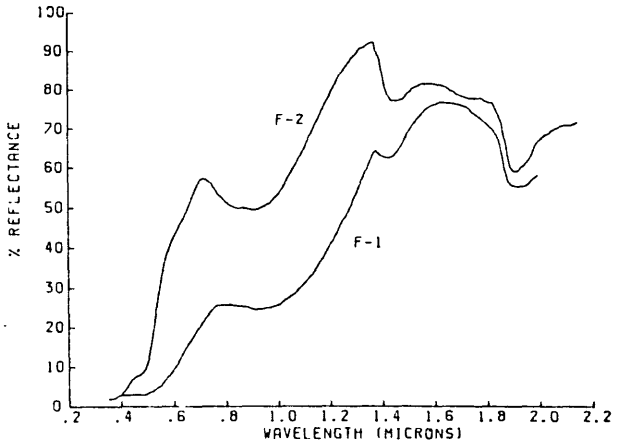


Fig. 8. Diffuse reflectance spectra of synthetic ferrihydrite.

oxides do exhibit some absorption in this region (R = 0.8-0.9) and, if present in sufficient quantity, will begin to have some effect on the spectrum of a mixture [Singer, 1981]. However, the Fe_2O_3 content of the Martian soil is at most 18-20% [Toulmin et al., 1977]. An important aspect of iron oxides is that they tend to crystallize with submicron particle sizes. Mixtures of iron oxides with most other minerals are frequently best described using a model which considers the iron oxides as coating the other materials. In the near infrared, the spectra of ferric oxide coatings are dominated by the spectrum of the substrate material. Figures 11 and 12 show the spectra of mixtures between hematite (5%) and augite (120 μm and 10-75 μm, respectively). In both cases, the iron oxide was observed to form a uniform coating on the pyroxene grains. In the wavelength region above 0.6 μm, the spectra are dominated by the pyroxene substrate. This effect can be generalized using the Kebulka-Munk relation [Wendlandt and Hecht, 1966]

$$R = \frac{1 - R_g\,(a - b\,\mathrm{ctgh}(bsd))}{a - R_g + b\,\mathrm{ctgh}(bsd)} \qquad (1)$$

where

R = diffuse reflectance;
R_g = reflectance of substrate;
$a = (s + k)/s$;
$b = (a^2 - 1)^{1/2}$;
d = coating thickness.

If the absorption coefficient (k) of the surface layer is small in comparison to the scattering coefficient (s), then a→1 and b→0 and relation (1) may be expanded in a truncated Taylor series to obtain

$$R \cong R_g\,(1 - sd) + sd$$
$$\cong R_g \qquad (2)$$

The above equality will hold for most of the samples investigated in this study since in the near infrared, k/s is of the order of 0.02. By comparing reflectance spectra with published transmission spectra [e.g., Mao and Bell, 1974] we estimate the scattering coefficient of these samples to be of the order of 10^2-10^3 cm^{-1} which is a reasonable range for particle sizes of the order of 0.1-1.0μm. Hence the product sd (equation 2) for a 0.1-1.0 μm-thick layer will be small, and the final equality (R ≈ Rg) will be a good approximation. The discrepancy between the spectra shown in Figure 12 indicates a coating thickness in the range of 0.8-8.0 μm. It has been suggested [Toulmin et al., 1977] that if iron oxides occur as coatings on Mars, the coating thickness must be less than 0.25μm. Under such conditions, one would expect the near-infrared spectrum of Mars to be nearly identical to the substrate material, at least in spectral shape. The above arguments (equations 1 and 2), however, fail to explain the negative slope in the near infrared spectra of the Martian dark regions. Morris and Neely [1982] attribute this feature to wavelength dependent scattering.

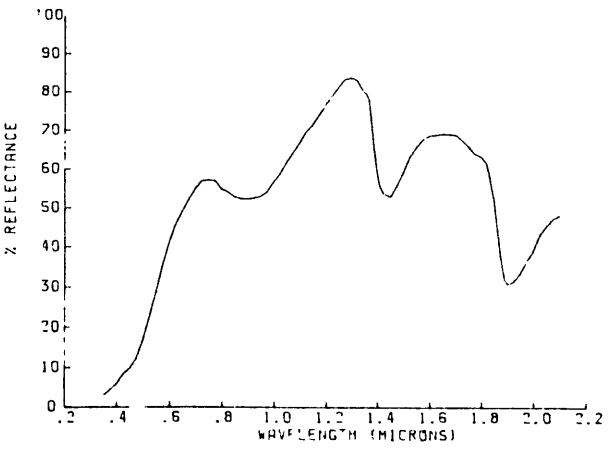


Fig. 9. Diffuse reflectance spectrum of iron-silica gel. Note that the Fe^{3+} crystal field bands are much weaker in intensity than those observed in the spectra of other ferric oxide polymorphs.

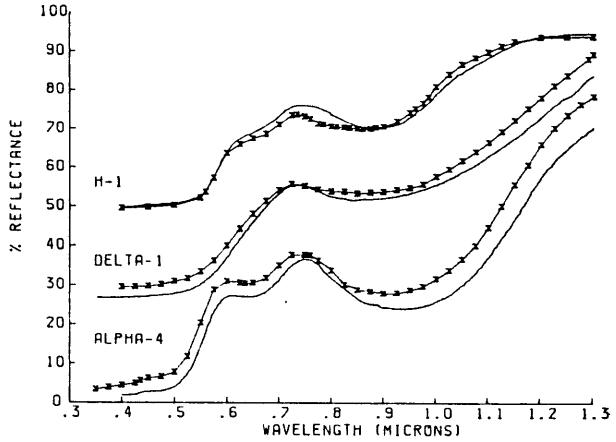


Fig. 10. Temperature dependence of the spectra of goethite (Alpha-4), hematite (H-1), and δ-FeOOH (delta-1). Solid curves are spectra obtained at 314°K; symboled curves are spectra at 268°K. The spectra of a given polymorph have been offset for clarity.

We can consider the case of simple mixtures between iron oxides and materials which are more strongly absorbing in the infrared. Physically, this would correspond to an intimate mixture between iron oxides and other very fine grained materials in which a coating model would not be applicable. Although the diffuse reflectances of two components are not additive, the Kebulka-Munk functions are [Wendlandt and Hecht, 1966; Kortum, 1969]. For a single component we have

$$F(R) = \frac{(1 - R)^2}{2R} = \frac{k}{s} \qquad (3)$$

while for an n-component mixture we can write

$$F(R) = \sum_{i=1}^{n} \frac{k_i X_i}{s_i}$$

where X_i is the fractional area component i. If the particle sizes of the iron oxides are small

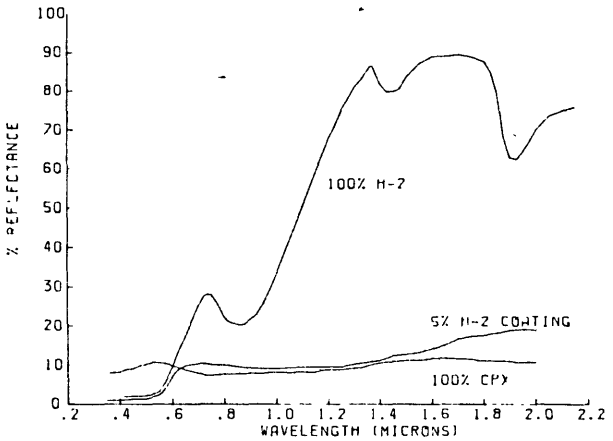


Fig. 11. Spectrum of hematite (sample H-2) coating on coarse-grained (ca. 120 μm) augite. The pyroxene substrate dominates the spectrum in the near infrared. In the visible region, the hematite coating dominates.

(1-10 μm) then the spectral contribution due to the iron oxides will be negligible at wavelengths above 1.0 μm where k/s = 0.02-1.0. Hence for a two-component mixture we may write

$$F(R) = \frac{k_1}{s_1} X_1 + \frac{k_2}{s_2} X_2 \cong \frac{k_2}{s_2} X_2 \qquad (4)$$

where subscript 1 refers to the iron oxide and subscript 2 to the second component. Using relation (2), we can solve for R to obtain

$$R = \frac{1 - (k_2X_2/(k_2X_2 + 2s_2))^{1/2}}{1 + (k_2X_2/(k_2X_2 + 2s_2))^{1/2}} \qquad (5)$$

which simply means that the iron oxide phase serves as a neutral dilutant. The wavelength range over which this approximation is valid depends on how strongly absorbing the second component is. For mixtures between nonabsorbing materials and iron oxides ($k_1/s_1 > k_2/s_2$), the approximation fails, and the Fe oxide spectral features (e.g., the $^6A_1 \rightarrow {}^4T_1$ band) persist. This is demonstrated in the spectra of natural mixtures of iron oxides and clay minerals [Hunt and Ashley, 1979]. For mixtures of iron oxides and strongly absorbing materials, $k_1/s_1 \ll k_2/s_2$. The approximation may be valid over the entire near infrared (0.7-2.2 μm), with the $^6A_1 \rightarrow {}^4T_1$ absorption feature being completely suppressed. Examples are the spectra of ferric oxide-magnetite mixtures given by Morris and Neely [1981]. Depending on the relative grain sizes of the different components, natural mixtures will fall somewhere in between the coating and simple mixture situations. If the fine-grained iron oxides occur with coarse grained primary ferromagnesian silicate minerals, then the coating model is expected to be more applicable while the case of an iron oxide-clay mineral assemblage would best be described as a simple mixture. In either case, we wish to point out that the rise in reflectance to 0.8-1.0 in the near infrared observed in the spectra of pure iron oxide phases is not, by itself, contradictory to these phases being present in significant amounts in the Martian soil. That the spectra of Mars exhibit a nearly uniform reflectance of only 0.4 [Singer et al., 1979] in the near infrared might be explained by either the presence of a strongly absorbing component (magnetite, Fe^{2+}-bearing maghemite or some ferromagnesian silicate minerals) or that the Fe^{3+} phases occur as thin surface coatings on a dark substrate (e.g. basalt). Singer [this issue] has argued that to remove the band contrast of the $^6A_1 \rightarrow {}^4T_1$ feature, the amount of opaque or strongly absorbing material required would lower the overall reflectance to values much below that observed in the bright region spectra of Mars. Although this is true for the case of a dispersed mixture (equation (5)), this is not necessarily true if the iron oxides occur as coatings on other minerals (equation (1) and Figure 12).

In the spectral region below 0.6-1.0 μm, however, the spectra of iron oxides exhibit strong absorption features due to the crystal field transitions and the $O^{2-} \rightarrow Fe^{3+}$ charge transfer absorption edge. Absorption coefficients in this region range from 10^2 to 10^4 cm^{-1} [Mao and Bell, 1974; Marusak et al., 1979]. For the case of an iron oxide coating, we note from (1) that as the absorption coefficient gets large, $a \rightarrow k/s$ and $b \rightarrow a$. Hence $\coth(bsd) \rightarrow \coth(kd)$. If the optical depth (1/k) becomes much less than the coating thickness (e.g., if $d \geq 1.0$ μm) then $\coth(kd)$ approaches unity, and the reflectance approaches that of an infinitely thick layer of iron oxide. Specifically, for the case of hematite, $k \approx 10^5$ cm^{-1} at 0.5 μm [Marusak et al., 1979], and for a 0.1-1.0 μm-thick layer we have $\coth(bsd) = \coth(kd) = 1.3$-$1.0$ at which value the spectrum is dominated by the hematite coating. This is demonstrated in the visible region of the spectra shown in Figs. 11 and 12. Note that both of these spectra constitute a rather extreme example since the augite substrate is strongly absorbing. Iron oxide coatings on less absorbing minerals (e.g., feldspars, low Fe^{2+} olivine and

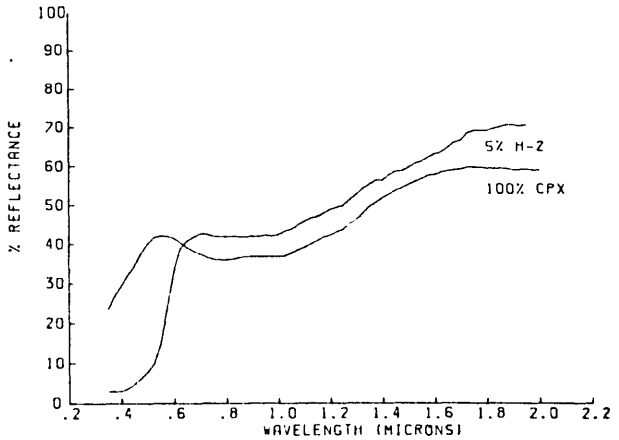


Fig. 12. Spectrum of a mixture of hematite (sample H-2) and fine grained augite (10-75 μm). The coating model (see text) is still applicable. The pyroxene substrate dominates in the near infrared while the hematite coating dominates the visible region spectrum.

pyroxenes) will exhibit spectral signatures with the $^6A_1 \rightarrow {}^4T_1$ band extending even further into the infrared (i.e., 1.3-1.4 μm).

We can also consider the visible region spectral characteristics of a dispersed mixture between iron oxides and other fine grained components. Over the wavelength range 0.4 to 1.3 μm, most Fe^{3+}-free minerals are weakly absorbing [e.g., Hunt and Salisbury, 1970] relative to the iron oxides. Using (5), where subscript 2 now refers to the iron oxide phase, one may estimate the effect of a twentyfold dilution of the iron oxide with another component. At the $^6A_1 \rightarrow {}^4A_1$, ^4E band maximum (ca. 0.5 μm) k/s = 25, and if $X_2 = 1.0$, the diffuse reflectance is 0.03 while for $X_2 = 0.05$ the reflectance is found to be 0.23. At the $^6A_1 \rightarrow {}^4T_1$ band maximum, k/s = 1.1, and a twentyfold dilution changes the reflectance from 0.25 to 0.72. The effect of dilution is to raise the reflectance, yet the spectral contrast between the visible and near infrared is maintained. In particular, dilution of iron oxides fails to remove the band saturation effect at wavelengths below 0.55μm in the spectra of hematite and maghemite. This has also been demonstrated by Singer [this issue] for mixtures of iron oxides and clay minerals.

The strong absorption at wavelengths below 0.6-1.3 μm suggests that this region is the most diagnostic of the nature and presence of iron oxides. Absorption features of these minerals persist not only in laboratory mixtures but also in the spectra of natural materials [Hunt and Ashley, 1979] where small (5%) amounts of goethite and hematite give rise to pronounced, and distinct, spectral signatures.

The visible region spectrum of Mars differs from the spectra of most of the samples investigated here. The primary difference is in the intensity of the $^6A_1 \rightarrow {}^4T_2$ and $^6A_1 \rightarrow {}^4E$, $^4A_1$ bands together with their relative positions. Although the spectra of most of the iron oxide polymorphs have only a poorly defined $^4A_1 \rightarrow {}^4T_2$ absorption feature, the $^6A_1 \rightarrow {}^4A_1$, ^4E transition is usually very intense and tends to persist in the spectra of mixtures containing iron oxide phases. The presence of a large amount of a second strongly absorbing material could have some effect on the visible region spectrum of an iron oxide-bearing mixture, yet we note that before such an effect is realized, the $^6A_1 \rightarrow {}^4T_1$ band in the near infrared is completely masked. In the spectra of Mars, the latter feature is fairly well defined and centered near 0.87 μm. We conclude, therefore, that the visible region absorption spectrum of Mars probably differs little from that of the pure Fe^{3+}-bearing phase present in the Martian soil.

The Fe^{3+} crystal field transitions are all spin-forbidden, and, as such, one would expect only weak crystal field absorption features in the spectra of Fe^{3+}-bearing minerals. In a number of minerals and polynuclear complexes, however, the spin selection rule is relaxed by antiferromagnetic (or ferromagnetic) coupling of spins between Fe^{3+} ions in adjacent octahedral sites [Lohr, 1972; Ferguson et al., 1966; Rossman, 1975, 1976]. The degree of magnetic coupling (magnetic ordering) is dependent upon the metal-metal distance (which can vary with edge-, face-, and corner-sharing arrangements) and the degree of cation ordering among sites. Consequently, the absorption coefficients of crystal field transitions among clay minerals and a number of the iron oxides (strong coupling) are several orders of magnitude greater than those of the same transitions in ferric bearing glasses and certain sulphate minerals (weak coupling).

Even among the iron oxides, one observes a correlation between the degree of magnetic coupling (indicated by the Curie and Neel temperatures) and the intensities of the crystal field absorption features. The absorption coefficient for the $^6A_1 \rightarrow {}^4T_1$ transition in hematite ($T_N = 958°K$) is about 1000 cm^{-1} [Marusak et al., 1979]. The absorption coefficient for the same transition in goethite ($T_N = 393°K$) is 175-350 cm^{-1} [Mao and Bell, 1974]. Both the magnetic and consequent spectral behavior can be rationalized from the crystal structure of these phases: hematite has both edge- and face-sharing FeO_6 octahedra while goethite possesses only edge- and corner-sharing octahedra. The effect of magnetic coupling in particular explains the strong absorption below 0.53 μm in the spectra of hematite and maghemite.

The iron-silica gels appear to have no magnetic ordering, and, as such, we may have an explanation for the spectral characteristics of these and related materials. The disordered iron oxide polymorphs ferrihydrite and feroxyhyte have a lower statistical population of adjacent Fe^{3+} ions, and one would expect these materials to exhibit lower absorption coefficients than the more crystalline phases. A consideration of the former two phases is more complex, however, since they appear to exhibit variable degrees of cation ordering and magnetochemistry. Okamoto et al. [1972] have shown that some ferrihydrites exhibit significant magnetic ordering (presumably resulting from antiferromagnetic super exchange between corner-sharing octahedra) with a Neel temperature similar to that of goethite. Hence it may be necessary to distinguish between truly amorphous ferric hydroxide gel and a more crystalline material. Ferrihydrite appears to be somewhere in between; depending on formation conditions, we may expect variable magnetic and consequent spectral behavior. The δ- and δ'-FeOOH phases, although disordered, do exhibit magnetic behavior. Okamoto [1968] has proposed that variations in the magnetic moment result from variations in ordering between two octahedral layers. For an equal population, the net magnetic moment is zero, and the material is antiferromagnetic. Other investigators, however, believe that super exchange occurs between Fe^{3+} ions occupying both an octahedral and a tetrahedral sublattice [e.g., Simpson, 1962].

An examination of the visible region absorption features in the spectra of Mars indicates that the absorption coefficient of the $^6A_1 \rightarrow {}^4A_1$, ^4E transition associated with the Martian Fe^{3+} material is smaller than that associated with the crystalline iron oxide phases. The same may be true regarding the $^6A_1 \rightarrow {}^4T_1$ transition; however, this feature is much weaker and may be suppressed by the presence of interfering components (e.g., Figures 11 and 12). Although further laboratory mixing experiments

and improved low temperature spectra may provide additional hypotheses, we tentatively suggest that the bulk of the Martian regolith Fe^{3+} occurs in a magnetically disordered phase. Possible candidates include amorphous gels [Evans and Adams, 1980], ferric sulphates, and, perhaps, some materials resembling ferrihydrite and feroxyhyte.

If taken further, the above considerations could imply that the magnetic material in the Martian regolith [Hargraves et al., 1979] is a different phase from that giving rise to the visible region absorption features. Magnetite and some Fe^{2+}-bearing maghemites exhibit rather featureless spectra with a low and fairly uniform reflectance in the visible and near infrared. The low reflectance in the near infrared spectra of Mars would be consistent with these phases being present; however, both materials frequently give rise to a negative slope in this spectral range which, although present in the dark region spectra [Singer et al., 1979], is absent from the bright region spectra.

An alternative hypothesis to explain the spectral characteristics of the Martian bright regions and materials which have been proposed as Martian analog materials [Evans and Adams, 1980; Singer, this issue] is that crystalline Fe oxides are in fact present yet occur as colloidal crystallites dispersed in a second medium. The effect of particle scattering might diminish spectral features in such cases. Application of Kebulka-Munk theory to colloidal dispersions is more complicated, however, since the spectral behavior of the dispersed phase will be a function of the refractive index of the host medium [Kortum, 1969]. This problem requires further investigation. In particular, it is of interest to know whether x-ray amorphous palagonites contain magnetically disordered Fe^{3+} in an amorphous host material or if these materials contain colloidal particles of crystalline ferric oxides (D. M. Sherman and R. B. Singer, manuscript in progress).

Given the present knowledge of the Martian regolith chemistry at the two Viking Lander sites, it is difficult to constrain the occurrence of a given iron oxide phase on the basis of genetic considerations alone. It is interesting to note that akaganeite and lepidocrocite require SO_4^{2-} and Cl^- for their formation and that both ions appear to be present in the Martian soil [Toulmin et al., 1977]. The suggestion that peroxides and superoxides might be present [Oyama and Berdahl, 1977] would open the possibility of ferrimagnetic δ-FeOOH formation. Although usually biogenic, the formation of ferrihydrite and related materials only requires rapid hydrolysis of Fe^{3+}, and hence a variety of inorganic formation pathways might be possible.

Amorphous materials are thermodynamically unstable and, with aging, will transform to more crystalline phases. The transformation of ferrihydrite and feroxyhyte to hematite and goethite, respectively, occurs via redissolution of the former phases. In the absence of liquid water, therefore, the poorly crystalline materials could persist metastably. As mentioned previously, the presence of silica appears to stabilize the amorphous ferric gels and ferrihydrite. Hence materials analogous to the synthetic iron silica gels might persist on the Martian regolith. Some (or all) palagonites might fall into this category although further characterization of these materials is necessary. If truly amorphous or poorly ordered Fe^{3+} bearing materials are actually present on Mars, then there may be some important implications. In general, such materials require very rapid kinetics for formation (e.g., fast hydrolysis of Fe^{3+} or fast oxidation of Fe^{2+}). The existence of amorphous materials might imply that weathering on Mars is a very transitive phenomenon and not a slow continuous process such as gas-solid or photochemical weathering.

Conclusions

Iron oxides have a high optical depth (low absorption coefficient) in the spectral region between 1.0 and 2.2 μm. The low reflectivity (ca. 0.4) of the Martian bright regions in this spectral region may be attributed to the presence of an opaque phase or may indicate that the Fe^{3+}-bearing materials occur as coatings on a low reflectance substrate (e.g., ferromagnesian silicate minerals).

The most diagnostic spectral region is between 0.3 and 1.0 μm where the iron oxide phases are strongly absorbing. In the spectra of iron oxide phases, the spin-forbidden crystal field absorption features are intensified by antiferromagnetic (or ferromagnetic) coupling between adjacent Fe^{3+} ions in the crystal structure. Hence there exists some correlation between the spectral behavior and magnetochemistry among these materials. The nature of the visible region absorption edge in the Martian bright region spectra indicates that the absorption coefficients of the $^6A_1 \rightarrow {}^4A_1$, ^4E and $^6A_1 \rightarrow {}^4T_2$ transitions associated with the predominant Fe^{3+}-bearing material on Mars are much smaller than those associated with the iron oxides. These observations are consistent with the presence of magnetically disordered amorphous materials or poorly crystalline ferrihydrite and feroxyhyte, where there is a frequently significant degree of cation disordering and a consequent lack of magnetic coupling.

If the iron oxide phase occurs as colloidal size crystallites dispersed in a second medium, the effect of particle scattering might also reduce band contrast and increase the reflectance in the visible region. Such an effect may allow some crystalline Fe^{3+} material to be present without introducing significant 'undesirable' spectral features, yet, at present, is poorly constrained in the absence of scattering coefficient data.

Acknowledgments. We wish to thank Henry Dick for goethite sample Alpha-2 collected during leg 5 of the Vulcan cruise, David Ross for feroxyhyte sample F-2 collected during leg 3 of the Chain 100 cruise, and Daniel Waite for providing synthetic specimens of goethite (sample Alpha-1) and akaganeite. We also wish to thank James Nakos who operated the MIT Center for Material Services and Engineering Transmission Electron Microscopes for us and Alan Kornacki and Ursula Marvin for assistance in the use of the

Smithsonian Astrophysical Observatory Microprobe. This work was supported by NASA grant NSG 7604.

References

Bernal, J. D., D. R. Dasgupta, and A. L. Mackay, The oxides and hydroxides of iron and their structural inter-relationships, Clay Miner. Bull., 4, 15-30, 1959.

Binder, A. B., and J. C. Jones, Spectrophotometric function, composition, and distribution of the surface materials of Mars, J. Geophys. Res., 77, 3005-3019, 1972.

Carlson, L., and U. Schwertmann, Natural occurence of feroxyhyte (δ'-FeOOH), Clays Clay Miner., 28(4), 272-280, 1980.

Carlson, L., and U. Schwertmann, Natural ferrihydrites in surface deposits from Finland and their association with silica, Geochim. Cosmochim. Acta, 45, 421-429, 1981.

Chukhrov, F. V., B. B. Zvyagin, L. P. Ermilova, and A. I. Gorshkov, New data on iron oxides in the weathering zone, Proc. Int. Clay Conf., 1972, 333-341, 1973a.

Chukhrov, F. V., B. B. Zvyagin, A. I. Gorshkov, L. P. Yermilova, and V. V. Balashova, Ferrihydrite, Int. Geol. Rev., 16, 1131-1143, 1973b.

Chukhrov, F. V., L. P. Ermilova, B. B. Zvyagin, and A. I. Gorshkov, Genetic system of hypergene iron oxides, Proc. Int. Clay Conf., 1975, 275-286, 1976.

Chukhrov, F. V., B. B. Zvyagin, A. I. Gorshkov, A. I. Yermilova, V.V. Korovushkin, Ye. S. Rudnitskaya, and N. Yu. Yakubovskaya, Feroxyhyte, a new modification of FeOOH, Int. Geol. Rev., 19, 873-890, 1977.

Clark, R. N., and T. L. Roush, Reflectance spectroscopy: quantitative analysis techniques for remote sensing applications, J. Geophys. Res., submitted, 1982.

Daniels, J. M., and A. Rosencwaig, Mossbauer spectroscopy of stoichiometric and non-stoichiometric magnetite, J. Phys. Chem. Solids, 30, 1561-1571, 1969.

Evans, D. L., and J. B. Adams, Amorphous gels as possible analogues to Martian weathering products, Lunar Planet. Sci. XI, 271-272, 1980.

Ferguson, J., H. J. Guggenheim, and Y. Tanabe, The effects of exchange interactions in the spectra of octahedral manganese, II, Compounds, J. Phys. Soc. Jpn., 21(4), 692-704. 1966.

Giovanoli, R., and R. Brütsch, Dehydration of δ-FeOOH: Direct observation of the mechanism, Chimia, 28, 188-191, 1974.

Graham, M. J., D. A. Channing, G. A. Swallow, and R. D. Jones, A Mossbauer study of the reduction of hematite in hydrogen at 535°C, J. Mater. Sci., 10, 1175-1181, 1975.

Haggarty, S. E., Oxidation of opaque mineral oxides in basalts, in Oxide Minerals, Mineralogical Society of America, Washington, D.C., Nov. 1976.

Hargraves, R. B., D. W. Collinson, R. E. Arvidson, and P. M. Cates, Viking magnetic properties experiment: Extended mission results. J. Geophys. Res.,84, 8379-8384, 1979.

Hovis, W. A., Infrared reflectivity of iron oxide minerals, Icarus, 4, 425-430, 1965.

Hunt, G. R. and R. P. Ashley, Spectra of altered rocks in the visible and near infrared, Econ. Geol., 74, 1613-1629, 1979.

Hunt, G. R., and J. W. Salisbury, Visible and near-infrared spectra of minerals and rocks: I. silicate minerals, Mod. Geol., 1, 283-300, 1970.

Jackson, T. A. and W. D. Keller, A comparative study of the role of lichens and "inorganic" processes in the chemical weathering of recent Hawaian lava flows, Am. J. Sci., 269, 446-466, 1970.

Kortum, G., Reflectance Spectroscopy, Interscience, New York, 1969.

Langmuir, D. Particle size effect on the reaction goethite=hematite + water, Am. J. Sci. 271, 147-156, 1976.

Lohr, L. L., Spin-forbidden electronic excitations in transition metal complexes, Coord. Chem. Rev., 8, 241-259, 1972.

Mao, H. K. and P. M. Bell, Crystal field effects of ferric iron in goethite and lepicrocite: Band assignments and geochemical applications at high pressure, Year Book Carnegie Inst., Washington, 73, 502-507, 1974.

Marusak, L. A., R. Messier, and W. B. White, Optical absorption spectrum of hematite, Fe_2O_3 near IR to UV (abstract), EOS Trans. AGU, 60(18), 416, 1979.

McCord, T. B. and J. B. Adams, Spectral reflectivity of Mars, Science, 163, 1058-1060, 1969.

Morris, R. V. and S. C. Neely, Diffuse reflectance spectra of pigmentary-sized iron oxides, iron oxyhydroxides and their mixtures: Implications for the reflectance spectra of Mars, Lunar Planet. Sci., XII, 723-725, 1981.

Morris, R. V., and S. C. Neely, Optical properties of hematite-magnetite mixtures: implications for Mars, Lunar Planet. Sci. XIII, 548-549, 1982.

Muller, O., R. Wilson and W. Krakow, δ-FeOOH and its solid solutions, 1, Preparation and crystal chemistry, J. Mater. Sci., 14, 2929-2936, 1979.

Murray, J. W., Iron oxides, in Marine Minerals, edited by R. G. Burns, Mineralogical Society of America, Washington, D.C., 1979.

Okamoto, S., Structure of δ-FeOOH, J. Am. Ceram. Soc., 51(10), 594-599, 1968.

Okamoto, S., and S. Okamoto, Coprecipitation of divalent metal ions in solution by ferrous hydroxide gel formation, Yogyo Kyokaihi, 85(10), 518-522, 1977.

Okamoto, S., H. Sekizawa and S. I. Okamoto, Characterization and phase transformation of amorphous ferric hydroxide, in React. of Solids, Proc. Int. Symp. 7th, 1972.

Osborne, M. D., K. M. Parkin, and R. G. Burns, Temperature dependence of Fe-Ti spectra in the visible region: Implications to mapping Ti concentrations of hot planetary surfaces, Proc. Lunar Planet. Sci. Conf., 9th, 2949-2960, 1978.

Oyama, V. I., and B. J. Berdahl, The Viking gas exchange experiment results from Cryse and Utopia surface samples, J. Geophys. Res., 82, 4669-4680, 1977.

Robin, M. B. and P. Day, Mixed valence chemistry--A survey and classification, Adv. Inorg. Chem. Radiochem., 10, 247-423, 1967.

Rossman, G. R., Spectroscopic and magnetic studies of ferric iron hydroxy sulfates: Intensification of color in ferric iron clusters bridged by a single hydroxide ion, Am. Mineral., 60, 698-704, 1975.

Rossman, G. R., Spectroscopic characteristics and magnetic studies of ferric iron hydroxyl sulphates - The sines $Fe(OH)SO_4 \cdot N_2O$ and the jarosites, Am. Mineral., 61, 398-404, 1976.

Russell, J. D., Infrared spectroscopy of ferrihydrite: Evidence for the presence of structural hydroxyl groups, Clay Miner. 14, 109-114, 1979.

Sagan, C., J. Phaneuf, and M. Ihmat, Total reflection spectrophotometry and thermogravimetric analysis of simulated Martian surface material, Icarus, 4, 43-61, 1965.

Simpson, A. W., Some superparamagnetic properties of fine particle δ-FeOOH, J. Appl. Phys., 33, 1203-1205, 1962.

Singer, R. B., Spectral evidence for the mineralogy of high albedo soils and dusts on Mars, J. Geophys. Res., this issue.

Singer, R. B., T. B. McCord, R. N. Clark, J. B. Adams, and R. L. Huguenin, Mars surface composition from reflectance spectroscopy: A summary, J. Geophys. Res., 84(B14), 8415-8426, 1979.

Suzdalev, I. P., Superparamagnetism of antiferromagnetic particles of ultramicro size, Proc. Conf. Appl. Mossbauer Eff., 1969, 193-196, 1971.

Taylor, R. M. and U. Schwertmann, Maghemite in soils and its origin, I, Properties and observations on soil maghemite, Clay Miner., 10, 289-298, 1974a.

Taylor, R. M. and U. Schwertmann, Maghemite in soils and its origin, II, Maghemite synthesis at ambiant temperature and pH = 7, Clay Miner., 10, 299-310, 1974b.

Toulmin, P., A. K. Baird, B. C. Clark, K. Keil, H. J. Rose, R. P. Christian, P. H. Evans, and W. C. Kelliher, Geochemical and mineralogical interpretation of the Viking inorganic chemical results. J. Geophys. Res., 82, 4625-4634, 1977.

Towe, K. M. and W. F. Bradley Mineralogical constitution of colloidal "hydrous ferric oxides," J. Colloid Sci., 24, 384-392, 1967.

Wendlandt, W., and H. G. Hecht, Reflectance Spectroscopy, Springer-Verlag, New York, 1969.

(Received November 16, 1981;
revised March 25, 1982;
accepted April 16, 1982.)